Measurement of the $t\bar{t}$ Production Cross Section in $p\overline{p}$ Collisions at $\sqrt{s} = 1.96$ TeV

A thesis presented

by

Salvatore Rocco Rappoccio

to

The Department of Physics

in partial fulfillment of the requirements

for the degree of

Doctor of Philosophy

in the subject of

Physics

Harvard University

Cambridge, Massachusetts

August 2005

Thesis advisor

Andrew Foland

Author

Salvatore Rocco Rappoccio

Measurement of the $t\bar{t}$ Production Cross Section in $p\overline{p}$ Collisions at $\sqrt{s} = 1.96$ TeV

Abstract

We present the measurement of the $t\bar{t}$ cross section in the lepton plus jets channel with ≥ 1 and ≥ 2 secondary vertex tags. We use the scalar sum of transverse energies of the event (H_T) to discriminate $t\bar{t}$ from the other backgrounds. We also use the transverse mass of the leptonic W-boson (M_T^W) to further reduce the Non-W backgrounds. We use a combination of data and Monte Carlo to estimate the backgrounds from electroweak processes, single top, fake leptons, $W+$ Light Flavor fake tags, and real $W+$ Heavy Flavor production.

We obtain a value of $\sigma_{\geq 1} = 8.7^{+0.9}_{-0.9}(stat)^{+1.2}_{-0.9}(sys)$ pb for the ≥ 1 tag cross section, and $\sigma_{\geq 2} = 8.7^{+1.8}_{-1.6}(stat)^{+1.9}_{-1.3}(sys)$ pb for the ≥ 2 tag cross section.

We also present a measurement of the $t\bar{t}$ cross section by fitting the N_{jet} spectrum. We combine the $= 1$ and ≥ 2 tag cross sections to obtain $\sigma_{t\bar{t}} = 8.9^{+0.9}_{-0.9}(stat)^{+1.4}_{-1.3}(syst)pb$.

Dedicated to my wife Roberta, and my family, those here and who have gone before us.

Acknowledgments

I would like to thank my advisors, Andrew Foland and Melissa Franklin. It would be hard to find a pair of people whose enthusiasm for interesting physics is paralleled only by their capability to do it. Andy would always be there with insightful ideas and new things to try (plus a Poisson probability calculator chip installed somewhere in his brain). Melissa would always be there to point out the very stupid things I was doing wrong by asking very simple questions. I would also like to thank Nima Arkani-Hamed for being an enthusiastic member of my advisory committee, and for having interesting insights and explanations for very complicated phenomena.

João G. P. Guimarães da Costa has been a constant guiding influence throughout my graduate career. We have worked together through many trials and tribulations from mistag matrices to tagger optimizations. We've had our share of "creative differences" over the years, but we always end up with the physics done. So thanks very much, I really appreciate the help you've given me.

I would also like to thank Lester Miller, Steve Nahn, and Rainer Wallny for showing me everything there is to know about the wonderful and beautiful world of SRC firmware development and the silicon readout system! I'd never realize that I could personally make a silicon SPL's facial color map the IMON coloring scheme (normal to pink to red). It's still referred to as "The SRC Incident of Feb 28, 2003". Ahem. I can't thank Sebastian Grinstein and Marcel Stanitzki enough for rounding out our little troupe of dwarves, and for teaching me how to stomp properly when looking for grounding loops, and for buying Jobu his chicken. Don't worry, I didn't forget about the CMX days. Phil Schlabach and Abraham Gallas taught me a whole lot about muon chambers and how to run one. And how to say the word "drogie".

Also, at Boston University, I would like to thank John Butler for giving me a chance and instilling in me a desire to do high energy particle physics, and Bernie Chasan, who was an excellent academic advisor.

My wife and my love, Roberta, without whom I would be nowhere, from the bottom of my heart, thank you. Thanks for putting up with my late nights and giving me unconditional love. And most of all, for moving with me to my Exile in Flatland, which simultaneously gave us great gifts and great heartaches. But we're almost done, babe!

I would also like to thank my parents, Paul and Arlene Rappoccio, for teaching me the important things in life, for giving constant support and love, and for believing in my dreams. Even when they entailed moving away from 125 Southern Blvd.

My grandparents have always been a constant source of love and inspiration. My grandfather Salvatore was always there to tell me stories about growing up with eight older siblings in Italia (like how he used to eat bread out of the oven before dinner so he'd have enough to eat!). My grandmother Angelina taught me the value of piety and hard work, and is always happy to see her grandchildren. My grandfather Rocco was always there with choice words of wisdom I carry to this day, like "Water and electricity don't mix, daddy boy, they don't mix. That's how I lost my finger!" And last but not least, I would like to thank my grandmother Diane, for always being

there to share a story that would make your sides split, and for singing "You and Me Against the World."

I would also like to thank my godparents, Rocco Russo and Carmella Rappoccio-Daubney, whose guidance is a beacon of hope and love, and the rest of my aunts and uncles, Aunt Judy, Zia Caterina, Uncle Tony, and Uncle Donny (aka Uncle Bo!).

Get comfortable, this is going to take awhile. I have a big family I want to thank: Peter, Paul, Rocco, and Edward, forever my partners in crime, The High Council, The Fratelli, Boney Arrows and Tomahawks exclusively, (I wonder if Nana's been bad recently?), you guys have been my best friends forever; Gina and Rich, my goddaughter Julia, and baby Leah, for being such loving and accepting people, and for showing us such a great exhibit in Chicago; Tina, for never being afraid to be herself; Genaro, for the days on Leedale Street playing ... well, we won't tell people what we were playing, they still haven't figured it out; Angela, for never letting me take myself too seriously; Diana, whose faith is an inspiration to all around her; Maria, making herself famous down in Atlanta; Joseph, who never fails to bring laughs where he goes; Helen, for dreaming of places to be seen; Domenica, for being such a good poet; Deanna, my other bookend, following her heart where she goes (and she'll go far, don't worry); Anthony, who never stops smiling; William, my godson, beaming love and exuberance wherever he waddles; Beckie, my sister-in-law, who will someday make her life one big fabulous shabby-chic dream; Danny, my brother-in-law, quietly helpful and generous; Karen, my mother-in-law, always accepting of those around her; Pam, Brian, Daniel, Francesca, and Mikayla for always being there for us; Julie and Tom, forever our "coffee-talk" buddies; Andrew, Cathy, Mike, and Destiny, my home away from home, the Boston crew; and Uncle Mike, may he rest in peace.

High energy physics at Harvard (and indeed the universe, or at least the restaurant at the end of it) would not be the same without the past, present, and honorary members of the LaPaPhyCo (fka HuHepl) crew (and/or Moving Company): Ayana, Daniel, Ingyin, Yosi, JP, Robyn M., George, Robyn S., John, Sarah, Nate, Guy, Alexei, Carter, Stephen, Devin, Sharon, and Kevin (and anyone else I've missed). "I was talking to the Top Cross Section. It hates me. No one wants to listen to me anymore. I'll finish my analysis, but I won't enjoy it." Daniel, I finished by August, I think you owe me a burrito. But seriously, where are we going for lunch? A special thank you goes to Andre and Irina, our co-conspirators in our crazy schemes in life. What is it now, vinyard in Tuscany? Or are we still travelling the world six months out of the year? Thanks for letting us keep dreams alive.

Karate played a big role in getting this analysis done. Trust me. So, Sensei, Cynthia, Tricia, Steve, Sammy, Josh, Tina, Fearghal, Otomu, Kihn, Michelle, Jen, Geoff, ChiChi, Jim, Geoff, Marius, Carlos, Ritchie, Inbal, Kate, Eric, Roberto, and all the rest of the dojo crew, thanks so much. To the members of Bar Club, "I caught you a delicious bass" while I was on the "Sloop John B".

My dogs and I would like to thank Aimee, Colleen, Terry, Betty, and Pam for the wonderful times and for introducing us to agility.

Finally, in the words of Galileo Galilei, who should be cannonized for believing in truth when others ridiculed him,

> *I do not feel obliged to believe that the same God who has endowed us with sense, reason, and intellect has intended us to forgo their use.*

They are not forgone, so I thank God for giving us these gifts, to use in the pursuit of truth. Or beauty, but that's someone else's thesis.

Contents

List of Figures

List of Tables

Chapter 1

Theory

The top quark is one of the most interesting particles currently accessible in particle physics. It is a very special fermion with a very large mass, much larger than any other fermion. As such, understanding the top quark's properties is essential to understanding the mechanism that gives rise to mass. It is also possible that new physics is present in the top quark data sample, and so it is important to understand all the different aspects of its production and decay.

This analysis examines the production cross section for $t\bar{t}$ events at $\sqrt{s} = 1.96$ TeV. This section examines the theoretical overview of phenomenology associated with the top quark's properties, production and decay.

1.1 The Standard Model

The Standard Model (SM) of particle physics ([3]-[4]) is a quantum field theory describing the dynamics of particles that interact via the electromagnetic, weak, and

strong interactions. Gravity is the weakest force and is not included in the SM. Numerous attempts have been made to include gravity, but none have been experimentally verified.

There are two types of particles that occur in nature, fermions (particles with half-integer spins) and bosons (particles with integer spins). In the SM, the force carries are all bosons, and the "matter" particles are all fermions. Each force has at least one force carrier boson. The electromagnetic force is mediated by the *photon* (γ). The strong force is mediated by a set of eight bosons collectively referred to as *gluons*. The weak interaction is mediated by three bosons, the W^+, W^-, and Z_0. The electromagnetic and weak interactions are actually the same force at high energies, and has implications for the dynamics associated with them (i.e. they are manifestations of the same underlying symmetry principle. See Appendix A.1.6 for details.)

The fermions are split into two categories, quarks and leptons. Quarks are "strongly interacting," i.e. they participate in the strong interaction. All the fermions participate in the weak interactions, and all the charged particles interact in the electromagnetic interaction [5].

Each fermion is coupled with a partner fermion via the weak interaction. Quarks are coupled with other quarks, and leptons are coupled with other leptons. Each pair is called a "generation" or a "family" of particles.

The first generation of particles is composed of the up and down quarks, and the electron and electron-type neutrino. These four particles construct almost all of everyday matter. The up and down quarks combine to make protons and neutrons,

which combine to make nuclei. Atoms are made of nuclei combined with electrons, and the neutrino partakes in nuclear decay.

There are two remaining generations, composed of the charm and strange quarks, the top and bottom quarks, the muon and muon-type neutrino, and the tau lepton and the tau-type neutrino. These generations are very similar to the first one, except for the particles' masses. There is a very vast discrepancy between the different masses of the fermions seen in nature. The least massive particles (the neutrinos) have masses very close (but not equal) to zero, while the top quark is as massive as an entire gold atom ($\sim 170 - 180$ GeV/c^2). Table 1.1 shows the hierarchy of the fermions along with their masses [6]. Figure 1.1 shows the mass of the various quarks. It is clear to see that the top quark has an abnormally large mass.

The question of why the top quark is so heavy compared to the rest of the fermions remains an open question. Thus, understanding the properties of the top quark is essential to fundamentally understand the mechanism that gives rise to mass. This thesis is devoted to the measurement of the production cross section of this particle.

		Generation		
		1	2	3
Quarks	Q= $+\frac{2}{3}$	up (u), $m_u \sim 1.5 - 4.5$ MeV/c^2	charm (c), $m_c = 1.3$ GeV/c^2	top (t), $m_t = 170 - 180$ GeV/c^2
	Q= $-\frac{1}{3}$	down (d), $m_d \sim 5.0 - 8.5$ MeV/c^2	strange (s), $m_s \sim 80 - 155$ MeV/c^2	bottom (b), $m_b = 4.2$ GeV/c^2
Leptons	Q= -1	electron (e), $m_e = 0.511$ MeV/c^2	muon (μ), $m_\mu = 106$ MeV/c^2	tau (τ), $m_\tau = 1.78$ GeV/c^2
	Q= 0	electron neutrino (ν_e), $0 < m_{\nu_e} < 3$ eV/c^2	muon neutrino (ν_μ), $0 < m_{\nu_\mu} < 0.2$ MeV/c^2	tau neutrino (ν_τ), $0 < m_{\nu_\tau} < 18.2$ MeV/c^2

Table 1.1: Fermion family structure.

For a more detailed overview, see Appendix A.1.

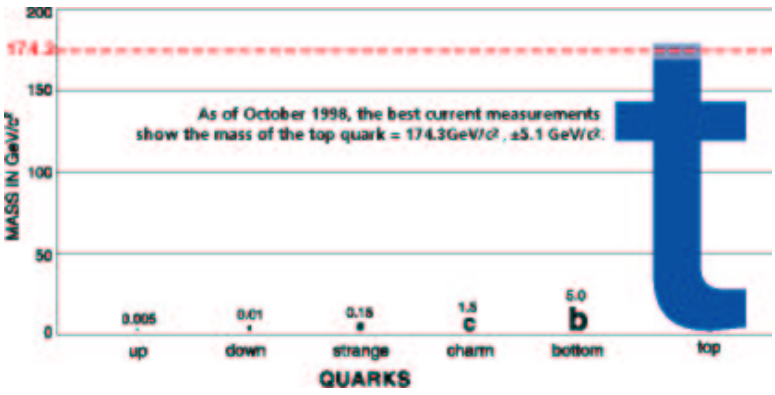

Figure 1.1: Masses of quarks.

1.2 Electroweak Symmetry Breaking

As discussed in detail in Appendix A.1.7, it is possible to introduce *spontaneous electroweak symmetry breaking* into the Standard Model by the addition of extra gauge fields that give the electroweak gauge fields longitudinal polarization (i.e. mass) without upsetting the underlying theory. In the $SU(2)_L \otimes U(1)_Y$ symmetry in the SM, one introduces a complex *doublet* of gauge bosons

$$\phi = \begin{pmatrix} \phi^+ \\ \\ \phi^0 \end{pmatrix} \tag{1.1}$$

which carries four degrees of freedom. The Lagrangian to be associated is

$$\mathcal{L} = \frac{1}{2}(D_\mu \phi)^\dagger (D^\mu \phi) + \frac{1}{2}\mu^2(\phi^\dagger \phi) - \frac{1}{4}\lambda^2(\phi^\dagger \phi)^2 \tag{1.2}$$

Figure 1.2(a) shows a 2-D representation of this potential, and 1.2(b) shows a 1-D projection around the z-axis.

Three of the four degrees of freedom become the longitudinal components of the W and Z bosons (hence giving them mass), and the last degree of freedom becomes

another gauge boson, the *Higgs boson*. The photon remains massless in the theory, as is seen from experiments.

The graphical interpretation is that if we examine Figure 1.2(a), the massless field moves along the "valley" of the potential, while the massive field oscillates up and down the "hills" of the potential. The vacuum expectation value (v) of the Higgs potential is the place where the potential has a minimum. It can be determined from the W mass, and is given by

$$v = \frac{\mu}{\lambda} = \frac{1}{\sqrt{\sqrt{2}G_F}} = 246\ GeV \tag{1.3}$$

It is also necessary to use the Higgs mechanism to give all the fermions mass. Without a Higgs, the fermions cannot have mass terms due to gauge symmetry. However, it requires the introduction of a parameter for each fermion in the theory that is completely unconstrained theoretically.

That is, for each fermion f, a term is added to the Lagrangian that has the form

$$\mathcal{L}_{Yukawa} = -\frac{1}{\sqrt{2}}\lambda_f H f \bar{f} \tag{1.4}$$

$$\equiv -(\sqrt{2}G_F)^{\frac{1}{2}} m_f H f \bar{f} \tag{1.5}$$

The Yukawa couplings λ_f are unconstrained (and hence are the masses).

The top quark turns out to have a very large Yukawa coupling (very close to unity). It is given by

$$\lambda_t = \frac{v}{\sqrt{2}} m_t \tag{1.6}$$

If $m_t = 175\ GeV/c^2$, $\lambda_t = 0.99$. A value so nearly equal to the number 1 could mean that the top quark plays an important role in EWSB. It is therefore necessary to understand all the physics associated with the top quark.

Additionally, because of its large mass, the top quark can be used to constrain the Higgs mass, as we shall now examine.

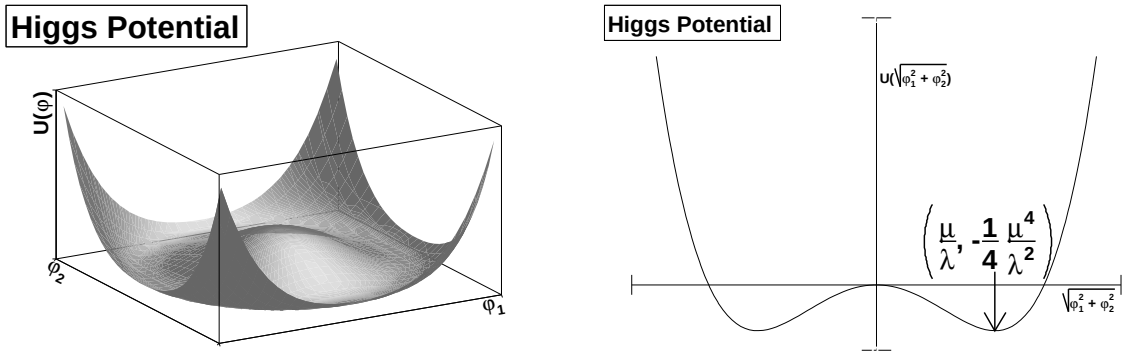

(a) (b)

Figure 1.2: Higgs mechanism potential and projection around the z axis.

1.2.1 Constraints on Higgs Mass

Due to its large mass, the top quark contributes significantly to the masses of the W and Z bosons via loop diagrams as in Figures 1.3(a) and 1.3(b). The Higgs boson also contributes to radiative corrections as in Figures 1.3(c) and 1.3(d). The ratio ρ is defined as

$$\rho = \frac{M_W^2}{M_Z^2}(1 - \sin\theta_W) = 1 + \Delta r \tag{1.7}$$

where Δr is the radiative correction and is given by

$$\Delta r = \frac{3G_F}{8\pi^2\sqrt{s}}M_t^2 + \frac{\sqrt{2}G_F}{16\pi^2}M_W^2\left[\frac{11}{3}\log\left(\frac{M_H^2}{M_W^2}\right)\right] \tag{1.8}$$

We see that this ratio has a quadratic correction from the top quark mass, and a logarithmic correction from the Higgs mass.

Thus, simultaneously measuring $\sin\theta_W$, the W, Z, and top quark masses can give an indirect measurement of the Higgs mass. Because the uncertainty is dominated by the W and top masses, it is a good approximation to consider the other parameters as fixed.

Figure 1.4(a) shows the W boson mass versus the top quark mass. The allowed values of the Higgs mass are given in diagonal bands. The 68% contours are from measurements of the W and top masses, and precision electroweak data.

The most probable value (taking into account all the precision electroweak data plus top quark mass measurements) is

$$m_H = 98^{+52}_{-38}\, GeV/c^2 \tag{1.9}$$

Figure 1.4(b) shows the χ^2 fit to all the data. Note that LEP has excluded Higgs masses below 114 GeV/c^2 by direct measurements. These are shown in the yellow band in Figure 1.4(b).

Therefore, the mass of the top quark constrains the mass of the Higgs boson. Although this uses the simplest Higgs model for illustrative purposes, similar constraints can be applied to other models. The top's suspiciously large Higgs coupling and its obvious difference in mass from all the other fermions motivates a close examination of its properties.

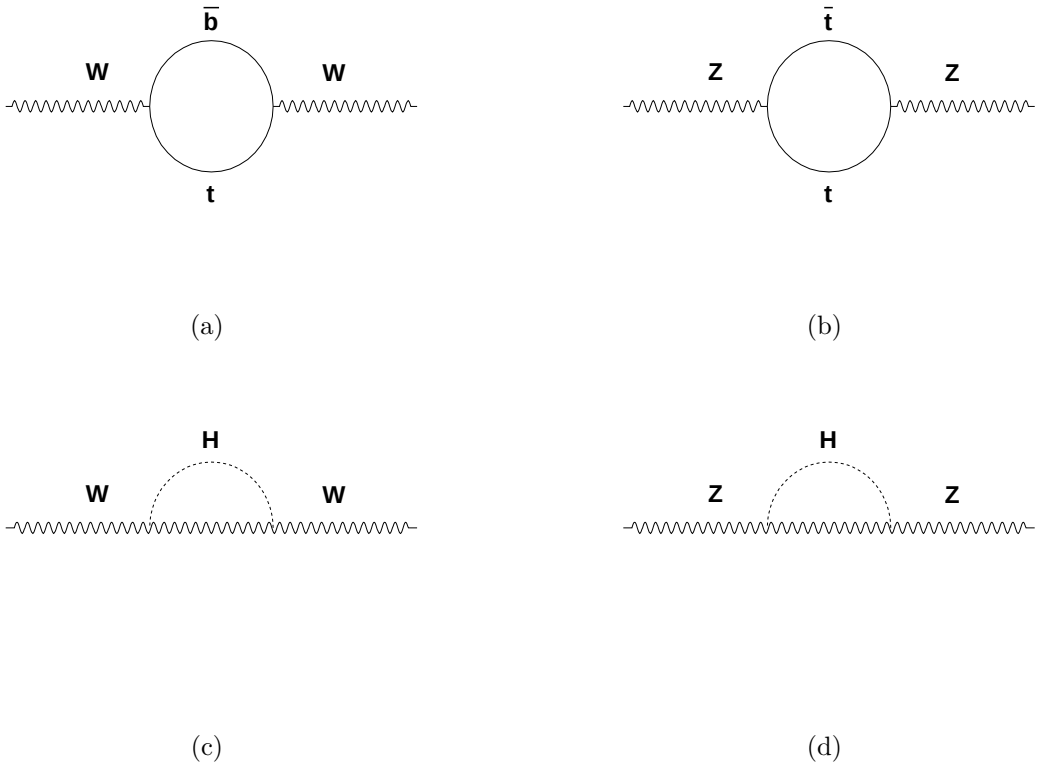

(a) (b)

(c) (d)

Figure 1.3: Corrections to W and Z masses due to loop diagrams involving top quarks and the Higgs boson.

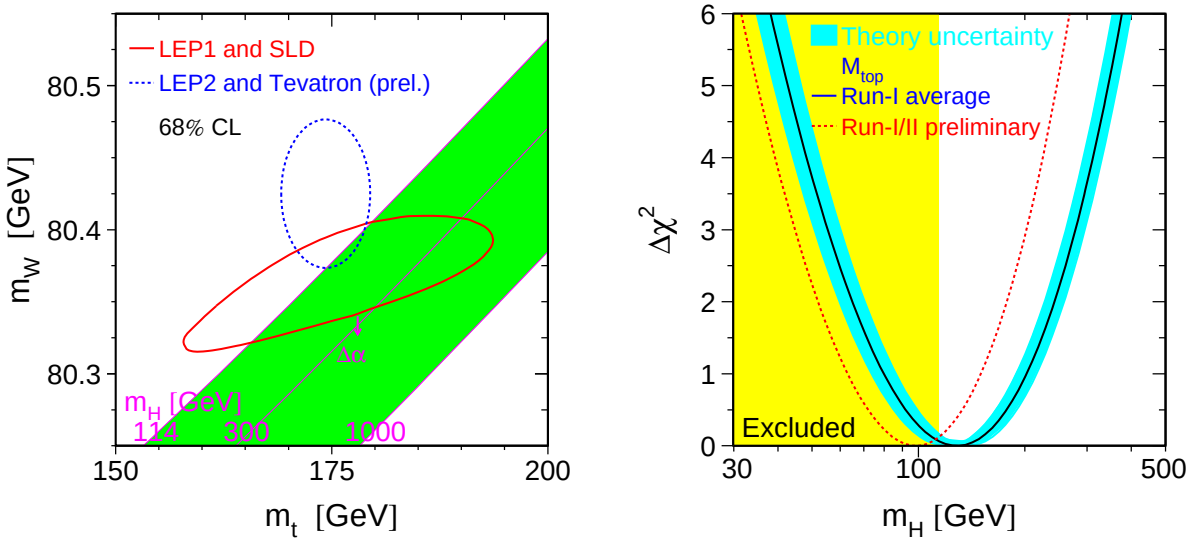

(a) Top mass versus W mass, and constraints on Standard Model Higgs boson mass (diagonal bands). The red curve is taken from indirect measurements at LEP1 and SLD, while the ellipse is taken from direct measurements at LEP2 and the Tevatron.

(b) χ^2 fit to all electroweak and top mass measurements for the Higgs mass. The yellow band is directly excluded by LEP, and the blue band is the theoretical uncertainty.

Figure 1.4: Constraints on Higgs mass given experimental data.

1.3 Quantum Chromodynamics (QCD)

The top quark is primarily pair-produced via the strong interaction at $p\overline{p}$ colliders. Thus, the interaction that is of primary interest for the $t\overline{t}$ production cross section is quantum chromodynamics (QCD). A full overview is given in Appendix A.1.8.

There are some theoretical challenges involved in making QCD calculations. It turns out that the coupling constant for QCD at low energy is close to unity, making perturbative calculations impossible.

However, it turns out that the coupling strength decreases with increasing energy, a trend opposite to QED. This is referred to as *asymptotic freedom*. The running coupling constant for QCD is given by [7]

$$\alpha_s(|q^2|) = \frac{\alpha_s(\mu^2)}{1 + (\alpha_s(\mu^2)/12\pi)(11n - 2f)\log\left(|q^2|/\mu^2\right)} \tag{1.10}$$

where n is the number of colors (3 for the SM), f is the number of flavors (6 in the SM), and μ is an arbitrary cutoff of the integral which diverges for low energies. If $11n > 2f$, the theory has antiscreening. This equation is only valid for $|q^2| \gg \mu^2$.

Notice that we cannot simply expand the running coupling starting from low-q^2 scales. That is precisely where the theory breaks down. Instead, we introduce a minimum scale for the QCD interaction. Introducing the quantity

$$\log \Lambda^2_{QCD} = \log \mu^2 - 12\pi / \left[(11n - 2f)\alpha_s(\mu^2)\right] \tag{1.11}$$

the running coupling constant becomes

$$\alpha_s(|q^2|) = \frac{12\pi}{(11n - 2f)\log\left(|q^2|/\Lambda^2_{QCD}\right)} \tag{1.12}$$

(see Appendix A.1.5 for details).

Λ is in principle calculable, but it is difficult to measure experimentally. It seems to be roughly $100 - 500\ MeV/c$. However, the fact that this parameter is not well-known presents difficulties when making QCD calculations, and is often a large source of theoretical uncertainty (as is the case for $t\bar{t}$ production). This is in addition to the theoretical uncertainty associated with the q^2 scale at which to evaluate α_s. We will use $q^2 = m_t^2$, and vary the scale from $m_t^2/4$ to $4m_t^2$ as a probe of systematic uncertainty.

Once we are in the regime in QCD where the coupling strength is weak ($\alpha_s < 1$), calculating quantum mechanical amplitudes is similar to QED as described in Section A.1.4. However, the $SU(3)$ symmetry in QCD means that there are vertices between the gluons themselves. Figure 1.5 shows the various couplings allowed in QCD.

There are several phenomenological implications of the peculiarities of QCD.

Firstly, due to the fact that quarks and gluons are confined within hadrons, it is impossible to make beams of bare quarks and gluons for colliding. Thus, it is necessary to understand the distribution of quarks and gluons within the hadrons we can collide. These are called *parton distribution functions*.

Secondly, quark confinement requires that outgoing partons must combine with other quarks in order to form color-neutral hadrons. This process of *hadronization* will be discussed below.

Finally, because the coupling is strong at low energies for QCD, *initial and final state radiation* becomes very important when colliding hadrons.

We now discuss these phenomena in turn.

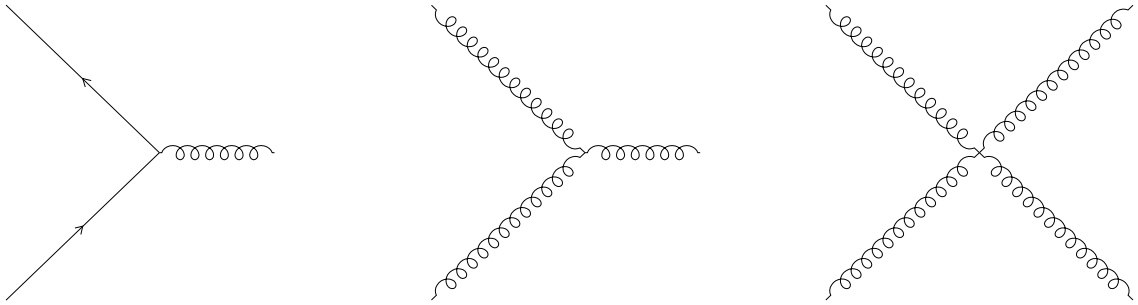

(a) (b) (c)

Figure 1.5: QCD vertices between fermions and gluons.

1.3.1 Parton Distribution Functions

Because of the asymptotically free nature of quarks within hadrons, the observable hadrons are not simple objects to deal with. While the hadron will have the same quantum numbers as it's simplest quark representation, there are large quantum fluctuations inside the hadrons that cause somewhat complicated behavior. There is no real idea of "constituent quarks", in that no single two or three quarks remains in existence for all time. Rather, the "quantum sea" of particles is constantly erupting into $q - \bar{q}$ pairs, with gluons interacting with all the quarks around and with each other. Figure 1.6(b) shows a typical situation, with quarks popping in and out of existence, exchanging gluons, producing gluons, etc.

All the types of quarks and gluons are present at some level in any given hadron (although some of them at undetectable levels). It is possible [8] to treat the underlying quarks and gluons as free in the limit of large momentum transfers. In

this limit, each parton carries some fraction of the total momentum of the hadron, $p_{parton} = xp_{hadron}$, where x is the fraction of momentum carried by the parton in question.

Thus, it is possible to construct probability densities (commonly referred to as *parton distribution functions*) that represent the probability that a parton q will carry a fraction x of the total momentum of the system. So, given a quark u, with probability density $u(x)$, the average momentum carried by that particle will be

$$\langle p \rangle = \int_0^1 xu(x)dx \tag{1.13}$$

These structure functions are extremely difficult to calculate theoretically. In practice, it is often easier to parameterize a given theory with experimentally verifiable factors, and use fits to data to extract the most appropriate PDF.

It is useful to separate "valence" quarks (i.e. those that contribute to the quantum numbers of the hadron) and "sea" quarks (i.e. those that are produced via $q - \bar{q}$ excitations of the vacuum).

$$u(x) = u_V(x) + u_S(x) \tag{1.14}$$

Given such definitions, the structure functions take the form

$$F_2(x) = \sum_i e_i^2 x f_i(x) \tag{1.15}$$

where x is the fraction of the hadron carried by parton i, $f_i(x)$ is the PDF, and e_i is the charge of the ith parton (For electromagnetic scattering, this is the electric charge. For hadron-hadron interactions, this is the coupling strength of that vertex.)

Thus, for example, for e-p scattering,

$$\begin{aligned} F_2(x) &= x\left(\frac{4}{9}\left[u_V(x)+u_S(x)+\bar{u_S}(x)\right]\right. \\ &+ \left.\frac{1}{9}\left[d_V(x)+d_S(x)+\bar{d_S}(x)+s_S(x)+\bar{s_S}(x)\right]+\ldots\right) \end{aligned} \tag{1.16}$$

The constraints on these structure functions come from requiring the overall hadron to have specific quantum numbers (i.e. charge). For a proton, for example, since it has strangeness of zero, all strange quarks come from the "sea", and so

$$\int_0^1 dx[s_S(x)-\bar{s_S}(x)]=0 \tag{1.17}$$

In fact, any quark from the sea must be accompanied by an antiquark of the same flavor, and so

$$\int_0^1 dx[q_S(x)-\bar{q_S}(x)]=0 \tag{1.18}$$

for any quark flavor q. Also, since the charge is 1,

$$\int_0^1 dx\left(\frac{2}{3}\left[u_V(x)\right]-\frac{1}{3}\left[d_V(x)\right]\right)=1 \tag{1.19}$$

Similar constraints can be formulated for other hadrons.

It is then possible to measure each contribution using electron or neutrino scattering experimental data. Given these tools, it is possible to calculate cross sections for hadronic processes at sufficiently high energy, even though the PDF's are theoretically not constrained. The usage of a particular PDF assumption is a systematic uncertainty on any result using them.

An example of a parameterization of some PDF's for the proton is given in Figure 1.6(a). This parameterization is taken from [9], and is for illustrative purposes.

We will use the PDF's in Ref [10, 11] for the calculation of the $t\bar{t}$ production cross section.

It must be noted that beyond the simplest parton model, the PDFs chosen depend on the momentum scale (Q^2) of the collision. Specifically, the full QCD expressions for scattering show that the probability for emission of gluons off of struck partons increases with increasing Q^2. Thus, the incoming particle will "see" less of the struck parton's momentum, which has gone into producing more and more gluons. Thus, the fraction of a hadron's energy that is carried by any single parton decreases with increasing Q^2. Also, as the Q^2 increases, more and more quark species are able to be seen inside the hadron. For example, above the c and b thresholds, these species can be created through gluon splitting, and hence will carry part of the hadron's energy. As $Q^2 \to \infty$, all partons carry equal amounts of the hadron's energy (i.e. they all tend to a delta function at $x = 0$). Figure 1.6(c) shows the evolution of the d-quark PDF in the proton as a function of Q^2 scale, in dimensionless units of Q_0^2. This is taken from the discussion of the Duke-Owens parameterization of the Altarelli-Parisi Equations in [9], where $Q_0^2 = 4\ GeV^2$. The trend toward lower fractions is clearly shown.

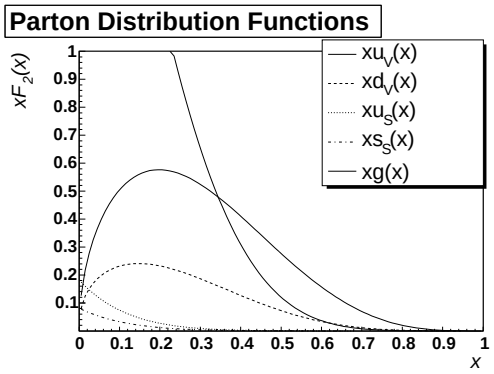

(a) Example parton distribution functions

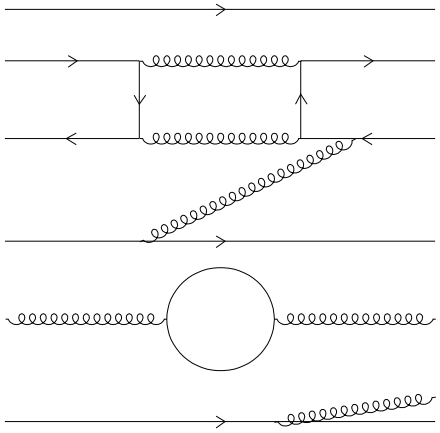

(b) Typical hadron with interacting particles.

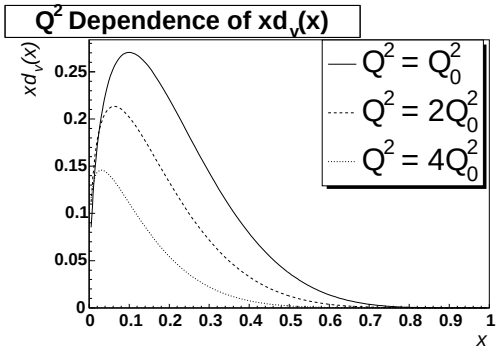

(c) PDF evolution with Q^2. Here, $Q_0^2 = 4\ GeV^2$.

Figure 1.6: Diagrams for parton distribution functions.

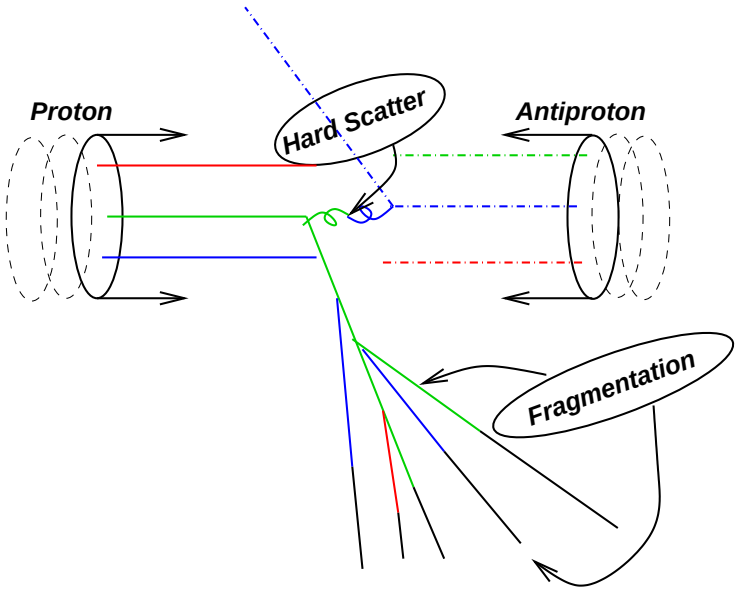

Figure 1.7: Figure showing fragmentation of initial hard-scatter partons to jets.

1.3.2 Hadronization

If a parton is struck by an external probe (i.e. an electron or a parton from another hadron) with sufficient energy, it is possible to treat the internal partons as free particles (as we've seen in the previous sections). That means if the incoming particle imparts enough momentum to the parton, it will be ejected. Of course, we already know that the parton cannot be free indefinitely. At some point, it will combine with partons from the sea and form colorless hadrons. However, because initially it was essentially free, the initial direction will more or less be preserved. Therefore, partons will "shower" (i.e. combine with other partons from the sea), forming *jets* of particles that are color-neutral. These jets are stable, and can be detected. Thus, in order to detect a parton-level interaction, it is necessary to actually measure the parton shower of the outgoing parton in a jet. Figure 1.7 shows how this process occurs.

In order to detect the hadronic products of $t\bar{t}$ decays, therefore, it is necessary to use jets to reconstruct the event. We will return to the implications of this below.

1.3.3 Initial and Final State Radiation

It is possible to radiate a massless virtual gauge boson (i.e. photon or gluon) off the incoming or outgoing partons of any given process. Figure 1.8(a) and 1.8(b) show initial and final state radiation, respectively.

Given sufficient energy, these photons or gluons can escape the interaction, and pair produce a fermion-antifermion pair (of course, only $q\bar{q}$ is allowed for the strong interactions). These fermions can then be detected, either as final state leptons, or,

after hadronization of quarks, as jets.

Because QED has such a weak interaction, the probability of emission is small ($\sim 1/137$). However, since QCD is strongly interacting for low momentum transfer, this has a very large probability of happening.

In fact, the "momentum transfer" in this case is proportional to the angle to the parton that radiated the gluon. If there are larger angles, the transfer is large, and conversely for smaller angles. Thus, the probability to emit a gluon at large angles is quite small, but the probability to emit a gluon at small (very close to zero) angles is quite large. The probability to emit a zero-energy gluon at zero angle approaches 1, according to QCD.

This has an impact on this analysis because the models for initial and final state radiation are not particularly well-constrained, and are a source of systematic uncertainty for this measurement.

Also, it turns out that W bosons produced in association with final state gluons (W+Jets) is the largest background to this analysis. We discuss this in the next section.

The initial and final state radiation also depends on the momentum transfer scale (Q^2), as with the parton distribution functions [12]. The Q^2 scale increases as the parton emission approaches the hard scatter (in time) and then decreases after the hard scatter. The scale is typically chosen to be $Q^2 = m^2 = E^2 - p^2$ for time-like particles (with $m^2 > 0$), and $Q^2 = -m^2 = E^2 - p^2$ for space-like particles (with $m^2 < 0$). Final state showers are timelike, and initial state showers are spacelike. The typical scales of Q^2 are of order Λ_{QCD} (Section 1.3). Variation of this definition

is a source of systematic uncertainty when using parton shower programs (as in this analysis, where we use the PYTHIA generator [12]).

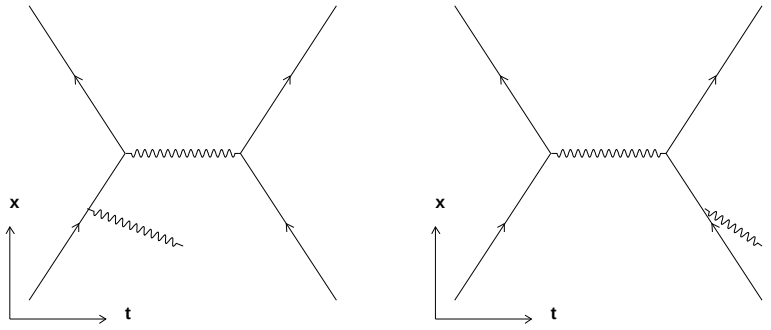

(a) (b)

Figure 1.8: Initial and final state radiation.

1.3.4 W+Jets Production

The most important background for this analysis is production of a W-boson associated with jets, either due to back-to-back production (see Figure 1.9(a)) or excitation of quarks in the initial state (see Figure 1.9(b)). Radiated gluons can then split into heavy-quark pairs, or the excited quark can be a charm (and in rare cases, a b-quark).

Currently, it is possible to calculate exact matrix elements from first principles for essentially any process, providing that the partons are widely separated (as was mentioned before, partons that are not widely separated corresponds to low momentum transfers, and QCD perturbative predictions break down). We currently use the

ALPGEN Monte Carlo generator [13] to calculate matrix elements of widely separated partons.

These matrix element generators (such as ALPGEN) are not capable of handling soft, collinear gluon radiation and hadronization very well (as was mentioned before, since QCD is non-perturbative at that stage). As such, it is necessary to pass the generated partons to another Monte Carlo program to handle the soft gluon radiation processes in a parametric way. These parameterizations are phenomenological models taken from fits to various sets of data. We refer to these MC programs as "parton-shower" programs. We use HERWIG [14] as a parton-shower program in this analysis. The generated hard-scatter partons are passed from ALPGEN to HERWIG to handle hadronization.

There are two difficulties with this procedure. Firstly, the leading-order diagrams are not adequate to describe the kinematics, so the next-to-leading-order terms must be included to compute the total cross section. Secondly, some care must be taken when adding together the contributions from, for example, $W+1$ parton production and $W+2$ parton production.

We must use leading-order matrix element calculations at this time simply because the technology of next-to-leading-order calculations is not developed enough to use in this analysis. However, work is currently being done to include next-to-leading-order diagrams in these matrix element calculators. Unfortunately, it is not quite ready to do so.

In order to mitigate this problem, we use the leading-order matrix element calculators, and assume there is a K-factor by which to multiply the prediction in order to

obtain the full cross section. In order to estimate this K-factor, we simulate a process that has a lot of data available, derive templates from this Monte Carlo prediction, and fit the fraction of events in the data, assuming the shape is well-modeled. The K-factor is then applied to other samples. We will return to this in a later section.

The second problem is mitigated as follows. In adding together the contribution from the various W+N parton samples, it is necessary to avoid overlapping phase space between the ALPGEN generated partons and any partons generated by HERWIG. That is, consider Figure 1.9(c). This diagram can arise in one of two ways. The first way is if ALPGEN generates the diagram as W+2 partons, assuming the final-state radiated gluon is widely separated and then passing the W+2 partons to HERWIG. The second way is if ALPGEN generates the diagram as W+1 parton, and then HERWIG emits a gluon which then forms a jet.

The problem is whether to call this diagram W+1 parton or W+2 partons. The diagram is taken into account twice, and so this part of phase space has been double counted.

In order to mitigate this, a procedure is used where partons at the generator level are clustered in a jet cone algorithm similar to that used at the detector level. These are henceforth referred to as "parton jets". It is then possible to match these "parton jets" to hard-scatter partons from ALPGEN.

There are two ways to combine W+N parton samples at this point. Firstly, it is possible to require that all parton jets are matched to ALPGEN hard-scatter partons, but allow extra parton jets in the sample. These events with extra jets are then ignored if a higher-order process has been simulated (i.e. the W+N+1 parton

sample). This is referred to as *inclusive matching* because we allow extra parton jets to exist.

The second way is to require all the parton jets to be matched to ALPGEN hard-scatter partons, but disallow any extra parton jets. The contributions are then combined weighted by the generated leading-order cross section predictions. This is referred to as *exclusive matching*.

In this analysis, we will use a combination of exclusive and inclusive matching. Our signal sample has up to 5 jets. However, only W+3 jets is simulated. Therefore, we use exclusive matching for W+1,2,3 jets, and inclusive matching for $W+ \geq 4$ jets.

1.4 Cross Sections and Decay Rates

1.4.1 Cross Sections

The definition of a cross section is as follows. Consider a reaction

$$A + B \rightarrow FINAL\ STATE \tag{1.20}$$

Then the cross section for this reaction is

$$\sigma = \frac{transition\ rate}{incident\ flux} \tag{1.21}$$

The transition rate is the number of times Reaction 1.20 occurs in a small time unit Δt. The incident flux is the number of A and B particles per unit area per unit time. Thus, the cross section has units of area, as expected. Because the length scale accessible to a given probe particle is inversely proportional to its energy, if a process

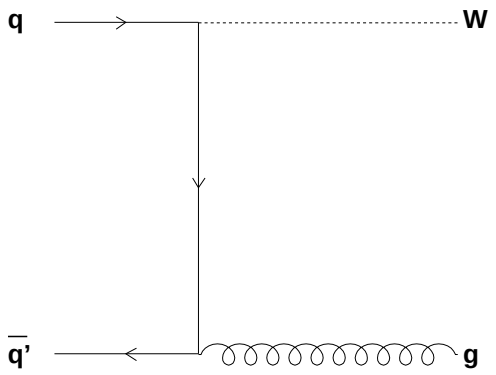

(a)

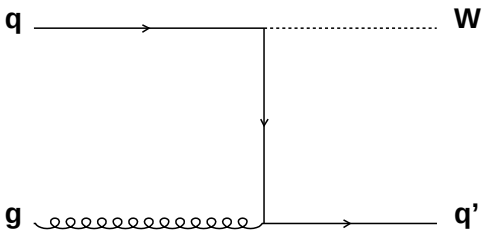

(b)

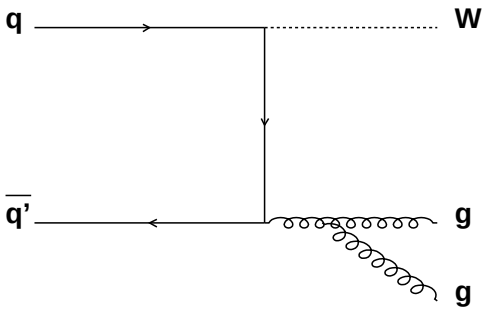

(c)

Figure 1.9: Base leading-order production diagrams for W+jets production. There are many other diagrams with gluon radiation in the initial and final states.

has a small cross section (i.e. small length scale over which it can occur) it requires a large amount of energy to probe that small length scale.

The typical cross sections in high energy physics are very small. 10^{-28} m is a comparatively large cross section, so it is called a barn (as in "You couldn't hit the side of a barn!") We often see cross sections on the order of picobarns (pb), for top quark production, or femptobarns(fb), for Higgs boson production.

When one wishes to know about the angular distribution of reaction rates, we use what is called the *differential cross section*. This simply modifies our definition to take care of the number of particles that scatter into a solid angle Ω. Thus, we note the differential cross section as

$$\frac{d\sigma}{d\Omega} \tag{1.22}$$

When you integrate over all solid angles, you regain the total cross section.

To obtain the cross section from a quantum mechanical amplitude, the formula for the scattering of particles

$$1 + 2 \rightarrow 3 + 4 + \ldots + n \tag{1.23}$$

is given by [7]

$$\begin{aligned} d\sigma &= |\mathcal{M}|^2 \frac{S}{4\sqrt{(p_1 \cdot p_2)^2 - (m_1 m_2)^2}} \left[\prod_{i=3}^{n} \left(\frac{d^3\vec{p}_i}{(2\pi)^3 2E_i} \right) \right] \\ &\times (2\pi)^4 \delta^4(p_1 + p_2 - p_3 - p_4 - \ldots - p_n) \end{aligned} \tag{1.24}$$

where $\mathcal{M}$ is the quantum-mechanical amplitude, S is a statistical factor ($1/j!$) for each group of j identical particles, p_i is the 4-momentum of the ith particle, $\vec{p}_i$ is the 3-momentum of the ith particle, E_i is the energy of the ith particle, and $\delta^4(x)$ is an energy-conserving delta function.

For $2 \rightarrow 2$ scattering in the center of mass frame, the differential cross section is

$$\frac{d\sigma}{d\Omega} = \frac{1}{64\pi^2} \frac{S|\mathcal{M}|^2}{(E_1 + E_2)^2} \frac{|\vec{p}_f|}{|\vec{p}_i|} \tag{1.25}$$

where $\vec{p}_f$ is the final momentum of either particle, $\vec{p}_i$ is the initial momentum, E_1 and E_2 are the energies of the incoming particles, $\mathcal{M}$ is the amplitude, and S is the statistical factor.

Thus, given the matrix element, it is possible to calculate this differential cross section quite easily. We will make use of this to calculate the theoretical prediction for the $t\bar{t}$ production cross section.

1.4.2 Decay Rates

The decay rate ($\Gamma = 1/\tau$) of a particle that decays as

$$1 \rightarrow 2 + 3 + \ldots + n \tag{1.26}$$

is given by [7]

$$\begin{aligned} d\Gamma &= |\mathcal{M}|^2 \frac{S}{2m_1} \left[\prod_i \left(\frac{d^3\vec{p}_i}{(2\pi)^3 2E_i} \right) \right] \\ &\times (2\pi)^4 \delta^4(p_1 - p_2 - p_3 - p_4 - \ldots - p_n) \end{aligned} \tag{1.27}$$

Most of the terms are the same as Equation 1.24.

In the special case of a 2-body decay $1 \rightarrow 2 + 3$ in the center of mass frame of the particle, the rate is

$$\Gamma = \frac{S|\vec{p}|}{8\pi m_1^2} |\mathcal{M}|^2 \tag{1.28}$$

where $\vec{p}$ is the momentum of either outgoing particle and m_1 is the mass of the incoming particle. Here, by momentum and energy conservation,

$$|\vec{p}| = \frac{1}{2m_1}\sqrt{m_1^4 + m_2^4 + m_3^4 - 2m_1^2m_2^2 - 2m_1^2m_3^2 - 2m_2^2m_3^2} \tag{1.29}$$

1.5 Cross Section for $p\overline{p} \rightarrow t\overline{t}$

In order to calculate the production cross section for $p\overline{p} \rightarrow t\overline{t}$, it is necessary to take into consideration the structure of the incoming protons. That is, we must weight our kinematics by the PDF's of the constituent particles.

The four diagrams that contribute to $p\overline{p} \rightarrow t\overline{t}$ are shown in Figure 1.10. If we ignore the proton mass, the minimum energy to produce a $t\overline{t}$ pair is given by

$$x_1 x_2 \geq \frac{4 \cdot m_t^2}{s} \tag{1.30}$$

If $x_1 = x_2 = x_{min}$, then the minimum momentum transfer is

$$x_{min} = \frac{2 \cdot m_t}{\sqrt{s}} \tag{1.31}$$

That is, to produce a $t\overline{t}$ pair, at least one parton must have this much momentum.

At the Tevatron, $\sqrt{s} = 1.96\ TeV$, and so the minimum fraction that needs to be carried by a parton is 0.18. At the LHC, $\sqrt{s} = 14\ TeV$, and so $x_{min} = 0.025$.

Examining Figure 1.6(a), we see that at $x = 0.18$, the gluon component is less than the combined fraction of u and d quarks. Thus, at $x = 0.18$, the dominant production mode is $q\bar{q} \rightarrow t\overline{t}$. At $x = 0.025$, the gluon contribution is much larger than the $q\overline{q}$ contribution, and so the dominant production mode is $gg \rightarrow t\overline{t}$.

Thus, at the Tevatron, the dominant production mode is $q\bar{q} \rightarrow t\overline{t}$, while at the LHC, the dominant mode is $gg \rightarrow t\overline{t}$. $q\bar{q} \rightarrow t\overline{t}$ (Fig 1.10(a)) contributes $\sim 85\%$ to

the cross section, and $gg \to t\bar{t}$ (Figs 1.10(b)-1.10(d)) contributes $\sim 15\%$ to the cross section.

The cross section formula is given by [9]:

$$\begin{aligned}
\sigma(p\overline{p} \to t\bar{t}) &= \sum_{q,\bar{q}} \frac{1}{9} \int dx_q dx_{\bar{q}} f_q(x_q) f_{\bar{q}}(x_{\bar{q}}) \widehat{\sigma}(q\bar{q} \to t\bar{t}) \\
&+ \sum_{g1,g2} \frac{1}{64} \int dx_{g1} dx_{g2} f_{g1}(x_{g1}) f_{g2}(x_{g2}) \widehat{\sigma}(g1g2 \to t\bar{t}) \qquad (1.32) \\
\widehat{\sigma}(q\bar{q} \to t\bar{t}) &= \frac{4\pi\alpha_s^2(m^2)}{9\hat{s}^4} \left[(m^2-\hat{t})^2 + (m^2-\hat{u})^2 + 2m^2\hat{s}\right] \qquad (1.33) \\
\widehat{\sigma}(g1g2 \to t\bar{t}) &= \frac{\pi\alpha_s^2(m^2)}{8\hat{s}^2} \left[\frac{6(m^2-\hat{t})(m^2-\hat{u})}{\hat{s}^2} - \frac{m^2(\hat{s}-4m^2)}{3(m^2-\hat{t})(m^2-\hat{u})} \right. \\
&+ \frac{4}{3} \frac{(m^2-\hat{t})(m^2-\hat{u}) - 2m^2(m^2+\hat{t})}{(m^2-\hat{t})^2} \\
&+ \frac{4}{3} \frac{(m^2-\hat{t})(m^2-\hat{u}) - 2m^2(m^2+\hat{u})}{(m^2-\hat{u})^2} \\
&- 3\frac{(m^2-\hat{t})(m^2-\hat{u}) + m^2(\hat{u}-\hat{t})}{\hat{s}(m^2-\hat{t})} \\
&- \left. 3\frac{(m^2-\hat{t})(m^2-\hat{u}) + m^2(\hat{t}-\hat{u})}{\hat{s}(m^2-\hat{u})} \right] \qquad (1.34)
\end{aligned}$$

where we have set the momenta of the two incoming partons (q or g) as p_1 and p_2, and the momenta of the outgoing top quarks as p_3 and p_4, and have defined kinematic variables $\hat{s} = (p_1+p_2)^2$, $\hat{t} = (p_1-p_3)^2$, $\hat{u} = (p_1-p_4)^2$. It is conventional to quote α_s at the mass scale of the top quark m. The uncertainties in this theoretical prediction are associated with the renormalization scale (chosen to be the top quark mass m, varied to $2m$ and $m/2$ as systematic uncertainties), the QCD cutoff scale Λ, and the behavior of the high-x (high momentum transfer) parton distribution functions.

With a little algebraic manipulation, the leading order $q\overline{q}$ diagram cross section

can be written as

$$\widehat{\sigma} = \frac{8\pi\alpha_s(m^2)}{27\widehat{s}}\sqrt{1-\frac{4m^2}{\widehat{s}}}\left(1+\frac{2m^2}{\widehat{s}}\right) \tag{1.35}$$

This formula has an initial kinematic turn-on due to the large energy threshold for production. The kinematic threshold is $\hat{s} = 4m_{top}^2$. Well above the threshold, the cross section falls as $1/\widehat{s}$, after peaking around $\widehat{s} \approx 5.6m_{top}^2$. Figure 1.11 shows this parton cross section, before convolution with the PDF. The central line is given for $m_{top} = 175$ GeV/c^2, and the two bounding curves are for $m_{top} = 170, 180$ GeV/c^2.

Figure 1.12(a) shows the theoretical cross section versus $\sqrt{s}$ (center-of-mass energy) for different top mass hypotheses. Figure 1.12(b) shows the theoretical cross section versus m_{top} for $\sqrt{s} = 1.96$ TeV. The shaded band in 1.12(a) shows the theoretical uncertainties. The theoretical predictions for these plots is taken from [15, 16]. These predictions are done at next-to-leading order, with re-summation of classes of large soft logarithms to all orders of perturbation theory. These predictions are the best available because they also make use of updated measurements of parton distribution functions to accurately determine theoretical uncertainties due to high-x PDF's. We can see that the upgrade in center of mass energy of the Tevatron from 1.8 TeV to 1.96 TeV results in a 40% increase in $t\bar{t}$ cross section because we are in the regime of the kinematic turn-on. Thus, small changes in the center of mass energy can result in large changes in the cross section.

Because there is little transverse momentum of the incoming partons, the $t\bar{t}$ system will have very low transverse momentum. The energies of each top quark are comparable to the mass of the top quark, and hence the decay will be roughly spherical. Because of this, there is no way to distinguish the $t\bar{t}$ system geometrically. Both

top quarks decay isotropically, mixing the decay products throughout the detector.

Figure 1.13(a) shows the energy of the $t\bar{t}$ system. The typical energies are of order 500 GeV, which is not very far above the kinematic threshold of 350 GeV. About 25% of the total energy available to the system at $\sqrt{s} = 1.96$ TeV goes into $t\bar{t}$ production, which is a very large fraction. Figure 1.13(b) shows the p_T of the $t\bar{t}$ system. It has an average p_T of about 15 GeV, much less than the 500 GeV of energy available to the system. Figure 1.13(c) shows the rapidity of the $t\bar{t}$ system. The system itself has low rapidity, which is a manifestation of the fact we are very close to the kinematic threshold for producing $t\bar{t}$ pairs. It is much more likely to get $x_1 = x_2 = x_{min}$ than it is to have one parton with much larger energies, resulting in a boost in the z-direction. This situation will be different at the LHC, where the center-of-mass energy is well above the kinematic threshold.

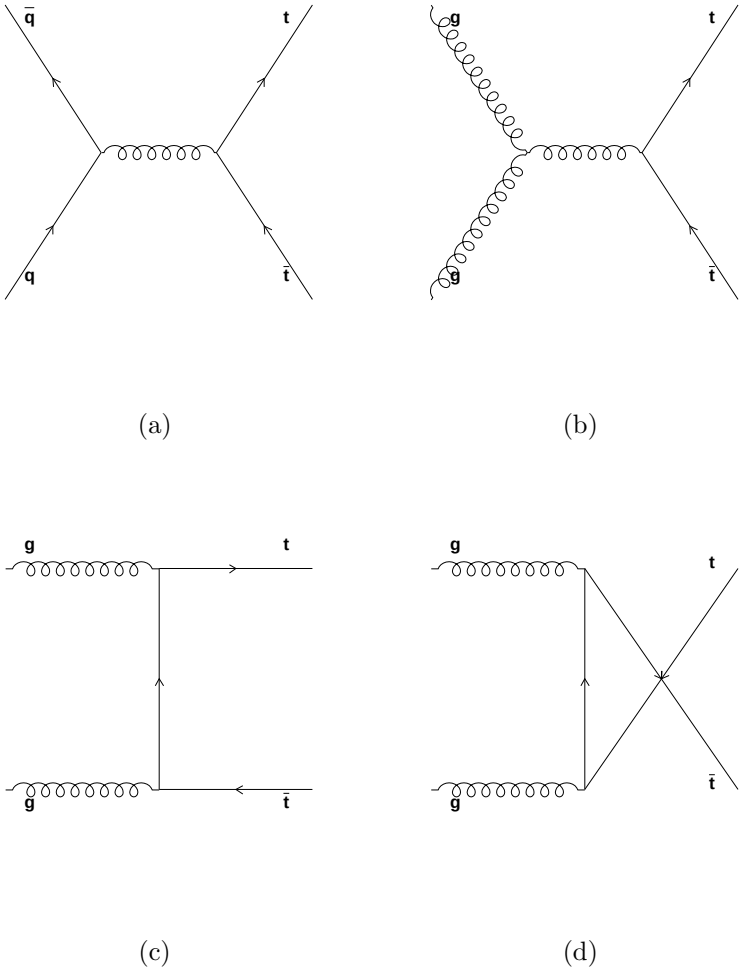

Figure 1.10: Production diagrams for $p\overline{p} \rightarrow t\overline{t}$.

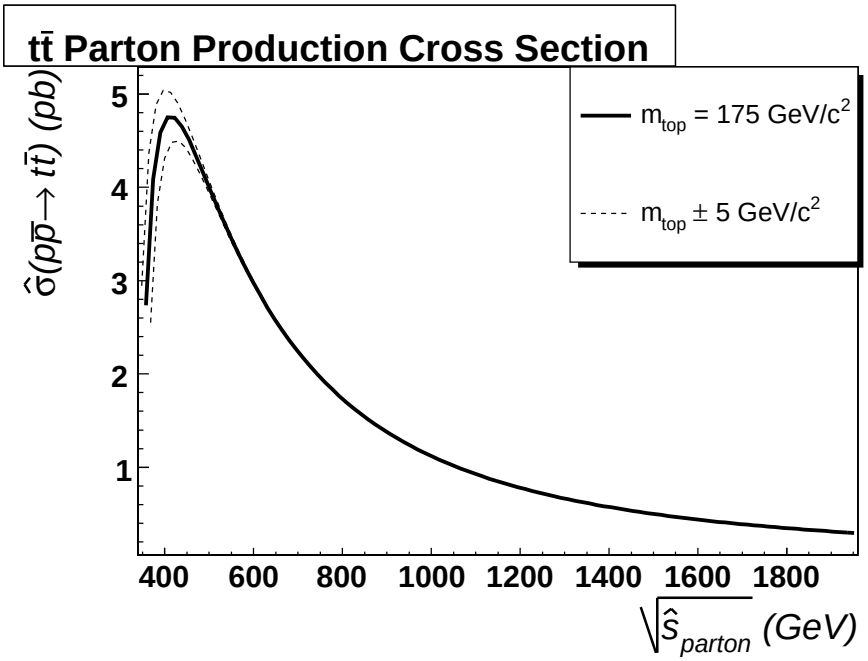

Figure 1.11: Parton production cross section versus $\sqrt{\hat{s}}$. This is the parton-level cross section before convolution with the parton distribution function. The central curve is taken at $m_{top} = 175$ GeV/c^2, and the bounding curves are for ± 5 GeV/c^2.

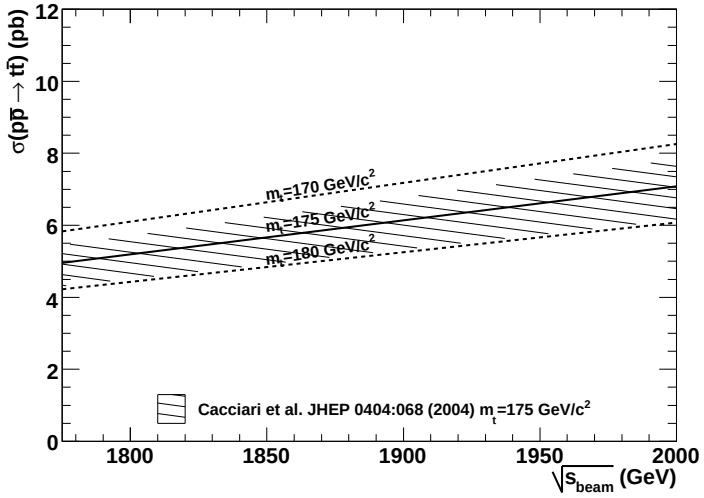

(a) Theoretical cross section versus$\sqrt{s}$ for different top mass hypotheses. The shaded region is the theoretical error, dominated by the parton distribution functions at high x, and the Q^2 scale uncertainty.

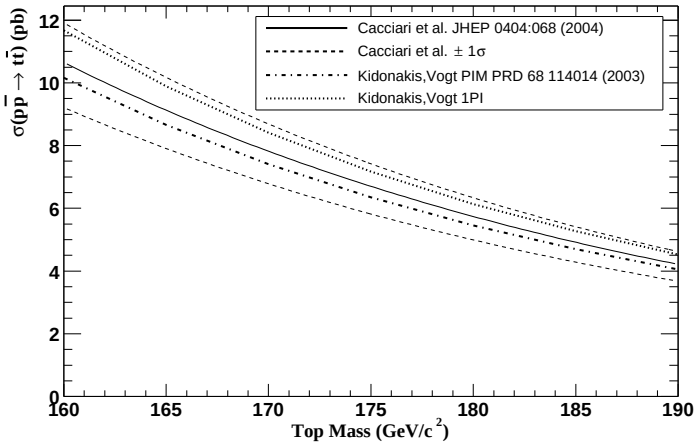

(b) Theoretical cross section versus top mass at $\sqrt{s} = 1.96$ TeV. The theoretical errors are dominated by the parton distribution functions at high x, and the Q^2 scale uncertainty.

Figure 1.12: Theoretical predictions for $\sigma(p\overline{p} \rightarrow t\overline{t})$.

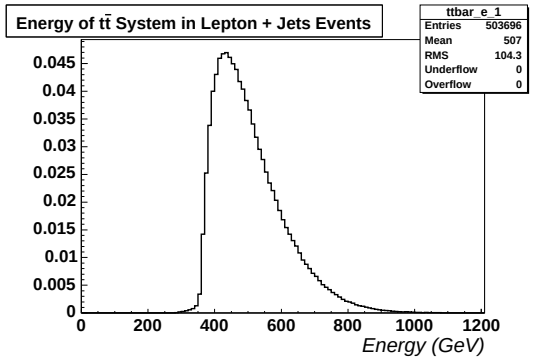

(a)

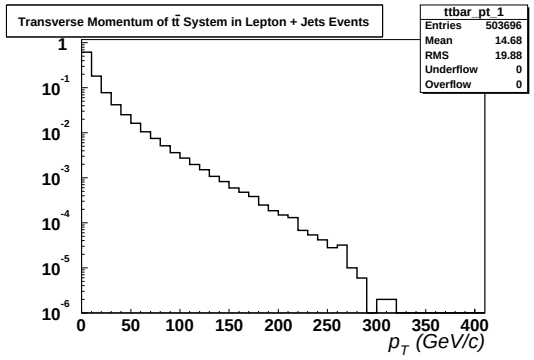

(b)

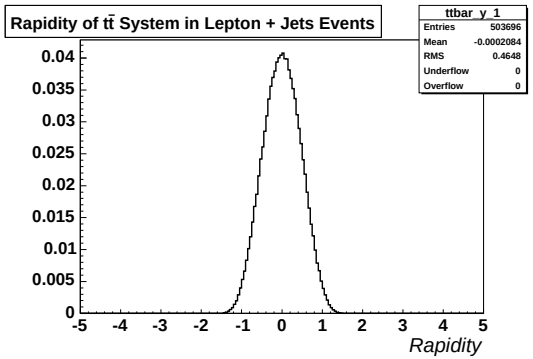

(c)

Figure 1.13: Kinematic Distributions for $t\bar{t}$ System in Lepton + Jets Events, in PYTHIA Monte Carlo at $m_{top} = 178$ GeV/c^2.

1.6 Top Quark Decay

The weak isospin partner of the top quark is the bottom quark. The CKM entry V_{tb} for this coupling is much larger than the couplings between top and down and top and strange. The suppression factors are $|V_{ts}|^2/|V_{tb}|^2 \approx 10^{-3}$, and $|V_{td}|^2/|V_{tb}|^2 \approx 5 \times 10^{-4}$. Because the top is so heavy, it produces an on-shell W boson in association with a bottom quark.

The timescale for hadronization is estimated to be $\Lambda_{QCD}^{-1} \approx (200\ MeV)^{-1} \approx 10^{-23}$ sec. The partial decay width for $t \to Wb$ is given by [17]

$$\Gamma(t \to Wb) = 175\ MeV \left(\frac{m_t}{m_W}\right)^3 |V_{tb}|^2 \tag{1.36}$$

If $m_t = 175\ GeV/c^2$, the partial width is 2 GeV, and therefore have a lifetime of $\tau \sim 4 \times 10^{-25}$ seconds. Thus, the top quark will decay before it has a chance to hadronize.

Because the top quark will decay almost 100% of the time to Wb, it is only possible to classify the $t\bar{t}$ event on the decay of the $W^{\pm}$ bosons. Figure 1.14 shows the decay chain for the $q\bar{q}$ annihilation production diagram.

Due to the high mass of the top, the outgoing daughters will have very large energies. Figures 1.15(a) and 1.15(c) show the energy and transverse momentum of the top and its immediate decay daughters, the bottom quark and W boson. The four-momentum is split between the W and b in the rest frame of the top quark. However, due to the large mass of the W, the energy of the b is less than that of the W.

The rapidity of the top, bottom, and W are given in Figure 1.15(e).

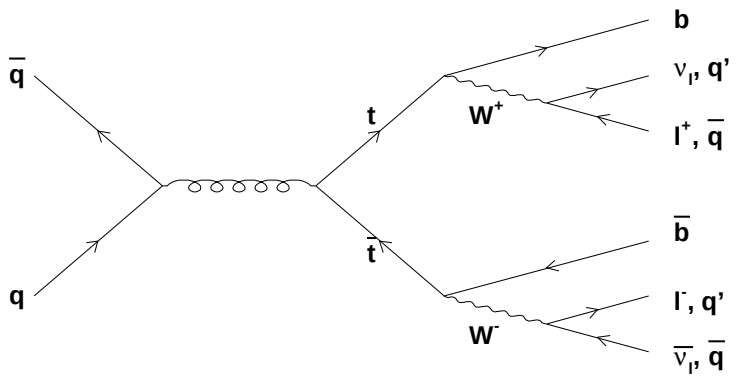

Figure 1.14: Decay diagram for $p\overline{p} \rightarrow t\overline{t}$.

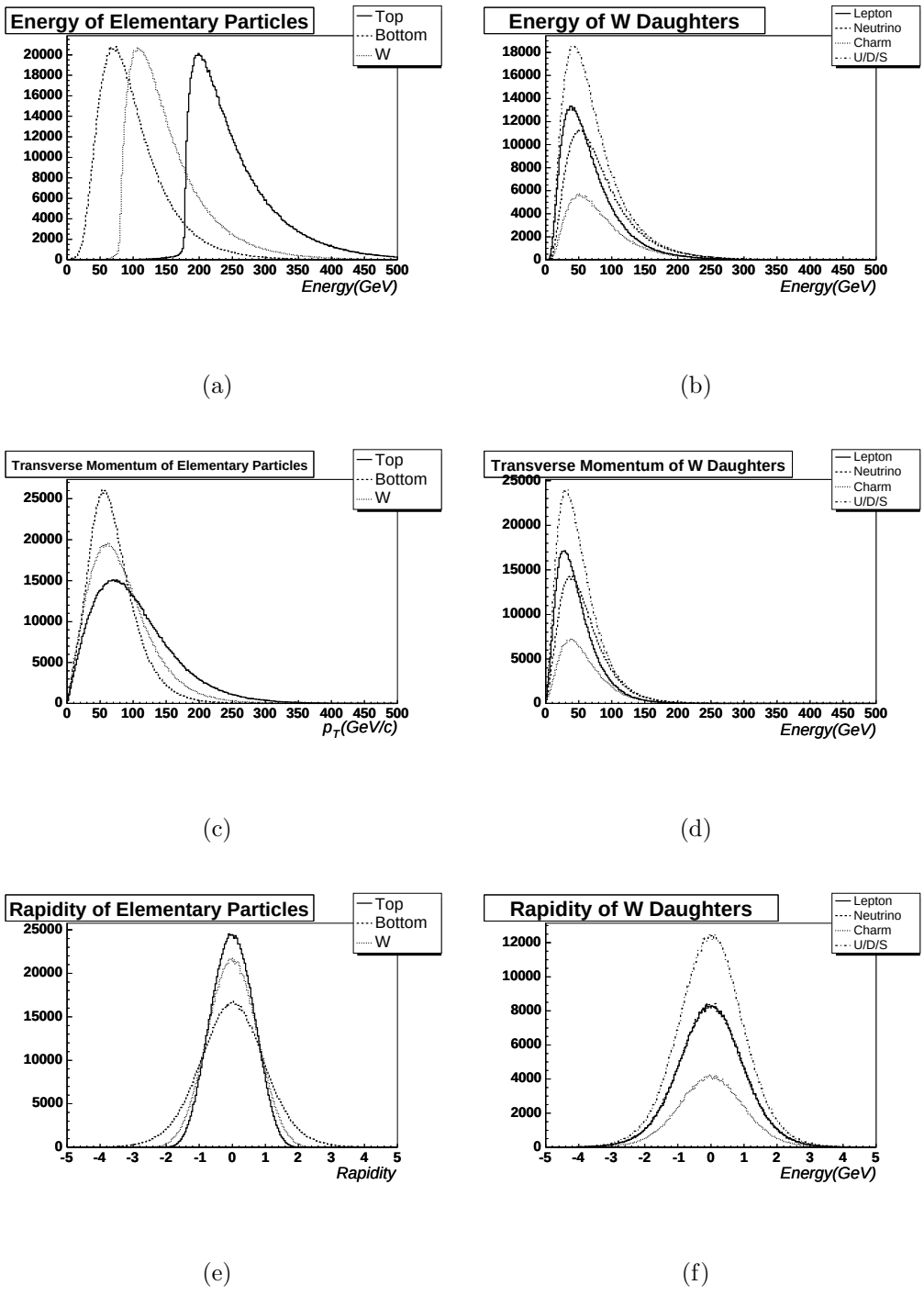

Figure 1.15: MC four-vector kinematic distributions (before detector simulation) for top, bottom, and W in lepton + jets events, and also kinematic distributions for daughters of W boson, all in PYTHIA Monte Carlo at $m_{top} = 178$ GeV/c^2.

1.7 $W^{\pm}$ Decay

The decay width of $W \to l\nu$ is given by [9]

$$\Gamma(W \to l\bar{\nu}) = \frac{1}{48\pi} g^2 M_W = \frac{G_F}{\sqrt{2}} \frac{M_W^3}{6\pi} \equiv \Gamma_W^0 \tag{1.37}$$

Given $M_W = 80.6$ GeV/c^2, $\Gamma_W^0 = 0.23$ GeV. The decay rates to $q\bar{q'}$ are given by

$$\Gamma(W \to q\bar{q'}) = 3|V_{qq'}|^2 \Gamma_W^0 \tag{1.38}$$

where $V_{qq'}$ is the CKM matrix element for qq'. The factor of three arises from summing over the quark colors.

The kinematically allowed W decays are $W \to e\nu$, $W \to \mu\nu$, $W \to \tau\nu$, $W \to ud'$ and $W \to cs'$ (where d' and s' refer to the CKM mixed weak eigenstate quarks). Because the CKM matrix is nearly diagonal, for the purposes of this discussion, $d' = d$ and $s' = s$. That leaves 3 leptonic decays, and 2 hadronic decays (which get a color enhancement of 3), and so there are 9 possible states for the W to decay into.

In this analysis, we use $t\bar{t}$ pairs, and so there are two W's in each event. Thus, there are 81 combinations of decays for the W^+ and W^-. Table 1.2 shows the various decay modes. The "dilepton" channel (i.e. both W's decay leptonically) has a branching ratio of 9/81. The "lepton plus jets" channel (i.e. one W decays leptonically, the other hadronically) has a branching ratio of 12/81 for each lepton type (e,μ,τ). The "all-jets" channel (i.e. both W's decay hadronically) has a branching ratio of 36/81.

This analysis uses a part of the "lepton plus jets" subsample, using only electrons and muons. This leaves $24/81 = 29.6\%$ of the sample for this analysis.

W^+ / W^-	$e^-\bar{\nu}_e$	$\mu^-\bar{\nu}_\mu$	$\tau^-\bar{\nu}_\tau$	jets (ud, cs)
$e^+\nu_e$	1/81	1/81	1/81	6/81
$\mu^+\nu_\mu$	1/81	1/81	1/81	6/81
$\tau^+\nu_\tau$	1/81	1/81	1/81	6/81
jets (ud, cs)	6/81	6/81	6/81	36/81

Table 1.2: W^+ versus W^- decay modes in $p\overline{p} \rightarrow t\bar{t}$. The dilepton channel has a branching ratio of 9/81. The lepton plus jets channel has a branching ratio of 12/81 for each lepton type (e,μ,τ). The all-jets channel has a branching ratio of 36/81.

1.8 Measurement of $\sigma(p\overline{p} \rightarrow t\bar{t})$

This analysis uses the decay chain

$$p\overline{p} \rightarrow t\bar{t} \rightarrow W^+bW^-\bar{b} \rightarrow l\nu b\bar{b}q\overline{q} \tag{1.39}$$

(where $l = e, \mu$) to measure the cross section. We are thus looking for the experimental signature of

$$p\overline{p} \rightarrow l\nu b\bar{b}q\overline{q} \tag{1.40}$$

Because other physics processes mimic this signature, it is only possible to extract the $t\bar{t}$ cross section statistically. To do this, we measure

$$\sigma_{t\bar{t}} = \frac{N_{obs} - \widehat{N_{bkg}}}{BR(W^\pm \rightarrow l\nu + q\overline{q}) \cdot \mathcal{A} \cdot \epsilon \cdot \int \mathcal{L}dt} \tag{1.41}$$

where N_{obs} is the number of observed events, $\widehat{N_{bkg}}$ is the expected average number of background events, $BR(W^\pm \rightarrow l\nu + q\overline{q})$ is the branching ratio for the lepton plus jets channel using electrons and muons (24/81), $\mathcal{A}$ is the geometrical acceptance, ϵ is the event efficiency, and $\int \mathcal{L}dt$ is the integrated luminosity.

Chapter 2

Detector

2.1 The Fermi National Accelerator Laboratory Tevatron

The Tevatron at the Fermi National Accelerator Laboratory (FNAL) is a $p\overline{p}$ collider with a center of mass energy of $\sqrt{s} = 1.96$ TeV. It is located in Batavia, IL, about 30 miles west of Chicago.

The Tevatron is a multi-staged accelerator comprised of the following elements:

1. Proton source
    - Cockcroft-Walton pre-accelerator (preacc)
    - Linear accelerator (linac)
    - Booster
2. Antiproton source

- Target
- Debuncher
- Accumulator
- Recycler

3. Main Injector

4. Tevatron Colliding Ring

Figure 2.1 shows the components of the Tevatron. We now consider each element in turn. For a detailed explanation of the Tevatron, see Reference [18].

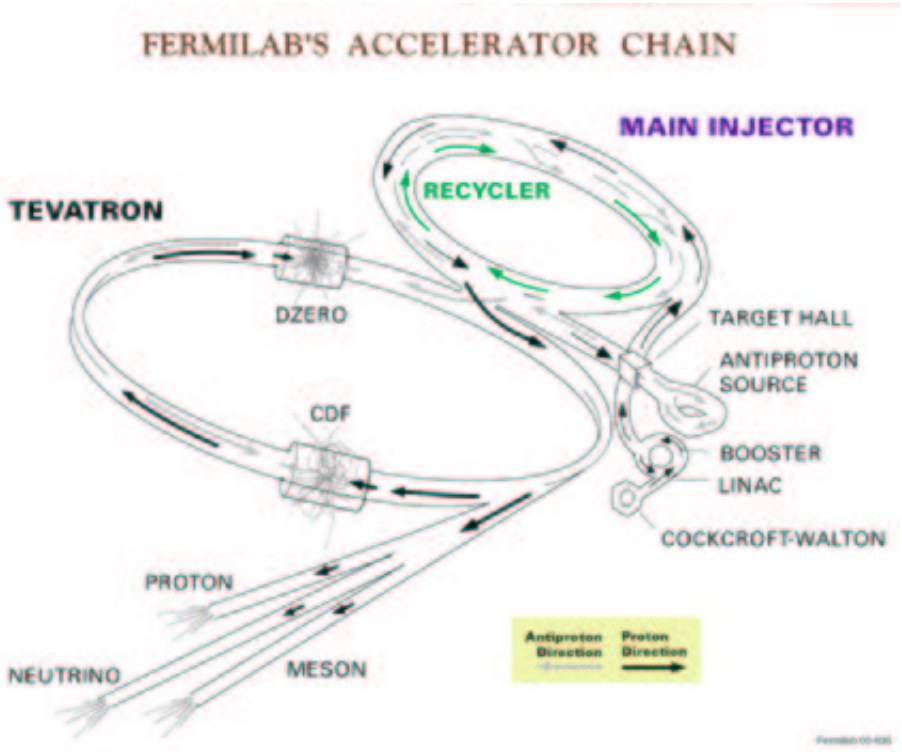

Figure 2.1: Schematic representation of the Fermilab Tevatron.

2.1.1 Proton source

The proton source is made up of three subsystems, the pre-accelerator (preacc), the linear accelerator (linac), and the booster ring. Together, these subsystems are capable of producing 8 GeV protons to be injected into the Main Injector.

Cockcroft-Walton pre-accelerator

The Cockcroft-Walton pre-accelerator (preacc) is a source of negatively charged, accelerated hydrogen ions. It takes hydrogen ions off a cesium target (made from hydrogen gas). The pre-accelerator produces 750-KeV hydrogen ions every 66 milliseconds. It then transfers the hydrogen ions into the linear accelerator (linac).

Linear accelerator

The linear accelerator (linac) receives negatively charged hydrogen ions at 750 KeV and accelerates them to an energy of 400 MeV. This is accomplished using *RF-pulses* of magnetic fields, carrying the particles along on a "wave" of electromagnetic radiation. This is also done once every 66 milliseconds (with an offset to catch the ions from the preacc).

The beam is also focused at this point using quadrupole magnets. This cooled beam of H^- ions is then sent to the booster.

Booster

The booster receives the cooled beam of H^- ions from the linac, and strips the electrons off, leaving bare protons (H^+ ions). It then accelerates the protons to 8

GeV. This is the first synchrotron (circular accelerator) in the Tevatron complex. It is composed of a series of 75 magnets arranged around a 75 meter radius circle, with 18 RF cavities inside. This stage of production is also operated at 66 milliseconds, with sufficient phase offsets to catch the ions from the linac.

At this point, the beam is sent to a transfer line, which then sends the proton beam to the main injector, and then on to the Tevatron for colliding physics.

2.1.2 Main Injector

The main injector is a circular synchrotron about half a kilometer in radius. It is composed of 18 accelerating RF cavities, and can accelerate 8 GeV protons from the booster to 150 GeV every 2.2 seconds, which are then passed to the Tevatron. It can also accelerate protons to 120 GeV which are then used to strike the antiproton source and create antiprotons. This process is called "stacking pbars".

2.1.3 Antiproton source

The antiproton source is made up of one target and three subsystems, the debuncher, accumulator, and the recycler. Together, the antiproton source is capable of producing antiprotons at 8 GeV, to be injected into the main injector.

In principle, another source of antiprotons is "recycled" antiprotons from the last stack that are stored in the recycler. This system would significantly decreases the time in between stores, so it would be possible to integrate more luminosity. However, this functionality is not yet commissioned, and there is little hope that the antiprotons will ever be recycled.

Target

The antiproton source is a nickel target. Protons from the main injector at 120 GeV strike the target, creating a spray of particles. The particles are then sent through a magnetic field, and the particles with different masses and charges will curve at different radii. The antiprotons are then selected from this spray. This is called magnetic spectroscopy. The antiprotons selected have a wide range of momenta, averaging 8 GeV.

Debuncher

The debuncher is a rounded triangular synchrotron with a mean radius of 90 meters. It can accept 8 GeV protons from the main injector for studies, or 8 GeV antiprotons from the target station. It can take the antiprotons from the target, which have a large momentum spread, using a process called "bunch rotation" which is an RF-manipulation. It is also where stochastic cooling is performed on the antiprotons to "cool" the beam's transverse energy, making it more linear. This is performed by examining the EM pulse generated by the beam at one end of the ring, and then short-cutting the beam by going directly across instead of around. Thus, the signal reaches a later point on the ring before the beam does, and the magnetic field can be adjusted so as to decrease the transverse momentum of the particles in the beam.

The cooled antiprotons are then injected into the accumulator at 8 GeV with small momentum spread.

Accumulator

The accumulator is also a rounded triangular synchrotron, in the same tunnel as the debuncher. The antiprotons are then accumulated and cooled here until they are sent into the main injector.

Recycler

The recycler is stored in the same ring as the main injector. In principle, it can accept antiprotons from the Tevatron after a store is ended, however this functionality has not been proved possible. The Recycler also maintains the antiprotons' momenta at 8 GeV. It can then transfer these antiprotons back into the Tevatron for shots.

Right now, while the Recycler is not capable of accepting recycled protons from the Tevatron, it is being used to pull antiprotons off the accumulator, "stacking" the antiprotons which can then be injected into the Tevatron.

2.1.4 Tevatron

The Tevatron is actually the name of the main circular ring at Fermilab, although we colloquially call the entire chain the "Tevatron". It is a circular synchrotron with a 1 km radius. It is composed of eight accelerating cavities, quadrupole and dipole focusing magnets. The Tevatron is also cryogenically cooled to 4K, and the accelerating cavities are made of superconducting niobium/titanium alloy. It is desirable to use superconducting magnets because the very large fields necessary to maintain TeV-scale energies would require currents so large that it is more cost effective to use superconducting magnets than ordinary resistive magnets.

The Tevatron is not a perfect circle. There are six sectors (A-F). each sector has five service buildings (0-4). The "0" sections have large straight sections. A0 is where the Tevatron tunnel connects to the switchyard. It also contains one of two beam aborts. B0 contains CDF (which will be described in detail below), and the D0 detector is aptly named for it's place along the ring. At B0 and D0, the colliding beams are focused into very narrow beamlines of order 32 μm, and the beams then collide. C0 is the location of the other beam abort (protons only). E0 used to be the the site of the old Main Ring transfer to the Tevatron, but is now unused. F0 houses the RF stations, which "kick" the beam back into position if it has wandered off its axis. It is also where the transfer lines from the Main Injector connect with the Tevatron. It also houses the transfer line to the antiproton source.

The Tevatron accepts protons and antiprotons from the Main Injector or the Recycler (for antiprotons) at 150 GeV. They are then accelerated ("ramped") to 980 GeV, which takes 85 seconds. Since the antiprotons and the protons are oppositely charged, they circle in opposite directions in the magnetic field, and are housed in the same ring. The Tevatron can then sustain both beams for hours at a time (called a "store"). The number of collisions per second is described by the "luminosity" (which will be described below). When the antiproton beam is used up by interactions, scraping, and losses, the luminosity drops below the point of utility for the colliding physics experiments, and the store is ended. At that point, the remaining antiprotons are sent to the recycler for the next shot.

2.1.5 Colliding Physics

In order to begin "colliding physics", it is necessary to load the Tevatron with protons and antiprotons. The Main Injector receives seven bunches of protons from the booster. There, they are accelerated to 150 GeV. The bunches are then "coalesced" into one bunch out of the seven originals. This bunch is then injected into the Tevatron. The process is repeated 36 times to obtain the 36 proton bunches necessary for a 36x36 store.

To load antiprotons, four sets of seven bunches are received by the Main Injector from the antiproton source accumulator. Each set of seven bunches are then coalesced into one bunch, leaving four coalesced bunches. These four bunches are then sent into the Tevatron. The process is repeated nine times to obtain the 36 antiproton bunches necessary for a 36x36 store.

When all the protons and antiprotons are loaded into the Tevatron, both beams are "ramped" to 980 GeV. They are then "squeezed" in the z direction, reducing the size from 1.7 m to 35 cm, using low-β quadrupole focusing magnets situated on either side of both CDF and D0. At this point, colliding physics begins by focusing the beams together at CDF and D0.

After colliding physics begins, the beam is "scraped" to remove beam halo (particles spraying around the main beamline with large transverse spread). This is done primarily to reduce radiation incident on the experiments, causing damage to sensitive components like silicon detectors.

2.1.6 Luminosity Measurements

The beam flux at colliders is measured in terms of *luminosity*. It has units of 1/Area. The expression for the luminosity is

$$\mathcal{L} = \frac{fBN_pN_{\overline{p}}}{2\pi\left(\sigma_p^2 + \sigma_{\overline{p}}^2\right)} \times F\left(\frac{\sigma_l}{\beta^*}\right) \tag{2.1}$$

where f is the revolution frequency in Hertz, B is the number of bunches, $N_{p/\overline{p}}$ is the number of protons/antiprotons per bunch, and $\sigma_{p/\overline{p}}$ is the RMS beam size at the interaction point. This is multiplied by a form factor that depends on the ratio of the bunch length in z (σ_l) and β^*, which is a measure of the transverse beam width. This form factor has an hourglass shape in z.

Table 2.1 shows the accelerator parameters for Run I and Run II. Figure 2.2 shows the total luminosity collected by CDF as of April 2005.

Run Bunches (p x $\overline{p}$)	Ib (6x6)	IIa (36x36)
Protons/bunch (N_p)	2.3×10^{11}	2.7×10^{11}
Antiprotons/bunch ($N_{\overline{p}}$)	5.5×10^{10}	3.0×10^{10}
Total antiprotons	3.3×10^{11}	1.1×10^{12}
Pbar production rate (hr^{-1})	6.0×10^{10}	1.0×10^{11}
Proton emittance (mm-mrad)	23π	20π
Antiproton emittance (mm-mrad)	13π	15π
β^* (cm)	35	35
Energy (GeV)	900	980
Bunch length (m)	0.60	0.37
Bunch spacing (ns)	3500	396
Interactions/crossing	2.5	2.3

Table 2.1: Accelerator parameters in Run I and Run II.

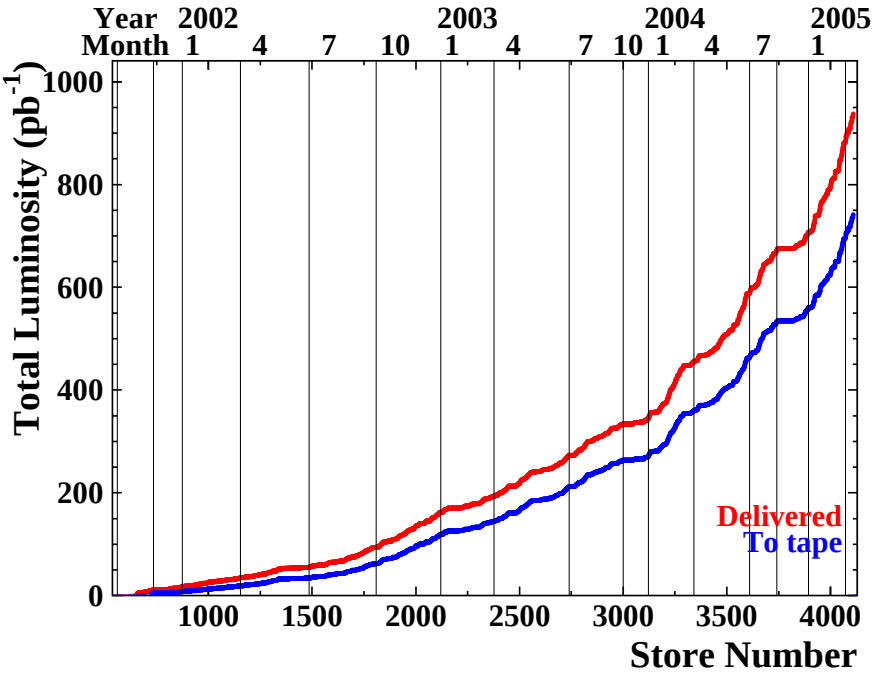

Figure 2.2: Total luminosity gathered by the CDF detector as of April, 2005. The red curve is luminosity delivered, and the blue curve is luminosity written to tape by CDF.

2.2 CDF Run II Detector

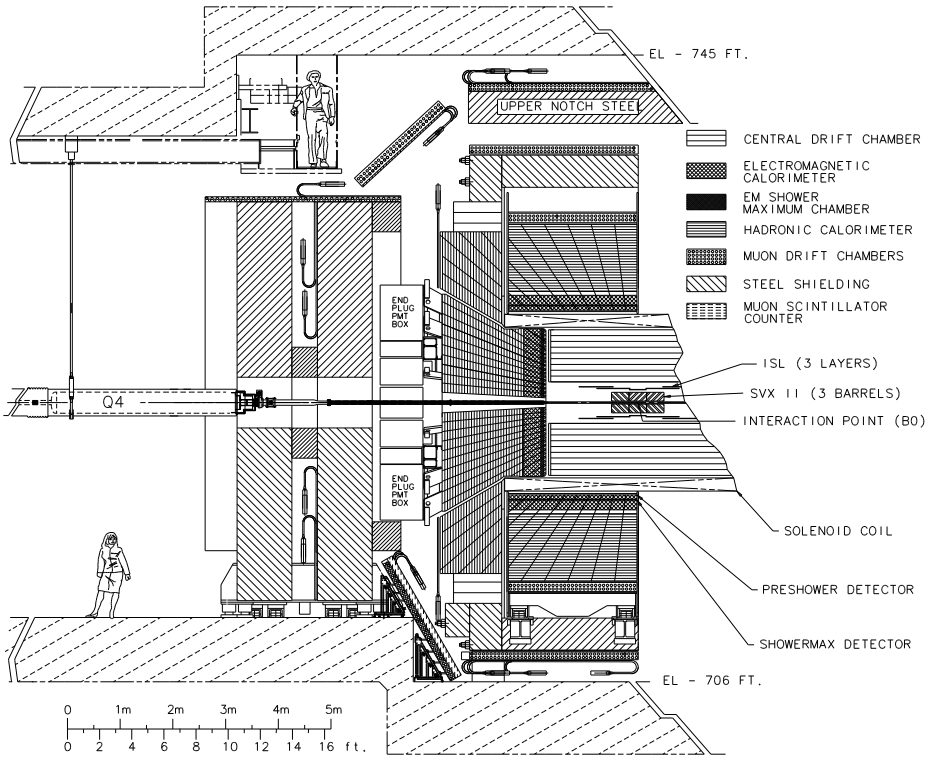

Figure 2.3: Schematic representation of the Collider Detector at Fermilab (CDF).

The Collider Detector at Fermilab (CDF) is a multi-purpose particle spectrometer. Figure 2.3 shows an elevation view of the detector. Protons enter the detector from the west side, and antiprotons enter from the east side. The positive z direction is defined as the direction the protons are traveling (i.e. pointing from west to east). CDF is roughly cylindrically symmetric, and so the coordinate system is most naturally cylindrical. The azimuthal angle is conventionally called ϕ, and is defined clockwise when looking from west to east (i.e. the "proton-eye-view"). The r dimension is transverse to the beamline. The y direction is defined as pointing upward, and thus

the x-direction is defined (using a right-hand coordinate system) to be facing into the Tevatron. All distances are measured in centimeters at CDF.

The most natural way to describe a vector in cylindrical coordinates is to quote the distance transverse to the beam (R), the angle relative to $x = 0$ in azimuth (ϕ) and the polar angle θ. Figure 2.4 shows the coordinate geometry of CDF.

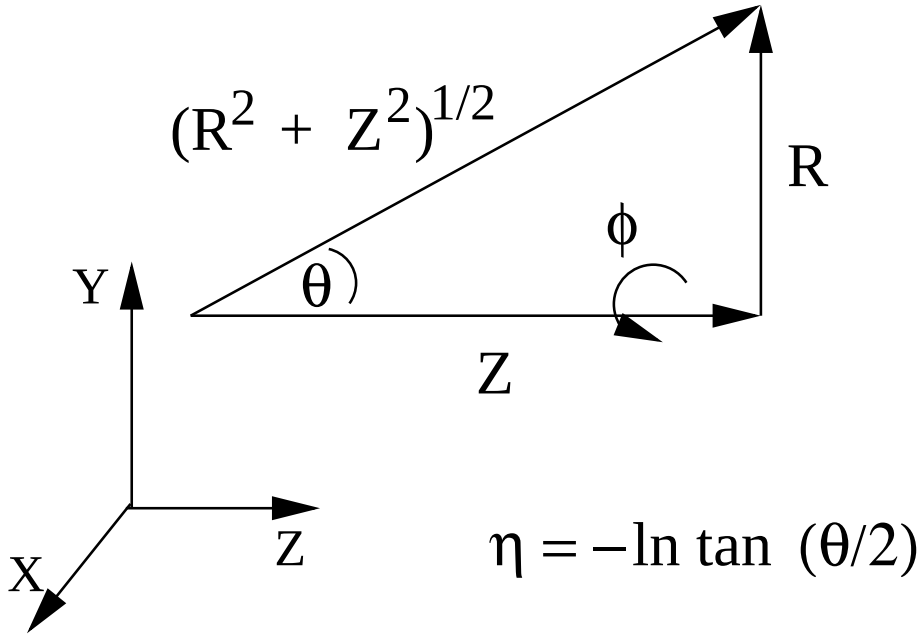

Figure 2.4: Coordinate system of the Collider Detector at Fermilab (CDF).

However, θ is not a good variable to use in this case because it is not a Lorentz invariant. Due to the fact that the proton (and antiproton) is an extended object, the actual constituent partons will not be traveling at 980 GeV. Thus, the number of particles per unit angle ($dN/d\theta$) will not be the same for particles with different velocity.

Instead, we use the concept of the *rapidity*, defined as

$$Y = \frac{1}{2} ln \frac{E + p_z}{E - p_z} \tag{2.2}$$

For a massless particle ($p \gg m$), the rapidity is approximated by the *pseudo-rapidity*, defined as

$$\eta = -ln\ tan(\theta/2) \tag{2.3}$$

In this case, the number of particles per unit rapidity ($dN/d\eta$) is invariant under boosts in the z direction.

2.2.1 Particle Detection

To fully reconstruct an event in a collider machine, it is desirable to reconstruct the energy, momentum, and type of every single particle in the interaction. While this is obviously difficult in any real detector, it is desirable to come as close as possible. We will now consider how to measure the momentum and energy of a given particle.

Particle Momenta

To begin abstractly, if we consider any charged stable particle, we know from elementary physics that, in the presence of a magnetic field, it will experience a force

$$\vec{F}(\vec{r}) = \alpha \cdot q\vec{v} \times \vec{B}(\vec{r}) \tag{2.4}$$

where q is the charge (in units of the electron charge), $\vec{v}$ is the particle's velocity vector (in units of the speed of light), and $\vec{B}(\vec{r})$ is the magnetic field at a point $\vec{r}$ (in Tesla). α is a constant that depends on the units chosen. If we consider a uniform

field in the z direction, $\vec{B}(\vec{r}) = B_0\hat{z}$, this reduces to

$$\vec{F}(\vec{r}) = \alpha \cdot q \cdot B_0 \vec{v} \times \hat{z} \tag{2.5}$$

Using Newton's second law, we write this as

$$\vec{F}(\vec{r}) = \dot{\vec{p}} = m\dot{\vec{v}} = \alpha \cdot q \cdot B_0 \vec{v} \times \hat{z} \tag{2.6}$$

In x,y, and z components, this is

$$\begin{pmatrix} \dot{v_x} \\ \dot{v_y} \\ \dot{v_z} \end{pmatrix} = \frac{\alpha \cdot q \cdot B_0}{m} \begin{pmatrix} v_y \\ -v_x \\ 0 \end{pmatrix}. \tag{2.7}$$

This is the equation of a helix in 3-dimensions. It is a circle in the xy plane, and the z direction has constant velocity. That is, the radius of the circle is constant, and the ϕ of the particle varies with time ($\phi = \phi(t)$). The radius of the projection in the xy plane can be determined by rewriting the magnitude of Eq2.5 using the equation for centripetal acceleration

$$F = \frac{m \cdot v_T^2}{R} = \alpha \cdot q \cdot v_T \cdot B_0 \tag{2.8}$$

where v_T is the velocity in the xy plane (perpendicular to the z-axis). Solving for R, we see

$$R = \frac{m \cdot v_t}{\alpha \cdot q \cdot B_0} = \frac{p_T}{\alpha \cdot q \cdot B_0}. \tag{2.9}$$

This also gives us a method in which to calculate p_T. We can measure the particle trajectory (ϕ and R), and then simply use Equation 2.9 to convert the radius into the transverse momentum. If we also realize that in the z direction, the momentum is a constant, we can then measure the angle with the z axis. In this way, we have all three components of the particle's momentum.

In order to measure the radius of the particle's trajectory, we actually measure it's curvature, C. At CDF, the half-curvature is actually measured,

$$C = \frac{1}{2R}. \tag{2.10}$$

Thus, the transverse momentum is measured as

$$p_T = \frac{\alpha \cdot B}{2C}. \tag{2.11}$$

Therefore, we can measure the momentum of any charged, stable particle by measuring the curvature of its trajectory after an interaction. If the particle is neutral, however, there is nothing we can learn about the particle's momentum.

The intrinsic momentum resolution, therefore, is equal to

$$\begin{aligned} p_T &= \frac{\alpha B}{2C} && (2.12)\\ dp_T &= -\frac{\alpha B}{2C^2} dC && (2.13)\\ \frac{dp_T}{p_T} &= -\frac{dC}{C} && (2.14)\\ &= -\frac{\alpha B}{2} p_T dC && (2.15) \end{aligned}$$

The particular resolution of dC is detector-dependent. At CDF, the resolution on p_T is about

$$\frac{dp_T}{p_T} = 0.15\% \times p_T \tag{2.16}$$

Overall there are five parameters to characterize a helix in 3-d. The parameters chosen at CDF are

- d_0: Impact parameter in $R - \phi$ to $(0, 0, 0)$
- z_0: Impact parameter in z to $(0, 0, 0)$

- ϕ: Azimuthal angle of tangent line at point of closest approach in $R - \phi$
- $\cot\theta$: Pitch, defined as the ratio of the helix step to its diameter.
- C: Curvature of track (actually half-curvature as described above).

We now turn to a discussion of a simple $2 - d$ tracking model to obtain a feel for the relevant parts of tracking.

Simple Tracking

To get a feel for how large tracking errors are given a set of N measurement points, it is instructive to look at a 2-d tracking algorithm assuming $B = 0$ (i.e. all tracks are straight lines). In this case, we are dealing with a set of N measurement points of position $x \pm \delta x$. Because the tracks are straight lines, we can use a linear fit to the data.

Figure 2.5 shows a track with measurement points from a detector parallel to the x-axis. So the measurement points have an (x, y) coordinate, where the y coordinate is assumed to be measured much better than the x coordinate. In this way, the fit is a simple 1-d linear fit. The measurement point on the kth layer can be represented by a simple model of multiple scattering, in that each layer contributes an equal amount to the total position resolution. That is, the error is

$$\delta x_k^2 = a^2 + kb^2 \tag{2.17}$$

The a^2 term is to account for the intrinsic resolution of the detector, while b^2 is the multiple scattering term. Each layer adds b^2 to the total error. In the simple example given in Figure 2.5, $a^2 = 1.0\ \mu m$ and $b^2 = 0.5\ \mu m$.

Given these points, it is useful to define [6]

$$\Lambda_{11} = \sum_i \frac{1}{\sigma_i^2} \tag{2.18}$$

$$\Lambda_{12} = \sum_i \frac{x_i}{\sigma_i^2} \tag{2.19}$$

$$\Lambda_{22} = \sum_i \frac{x_i^2}{\sigma_i^2} \tag{2.20}$$

$$g_1 = \sum_i \frac{y_i}{\sigma_i^2} \tag{2.21}$$

$$g_2 = \sum_i \frac{y_i x_i}{\sigma_i^2} \tag{2.22}$$

If we fit to a line

$$y = \alpha_1 + \alpha_2 x \tag{2.23}$$

the equations for α_1 and α_2 are

$$\alpha_1 = \frac{g_1\Lambda_{22} - g_2\Lambda_{12}}{\Lambda_{11}\Lambda_{22} - \Lambda_{12}^2} \tag{2.24}$$

$$\alpha_2 = \frac{g_2\Lambda_{11} - g_1\Lambda_{12}}{\Lambda_{11}\Lambda_{22} - \Lambda_{12}^2} \tag{2.25}$$

Given these values, the error on the track extrapolation at a path length s (which parameterizes the line $y = \alpha_1 + \alpha_2 x$) is given by

$$\Delta f^2(s) = \frac{1}{\Lambda_{11}} + \frac{\Lambda_{11}}{\Lambda_{11}\Lambda_{22} - \Lambda_{12}^2}\left(s - \frac{\Lambda_{12}}{\Lambda_{11}}\right)^2 \tag{2.26}$$

To get a sense of how the errors are related to distance from the measurement points, we consider Equation 2.26 in the limit where the multiple-scattering is negligible compared to the intrinsic resolution of the device. That is, Equation 2.17 becomes

$$\sigma_i = \sigma \tag{2.27}$$

Then we see that Equations 2.18-2.22 become

$$\Lambda_{11} = \frac{N}{\sigma^2} \tag{2.28}$$

$$\Lambda_{12} = \frac{1}{\sigma^2}\sum_i x_i \tag{2.29}$$

$$\Lambda_{22} = \frac{1}{\sigma^2}\sum_i x_i^2 \tag{2.30}$$

$$g_1 = \frac{1}{\sigma^2}\sum_i y_i \tag{2.31}$$

$$g_2 = \frac{1}{\sigma^2}\sum_i y_i x_i \tag{2.32}$$

$$\tag{2.33}$$

Realizing that $\frac{1}{N}\sum_i x_i =< x >$ (the average value of x), and $\frac{1}{N}\sum_i x_i^2 - < x >^2 = \Delta x^2$ (the variance of the x-values), Equation 2.26 becomes

$$\Delta f(s) = \frac{\sigma}{\sqrt{N}}\sqrt{1 + \frac{1}{\Delta x^2}\left(s - < x >\right)^2} \tag{2.34}$$

If let $t = (s - < x >)/\Delta x$, this is

$$\Delta f(t) = \frac{\sigma}{\sqrt{N}}\sqrt{1 + t^2} \tag{2.35}$$

Qualitatively, the more measurement points there are, the smaller the error is (by $1/\sqrt{N}$). Also, the farther you are from the average measurement point, the larger your error is. For $t \ll 1$, the errors are quadratic in t, but for $t \gg 1$, the errors are linear in t. And of course, the better the intrinsic resolution of the detector, the better the resolution on the tracks.

If we wish to turn this into a measurement of the error on the impact parameter (d_0), we solve for the point of closest approach, which is the intersection of the fit line

and a perpendicular line through the origin:

$$y_1 = \alpha_1 + \alpha_2 x_0 \tag{2.36}$$

$$y_\perp = \frac{-1}{\alpha_2} x_0 \tag{2.37}$$

$$x_0 = \frac{-\alpha_1}{\alpha_2 + \frac{1}{\alpha_2}} \tag{2.38}$$

The displacement along the length of the track is

$$r^2 = (x_0 - < x >)^2 + (y_0 - < y >)^2 \tag{2.39}$$

We use the equation of the fit line to write this as

$$r^2 = (x_0 - < x >)^2 + [(\alpha_1 + \alpha_2 x_0) - (\alpha_1 + \alpha_2 < x >)]^2 \tag{2.40}$$

$$= (x_0 - < x >)^2 (1 + \alpha_2^2) \tag{2.41}$$

Plugging this into Equation 2.34, we obtain the error at the point of closest approach (pca):

$$\Delta f(pca) = \frac{\sigma}{\sqrt{N}} \sqrt{1 + \frac{1}{\delta x^2} \left((x_0 - < x >) \sqrt{1 + \alpha_2^2} - < x > \right)^2} \tag{2.42}$$

$$= \frac{\sigma}{\sqrt{N}} \sqrt{1 + \frac{1}{\delta x^2} \left[x_0 \sqrt{1 + \alpha_2^2} - < x > \left(1 + \sqrt{1 + \alpha_2^2} \right) \right]^2} \tag{2.43}$$

$$\tag{2.44}$$

Since d_0 is perpendicular to the line, the error on f at the point of closest approach is the error on d_0. The qualitative features of this expression are that the farther the track is from the origin (large $< x >$), the larger the track errors, linearly. Also, the error scales linearly with the slope (α_2). A helpful case is to examine this if the slope is zero (parallel to the x axis). In that case, $x_0 = 0$ and the error is

$$\Delta f(0) = \frac{\sigma}{\sqrt{N}} \sqrt{1 + \left(\frac{2 < x >}{\Delta x} \right)^2} \tag{2.45}$$

Thus, at large $< x >$, the errors on d_0 grow linearly with $< x >$, at a rate of about $2 < x > /\Delta x$.

If the slope is very large ($\alpha_2 \gg 1$), then the error on the impact parameter becomes

$$\Delta f = \frac{\sigma}{\sqrt{N}} \sqrt{1 + \alpha_2^2 \left(\frac{x_0 - < x >}{\Delta x} \right)^2} \tag{2.46}$$

In this case, corrections will be linear in the slope (α_2), and also depend on how far the impact parameter is from the average measurement point.

Figure 2.5 shows the situation for the full expression, including multiple scattering. The qualitative features are the same with and without multiple scattering. The errors are still quadratic near the average of the measurement points, and the errors grow linearly for large s. The error on d_0 also shows the same qualitative features.

Particle Energy

The measurement of particle energies is done using calorimetry. Essentially, calorimeters use scattering to measure the energy of an incoming particle. The calorimeters used at CDF are made of very dense material (lead or steel) to maximize the number of interactions per unit length. Incoming particles collide with electrons or nuclei inside the material and produce showers of particles. A thin layer of detecting material is then placed behind the dense material to measure the outgoing particles. These pairs of detectors are then placed in sequence, in a sandwich. The detector material itself is typically made of scintillators. Figure 2.6 shows a schematic of one sandwich. The detector itself would have several.

The number of particles remaining after a length x will be

$$N(x) = N_0 e^{x/k} \tag{2.47}$$

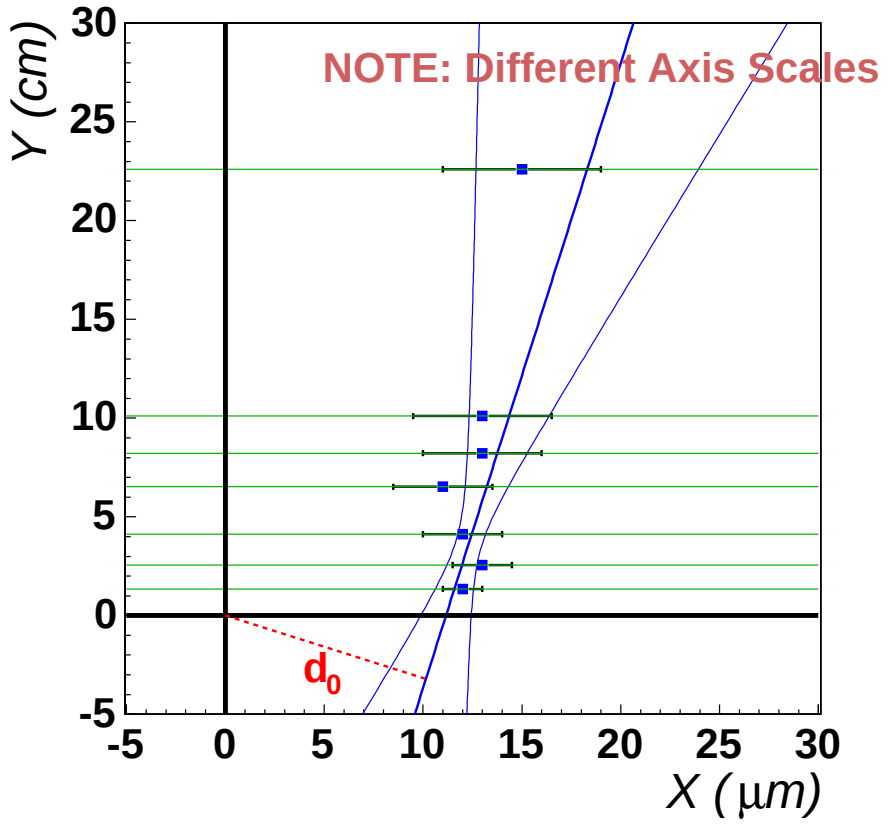

Figure 2.5: Simple tracking model for a 2-d tracking algorithm with $B = 0$.

where N_0 is the number of particles initially, and k is a constant dependent on the material. For electromagnetic showers, this is the radiation length, denoted by X_0. For hadronic showers, this is the nuclear interaction length, denoted by λ.

Each layer samples a percentage of the incoming particle's energy (typically about 10%). By sandwiching infinite numbers of these blocks together, it is theoretically possible to sample enough to measure the total energy of the incoming parton. However, given the limited spatial extent constraint (a.k.a. cost of building materials for the entire detector), it is not possible to measure all the energy of all the particles that

come in. The remaining particles "punch through" the calorimeter, and go through other detector elements (more on this later). Thus, it is necessary to measure the response of the calorimeter by calibrating with a beam of precisely known energy and comparing the input and output energies.

The intrinsic energy resolution is therefore stochastic in nature. Thus, the energy resolution will be proportional to $1/\sqrt{N}$, where N is the number of outgoing particles. Since the number of outgoing particles is proportional to the incoming energy, the energy resolution is proportional to $1/\sqrt{E}$. The proportionality constant depends on the detector used, and will be discussed below.

At CDF, there are two types of calorimeters, electromagnetic and hadronic. Electromagnetic calorimeters are designed to measure the energy of photons and electrons. Electrons will collide with other electrons in the material and undergo "Bremsstrahlung" radiation. Photons will pair-produce in the presence of atomic nuclei, and the pair-produced electrons will then undergo Bremsstrahlung. The hadronic calorimeters are designed to detect all other strongly interacting particles. The incoming particles will interact with nuclei in the material and produce showers.

The formula governing the radiation length due to Bremsstrahlung radiation is given by [6]:

$$\frac{1}{X_0} = 4\alpha r_e^2 \frac{N_A}{A} \left[Z^2 \left(L_{rad} - f(Z) \right) + Z L'_{rad} \right] \tag{2.48}$$

where X_0 is the radiation length, $\alpha = 1/137$ is the fine structure constant, N_A is Avogadro's number, A is the atomic mass of the absorber, Z is the atomic number of the absorber, L_{rad} and L'_{rad} are experimentally determined constants, and $f(Z)$ is an infinite sum. The electromagnetic shower is very well-characterized because

only electrons and photons are involved in this process, and the radiation lengths for electrons and photons are always small.

The nuclear interaction length for hadronic showers is given very approximately by [6]:

$$\lambda \approx 35\ g - cm^{-2} A^{1/3} \tag{2.49}$$

where A is the atomic mass of the absorber. Unlike the electromagnetic case, there are large variations in the amount of energy transferred to secondary particles. Also, any neutral pions that are created decay into two photons, which then deposit their energy in the calorimeter, making it very difficult to measure their energies. These large variations in the energy deposited in the hadronic calorimeter make it very difficult to characterize the response of the calorimeter.

In order to maximize the ability to distinguish electromagnetic showers and hadronic showers, it is therefore necessary to make the electromagnetic calorimeter much denser than the hadronic calorimeter, since the electromagnetic shower radiation length depends on A/Z^2, while the hadronic shower radiation length depends on $A^{1/3}$. A higher density electromagnetic calorimeter will ensure that most of the EM energy is deposited in the EM calorimeter and will not leak into the hadronic calorimeter. This is why the electromagnetic calorimeter is made with lead and the hadronic calorimeter is made with steel.

The active part of a sampling calorimeter is typically made of scintillators. These detectors give off scintillating light when charged particles pass through it, exciting particles in the material which subsequently decay (emitting a photon). Scintillators can be chosen that have high indices of refraction, and hence it is possible to choose a

geometry such that most of the light does not escape the material. It is then possible to pass the light to a photomultiplier tube (PMT) to produce an electrical signal. Typically, the light is produced at a frequency that is not optimal for collection by the PMT, so the light is passed through a wavelength-shifting material before it reaches the PMT. Figure 2.7 show a schematic of the detector.

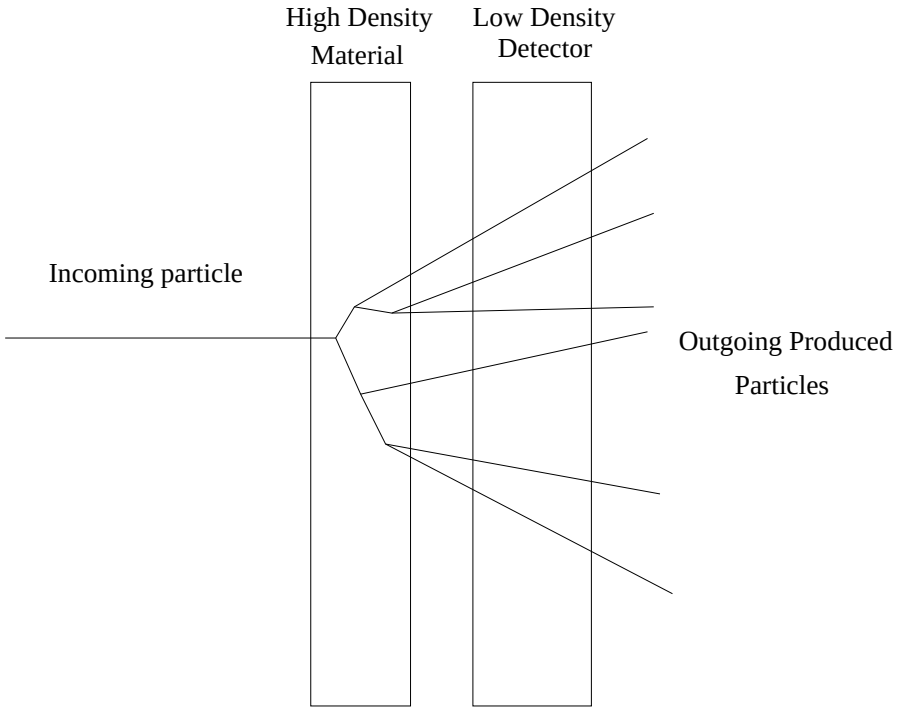

Figure 2.6: Measurement of a particle's energy with a calorimeter.

Jet Clustering and Energy Corrections

Due to the physically wide scales over which particles hadronize, it is necessary to develop an algorithm to "cluster" physical calorimeter tower deposits into an estimate of the actual jet of particles. In this analysis, we use a method called `JetClu` [19], in

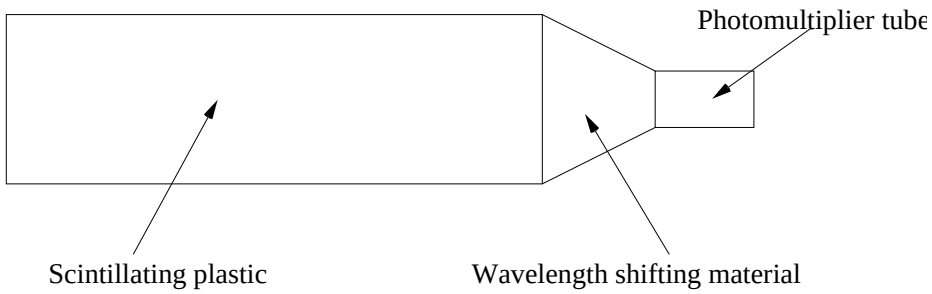

Figure 2.7: Diagram of scintillator detector.

which a seed tower is selected, and neighboring towers are added within a certain cone (in our case, $\Delta R < 0.4$). The centroid of that cluster is then calculated by weighting the towers by their energies, and re-estimating the average pointing vector. This pointing vector is then input back into the algorithm, and the procedure is iterated until the pointing vector is stable.

The sampling nature of the calorimeter gives rise to uncertainties in the jet energy. Similarly, if the jet clustering algorithm does not pick up all the energy deposited in the detector, the jet energy is further degraded.

There are various ways the measured energy of a jet and the actual energy are not the same. There are eight levels of corrections at CDF [20] (however two are deprecated and are kept for historical reasons):

0. Online/Offline calibrations. Calibrate using particle beams with known energies comparing to test beams.

1. Eta-dependent. Makes the responses uniform in η.

2. Not in use

3. Not in use

4. Multiple Interactions. Corrects for the effect of multiple interactions using the number of z vertices in the event.

5. Absolute. Corrects for any non-linearity and energy loss in the un-instrumented regions of each calorimeter.

6. Underlying event. Corrects for energy associated with spectator partons in the event.

7. Out-of-cone. Corrects for energy that is deposited outside the cone of the particular jet clustering algorithm.

8. Splash-out. Corrects for energy that exits the calorimeter.

Figure 2.8 shows a schematic of the various jet correction levels.

It is necessary to simulate the response of the calorimeter to these effects using various methods. The overall response can be determined by firing particles with known energies into the calorimeter and measuring the output before the calorimeter is installed. This gives rise to calibrations of the detector. Furthermore, it is possible to use the resolution of the electromagnetic calorimeters to measure the resolution of the hadronic calorimeter. This is done by performing *photon-jet balancing*, in which a photon is selected back-to-back with another jet. The energy of the photon is well-measured by the electromagnetic calorimeter, and so momentum and energy conservation can be applied to measure the response of the "probe jet".

By measuring the *photon-jet balancing* in both the data and the simulation of the detector, it is possible to measure the accuracy of the simulation. Where there is a

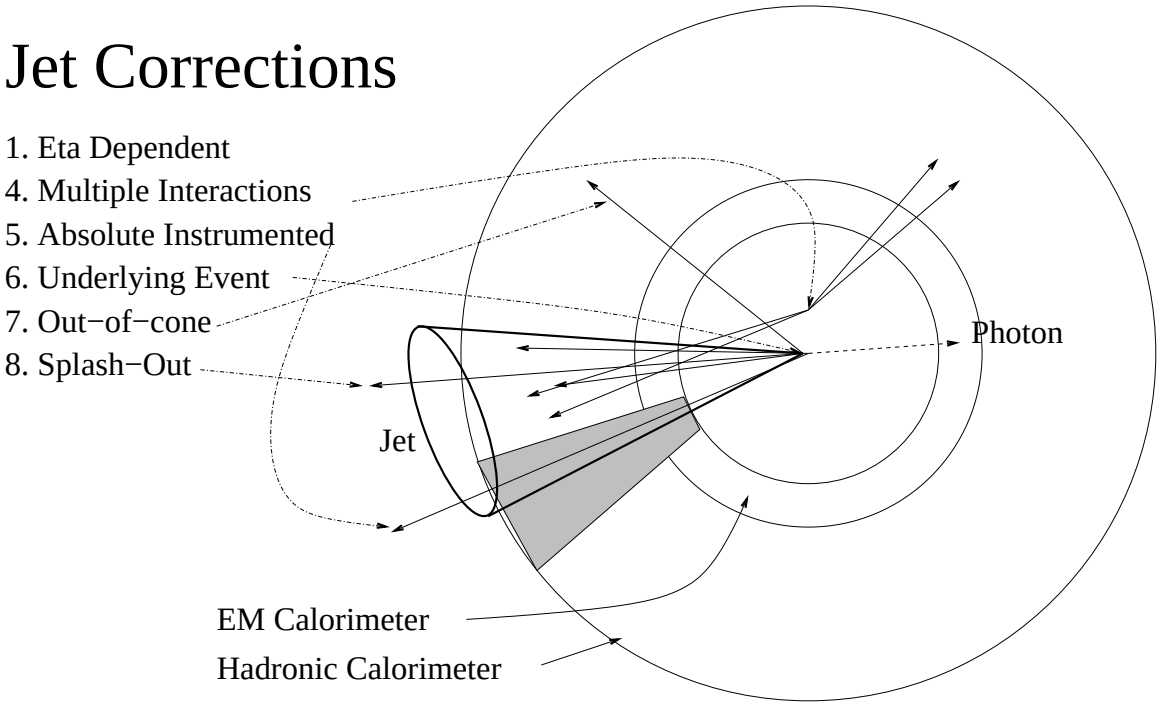

Figure 2.8: Schematic of jet correction levels.

discrepancy, it is possible to determine a correction factor, known as the *jet energy scale*

In this analysis, we correct jets to Level 4 to make our event selection. In order to calculate an invariant mass of a jet object, it is better to use level 5 corrections.

Particle Lifetime

It is possible to determine the flight distance of a particle by detecting its decay products. Figure 2.9 gives a schematic of how this is accomplished. This distance can be related to the decay time by

$$D = \beta ct = \beta\gamma c\tau \tag{2.50}$$

where β is the velocity in units of the speed of light, γ is the relativistic factor, t is the lab flight time, and τ is the proper lifetime.

Firstly, the primary interaction vertex is reconstructed. Because the decaying particle will not come from the primary vertex, it will form a secondary vertex. The decay products will not point back to the primary vertex (because they come from the displaced secondary vertex). The impact parameter (d_0) of these tracks will therefore be large when measured with respect to the primary vertex. It is then possible to select these tracks, and form the secondary vertex by examining where they intersect in space. Using these decay products, it is possible to reconstruct the flight distance of these particles.

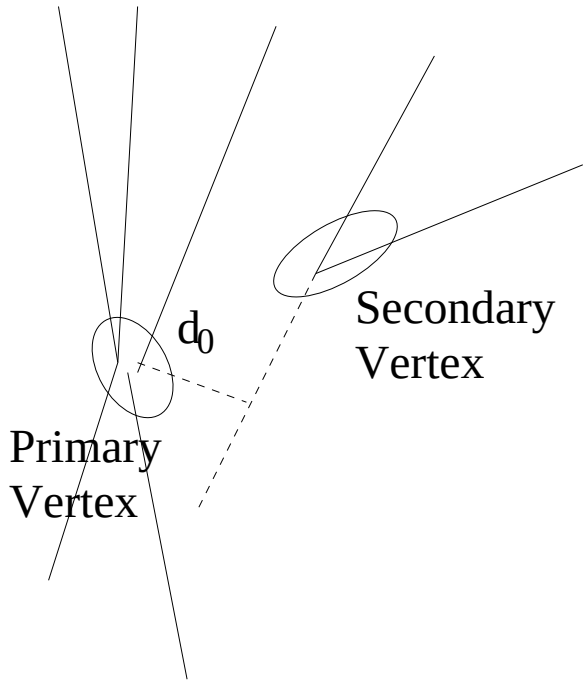

Figure 2.9: Measurement of a particle's lifetime via decay products.

Simple Vertexing

In order to get a sense of some relevant issues for vertexing tracks, it is useful to consider a very simple case with straight-line (i.e. $B = 0$) tracks, as in Section 2.2.1, and considering only 2-d vertices. In this case, the vertex is trivial (the solution of two lines intersecting in a plane). The solution for the errors is more interesting and gives some insight into the full solution.

Consider two lines

$$y_1 = \alpha_{11} + \alpha_{12} x_1 \tag{2.51}$$

$$y_2 = \alpha_{21} + \alpha_{22} x_2 \tag{2.52}$$

These intersect at

$$x = \frac{\alpha_{11} - \alpha_{12}}{\alpha_{22} - \alpha_{21}} \tag{2.53}$$

$$y = \alpha_{11} + \alpha_{21} \left(\frac{\alpha_{11} - \alpha_{12}}{\alpha_{22} - \alpha_{21}} \right) \tag{2.54}$$

The simplest way to construct the errors on this vertex is to consider

$$\begin{pmatrix} x \\ y \end{pmatrix} = \begin{pmatrix} x_1 - x_2 \\ y_1 - y_1 \end{pmatrix} = f \begin{pmatrix} x_1 \\ y_1 \\ x_2 \\ y_2 \end{pmatrix} \tag{2.55}$$

and take the limit as $(x, y) \to (0, 0)$.

The error matrix for this function is

$$J = \begin{pmatrix} 1 & 0 & -1 & 0 \\ 0 & 1 & 0 & -1 \end{pmatrix} \tag{2.56}$$

If each track is at an angle ϕ_1 and ϕ_2 with the x-axis, and consider tracks where the errors are only in one-dimension (i.e. hit position is known to lie in a plane), then we use the error matrix from Equation 2.26, and rotate the angles by ϕ_1 and ϕ_2 to obtain

$$C = \begin{pmatrix} f_1^2(s_1)\cos^2(\phi_1) & f_1^2(s_1)\sin(\phi_1)\cos(\phi_1) & 0 & 0 \\ f_1^2(s_1)\sin(\phi_1)\cos(\phi_1) & f_1^2(s_1)\sin^2(\phi_1) & 0 & 0 \\ 0 & 0 & f_2^2(s_2)\cos^2(\phi_2) & f_2^2(s_2)\sin(\phi_2)\cos(\phi_2) \\ 0 & 0 & f_2^2(s_2)\sin(\phi_2)\cos(\phi_2) & f_2^2(s_2)\sin^2(\phi_2) \end{pmatrix} \tag{2.57}$$

Then the error matrix in this coordinate system is

$$C' = JCJ^T \tag{2.58}$$

$$= \left(\begin{array}{c|c} f_1^2(s_1)\cos^2(\phi_1) & f_1^2(s_1)\sin(\phi_1)\cos(\phi_1) \\ +f_2^2(s_2)\cos^2(\phi_2) & +f_2^2(s_2)\sin(\phi_2)\cos(\phi_2) \\ \hline f_1^2(s_1)\sin(\phi_1)\cos(\phi_1) & f_1^2(s_1)\sin^2(\phi_1) \\ +f_2^2(s_2)\sin(\phi_2)\cos(\phi_2) & +f_2^2(s_2)\sin^2(\phi_2) \end{array}\right) \tag{2.59}$$

$$\equiv \begin{pmatrix} \sigma_x^2 & \rho\sigma_x\sigma_y \\ \rho\sigma_x\sigma_y & \sigma_y^2 \end{pmatrix} \tag{2.60}$$

We see the correlation coefficient is

$$\rho^2 = \frac{f_1^4\sin^2\phi_1\cos^2_{\phi_1} + f_2^4\sin^2\phi_2\cos^2\phi_2 + 2f_1^2f_2^2\cos\phi_1\sin\phi_1\cos\phi_2\sin\phi_2}{f_1^4\sin^2\phi_1\cos^2_{\phi_1} + f_2^4\sin^2\phi_2\cos^2\phi_2 + f_1^2f_2^2(\cos^2\phi_1\sin^2\phi_2 + \cos^2\phi_2\sin^2\phi_1)} \tag{2.61}$$

We can draw this as an ellipse with center (a_x, a_y) with p_1 as the major axis and p_2 as the minor axis at an angle α as

$$1-\rho^2 = \left(\frac{x-a_x}{\sigma_x}\right)^2 - 2\rho\left(\frac{x-a_x}{\sigma_x}\right)\left(\frac{y-a_y}{\sigma_y}\right) + \left(\frac{y-a_y}{\sigma_y}\right)^2 \tag{2.62}$$

$$p_1^2 = \frac{\sigma_x^2\sigma_y^2(1-\rho^2)}{\sigma_y^2\cos^2\alpha - 2\rho\sigma_x\sigma_y\sin\alpha\cos\alpha + \sigma_x^2\sin^2\alpha} \tag{2.63}$$

$$p_2^2 = \frac{\sigma_x^2\sigma_y^2(1-\rho^2)}{\sigma_y^2\sin^2\alpha + 2\rho\sigma_x\sigma_y\sin\alpha\cos\alpha + \sigma_x^2\cos^2\alpha} \tag{2.64}$$

$$\alpha = \frac{1}{2}\arctan\frac{2\rho\sigma_1\sigma_2}{\sigma_1^2 - \sigma_2^2} \tag{2.65}$$

Figure 2.10(a) shows an example of this simple vertexing scheme. It shows two tracks with their errors described as in Sec 2.2.1, and the inset is a close-up of the vertex that is formed by those two tracks. We now consider special cases of these equations to gain insight as to their nature.

If $\phi_1 = \phi_2$ (i.e. the lines are parallel), Equation 2.61 becomes:

$$\rho^2 = \frac{f_1^4 \sin^2\phi_1 \cos^2_{\phi_1} + f_2^4 \sin^2\phi_2 \cos^2\phi_2 + 2f_1^2 f_2^2 \cos\phi_1 \sin\phi_1 \cos\phi_2 \sin\phi_2}{f_1^4 \sin^2\phi_1 \cos^2_{\phi_1} + f_2^4 \sin^2\phi_2 \cos^2\phi_2 + f_1^2 f_2^2(\cos^2\phi_1 \sin^2\phi_2 + \cos^2\phi_2 \sin^2\phi_1)} \quad (2.66)$$

$$= \frac{f_1^4 \sin^2\phi \cos^2_{\phi} + f_2^4 \sin^2\phi \cos^2\phi + 2f_1^2 f_2^2 \cos\phi \sin\phi \cos\phi \sin\phi}{f_1^4 \sin^2\phi \cos^2_{\phi} + f_2^4 \sin^2\phi \cos^2\phi + f_1^2 f_2^2(\cos^2\phi \sin^2\phi + \cos^2\phi \sin^2\phi)} \quad (2.67)$$

$$= \frac{(f_1^4 + f_2^4 + 2f_1^2 f_2^2)\cos^2\phi \sin^2\phi}{(f_1^4 + f_2^4 + 2f_1^2 f_2^2)\cos^2\phi \sin^2\phi} \quad (2.68)$$

$$= 1 \quad (2.69)$$

So for parallel tracks, the correlation coefficient is unity, and the ellipse becomes very narrow, with the major axis along the direction of the lines (actually along the direction of the bisector of the smaller angle between them, see Figure 2.10(a)).

If $\phi_1 = \phi_2 - \pi/2$ (i.e. the lines are perpendicular), it is easiest to consider the case where $\phi_1 = \pi/2$ and $\phi_2 = 0$ (without loss of generality):

$$\rho^2 = \frac{f_1^4 \sin^2\pi/2 \cos^2_{\pi/2} + f_2^4 \sin^2 0 \cos^2 0 + 2f_1^2 f_2^2 \cos\pi/2 \sin\pi/2 \cos 0 \sin 0}{f_1^4 \sin^2\pi/2 \cos^2_{\pi/2} + f_2^4 \sin^2 0 \cos^2 0 + f_1^2 f_2^2(\cos^2\pi/2 \sin^2 0 + \cos^2 0 \sin^2\pi/2)} \quad (2.70)$$

$$= \frac{f_1^4 \cdot 1 \cdot 0 + f_2^4 \cdot 0 \cdot 1 + 2f_1^2 f_2^2 \cdot 0 \cdot 1 \cdot 1 \cdot 0}{f_1^4 \cdot 1 \cdot 0 + f_2^4 \cdot 0 \cdot 1 + f_1^2 f_2^2(\cdot 0 \cdot 0 + \cdot 1 \cdot 1)} \quad (2.71)$$

$$= 0 \quad (2.72)$$

So for perpendicular tracks, the correlation coefficient is zero, and the ellipse reduces to a circle. In this case, it is also instructive to see the size of the circle. In this case

$\alpha = 0$, and the major and minor axes are

$$p_1^2 = \frac{\sigma_x^2 \sigma_y^2}{\sigma_y^2} = \sigma_x^2 \tag{2.73}$$

$$p_2^2 = \frac{\sigma_x^2 \sigma_y^2}{\sigma_x^2} = \sigma_y^2 \tag{2.74}$$

$$\tag{2.75}$$

So we see that the major and minor axes reduce to σ_x and σ_y. Figure 2.10(b) shows how the error ellipse looks when the tracks are roughly perpendicular. It is clear that the ellipse is now a circle, and the error is the track error.

These two features will be present for any vertex scheme, even if the tracks are circular (as is the case if $B \neq 0$), and if the vertex is in 3-d. The vertex will point along the line bisecting the smaller of the angles of the tracks for tracks at an arbitrary angle, and the vertex will be circular for tracks that are perpendicular, with errors the same size as the track errors at that position.

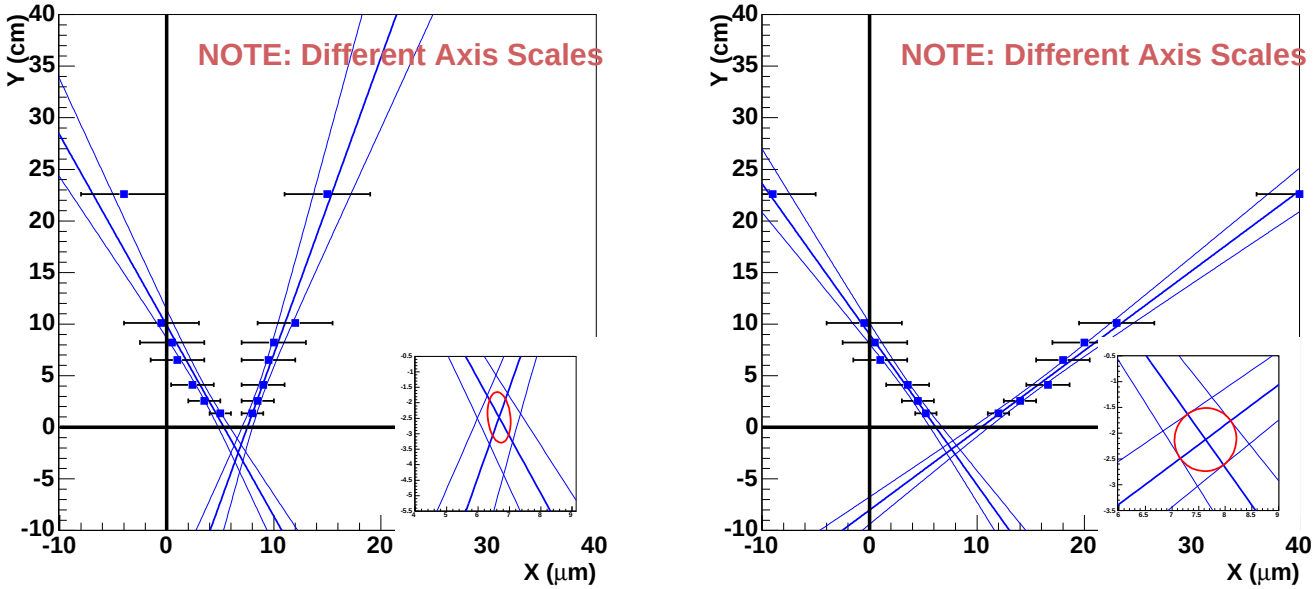

(a) Simple vertex between two tracks.

(b) Simple vertex with perpendicular tracks.

Figure 2.10: Simple vertex examples. Note the axis scales are microns (on the x axis) and centimeters (on the y axis). The central lines are the best fits, and the bounding curves are the 1σ error bars. The ellipses are the error ellipses on the vertex fits.

Particle ID

The particles we would like to measure at any collider are

- Stable charged hadrons
- Stable neutral hadrons
- Unstable hadrons (charged or neutral) and tau leptons
- "V" decays (K_0^S, Λ, $\gamma \rightarrow e^+e^-$, so named because there are two decay products of opposite charge)
- Electrons
- Photons
- Muons
- Neutrinos

Each individual particle will be detected differently because each will interact in a unique way with material. Figure 2.11 shows the ways various particles interact in a particle detector.

Both stable and charged hadrons will produce jets. The momentum of the charged tracks inside jets can be measured with the tracking chambers. They will also deposit some small amount of energy in the electromagnetic calorimeter. The majority of their energy will be deposited in the hadronic calorimeter. Depending on how much material is in the hadronic calorimeter, some particles will "punch through" the calorimeter and leak out of the calorimeter.

Unstable hadrons are identified via their decay products. Tau leptons are also included in this category, although they are not hadrons but leptons. $\Lambda \rightarrow p\pi$, for example, can be detected by examining the outgoing proton and pion. We detect unstable hadrons by reconstructing their displaced vertices. These include "V" particles like Λ hadrons, K_0^s, and heavy flavor hadrons such as b and c hadrons. The detection of b hadrons is very important for this analysis, because the top quark will decay almost 100% of the time to a W boson and a b quark. Identifying the b quark from a top decay will be of utmost importance to this analysis.

Some special cases are particles with zero lifetime that decay into two leptons, such as J/ψ's and Υ's, so it is still possible to reconstruct these objects using their decay products.

Electrons and photons are detected using the electromagnetic calorimeter as described above. The way to discriminate between them is that the electron is charged, and thus will leave a track in the tracking chamber, while the photon is neutral and will have no associated track.

Muons also do not partake in the strong interaction, and only interact electroweakly. However, because of their large mass, they will not interact very often with electrons in the calorimeter, and thus cannot be detected by the electromagnetic calorimeter as electrons are. Instead, we take advantage of the fact that they don't interact much with the calorimeter, and detect them after all the other particles have been absorbed. Thus, we place additional drift chambers outside the calorimeters, and place shielding between them to absorb any particles that "punched through" the calorimeter. It is then possible to identify the muons very cleanly. The hits

in the muon chambers are linked into "tracklets" called "stubs", and those stubs can be matched back to the track in the tracking chamber to obtain momentum measurements.

Neutrinos are not detected by our apparatus. They only interact weakly, and thus will almost never interact. The way we "detect" them is to add up all the other transverse energies in the event, and examine any missing transverse energy. In that way, we can detect the transverse energy of the inferred neutrino.

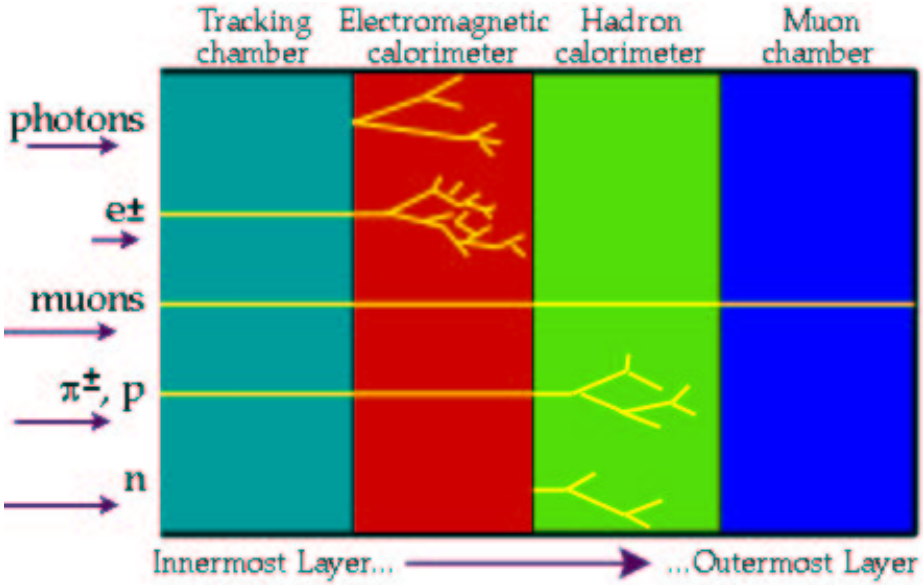

Figure 2.11: Interaction of different particles with detector subsystems.

2.2.2 Cerenkov Luminosity Counters

The Cerenkov Luminosity Counters (CLC) is a collection of 48 thin, long conical, gaseous isobutane Cerenkov detector designed to measure the average number of inelastic $p\overline{p}$ collisions by measuring the number of particles, and their arrival time, in

each bunch crossing ([21]). Cerenkov light is captured by photomultiplier tubes and amplified to measure the number of particles. It is situated in the "3-degree holes" inside the CDF endplug calorimeters in the forward and backward region and which cover the pseudorapidity range $3.7 < \eta < 4.7$.

The CLC measures the luminosity both online (to report back to the Main Control Room), and offline (for analysis). The luminosity ($\mathcal{L}$) is measured by the following formula [22]:

$$\mathcal{L} = \frac{f \cdot \mu}{\epsilon_{CLC} \cdot \sigma_{p\overline{p}}} \tag{2.76}$$

where f is the bunch crossing frequency, μ is the measured average number of interactions per crossing, ϵ_{CLC} is the CLC acceptance times efficiency, and $\sigma_{p\overline{p}}$ is the total $p\overline{p}$ interaction cross section. The CLC measures offline luminosity to an accuracy of 5.9%. This measurement is limited by the uncertainty in μ ($\sim$ 4.2%), and the uncertainty in the total $p\overline{p}$ inelastic cross section ($\sim$ 4.0%). The uncertainty in μ is determined from counting *empty crossings* (crossings with no interactions) [22]. A statistical method is used to extract μ from the Poisson distribution of the total number of $p\overline{p}$ interactions per crossing n. The probability of observing zero interactions, P_0, is related to μ by $P_0(\mu) = e^{-\mu}$. Thus, measuring P_0 can be used to determine μ.

2.2.3 Tracking Subsystems

There are two tracking subsystems at CDF, the silicon detectors (SVXII: Silicon Vertex Detector, L00: Layer 00, and ISL: Intermediate Silicon Layers) and the drift chamber (COT: Central Outer Tracker). The silicon detectors provide excellent impact parameter, azimuthal angle, and z resolution. They are also instrumental

in vertexing. The COT provides excellent resolution of the curvature, ϕ, and η. Together, they provide very accurate measurements of the helical paths of charged particles.

The tracking volume is enclosed within the electromagnetic calorimeter. It has a nearly uniform magnetic field in the z direction of 1.4 Tesla. The silicon detectors are closest to the beamline, ranging from $R = 1.2$ cm to $R = 28$ cm. The COT is outside the ISL, from $R = 44$ cm to $R = 132$ cm.

Figure 2.12 shows the detector subsystems.

We now consider each subsystem in turn.

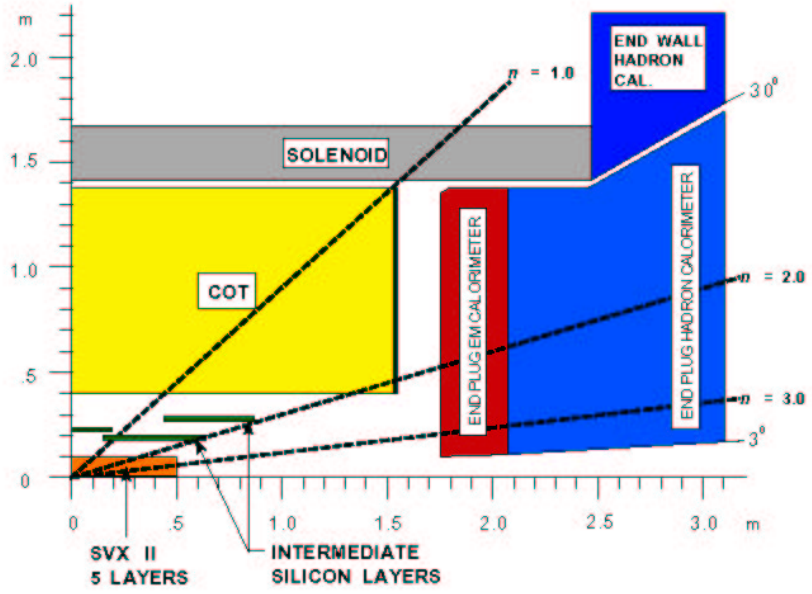

Figure 2.12: Tracking volume at CDF.

Silicon Vertex Detector II (SVXII)

The Silicon Vertex Detector II ([24]) is the primary detector of the silicon subsystems. It is comprised of 5 layers of double sided silicon strip detectors. In all five layers, there is an $R-\phi$ strip, in three layers there are 90° strips, and the other two have 1.25° strips. The $R-\phi$ strips are situated lengthwise on the p-n junction of the detector, and both the 90° and 1.25° strips are located on the n-side. The strips are situated in three cylindrical barrels, each 30 cm long. There are 360 "ladders" (four sensors connected by wire bonds) in 12 x 30° ϕ-slices. The radii of the layers are between 2.5 cm and 10.6 cm. Figure 2.13 shows the barrel structure of the SVXII detector.

Table 2.2 compares the technical specifications of the Run I and Run II detectors.

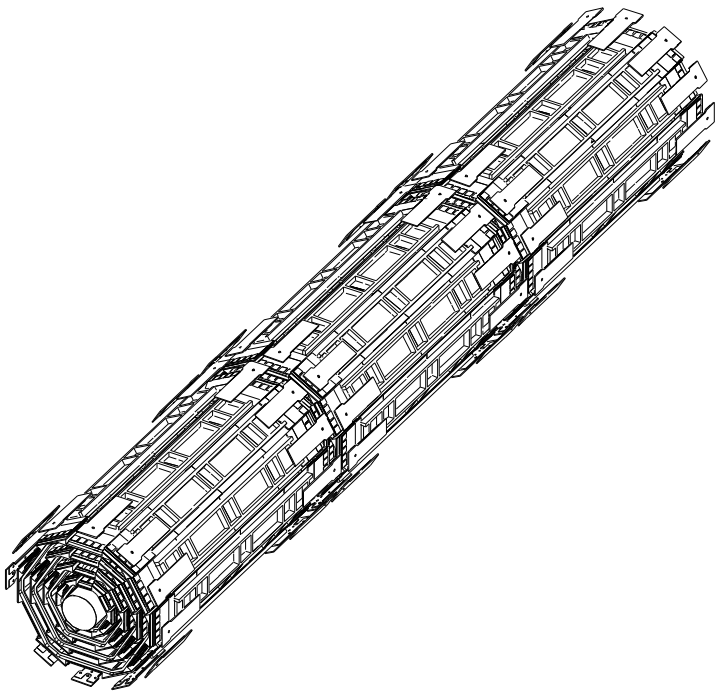

Figure 2.13: SVXII barrel structure.

Detector Parameter	SVX	SVX II
Readout coordinates	r-ϕ	r-ϕ;r-z
Number of barrels	2	3
Number of layers per barrel	4	4
Number of wedges per barrel	12	12
Ladder length	25.5 cm	32.0 cm
Combined barrel length	51.0 cm	96.0 cm
Layer geometry	3° tilt	staggered radii
Radius innermost layer	3.0 cm	2.4 cm
Radius outermost layer	7.8 cm	8.7 cm
r-ϕ readout pitch (4 layers)	60;60;60;55 μm	60;62;58;60 μm
r-z readout pitch (4 layers)	-	150;133;133;150 μm
Length of readout channel (r-ϕ)	25.5 cm	16.0 cm
r-ϕ readout chips/ladder (4 layers)	2;3;5;6	4;6;10;12
r-z readout chips/ladder (4 layers)	-	4;6;6;8
r-ϕ readout channels	46,080	147,456
r-z readout channels	-	119,808
Total number of channels	46,080	267,264
Total number of readout chips	360	2088
Total number of detectors	288	576
Total number of ladders	96	144
Silicon area (m^2)	0.68	1.5
Diode length (miles)	7.3	17.5

Table 2.2: Parameters of the Silicon Vertex Detector (SVX II).

Layer 00 (L00)

Layer 00 ([23]) is a radiation-hard, single sided silicon detector mounted directly on the beampipe. The beampipe radius is 1.2 cm. The geometry of L00 is such that there are two overlapping hexagonal structures, one at $R = 1.25$ cm and the other at 1.5 cm.

Figure 2.14 shows the d_0 resolution versus track p_T with and without L00 hits. Note that the beamline is included in this plot ($\sim 25\ \mu m$). The asymptotic value

for large p_T is about 10-12 μm, and it blows up for low p_T. L00 helps improve the resolution by about 20% at low p_T.

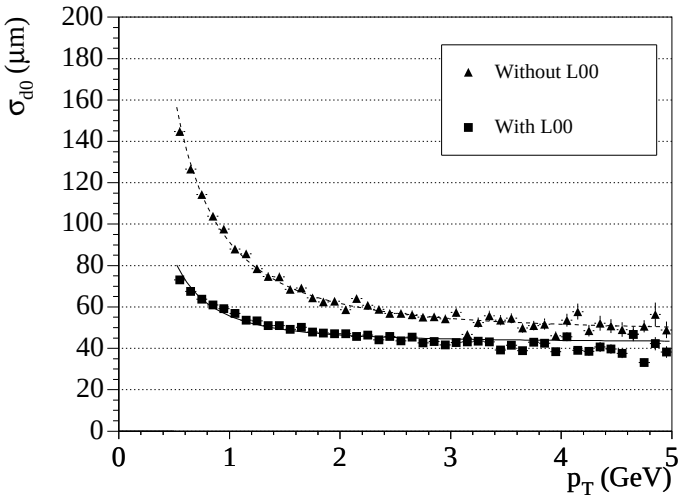

Figure 2.14: d_0 resolution versus track p_T with (squares) and without (triangles) L00 hits. Note that the beamline is included in this plot ($\sim 25\ \mu m$).

Intermediate Silicon Layers (ISL)

The Intermediate Silicon Layers ([25],[26]) provides large radius silicon coverage. It consists of three concentric layers offset in z. For $|\eta| < 1$, there is one layer, and for $1 < |\eta| < 2$, there are two. Figure 2.15 shows the detector layout of the ISL versus η.

The primary purpose of the central layer is to provide accurate linking information with the Central Outer Tracker, and the high-η layers provide measurements for tracks at high-η. The ISL layers are comprised of $R-\phi$ strips on the p-n junction and 1.25° on the n-side.

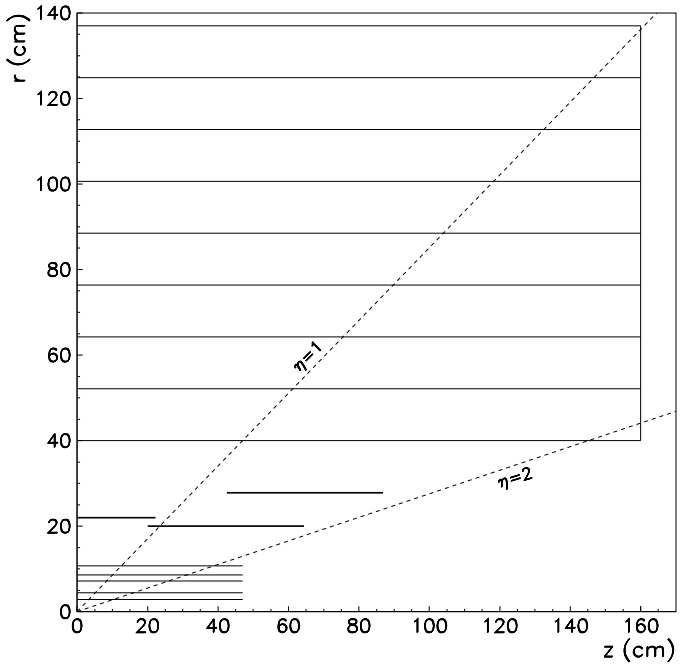

Figure 2.15: ISL Configuration.

Central Outer Tracker (COT)

The Central Outer Tracker([27]) is a multiwire drift chamber situated between $R = 44$ cm to $R = 132$ cm, covering $|\eta| < 1.0$ with the full detector, and partial coverage up to $|\eta| < 2.0$. There are 96 sense layers grouped into 8 "superlayers", each consisting of 12 layers. Four superlayers provide $R - \phi$ measurements (axial superlayers) and the remaining four provide 2° measurements (stereo superlayers). Figure 2.16 shows the east side end plate, which shows the detector configuration.

The drift chambers are filled with an Argon/Ethane gas mixture (50:50), with 1.7% isopropyl alcohol. This allows a maximum drift time of 177 ns with drift velocity of 100μm/ns. This prevents pileup of events in the drift chamber from the previous event. The alcohol is introduced to reduce buildup of ion discharge on the inside of

the chambers ("aging").

The cathode of the drift chamber is actually a "field sheet" consisting of 354 $\circ A$ gold on 6.4 μm thick Mylar sheets. The anode is gold-plated tungsten wires with 40μm diameter. The same wire is used for both sense and field shaping. Figure 2.17 shows a schematic of one COT cell.

Overall, the p_T resolution is roughly $\sigma_{p_T}/p_T \sim 0.15\% \times p_T$.

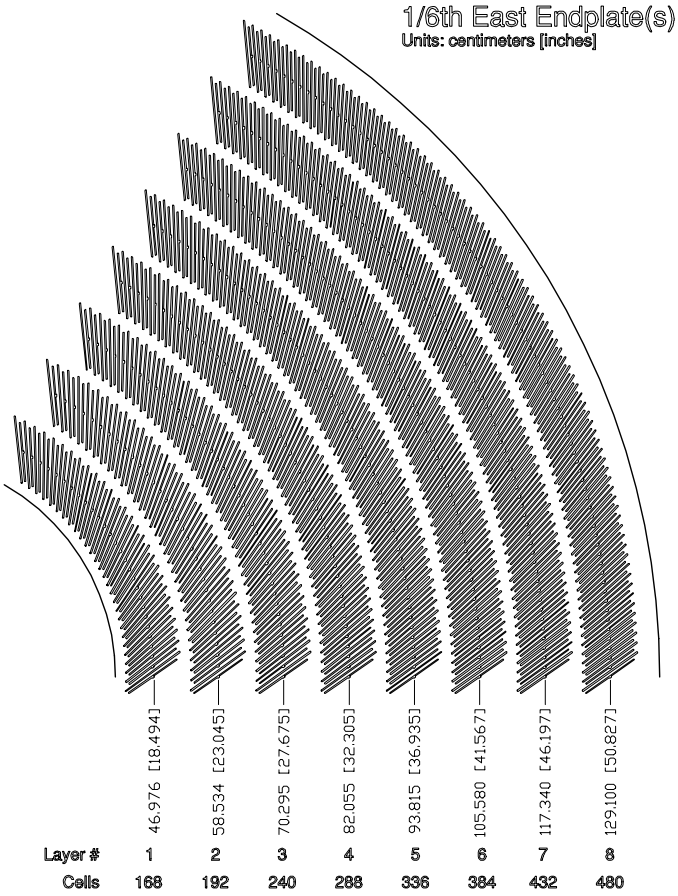

Figure 2.16: COT end plate.

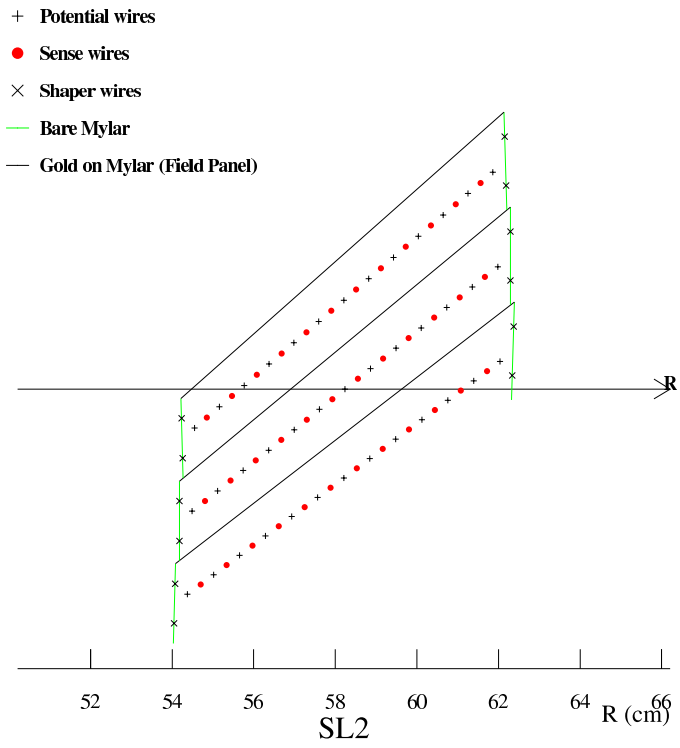

Figure 2.17: COT cell configuration.

2.2.4 Calorimetry

The basic structure of the CDF calorimeters is as follows. They are all based on scintillator sampling. That is, as per the discussion in Section 2.2.1, the detector after the absorbing material is a scintillating sheet, guided into a fiber, where the light produced from the incoming particles is passed through a wavelength shifting fiber to a photomultiplier tube, and then on to an amplifier. The details of each calorimeter are based on the specific physics needs and are discussed below.

Table 2.3 summarizes the calorimeters at CDF.

Calorimeter	Coverage	Thickness	Energy Resolution
CEM	$\|\eta\| < 1.1$	18 X_0	$\frac{13.5\%}{\sqrt{E_T}} \oplus 2\%$
CHA	$\|\eta\| < 0.9$	4.5 λ_0	$\frac{75\%}{\sqrt{E_T}} \oplus 3\%$
WHA	$0.7 < \|\eta\| < 1.2$	4.5 λ_0	$\frac{75\%}{\sqrt{E_T}} \oplus 3\%$
PEM	$1.1 < \|\eta\| < 3.6$	21 X_0, 1 λ_0	$\frac{16\%}{\sqrt{E_T}} \oplus 1\%$
PHA	$1.2 < \|\eta\| < 3.6$	7 λ_0	$\frac{80\%}{\sqrt{E_T}} \oplus 5\%$

Table 2.3: Parameters of the calorimetry subsystems at CDF.

Central Calorimeter (CEM + CES + CHA + WHA)

The Central Electromagnetic Calorimeter (CEM:[28]) is a lead+scintillator sandwich configuration. It is segmented into 15° ϕ-wedges and 0.11 radians in η. It covers the range $|\eta| < 1.1$, and is 18 radiation lengths thick. The resolution of the CEM is $\sigma_E/E = 13.5\%/\sqrt{E_T} \oplus 2\%$.

The Central EM shower Max Detector (CES:[28]) is a strip chamber that is designed to provide a measurement of charged tracks very close to the calorimeter, with very little material in between. This is done to distinguish electrons from photons, which otherwise look very similar in the calorimeter.

The Central Hadronic Calorimeter (CHA:[29]) is a steel-scintillator sandwich, segmented in the same way as the CEM. It covers the range $\eta < 0.9$ and is 4.5 nuclear radiation depths thick. It has a resolution of $\sigma_E/E = 75\%/\sqrt{E_T} \oplus 3\%$.

The Wall Hadronic Calorimeter (WHA) is essentially the same as the CHA and covers the range $0.7 < |\eta| < 1.2$.

Electron ID

Electrons are detected by examining a group of towers in the CEM electromagnetic calorimeter, which are clustered together into a single object. Tracks are associated geometrically to the electron by extrapolating the track to the calorimeter face, and hits are required to be in the CES detector within a certain window. Additional cuts are applied to the CES strip χ^2 and shape, L_{shr} (compared to test beam electrons), the ration of energy depositions in the hadronic and electromagnetic calorimeters, calorimeter tower E_T and track p_T. For specific cuts, see Section 4.2.1. Figure 2.18 shows a schematic of the electron identification procedure.

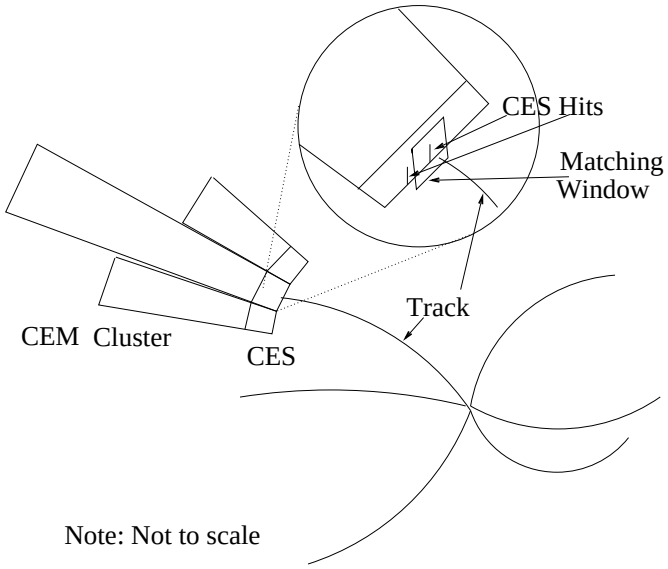

Figure 2.18: Schematic of electron identification at CDF.

2.2.5 Muon Systems

The muon detectors at CDF make use of single wire drift chambers as well as scintillator counters for fast timing. Overall, there is muon ID up to $|\eta| < 2.0$. The various subsystems are the Central Muon Detector (CMU), the Central Muon Upgrade (CMP), Central Scintillator Upgrade (CSP), Central Muon Extension (CMX), Central Scintillator Extension (CSX), the Toroid Scintillator Upgrade (TSU), the Barrel Muon Upgrade (BMU) and the Barrel Scintillator Upgrade (BSU). The CMU/CMP/CSP cover $|\eta| < 0.6$, the CMX/CSX cover $0.6 < |\eta| < 1.0$ and the TSU/BMU/BSU cover $1.0 < |\eta| < 2.0$. For this analysis, the data from the TSU/BMU/BSU system was not available for triggering. Also, tracking is only available for $|\eta| < 1.0$. For these two reasons, we only use leptons with $|\eta| < 1.0$ in this analysis.

The CMU [30] detector is the closest to the interaction point. It is situated behind the calorimeter, which provides roughly 5.5 interaction lengths for pions. The p_T threshold of the CMU is 1.4 GeV/c. It is cylindrical in geometry with a radius of 350 cm, arranged into 12.6° wedges. Each wedge contains three modules (stacks) with four layers of 4 rectangular drift cells. The cells have 50 μm sense wires at the center of the cell, parallel to the z-direction. The gas used is the same Argon-Ethane (50:50) mixture with 1.7% alcohol as the COT.

The CMP is situated outside an additional 60 cm of steel to act as an absorber, which is 3.5 additional interaction lengths (for a total of 9.0 λ_0). The p_T threshold of the CMP is 3.0 GeV/c. It is rectangular in geometry, consisting of four layers of drift cells, staggered by one-half cell per layer.

The CSP [31] is a single layer of rectangular scintillator tiles, with a waveguide to move the scintillated light into a photomultiplier tube (PMT). This provides a fast detection mechanism used in triggering muons.

The CMX is located on either side of the detector straddling the beamline. It is a conical geometry with drift chambers similar to the CMP. The CSX is another scintillator array similar to the CSP. The CMX covers 360° degrees in ϕ. The segmentation is in 15° wedges in azimuthal angle. Each wedge consists of 8 layers of rectangular tubes in the radial direction, also offset to provide better resolution.

Figure 2.19 shows the muon coverage upgraded for CDF Run II.

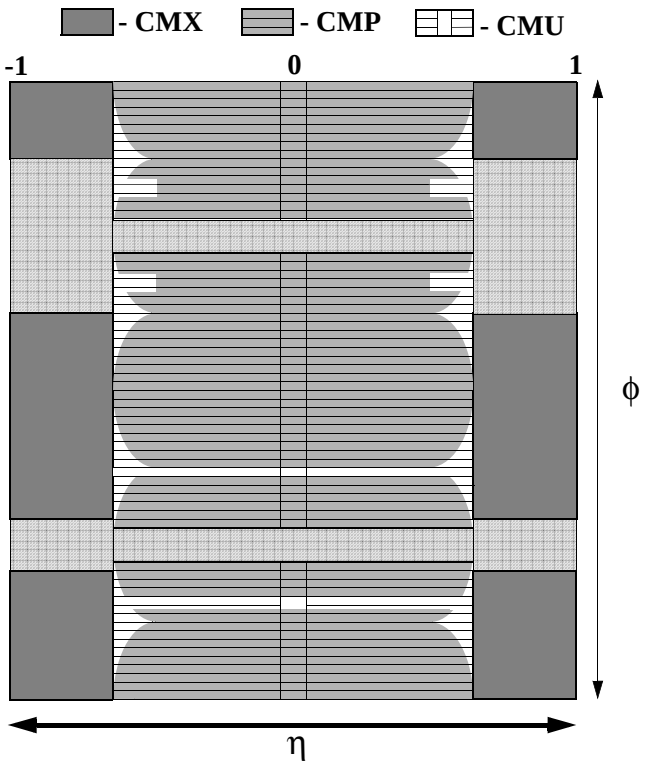

Figure 2.19: Muon coverage for the different subsystems. Note that although the "keystone" regions at $\eta = \pm 1.0$ and $\phi = \pi/2$ are shaded, only the one at $\eta = +1$ is functional.

Chapter 3

Heavy Flavor Tagging

There are several distinguishing characteristics of heavy flavor jets that allow us to separate them from light flavor jets (albeit on a statistical basis).

The primary difference between heavy flavor and light flavor jets is that heavy flavor jets will decay, after traveling a few millimeters from production, via the weak interaction. Because of this, we can take advantage of the fact that the tracks coming from a heavy flavor decay will be displaced with respect to the primary interaction vertex. With sufficient resolution, we can reconstruct these secondary vertices and obtain information on the lifetime of the decaying hadron.

It is also possible to identify heavy flavor jets via soft leptons from the decay of the virtual W from the $b \rightarrow Wc$ vertex. This method of tagging heavy flavor is not used in this analysis.

Section 2.2.1 explains how particles can be identified via their decay products. The overall picture is to reconstruct the primary vertex, and select tracks that are displaced from that vertex. Those displaced tracks are then vertexed using a pre-

scription similar to the scheme outlined in Sec 2.2.1. The differences are that now the tracks are in a magnetic field (and so the straight-line approximation is no longer valid) and that the tracks are in three dimensions.

We will now examine secondary vertex tagging in detail.

3.1 Tagging Variables

Any vertex tagger has a number of variables it uses to discriminate between long-lived and prompt vertices. It is thus useful to define these quantities prior to describing the specifics of our secondary vertex algorithm.

3.1.1 Decay Length

The secondary vertex decay length is expected to have the most discriminating power between heavy flavor (b and c quarks) and light flavor. We define the decay length in 2-D as

$$L_{2D} = \vec{r_{vtx}} \cdot \hat{p_{jet}} \tag{3.1}$$

where $\vec{r_{vtx}}$ is the position vector of the vertex and $\hat{p_{jet}}$ is the direction of the jet momentum. Figure 3.1 shows a schematic of this dot product.

If the dot product is positive (i.e. the vertex flies in the direction of the jet), the vertex is called a *positive* vertex, and if the dot product is negative (i.e. the vertex flies opposite to the direction of the jet), the vertex is called a *negative* vertex. Negative vertices are an unphysical situation, and are generally used to estimate the number of tags obtained due to imperfect detector resolution. Figure 3.2 shows the difference

between positive and negative vertices.

Figures 3.3(b) and 3.3(a) show the 2-d and 3-d decay lengths of Monte Carlo b-hadrons. There are no cuts on the minimum decay length, so the most probable value is zero lifetime. The mean value is about 60 mm in 3-d, and about 42 mm in 2-d.

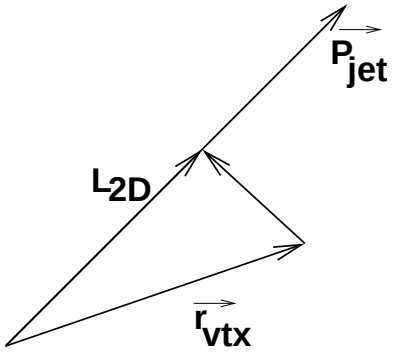

Figure 3.1: Definition of 2-dimensional decay length L_{2D}.

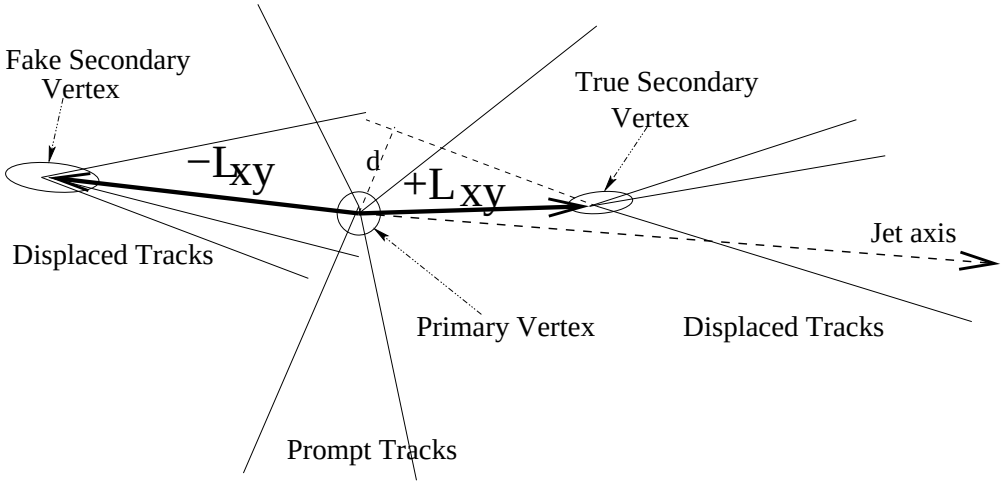

Figure 3.2: Diagram showing positive and negative tags.

3.1.2 Mass and p_T

The vertex mass and p_T are also useful to discriminate b quarks from c quarks, and also from fake vertices (negative tags). The mass is simply the invariant mass of the tracks in the vertex, and the p_T is the vertex momentum in the flight direction ($\hat{R}$):

$$p^{\mu} = \sum_{tracks} p^{\mu}_{track} \tag{3.2}$$

$$m^2_{vtx} = p^{\mu}\, p_{\mu} \tag{3.3}$$

$$p_T^{vtx} = \vec{p_{vtx}} \cdot \hat{R} \tag{3.4}$$

where p^{μ}_{track} is the four-momentum of each track, p^{μ} is the four-momentum of the vertex, $\vec{p_{vtx}}$ is the three-momentum of the vertex, and $\hat{R}$ is a unit vector in the flight direction.

Figures 3.4(a)-3.4(c) show the energy, momentum, transverse momentum, and γ for b-hadrons in the Monte Carlo. The mean energy of the b-hadron is about 69 GeV. The mean momentum is also about 69 GeV/c. The mean transverse momentum is about 48 GeV/c. The mean relativistic factor is 13. The b-hadrons are very boosted, and are also mostly transverse to the beamline, as expected.

3.1.3 Pseudo-cτ

The proper lifetime can discriminate b-hadrons, c-hadrons and light flavor hadrons better than the decay length. Although c-hadrons and b-hadrons have different lifetimes, since c-hadrons are lighter, it turns out that they travel roughly the same distance at this energy scale. Thus, the decay length is not the best discriminating

variable to distinguish bottom from charm hadrons.

The distance a hadron travels is proportional to its proper lifetime $c\tau$. The proportionality constant is the Lorentz boost γ.

$$R = \gamma \times c\tau \tag{3.5}$$

Using $E = \gamma m$, we can write the proper lifetime in terms of the flight distance

$$c\tau = \frac{m}{E} \times R \tag{3.6}$$

We do not have access to the total mass of the hadron, nor to its total displacement. We have only the mass of the reconstructed vertex (which will have no neutral particles or neutrinos), and the displacement in $R - \phi$. We thus construct a variable that is approximately equal to $c\tau$:

$$\begin{aligned}
c\tau &= \frac{m}{E} \times R && (3.7)\\
&= \frac{m}{\sqrt{p^2 + m^2}} \times R && (3.8)\\
&= \frac{m}{p} \times R \times \frac{1}{\sqrt{1 + \left(\frac{m}{p}\right)^2}} && (3.9)\\
&\approx \frac{m}{p} \times R \times \left(1 - \frac{1}{2}\left(\frac{m}{p}\right)^2\right) && (3.10)\\
&\approx \frac{m_{vtx}}{p_T^{vtx}} \times L_{2D} && (3.11)
\end{aligned}$$

where we have used the binomial expansion $1/\sqrt{1+\epsilon} \approx 1 - \frac{1}{2}\epsilon$. This approximation is exact if the vertex is perfectly reconstructed (i.e. $m_{vtx} = m$) and moving perpendicular to the beamline (i.e. $p_T = p, p_z = 0$), in the limit of small mass. Thus corrections will be related to the tracking efficiency, the η of the hadron, and the ratio $\left(\frac{m}{p}\right)^2$.

Figures 3.3(c) and 3.3(d) show $c\tau$ and pseudo-$c\tau$ for b hadrons in the Monte Carlo (except that pseudo-$c\tau$ uses the hadron mass and p_T instead of the vertex mass and p_T at this stage). Also shown are the fits for these quantities. The mean $c\tau$ is about 0.47 mm, and the mean pseudo-$c\tau$ is also about 0.47 mm. The fit slope is about -21.1/cm for pseudo-$c\tau$, and about -21.3/cm for $c\tau$. Both are quite similar. Since these two distributions are very similar, the main corrections to pseudo-$c\tau$ will be mis-reconstructed b-hadrons.

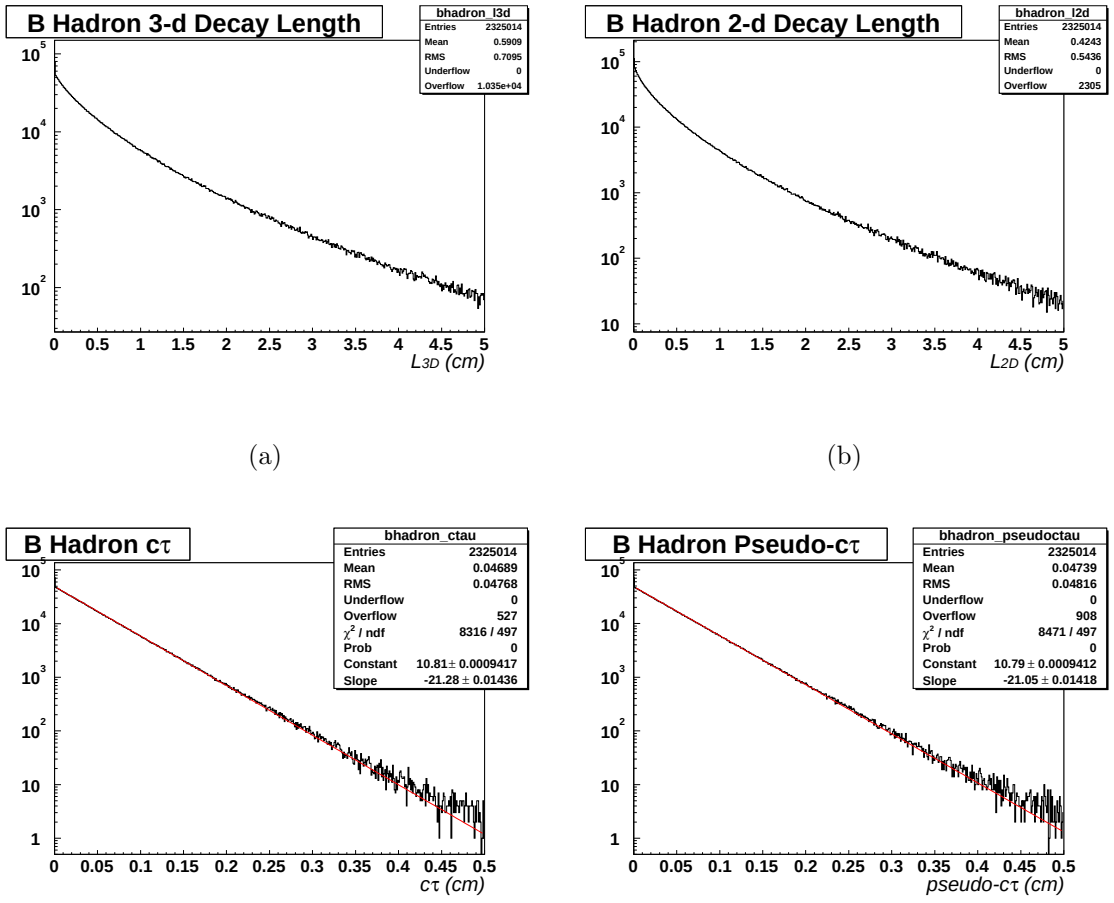

Figure 3.3: Monte Carlo b-hadron decay length quantities, taken from PYTHIA $t\bar{t}$ Monte Carlo with $m_{top} = 178$ GeV/c^2.

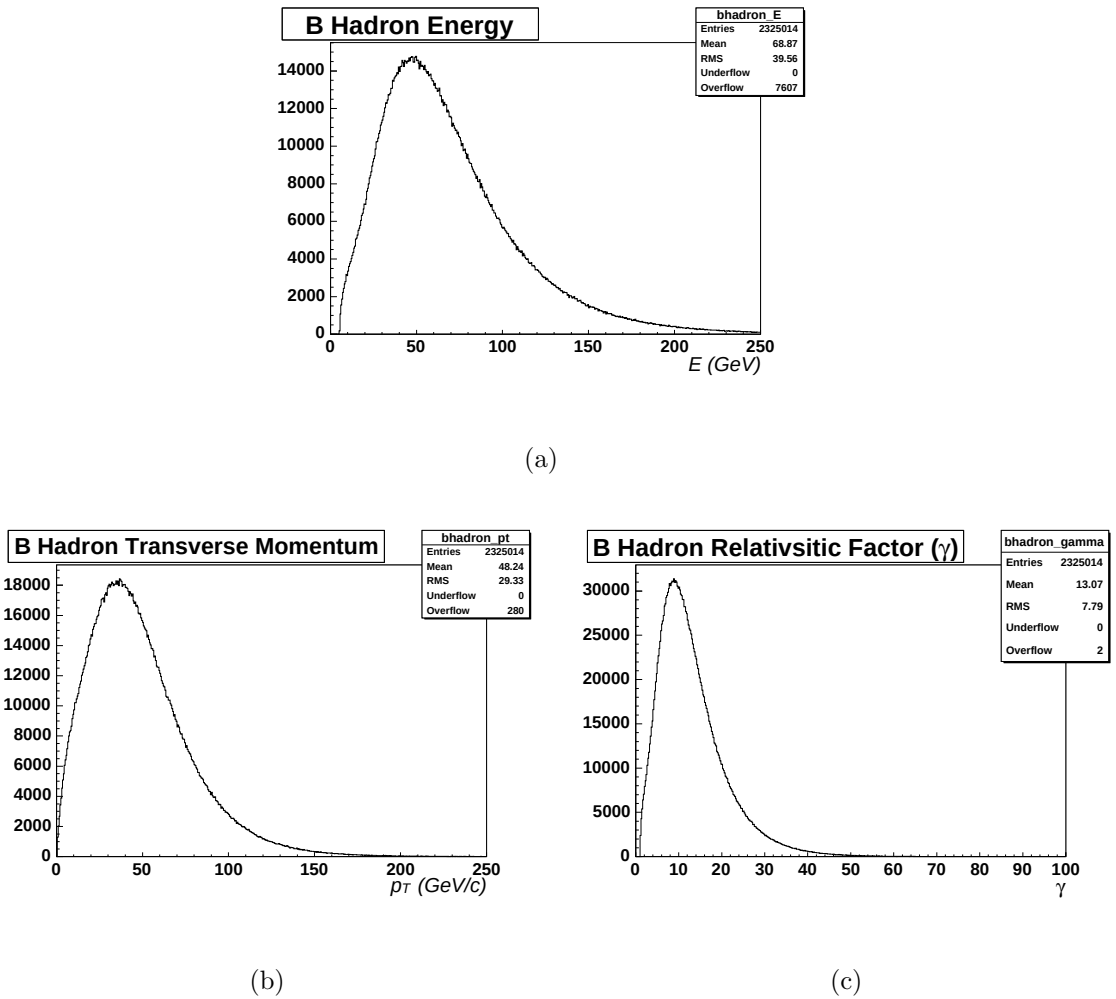

(a)

(b)

(c)

Figure 3.4: Monte Carlo b-hadron kinematic quantities, taken from PYTHIA $t\bar{t}$ Monte Carlo with $m_{top} = 178$ GeV/c^2.

3.2 Primary Vertex Selection (PrimeVtx)

In order to calculate the primary vertex, we use a vertexing strategy similar to that of our secondary vertex finder. The algorithm we use is called PrimeVtx.

The PrimeVtx algorithm is an event-by-event primary vertex finder. It begins with an input seed (x_0, y_0, z_0). Here, x_0 and y_0 are the x and y positions of the run-averaged beamline, and z_0 is the highest sum-p$_T$ z vertex in the event. PrimeVtx then selects tracks that are significantly displaced from the run-averaged beamline, and orders them by decreasing p_T. The 50 highest p_T displaced tracks are then passed to CTVMFT [1] to fit the vertex. The position of the run-averaged beamline is also input into the fit as another measurement point. At that point, PrimeVtx begins removing tracks with the worst χ^2 relative to the fit vertex (with $\chi^2 > 10$). The process is then iterated until there are no tracks with $\chi^2 > 10$ in the vertex. If fewer than one track is associated with the primary vertex, the run-averaged beamline is passed along as the $x - y$ position and errors of the primary vertex, and the highest sum-p_T z vertex is used as the z-component. This is then passed along as the best primary vertex in the event.

The algorithm to calculate the highest p_T z vertex is called `ZVertexModule`. It histograms all the track z_0's and selects the vertex with the highest $\sum p_T$ within 5 cm of the primary lepton.

The track cuts used are:

- Reject tracks with no silicon hits.
- $p_T \geq 0.5\ GeV$

[1] See Glossary

- $|d_0| \leq 1.0$ cm, $|d_0|/\sigma \leq 3.0$ (with respect to beamline)
- COT: 2 Axial, 2 Stereo segments with $\geq$6 hits each
- Silicon: OI - $\geq$3 hits
- Silicon: OIS, OIZ - $\geq$5 hits, $\geq$3 $r-\phi$, $\geq$2 stereo, $\geq$2 Z

Figure 3.5(a) shows the number of tracks used in the PrimeVtx vertex in PYTHIA $t\bar{t}$ Monte Carlo with $m_{top} = 178\ GeV/c^2$. Figure 3.5(b) shows the error in the xy plane in $t\bar{t}$ Monte Carlo.

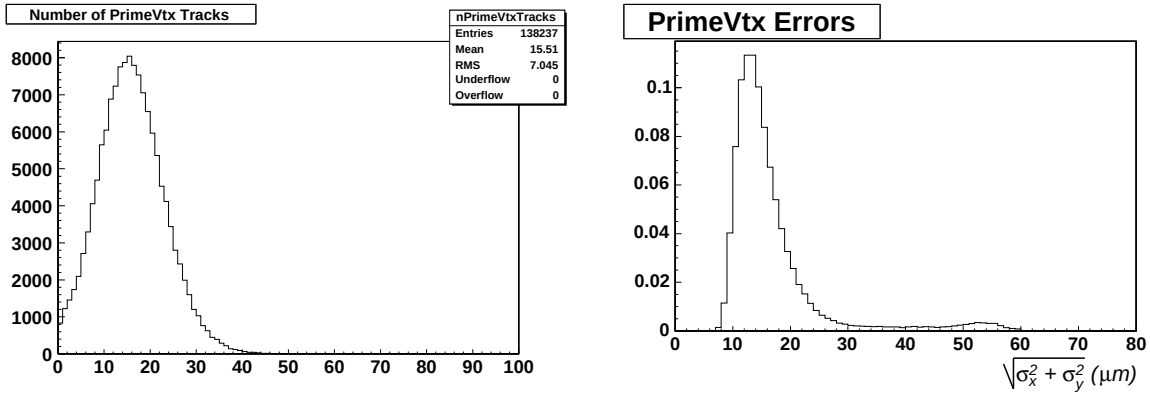

(a) Number of PrimeVtx tracks, taken from PYTHIA $t\bar{t}$ Monte Carlo with m_{top} = 178 GeV/c^2

(b) Error of PrimeVtx in the xy plane, taken from PYTHIA $t\bar{t}$ Monte Carlo with m_{top} = 178 GeV/c^2

Figure 3.5: PrimeVtx quantities.

3.3 Secondary Vertex Tagger (SecVtx)

The secondary vertex tagger used in this analysis is called SecVtx. It selects tracks displaced from the primary vertex (as found by PrimeVtx) and attempts to find a secondary vertex. If this secondary vertex is significantly displaced from the primary vertex, the vertex is flagged as "displaced" and is henceforth known as a *tag*.

SecVtx is a two-stage algorithm. It first tries to form a vertex with at least three tracks (*Pass 1*). If that fails, it then tries to form a vertex with at least two tracks with tighter track cuts (*Pass 2*). Tracks consistent with K_0^s or Λ decays are not considered by the algorithm. Table 3.1 shows a summary of the relevant parameters.

We require all jets considered by SecVtx to be *fiducial*, i.e. satisfy $E_T > 10\ GeV$ (no jet corrections), $|\eta| < 2.4$. Furthermore, we define *taggable jets* to be tracks with at least two *good tracks* (defined below).

In detail, the algorithm is

1. **Track Selection:** Loop over tracks
   (a) Extrapolate track parameters and errors to the primary vertex (see Section 2.2.1)
   (b) Define *good tracks* to be
      - $p_T > 0.5\ GeV$
      - $|d_0| < 0.15\ cm$ to the primary vertex
      - $|z_0| < 1.0\ cm$ to the primary vertex
      - Number axial SL with 5 or more hits ≥ 2 and number of stereo SL with 5 or more hits is ≥ 2
      - Number of SVX $r - \phi$ hits ≥ 3
      - Track fit $\chi^2/dof < 8.0$.
   (c) Remove tracks with an oppositely charged partner track that have $0.4876 < M_{\pi\pi} < 0.5076$ (consistent with $K_0^s \rightarrow \pi^+\pi^-$) or $1.10963 < m_{\pi p} < 1.12163$ (consistent with $\Lambda \rightarrow p\pi$)
   (d) Associate tracks to jets using a $\Delta R < 0.4$ cone

2. **Obtain a tag candidate:** Loop over jets

   (a) **Pass 1:** Select tracks with $d_0/\sigma_{d_0} > 2.0$, $p_T > 0.5$, ordered in d_0 and p_T, loop over pairs of tracks

      i. Form a seed vertex between two tracks
      ii. Extrapolate track parameters and errors to the seed vertex
      iii. Add tracks to the vertex with $d_0/\sigma_{d_0} < 3.0$ (relative to seed vertex)
      iv. Prune tracks that contribute $\chi^2 > 50.0$ away, until at least three tracks remain with $\chi^2 < 50.0$
      v. If no 3-track vertex is found, select next track pair
      vi. If a 3-track vertex is found, require vertex to satisfy
         - $p_T^{max-track} > 1.0\ GeV/c$
         - Overall vertex $\chi^2 < 50$
         - $L_{2D}/\sigma_{L_{2D}} > 7.5$
         - Pseudo-c$\tau < 1.0\ cm$
         - $|L_{2D}| < 5.0\ cm$
         - Average z_0 of tracks $< 5.0\ cm$
         - Remove neutral vertices with $0.4776 < M_{\pi\pi} < 0.5176$ (consistent with $K_0^s \to \pi^+\pi^-$) or $1.09563 < m_{\pi p} < 1.13563$ (consistent with $\Lambda \to p\pi$)
         - $R_0 < 2.5\ cm$ (where R_0 is the distance of the vertex from the center of the SVX)
         - If no Pass 1 vertex is found, examine next pair of seed tracks.

   (b) **Pass 2:** If no 3-track vertex is found, select tracks with $d_0/\sigma_{d_0} > 3.5$, $p_T > 1.0$, ordered in d_0 and p_T, loop over pairs of tracks. Require vertex to satisfy

      - $p_T^{max-track} > 1.5\ GeV/c$
      - Overall vertex $\chi^2 < 50$
      - $L_{2D}/\sigma_{L_{2D}} > 7.5$
      - Pseudo-c$\tau < 1.0\ cm$
      - $|L_{2D}| < 5.0\ cm$
      - Average z_0 of tracks $< 5.0\ cm$
      - Remove neutral vertices with $0.4776 < M_{\pi\pi} < 0.5176$ (consistent with $K_0^s \to \pi^+\pi^-$) or $1.09563 < m_{\pi p} < 1.13563$ (consistent with $\Lambda \to p\pi$)
      - $R_0 < 1.2\ cm$ or $1.45\ cm < R_0 < 2.5\ cm$, unless vertex has more than 2 pass 1 tracks. (where R_0 is the distance of the vertex from the center of the SVX). This is to mitigate the effects of conversions and nuclear interactions.

Source		Tight SecVtx			
		4.11.2		5.3.3	
		pass 1	pass 2	pass 1	pass 2
Use L00	$>$	no		yes	
Use IO tracks	$>$	no		yes	
COT cuts	$>$	varies		defTracks	
SVX layers	$>$	varies		3	
Track-χ^2	$<$	varies		8.0	
Δ track-z_0 (cm)	$<$	5.0		2.0	
Track-d_0 (cm)	$<$	0.3		0.15	
Track-p_T (GeV)	$>$	0.5	1.0	0.5	1.0
Track-d_0 Sign.	$>$	2.5	3.0	2.0	3.5
Attachment cut d_0 Sig.	$<$	4.0	–	3.0	–
Seed Vertex χ^2	$>$	50			
At least one Track-p_T (GeV)	$>$	1.0	1.5	1.0	1.5
Track prune χ^2	$>$	1000	1000	45	30
Vertex fit χ^2	$<$	2000	2000	50	
Lifetime track χ^2	$<$	50			
L_{xy} Significance	$>$	3.0		7.5	
TryHarderPass1		no		yes	
Material Removal		no		yes	

Table 3.1: Comparison of the *tight* version of the SecVtx algorithm used in Gen4 (4.11.2) analyses and the new version for Gen5 (5.3.3_nt).

3.3.1 Plots of SecVtx Variables

Figures 3.6-3.9 show various track quantities for all tracks from fiducial b-jets and fiducial $udsg$-jets with $p_T > 0.5$ GeV/c, in PYTHIA $t\bar{t}$ Monte Carlo with $m_{top} = 178$ GeV/c^2. Figures 3.10 and 3.12 show various jet quantities for fiducial b-jets and fiducial light flavor jets ($udsg$-jets) in $t\bar{t}$ Monte Carlo. Figures 3.13 and 3.14 show various vertex quantities for b-jets and $udsg$-jets tagged by SecVtx in $t\bar{t}$ Monte Carlo.

Figure 3.6(a) shows the track transverse momentum distribution. Tracks from b-jets have a mean p_T of 3.1 GeV/c, while tracks from $udsg$-jets have a mean p_T of 2.9 GeV/c, so b-jet tracks are slightly harder. Figure 3.6(b) shows the track η distribution. Tracks from b- and $udsg$-jets are very similar, although the tracks from b-jets are slightly more central.

Figure 3.7(a) shows the total number of silicon $R-\phi$ hits on each track, Figure 3.7(b) shows the number of good silicon $R-\phi$ hits on each track, and Figure 3.7(c) shows the number of COT hits on each track. Figure 3.7(d) shows the χ^2/dof for the track fit. We select tracks with $N_{hits} > 3$ and $\chi^2_{trk} < 8.0$, shown by vertical dashed lines in the plots.

The major discrimination between b- and $udsg$-jets will be in the impact parameter distributions. Figures 3.8(a),3.8(b), and 3.8(c) show the 2-d impact parameter to the primary vertex (d_0) and its error (σ_{d_0}), as well as the significance (d_0/σ_{d_0}). It is clear that the tracks from the b-jet are much more displaced than the tracks from the p-jet. Figures 3.9(a),3.9(b), and 3.9(c) show the same quantities for the z-displacement to the primary vertex. We select tracks with $|d_0| < 0.15$ cm to remove long-lived light flavor hadrons, conversions, and nuclear interactions. We also select $d_0/\sigma_{d0} > 2.0$ (for

pass 1) and > 3.5 (for pass 2).

Figure 3.10(a) shows the transverse energy of all fiducial b- and $udsg$-jets. Because the $udsg$-jets decay from the W while the b-jets decay from the top directly, the E_T spectrum is significantly harder for b-jets. Figure 3.10(b) shows the jet pseudorapidity. This distribution is roughly the same for p- and b-jets.

Figure 3.10(d) shows the number of good tracks in b- and $udsg$-jets. It is clear that the b-jets have a higher track multiplicity. The average number of good tracks in b-jets in our sample is 6.4, while the average number in $udsg$-jets is 3.9. Therefore, the input number of tracks already shows discrimination between b and p jets. We define jets with $N_{good} \geq 2$ to be considered "taggable" for the SecVtx algorithm, as mentioned above.

Furthermore, Figures 3.11(a) and 3.11(b) show the number of pass 1 and pass 2 tracks in b- and $udsg$-jets, respectively. We require at least 3 pass 1 tracks, and at least 2 pass 2 tracks to form a vertex. Recall that pass 1 requires $d_0/\sigma_{d_0} > 2.0$, and pass 2 requires $d_0/\sigma_{d_0} > 3.5$. It is clear that hardly any $udsg$-jets satisfy this requirement. Most of the p-jet tracks are not significantly displaced. Again, the input track selection itself is discriminating between b- and $udsg$-jets. Figure 3.11(c) shows the number of tracks after tagging. The b-jets have more tracks in the vertex on average.

Figures 3.12(a), 3.12(b) and 3.12(c) show the track p_T for the first, second and third highest p_T tracks in the jets for b- and $udsg$-jets. Because the b quark is directly from the top (as mentioned above), and because the b quark has a much larger mass than udsg partons, the highest p_T tracks in the jet should be more boosted for b-jets

than *udsg*-jets. This is what is observed in these figures. The average p_T for the first track in a *b*-jet is 12.2 GeV/c, while the average p_T for the first track in a *p*-jet is 10.8 GeV/c.

The rest of the plots show vertex quantities after a candidate secondary vertex has been formed (but before final vertex selection). Figures 3.13(a),3.13(b), and 3.13(c) show the vertex L_{2D} distribution, the error in L_{2D}, and the significance $L_{2D}/\Delta L_{2D}$ for *b*- and *udsg*-jets. The *b*-jets have a very large number of vertices with $L_{2D} > 0$, while the *udsg*-jets have roughly equal numbers positive and negative. Furthermore, because the *b*-jets have more tracks in the tag on average, the error of the vertex is smaller for *b*-jets than it is for *udsg*-jets, on average. These two effects combine to give *b*-jets a much larger decay length significance. We cut on $L_{2D}/\Delta L_{2D} > 7.5$ for the vertex to be considered "tagged". Notice also that the *p*-jet distribution has a very long positive tail. These are long-lived Λ and K_0^s particles, as well as conversions and nuclear interactions. These physical processes give rise to an asymmetry in the light flavor tags, which will be discussed later in Section 3.5.10.

Figure 3.13(d) shows the pseudo-$c\tau$ for *b*- and *udsg*-jets. Since this variable is derived from the decay length, it looks very similar to Figure 3.13(a). Figure 3.14(a) shows the vertex mass. Because the b has a much larger mass than *udsg*, the reconstructed vertex mass is higher. Also, examining Figure 3.14(c), we see that the *b*-vertices have a larger transverse momentum than the *p*-vertices. This is because the b has a large boost from the top quark decay.

Figure 3.14(d) shows the vertex radius from the center of the SVX detector. The *udsg*-jets are mostly clustered at smaller radii, but there is a long tail (as mentioned

earlier). We require our tags to be within the SVX innermost layer, so we require $R < 2.5$ cm. We do allow tags from $1.2 < R < 2.5$ even though there is material in those regions. However, we disallow vertices with only 2 displaced (pass 1) tracks in regions where there is material in order to cut down on the number of vertices from conversions.

Finally, Figure 3.14(b) shows the vertex fit χ^2/dof. We require $\chi^2/dof < 50.0$ for the vertex to be considered "tagged".

3.3.2 Optimization of SecVtx Tagger

The tagger used for the cross section measurement in Ref [40] was optimized for a different tracking version as the current analysis. That analysis is referred to as *Generation 4* (or *Gen4* for short), named after the version of the offline software used for the analyses, `4.11.2`.

The current analysis is produced in offline release `5.3.3_nt`, and is hence referred to as *Generation 5* or *Gen5*.

The algorithm was reoptimized between Gen4 and Gen5. The Gen4 tagger needed to place very stringent cuts on the input track selection, and then loosen the final vertex quality very much in order to obtain a high efficiency and low mistag rate simultaneously. The current algorithm allowed many more tracks to pass the selection, while simultaneously tightening the vertex quality. Table 3.1 compares the variables between the Gen4 and Gen5 versions of SecVtx. These cuts resulted in a 20% increase in efficiency, and a 30% increase in negative tag rate. The net effect is an increase in the precision of this measurement.

At the same time, another version of the SecVtx algorithm was developed, the *loose* version. This version will be discussed below.

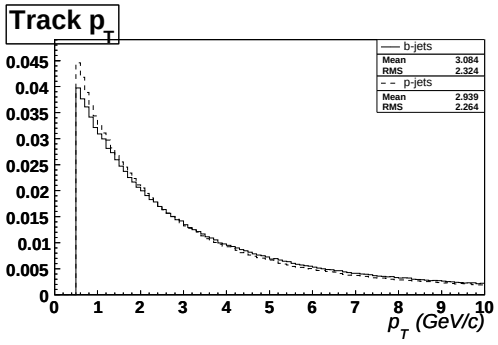

(a) Track p_T

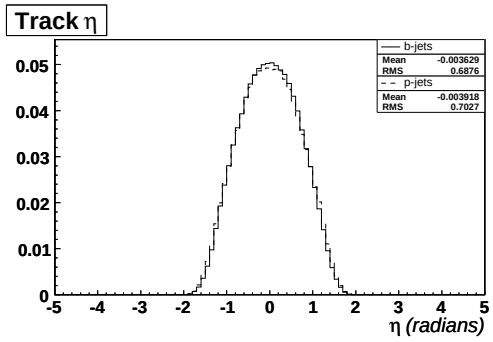

(b) Track η

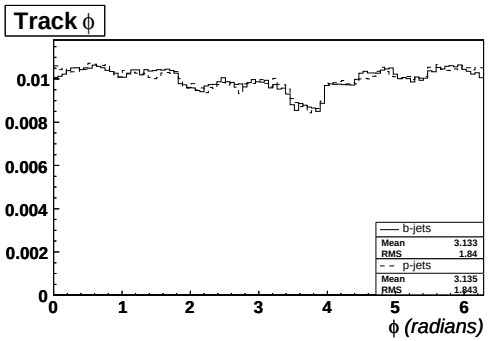

(c) Track ϕ

Figure 3.6: Track quantities for all tracks from b-jets (solid) and $udsg$-jets (dashed) in PYTHIA $t\bar{t}$ Monte Carlo with $m_{top} = 178$ GeV/c^2.

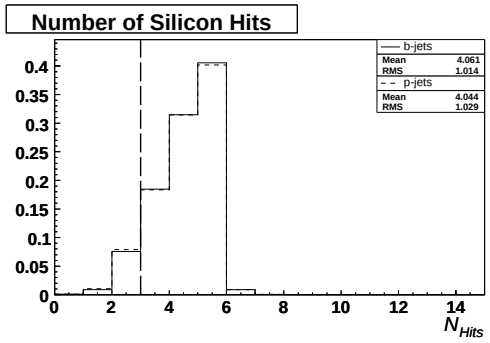

(a) Number of silicon $r - \phi$ hits

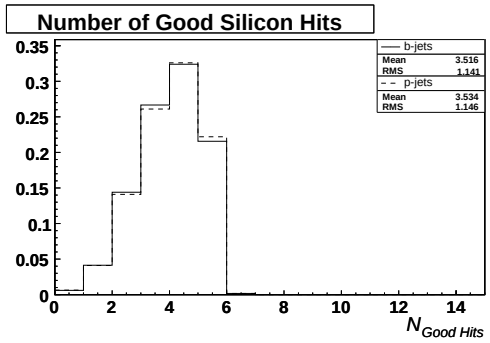

(b) Number of good silicon $r - \phi$ hits

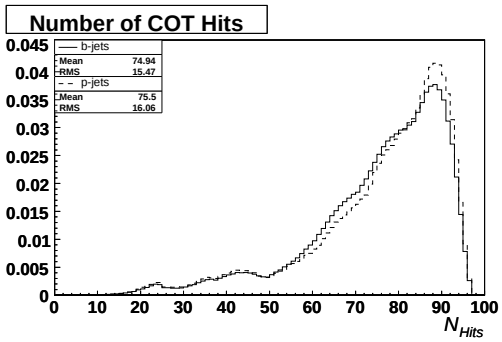

(c) Number of COT hits

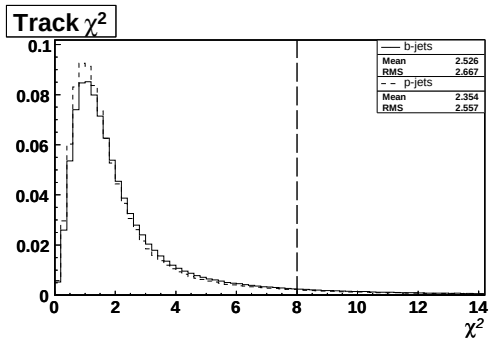

(d) Track χ^2

Figure 3.7: Track quantities for all tracks from b-jets (solid) and $udsg$-jets (dashed) in PYTHIA $t\bar{t}$ Monte Carlo with $m_{top} = 178$ GeV/c^2.

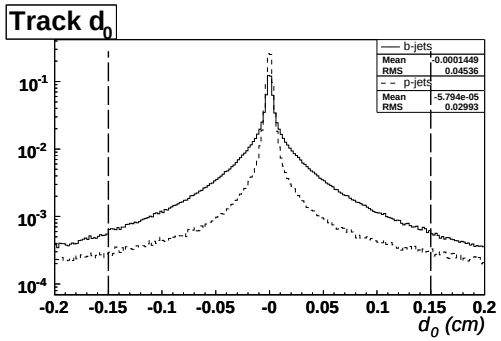

(a) Track d_0

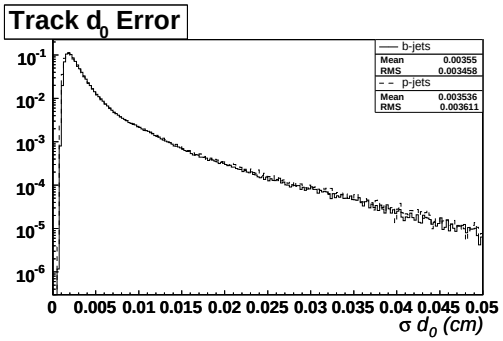

(b) Track d_0 Error

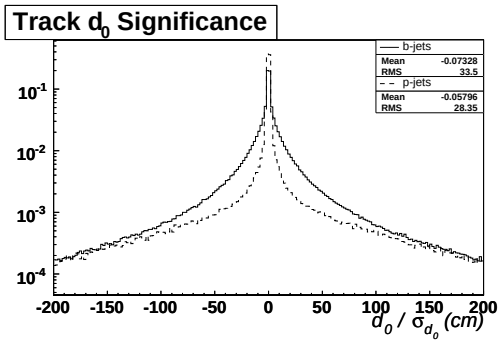

(c) Track d_0 Significance

Figure 3.8: Track quantities for all tracks from b-jets (solid) and $udsg$-jets (dashed) in PYTHIA $t\bar{t}$ Monte Carlo with $m_{top} = 178$ GeV/c^2.

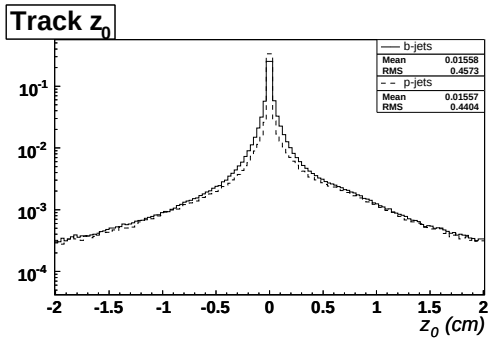

(a) Track z_0

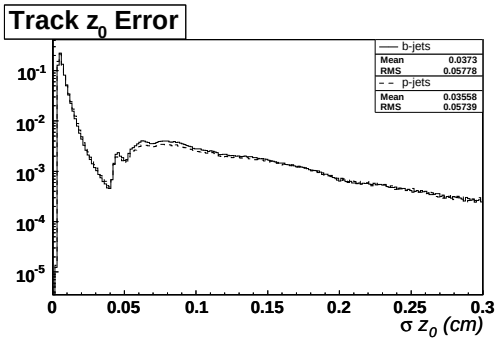

(b) Track z_0 Error

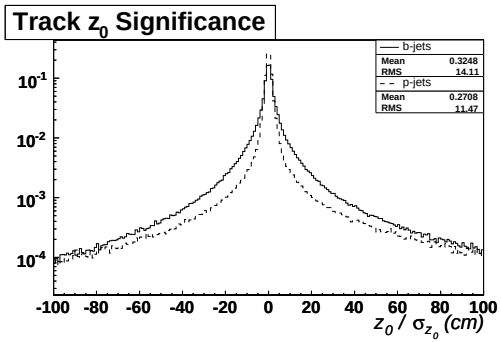

(c) Track z_0 Significance

Figure 3.9: Track quantities for all tracks from b-jets (solid) and $udsg$-jets (dashed) in PYTHIA $t\bar{t}$ Monte Carlo with $m_{top} = 178$ GeV/c^2.

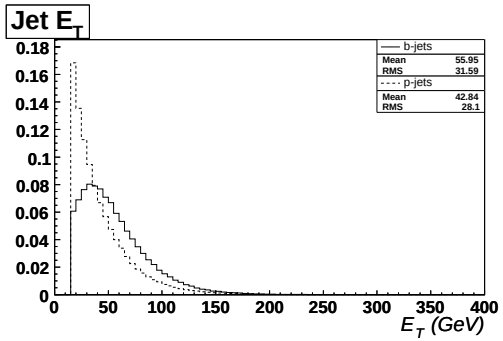

(a) Jet E_T

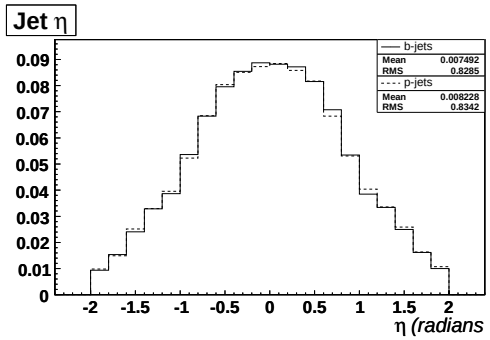

(b) Jet η

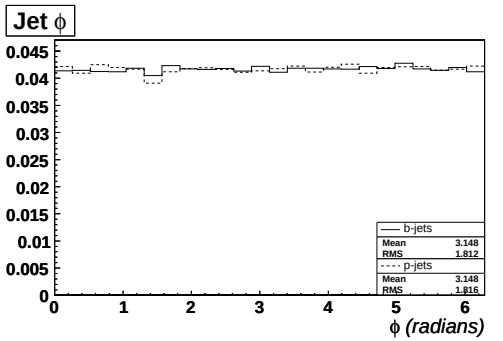

(c) Jet ϕ

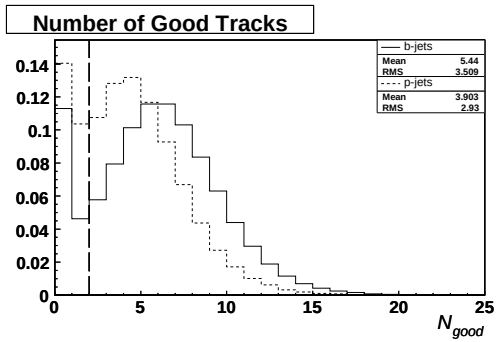

(d) Number of Good Tracks

Figure 3.10: Kinematic quantities for b-jets (solid) and $udsg$-jets (dashed) in PYTHIA $t\bar{t}$ Monte Carlo with $m_{top} = 178$ GeV/c^2.

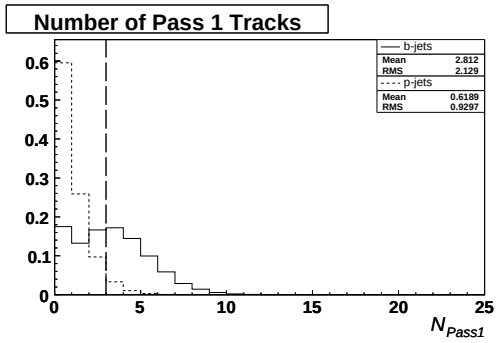

(a) Number of Pass-1 Tracks

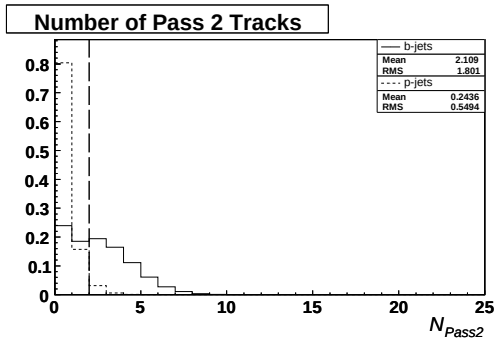

(b) Number of Pass-2 Tracks

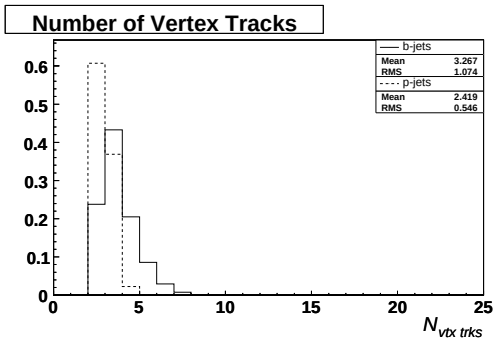

(c) Number of Tracks Used in Secondary Vertex

Figure 3.11: Kinematic quantities for b-jets (solid) and $udsg$-jets (dashed) in PYTHIA $t\bar{t}$ Monte Carlo with $m_{top} = 178$ GeV/c^2.

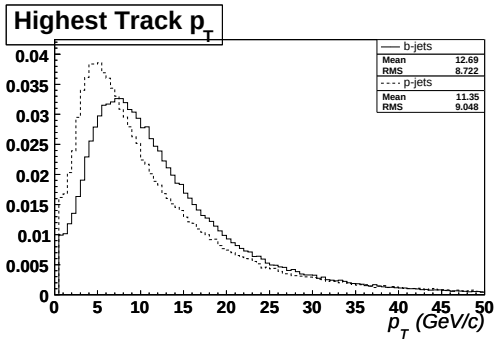

(a) p_T of Highest p_T Track

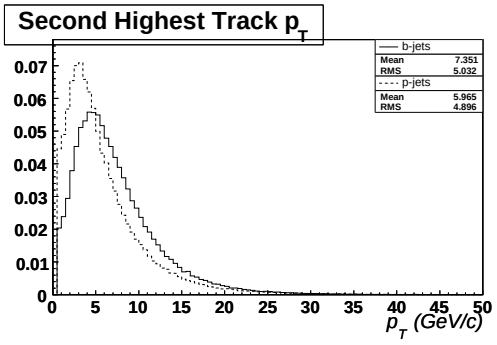

(b) p_T of Second Highest p_T Track

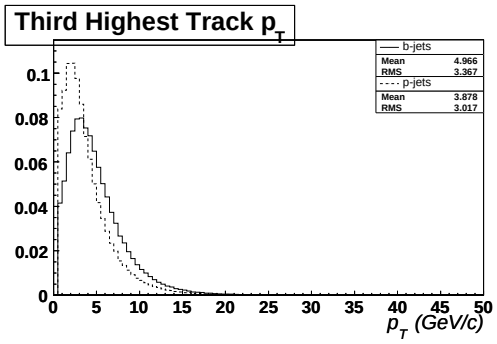

(c) p_T of Third Highest p_T Track

Figure 3.12: Kinematic quantities for b-jets (solid) and $udsg$-jets (dashed) in PYTHIA $t\bar{t}$ Monte Carlo with $m_{top} = 178$ GeV/c^2.

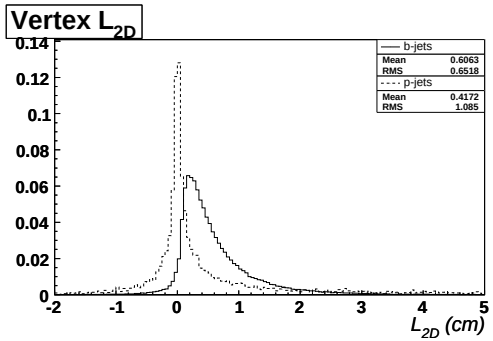

(a) Secondary Vertex L_{2D}

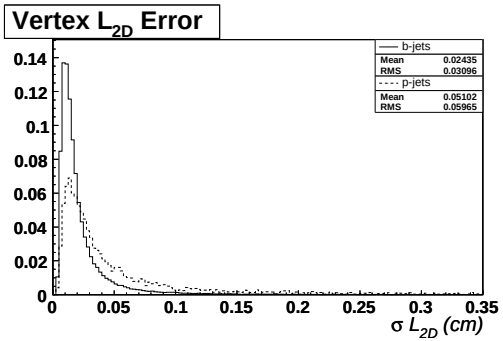

(b) Secondary Vertex L_{2D} Error

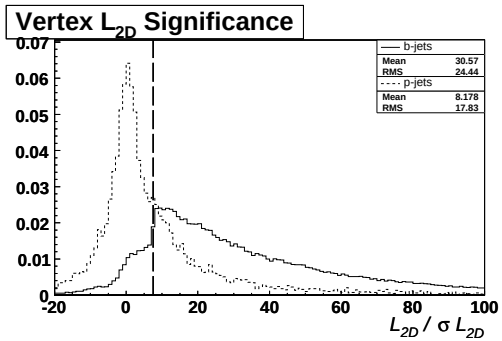

(c) Secondary Vertex L_{2D} Significance

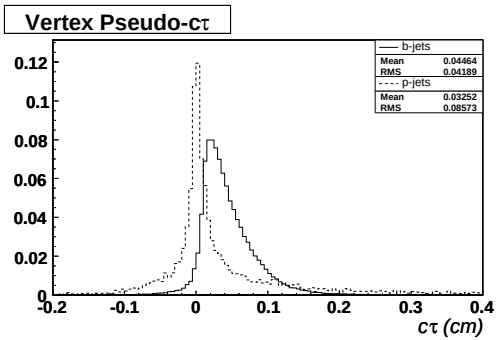

(d) Secondary Vertex $c\tau$

Figure 3.13: Vertex quantities for b-jets (solid) and $udsg$-jets (dashed) considered by SecVtx in PYTHIA $t\bar{t}$ Monte Carlo with $m_{top} = 178$ GeV/c^2.

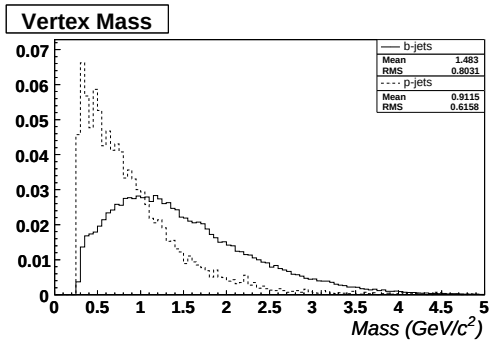

(a) Secondary Vertex Mass

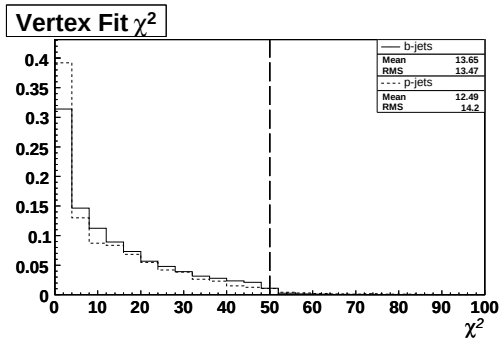

(b) Secondary Vertex χ^2

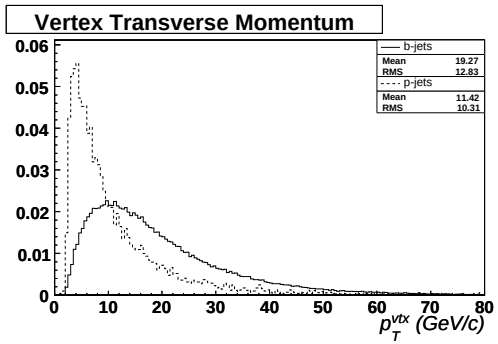

(c) Secondary Vertex Momentum

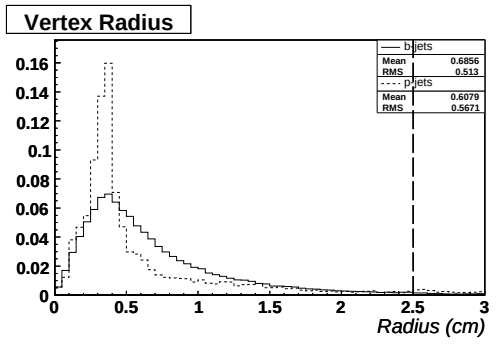

(d) Secondary Vertex Radius

Figure 3.14: Vertex quantities for b-jets (solid) and $udsg$-jets (dashed) considered by SecVtx in PYTHIA $t\bar{t}$ Monte Carlo with $m_{top} = 178$ GeV/c^2.

3.4 b-Tagging Efficiency

While the efficiency of a given tagger is often measured directly from simulation, it is not possible to do so in our case because the Monte Carlo does not accurately predict the number of tracks seen in data, and that there are problems with the b-jet modelling in our Monte Carlo. This can arise due to imperfect detector descriptions, tracks from underlying event interactions which are difficult to model, multiple interactions which are not reproduced in the Monte Carlo, and different heavy flavor contents of the samples. Because of all these considerations, it is necessary to introduce a data-to-Monte Carlo *scale factor* to account for differences between the data and the Monte Carlo. So, we shall measure the efficiency in the Monte Carlo but correct for the scale factor.

In order to estimate the efficiency of the SecVtx tagger in data, it is necessary to have a control sample of pure b-jets with which to do so. We then examine the ratio of the efficiencies in the data and the Monte Carlo (the *scale factor*, or SF). This scale factor is then assumed to be the same for all the Monte Carlo samples available. We then calculate the efficiency of the tagger in a given signal sample (such as the $t\bar{t}$ sample) and apply the scale factor to estimate its efficiency in the data.

As a control sample, we select dijet events which have a lepton within one jet (henceforth referred to as the "lepton-jet", l-jet, e-jet or μ-jet, depending on the lepton sample). We require at least one tagged jet back-to-back with the lepton jet (henceforth referred to as the "away-jet", or a-jet). The lepton-jet is thus enhanced in heavy flavor both by the requirement of a lepton within the jet (consistent with a semileptonic decay), and by tagging the away side jet (hence preferentially selecting

$b\overline{b}$ events). We then examine tag rates on the lepton-jet to determine the efficiency. The remaining problem is to determine the residual light flavor contribution to the lepton-jet tags (a.k.a. the heavy flavor fraction). Figure 3.15 shows a diagram of the lepton-jet and the tagged away-jet.

We use a combination of two methods to measure the efficiency, the *electron method* and *muon method*. The electron method makes use of conversions in order to calculate the residual light flavor contribution to the lepton-jet tags, while the muon method uses a Monte-Carlo template of the transverse momentum of the muon relative to the jet axis, fit to the data.

Both methods make the assumption that the scale factor for tagging both jets is the same as the scale factor for tagging only one. They also assume that tagging the lepton side is uncorrelated with tagging the away side. Finally, both methods also assume the scale factor is the same for b and c jets.

We now consider each in detail, as well as the combination of the two methods.

3.4.1 b-Tagging Scale Factor With Electron Data

The electron method relies on conversions to estimate the residual light flavor contribution to the lepton-jet efficiency. The idea is that conversion jets are not very likely to contain heavy flavor, and so are a good control sample of essentially light flavor jets.

The full analysis for the electron method is given in Ref [32].

We write ϵ^{+H} for the tagging efficiency for heavy flavor e-jets in data and $\mathfrak{e}^{+H}$ for the corresponding efficiency in Monte Carlo. Hence the scale factor is $(SF) \equiv \frac{\epsilon^{+H}}{\mathfrak{e}^{+H}}$. It

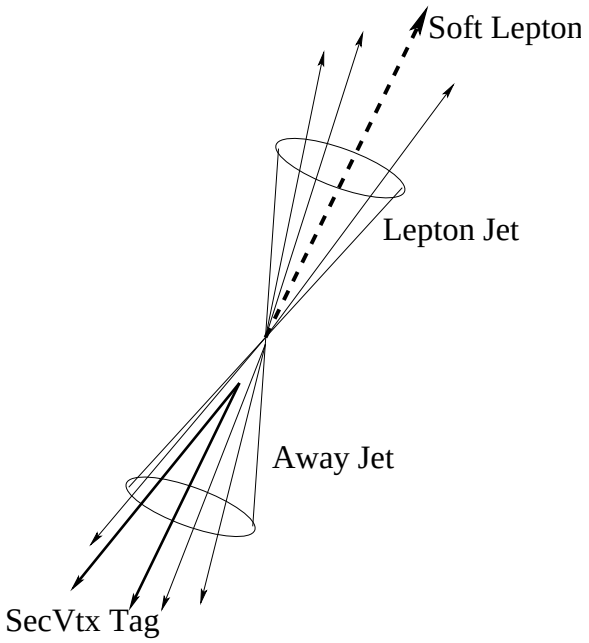

Figure 3.15: Diagram showing the soft lepton samples with which we measure the data to Monte Carlo scale factor (SF). The diagram shows the tagged away-jet, and the lepton-jet with which we use to measure the efficiency.

is measured as a function of the number of events in a sample of size $\boxed{N}$ which have tags on the e-jet ($\boxed{N}^{\text{e-tag}}$), the a-jet, ($\boxed{N}_{\text{a-tag}}$,) or both ($\boxed{N}^{\text{e-tag}}_{\text{a-tag}}$). The e-tag and a-tag can be positive (+) or negative (−), depending on the secondary vertex displacement with respect to the jet axis. A complete dictionary of the notation can be found in Appendix B.1.1.

The additional assumptions of this method are that the negative-tag scale factor is the same as the positive-tag scale factor, and that the heavy flavor fraction in the Monte Carlo ($\boxed{F_{\text{mc}}}^{H}$) is set to 1.

A full derivation of the scale factor equations is given in the Appendix. To summarize, the scale factor is written as

$$(SF) = \frac{\frac{(\boxed{N}^{+}_{+} - \alpha\boxed{N}^{+}_{-}) - \beta(\boxed{N}^{-}_{+} - \alpha\boxed{N}^{-}_{-})}{(\boxed{N_{\text{mc}}}^{+}_{+} - \alpha\boxed{N_{\text{mc}}}^{+}_{-}) - \beta(\boxed{N_{\text{mc}}}^{-}_{+} - \alpha\boxed{N_{\text{mc}}}^{-}_{-})} \frac{(\boxed{N_{\text{mc}}}_{+} - \alpha\boxed{N_{\text{mc}}}_{-})\boxed{F_{\text{mc}}}^{H}_{H}}{\boxed{F_{\text{mc}}}_{H}} - \frac{(\boxed{N}^{+} - \beta\boxed{N}^{-})}{\boxed{N_{\text{mc}}}^{+} - \beta\boxed{N_{\text{mc}}}^{-}} (\boxed{N_{\text{mc}}}\boxed{F_{\text{mc}}}^{H})\chi}{(\boxed{N}_{+} - \alpha\boxed{N}_{-}) - \boxed{N}\chi}. \quad (3.12)$$

where

$$\chi \equiv \frac{(\boxed{N}^{+} - \beta\boxed{N}^{-})(\boxed{N_{\rm conv}}_{+} - \alpha\boxed{N_{\rm conv}}_{-}) - (\boxed{N}_{+} - \alpha\boxed{N}_{-})(\boxed{N_{\rm conv}}^{+} - \beta\boxed{N_{\rm conv}}^{-})}{\boxed{N_{\rm conv}}(\boxed{N}^{+} - \beta\boxed{N}^{-}) - \boxed{N}(\boxed{N_{\rm conv}}^{+} - \beta\boxed{N_{\rm conv}}^{-})}. \quad (3.13)$$

Data Samples

We use a dataset triggered with an 8-GeV electron. The electron data are selected with the cuts in Table 3.2.

$\lvert z_{\text{electron track}}\rvert$ at $r = 10.6$ cm	< 43.5 cm
$\lvert z_{\text{electron track}}\rvert$ at $r = 2.44$ cm	< 43.5 cm
`fidele`	1
Electron E_T	> 9 GeV
P_T	> 8 GeV
$\frac{E}{P}$	(0.5,2.0)
$\frac{\text{had}}{\text{em}}$	< 0.05
L_{shr}	< 0.2
$\lvert\Delta_{x_{\text{CES}}}\rvert$	< 3 cm
$\lvert\Delta_{z_{\text{CES}}}\rvert$	< 5 cm
$\chi^2_{\text{CES strip}}$	< 10
$\lvert z_{\text{e}} - z_0^{\text{event}}\rvert$	< 5 cm
δR_{jet}	< 0.4 from fiducial, 15 GeV (corrected), central cone-0.4 jet.
Isolation	> 0.1 15 GeV (corrected) a-jet with $\lvert\eta\rvert < 1.5$, opposite in phi ($\delta\phi > 2.0$).

Table 3.2: Cuts on the 8 GeV electron sample. The electron chosen is the highest E_T electron passing all cuts, the electron jet is the closest passing jet to the electron, and the away jet is the highest energy jet in the allowed (η, ϕ) region.

The Monte Carlo sample used for this measurement was generated with HERWIG 6.4 within CDF offline release 4.9.1, and simulated with the Gen5 release of 5.3.3_nt offline. The generation is generic 2-2 scattering QCD events with a minimum outgoing

parton transverse momentum of 15 GeV (`IPROC=1500; PTMIN=15`). QQ was used to re-decay heavy flavor hadrons. A filter requiring an 8-GeV lepton with $Y_{max} < 2.0$ (electron or muon) in the generator-level particle list discards most light flavor events. Unlike the 8 GeV electron data, every Monte Carlo event contains a lepton that was not created by material interactions.

Monte Carlo events are accepted or rejected according to a trigger parameterization of the 8 GeV L2 lepton trigger. These parameterizations describe the trigger's efficiency to identify an electron based on its fully reconstructed E_T, p_T and, in part, calorimeter isolation. We choose the parameterization corresponding to the moderate isolation cut ($\mathrm{Isol}_{0.4} < 4$), although the shape of the function does not vary strongly with isolation. For such electrons, the trigger response efficiency is given by [33]:

$$freq\left(\sqrt{E_T} - \sqrt{E_{T0}})/(2\sigma_E)\right) \times freq\,(p_T - p_{T0})/(2\sigma_p p_T p_{T0})) \times (1 - e^{(2.0-E_T)/(2\sigma_{E_2})}) \tag{3.14}$$

with

$$\begin{aligned} E_{T0} &= 7.93 \\ \sigma_E &= 0.096 \\ \sigma_{E_2} &= 1.10 \\ p_{T0} &= 7.56 \\ \sigma_p &= 0.0139. \end{aligned}$$

After selecting events based on the trigger parameterization, the Monte Carlo events are subjected to analysis cuts identical to those described for the data. The heavy flavor content of selected Monte Carlo events is listed in Table 3.3. Here, heavy flavor jets are identified by looking for 5-GeV b's and c's within a cone of $\Delta\mathrm{R} = 0.4$ around the jet axis.

Comparisons between the data and Monte Carlo for electron quantities are given in Figure 3.16. Comparisons between the jet quantities is given in Figure 3.17. Comparisons between the number of tracks are given in Figure 3.18. All agree except for the number of good tracks, which is the primary reason there is a scale factor.

Conversion Finding

Conversions were used to preferentially select light flavor electron jets from the data. The tracks in each event were searched for a track with charge opposite the electron charge, which when parallel (in the transverse plane) to the electron track was within $\Delta r_{xy} \leq 0.2$ cm and $\Delta \cot\theta \leq 0.04$ of the track. The algorithm is the same as the conversion finding implemented in the offline code and described in [34]. Conversions that had multiple matching tracks were accepted.

Scale Factor Results

We apply the measurements listed in Table 3.5 to Equation 3.12. For the central value we use $\alpha = \beta = 1$ for data and MC, which is consistent with the values in [35]. A more in-depth discussion of this choice is in the following section. With these parameters, we obtain for the tight tagger,

$$SF = 0.890 \pm 0.022(\text{stat}) \pm 0.018(\text{MC stat}) \pm 0.053(\text{syst}). \tag{3.15}$$

Figure 3.19 shows the double tag efficiency as a function of electron jet E_T for both data and Monte Carlo. The sources of systematic uncertainty are described in detail in Section 3.4.1. We point out several that depend on where the scale factor is

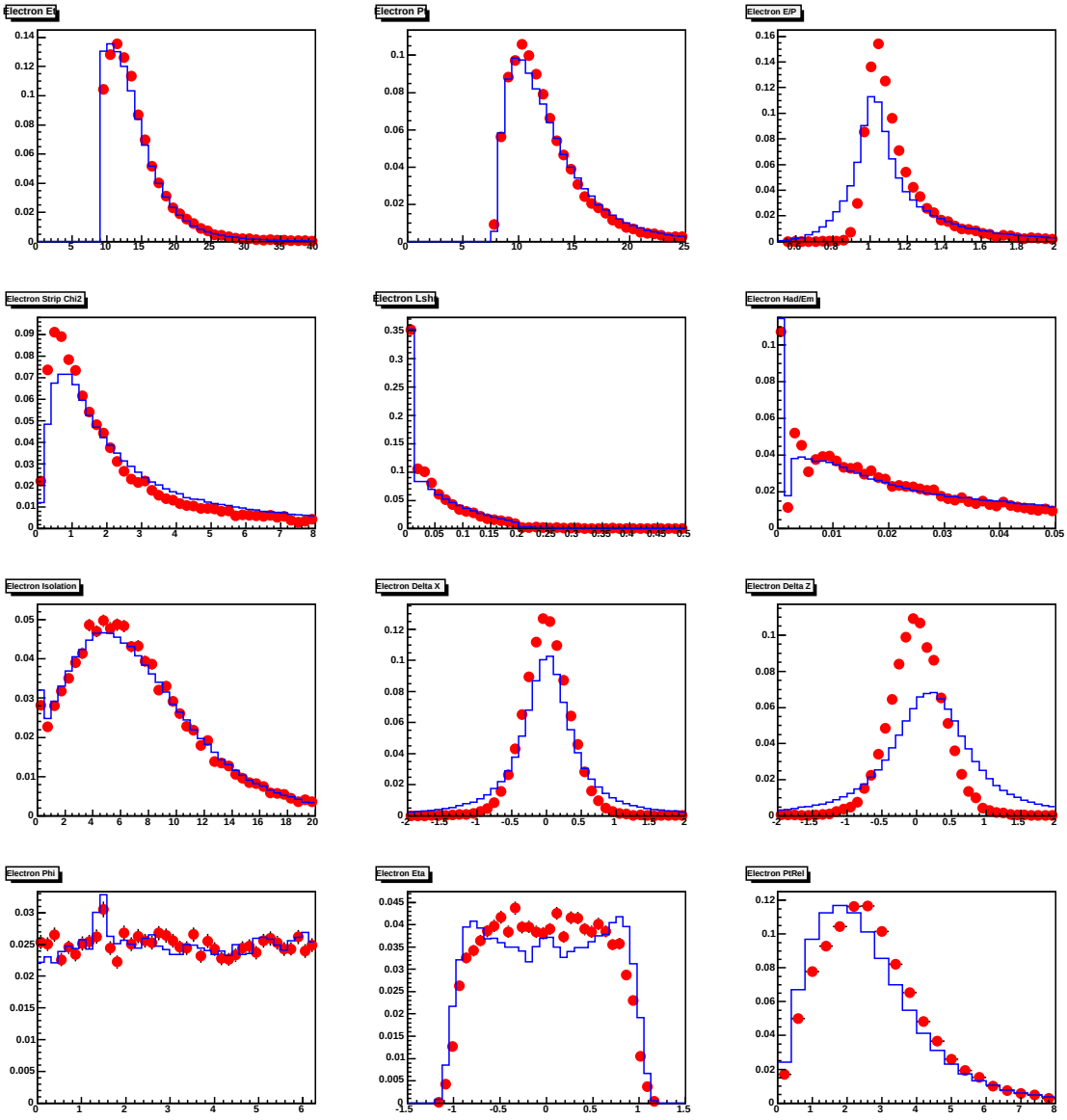

Figure 3.16: Electron variables for electrons passing all selection criteria. The points are from from HERWIG $2 \to 2$ Monte Carlo and the histogram is from 8-GeV electron data. The variables are electron E_T, p_T, E/P, CES strip χ^2, L_{shr}, Had/Em, isolation, Δx, Δz, ϕ, η, and p_T^{rel} (momentum relative to jet axis).

E-jet flavor	A-jet flavor	Fraction of events after all analysis cuts
heavy(includes $g \Rightarrow b\bar{b}/c\bar{c}$)	heavy	24.4%
heavy	light	61.4%
light	heavy	1.2%
light	light	12.9%

Table 3.3: Composition of Monte Carlo sample after applying analysis cuts and a trigger parameterization.

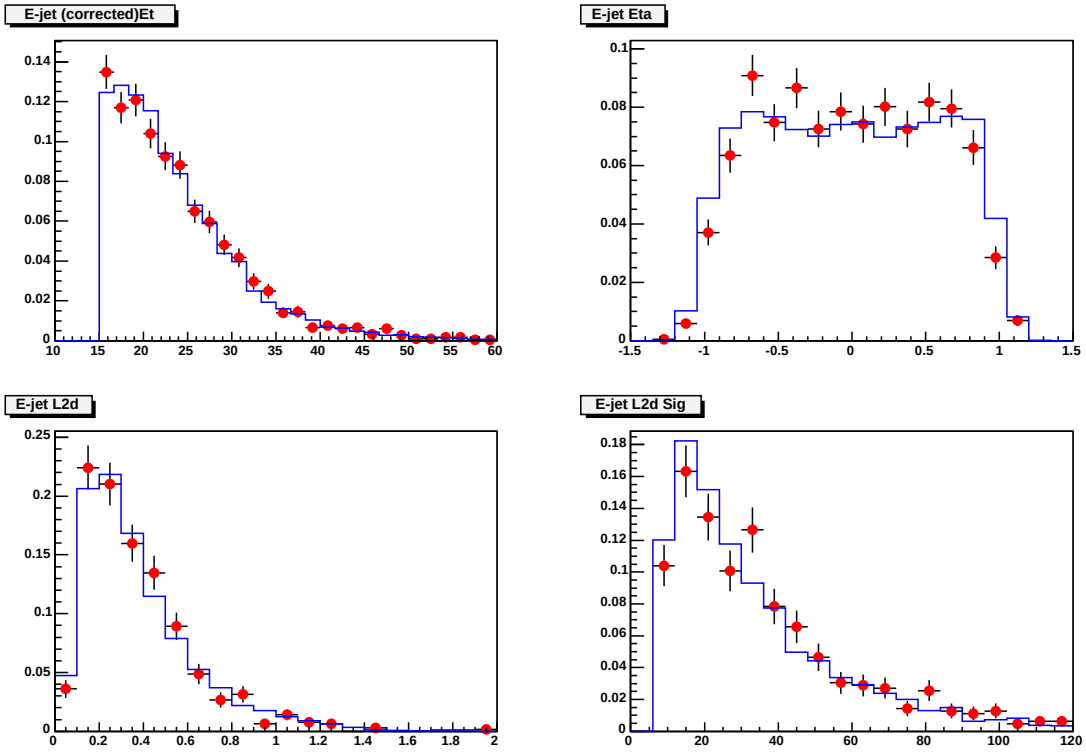

Figure 3.17: Jet kinematic variables after our event selection. The points are from from HERWIG $2 \rightarrow 2$ Monte Carlo and the histogram is from 8-GeV electron data.

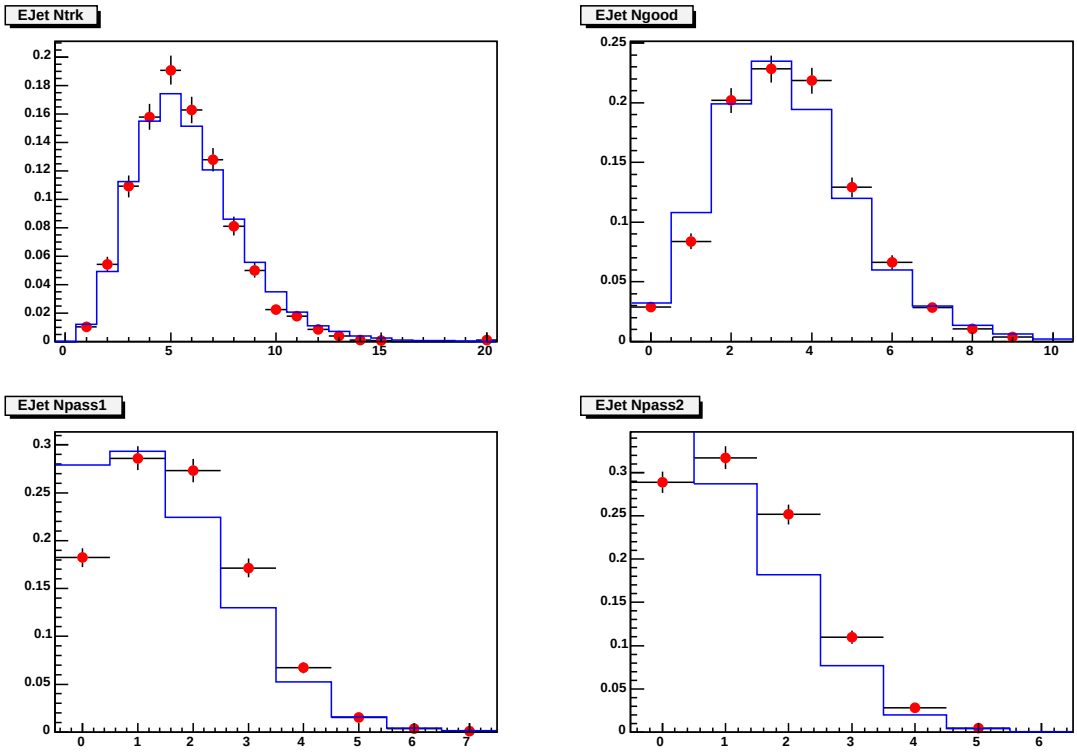

Figure 3.18: Number of track distributions for electron jet. Shown in clockwise order are the number of SecVtx tracks, number of good tracks, number of pass1 and number of pass2 tracks. The points are from from HERWIG $2 \rightarrow 2$ Monte Carlo and the histogram is from 8-GeV electron data.

	Total	Positive Tag Rate (%)	Negative Tag Rate (%)
Data Conversions	255218	1.55	0.26
Data Non-Conversions	393532	8.41	0.28
MC Conversions	4358	9.71	0.30
MC Non-Conversions	21228	25.5	0.41

Table 3.4: Opposite sign conversions found in data and Monte Carlo e-jets, and tight SecVtx tag rates. The Monte Carlo events include light flavor e-jet events, which are not used elsewhere. The higher ratio of positive to negative tag rates in non-conversions points to an enhancement in heavy flavor.

applied; these should be considered when (SF) is used in a physics measurement.

	Data	Monte Carlo (HF)	Conversions (Data)
$\boxed{N}$	648750	21958	255218
$\boxed{N}^{+}$	20795	1988	4708
$\boxed{N}^{-}$	2237	56	888
$\boxed{N}^{+}$	37045	5831	3951
$\boxed{N}^{+}_{+}$	3972	689	330
$\boxed{N}^{+}_{-}$	178	14	18
$\boxed{N}^{-}$	1790	96	682
$\boxed{N}^{-}_{+}$	73	8	20
$\boxed{N}^{-}_{-}$	12	0	7

Table 3.5: Total number of tags, as used in Equation 3.12.

Systematic Uncertainties

There are several systematic uncertainties in the electron method. These are

- Changes in heavy flavor content of the Monte Carlo.
- Assuming the scale factor is the same for b, c, and light quark jets.
- Correlations between the conversion rate and tagging rate.
- Mistag subtraction.
- Jet E_T dependence.
- Semileptonic decay bias.

Each of these assumptions carries a systematic uncertainty associated with it. Table 3.6 shows the size of these systematics. See Ref [32] for full discussion.

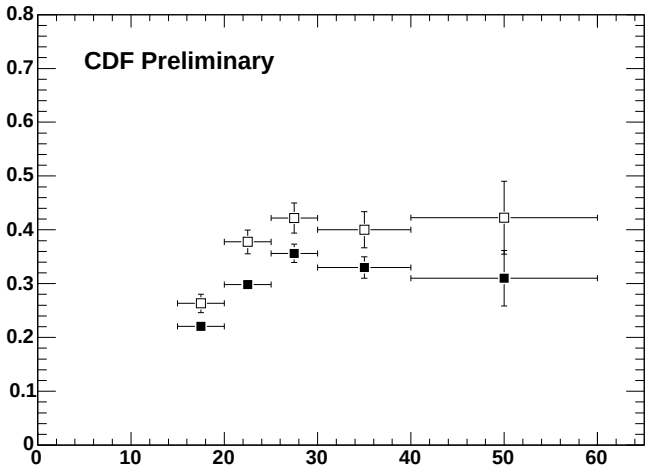

Figure 3.19: Tagging efficiency as a function of electron jet E_T. Open (full) squares are MC (data).

3.4.2 *b*-Tagging Scale Factor With Muon Data

The muon method makes use of the differences in the transverse momentum of the muon relative to the jet axis between b, c, and light flavor hadrons. It uses templates of these quantities from the Monte Carlo and then fits them to data to calculate the efficiency of the tagger in the data. The details for this work can be seen in [36].

Data Sample And Event Selection

The muons dataset is constructed similarly to the electron dataset. An 8-GeV muon trigger is used for the data sample. Table 3.7 shows the event selection for the muon variables.

Furthermore, the energy and momentum of the muon-jet are corrected for the

Source	Relative Error (%) Tight
Semi-Leptonic Decay	2.0
Mistag Subtraction	2.4
c/b Fraction	2.6
Conversion Finding	2.7
SF^c	1.1
MC Jet E Correction	2.0
Total	5.3
E_T-Dependence	3

Table 3.6: Sources of systematic error in electron method of calculating the scale factor.

presence of the muon via

$$E_T^{corr} = E_T \frac{E_{jet} - 2 \text{ GeV}}{E_{jet}} + p_T^{\mu} \tag{3.16}$$

$$\vec{p_{corr}} = \vec{p_{jet}} + \left(1 - \frac{2 \text{ GeV/c}}{|\vec{p_{\mu}}}\right) \vec{p_{\mu}} \tag{3.17}$$

where E_{jet} is the energy of the jet, E_T is the transverse energy of the jet, p_T^{μ} is the muon transverse momentum, and 2 GeV is chosen as the most probably energy deposition of a muon in the p_T range under consideration (see [36] for details).

As with the electron method, the away-jet is required to have a tag to enhance the b-content of the muon-jet.

The Monte Carlo sample is the same one used for the electron method, except that now we require a muon that passes the same analysis cuts as the data.

Figure 3.20 shows a comparison of quantities between data and Monte Carlo. All agree except for the number of good tracks, which is the primary reason there is a scale factor.

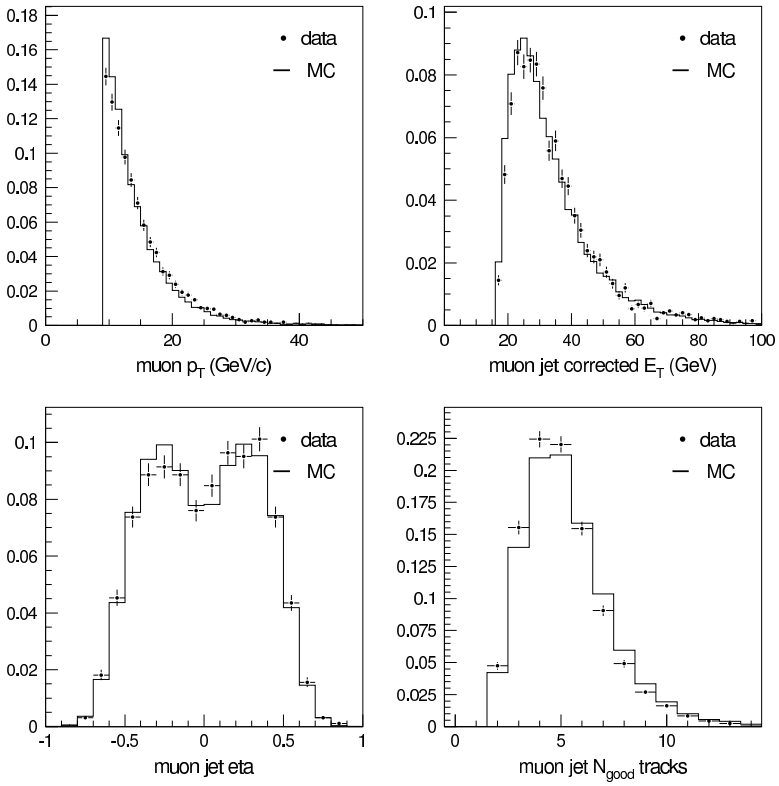

Figure 3.20: Comparison of quantities between data and HERWIG Monte Carlo in the 8-GeV muon sample. Taken from [36].

Muon p_T^{REL} Fits

The muon method takes the light flavor composition of the sample into account by performing fits to the transverse momentum of the muon relative to the jet axis. The b content is then analyzed for both tagged and untagged jets, and hence the efficiency can be determined in both the data and the Monte Carlo, which then gives the scale factor (SF).

The only two species considered in these fits is b versus non-b. The templates used are shown in Figure 3.21. The various non-b templates are used separately, and then a systematic uncertainty is assigned to cover the spread. The non-b models are

- Monte Carlo light flavor jets.
- Monte Carlo charm jets.
- Data with $N_{pass1} = 0$.
- Data with muon matching variables reversed (anti-matched).

The major systematic associated with this method is the E_T dependence of the templates. Figure 3.22 shows the difference in the b-templates as a function of E_T. Thus, the fits are binned in E_T and the spread is assigned as a systematic uncertainty.

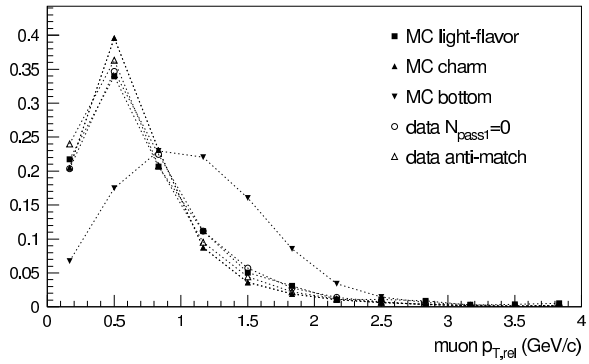

Figure 3.21: p_T^{rel} templates for b-jets (downward arrow) and non-b-jets (other distributions), for the muon method of determining the Scale Factor. The various non-b-templates are taken from c-jets in Monte Carlo, $udsg$-jets in Monte Carlo, data with $N_{pass1} = 0$, and data with muon matching variables reversed. Taken from [36].

Scale Factor Results

To determine the scale factor, the efficiency is calculated by taking the fit number of b-jets in the tagged sample (Figure 3.23, right plot), and dividing it by the fit number of b-jets in the pretagged sample (Figure 3.23, left plot).

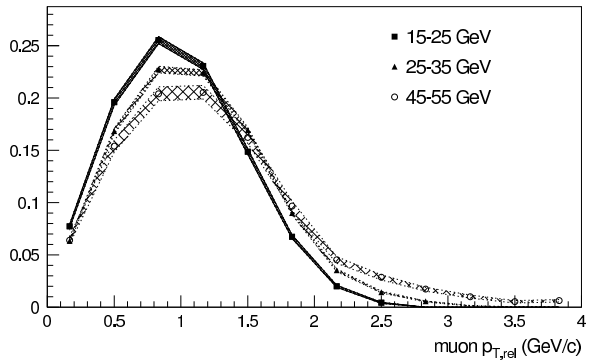

Figure 3.22: E_T dependence of p_T^{rel} distribution for b-jets in Monte Carlo. Each distribution is taken from a separate bin of jet E_T. Taken from [36].

Figure 3.23 shows the fit results for the entire E_T range. The scale factor derived is

$$SF = 0.915 \pm 0.017(stat) \pm 0.018(syst) \tag{3.18}$$

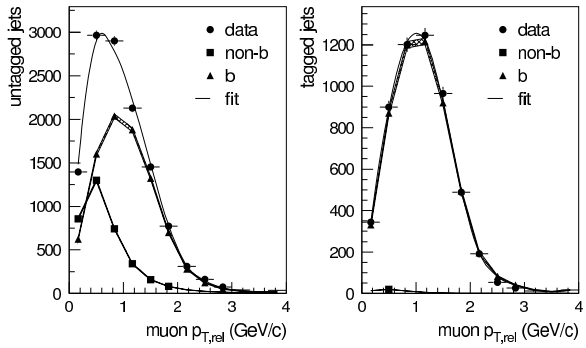

Figure 3.23: Final p_T^{rel} fits to muon data to determine scale factor using muon method. The left side is the pretagged sample. The right side is the tagged sample. Both b and non-b contributions are shown, along with the total amount of data. There is almost zero non-b component in the tagged sample. Taken from [36].

Systematic Uncertainties

There are also several systematics that must be applied to the muon method. They are

- Monte Carlo template statistics.
- Changes in the non-b template model.
- Jet direction uncertainties.
- Jet energy scale uncertainties.
- Biases in vertex mass when the jet is tagged versus untagged.
- Semileptonic decay bias.
- Trigger bias of muon.
- Fake muons in real b-jets.
- Number of tracks per jet dependence.
- Jet E_T dependence
- Jet η dependence

Table 3.8 shows the size of the systematics associated with these effects. See Ref [36] for full discussion of the systematic uncertainties.

P_T	> 8 GeV
z_0	$< 60\ cm$
$\lvert z_e - z_0^{\text{event}} \rvert$	< 5 cm
CMU stub $\lvert\delta x\rvert$	< 3 cm
CMP stub $\lvert\delta x\rvert$	< 5 cm
SVX layers requirement	Must pass through all layers (no hit requirement)
δR_{jet}	< 0.4 from fiducial, 15 GeV (corrected), central cone-0.4 jet.
Isolation	> 0.1 15 GeV (corrected) a-jet with $\lvert\eta\rvert < 1.5$, opposite in phi ($\delta\phi > 2.0$).

Table 3.7: Cuts on the 8 GeV muon sample. The muon chosen is the highest E_T muon passing all cuts, the muon jet is the closest passing jet to the muon, and the away jet is the highest energy jet in the allowed (η, ϕ) region. Taken from [36].

Source	Relative Error (%)	
	Tight	Loose
Template statistics	0.6	0.5
MC tag efficiency	0.4	0.4
Non-b template model	2.0	1.8
Jet direction	1.4	2.2
Jet energy scale	1.9	1.5
Template tag bias	0.7	0.9
$b \to \mu$ momentum	0.7	0.5
$b \to c \to \mu$	0.3	0.3
Semileptonic BR	0.2	0.2
Subtotal	3.3	3.5
b decay multiplicity	2.0	0.8
E_T dependence	5.0	5.0
η dependence	1.2	3.1
Total	6.4	6.9

Table 3.8: Sources of systematic error in our measurements of (SF) for Winter 2004 and 2005 conferences.

Results

When applying the procedure for the muon method, the scale factor is determined to be

$$SF = 0.915 \pm 0.060 \tag{3.19}$$

3.4.3 Scale Factor Combination

The combination of the two scale factor measurements has been performed by minimizing a generalized likelihood. This requires the determination of the correlation between the two scale factor measurements [37].

The systematics that are taken to be correlated are the jet energy scale systematic, the semileptonic decay systematic, jet η dependence, and the jet energy scale.

Combining these two methods yields a result of

$$SF = 0.909 \pm 0.060 \tag{3.20}$$

Table 3.9 shows the combination of the two scale factor measurements.

	Electron	Muon
SF	0.890 ± 0.072	0.915 ± 0.060
Correlation	0.592	
Weight	0.242	0.758
Combined stat error	0.015	
Combined syst error	0.058	
Combined SF	0.909 ± 0.060	

Table 3.9: Combination of electron and muon methods for scale factor determination.

3.5 Measurement of Mistag Rate

Any tag on a jet that does not contain heavy flavor is referred to as a *fake tag* or *mistag*. These can come from several sources.

Firstly, there are tags that are due to tracking resolution. That is, any given track has a probability to be displaced simply due to the Gaussian nature of its error ellipse. When several tracks randomly have large displacement significances, they can combine to form a mistag. These mistags can be mitigated by selecting good-quality vertices with large displacements.

Secondly, there are tags from long-lived light-flavor jets such as K_0^s and Λ. These can be mitigated to some extent by requiring tags to fall outside their mass window.

Finally, there are tags due to material interactions and conversions on the beampipe and inner silicon detector. These can be mitigated by disallowing two-track vertices within the detector material.

Although the mistags can be mitigated in some sense, no method is 100% effective, and so we must measure the residual mistag rate and apply it to data. The strategy for doing this is to use the negative tag rate (which gives the mistags due to resolution of the detector), and correct for the (positive L_{2D}) long-lived light flavor like K_0^s, Λ, conversions and material interactions.

It is convenient to make an additional definition at this point. We define a *taggable jet* as a jet with at least two tracks that are considered "good" by the SecVtx algorithm, as defined in Section 3.3. We then consider tag rates with taggable jets as the denominator in order to account for run-dependent considerations such as non-uniform coverage over time and luminosity differences.

3.5.1 Data Samples and Prescription

We use di-jet data triggered by one jet with Level 2 E_T thresholds of 20, 50, 70, and 100 GeV as a sample depleted in heavy flavor. We refer to these samples as JET20,50,70,100. Data that is triggered by requiring at least 4 jets and $\sum E_T$ is used for various cross-checks of the method. This sample is referred to as the $\sum E_T$ sample.

3.5.2 Tag Rates in Di-jet Samples

Table 3.10 shows the comparison of the rates of obtaining a taggable jet, a positive, and a negative tag in jet data in `4.11.2` versus `5.3.3_nt`, for the different triggers involved.

3.5.3 Tag Matrices

The tag matrices for the tagger outlined in Section 3.3 were measured in the same way as in Ref [38] and Ref [39]. Tagged, mistagged, and taggable jets in the JET20,50,70,100 samples are counted in bins of E_T, number of good tracks, jet η, jet ϕ, and $\sum E_T$ of the event. Table 3.11 shows the binning of the tag matrices.

As in Ref [38], we calculate the positive and negative tag rates:

$$r_+^i \equiv \frac{\#\text{tagged jets with } L_{2D} > 0 \text{ in bin } i}{\#\text{taggable jets in bin } i} \tag{3.21}$$

$$r_-^i \equiv \frac{\#\text{tagged jets with } L_{2D} < 0 \text{ in bin } i}{\#\text{taggable jets in bin } i} \tag{3.22}$$

$L_{2D}$is the distance in the plane transverse to the beam, along or against the direction

Fiducial Rates (%)	**5.3.3_nt Tight**	**4.11.2 Tight**
	Jet20	
Taggability Rate	45.913± 0.017	43.233 ± 0.014
Pos. Tag Rate	0.760 ± 0.003	0.690 ± 0.002
Neg. Tag Rate	0.143 ± 0.001	0.148 ± 0.001
	Jet50	
Taggability Rate	57.367± 0.021	49.272 ± 0.022
Pos. Tag Rate	1.720 ± 0.006	1.307 ± 0.005
Neg. Tag Rate	0.478 ± 0.003	0.362 ± 0.003
	Jet70	
Taggability Rate	60.993± 0.030	52.924 ± 0.032
Pos. Tag Rate	2.191 ± 0.010	1.608 ± 0.009
Neg. Tag Rate	0.692 ± 0.005	0.507 ± 0.004
	Jet100	
Taggability Rate	63.462± 0.027	55.832 ± 0.029
Pos. Tag Rate	2.672 ± 0.014	1.928 ± 0.011
Neg. Tag Rate	0.945 ± 0.005	0.681 ± 0.005
	$\sum E_T$	
Taggability Rate	57.537± 0.014	49.684 ± 0.023
Pos. Tag Rate	1.808 ± 0.004	1.372 ± 0.008
Neg. Tag Rate	0.463 ± 0.002	0.355 ± 0.004

Table 3.10: Fiducial tag rate comparison between `SecVtx` in `4.11.2` and `5.3.3_nt`.

of the jet, from the reference point of the highest $\sum p_T$ primary vertex. A jet is taggable if it satisfies the following requirements:

- uncorrected $E_T > 10GeV$
- $|\eta| < 2.4$
- $N_{\rm trk}^{\rm good} \geq 2$

The $\sum E_T$ of the event needs some explanation. We define

$$\sum E_T = \sum_{i=1}^{N_{jets}} E_T^{jet-i} \tag{3.23}$$

Bin	E_T (GeV)	Track Multiplicity	$\sum E_T$ (GeV)	abs(η)	ϕ (rad)
1	0	2	0	0	$-\pi/12$
2	15	3	80	0.4	$3\pi/12$
3	22	4	140	0.8	$7\pi/12$
4	30	5	> 220	$1.1(< 2.4)$	$11\pi/12$
5	40	6			$15\pi/12$
6	60	7			$19\pi/12$
7	90	8			$23\pi/12$
8	> 130	10			
9		≥ 13			

Table 3.11: Tag rate matrix variables and bin boundaries. The numbers shown are the lower bin boundaries, except for the last bin in η and ϕ where we also show the upper bound. The last bin in E_T, track multiplicity and $\sum E_T$quantities do not have upper limits.

where E_T is the uncorrected jet transverse energy, η is the jet pseudorapidity, corrected for the interaction point, and N_{jets} is the number of jets with $E_T > 10GeV$ and jet $|\eta| < 2.4$.

3.5.4 Cross Checks

We perform cross checks on the tag matrix, in these categories:

1. **Self-consistency:** A matrix is created using only even numbered events, and the predicted tag rates are compared to the observed rates in odd numbered events. (This division the data into statistically independent samples is merely a sanity check of the code rather than a test of the matrix.)

2. **Predictivity:** The even numbered matrix is used to predict rates versus variables that are not part of the matrix in odd numbered events.

3. **Sample dependence:** A matrix is created using events collected by different triggers, and its predictions are tested in events from other triggers.

Both the total tag rates, R_+ and R_-, and the tag rates as a function of physical quantities are used to judge how well the matrix predicts the observed data. The positive tag rate for jets in bin k of some distribution, such as the distribution of z-positions of the primary vertices, is given by

$$r_+^k = \frac{\sum_{j=0}^{N_{\rm jet}^k} R_+^{\rm bin(E_T^j, N_{\rm trk}^j, \sum E_T^j, \eta^j, \phi^j)}}{N_{jet}^k}, \tag{3.24}$$

3.5.5 Cross Check: Self-Consistency

We create a matrix from the even event numbers in the jet samples, and use it to predict the odd events in the same sample. This allows us to validate our code.

Figure 3.24 shows an example of the "even-odd" cross check on one of the matrix variables (number of good tracks) for the tight tagger. All of our distributions agree perfectly, and we conclude that our matrix is self-consistent.

3.5.6 Cross Check: Sample Dependence

We test the matrices' tag rate predictions in events coming from different triggers. We run the tag matrix on the following samples:

- `SUMET`
- `JET20`
- `JET50`

- `JET70`
- `JET100`

The tag matrices used in the sample dependence study for the `SUMET` sample are based on the full sample of all jet data. However, using the matrix to predict variables in the same datasets used to create the matrix (`JET20/50/70/100`) are based on the even numbered events, and applied to the odd numbered events to have statistically independent samples.

There is a discrepancy in the *average* observed and predicted tag rates due to a different heavy flavor composition in the `SUMET` sample (see Table 3.12, line 6 for both positive and negative tags) This discrepancy is taken as a systematic uncertainty (5%).

Figure 3.25 shows the results of the cross checks on the $\sum E_T$ dataset for the SecVtx tagger for the number of good tracks distribution. This shows the worst agreement over all variables, but it is not a problem because the average total number of tracks in the event is roughly the same for all the datasets.

A summary of all subsample cross checks are shown in Table 3.12.

3.5.7 Cross Check: Predictivity

The matrix we created from even-numbered events is next used to predict the tag rate as a function of variables that are not in the matrix. We check the following variables:

- Number of z vertices in the event

- `PrimeVtx` z
- Run number
- Luminosity
- Number of jets
- `PrimeVtx` x error
- `PrimeVtx` y error
- Number of tracks

See Ref [38] for a full explanation of our choice of variables to examine and for figures of all the cross checks. We see good predictivity in all variables, except for rates at much higher luminosity (luminosity and total number of tracks). In those rates, the matrix does not accurately predict the luminosity behavior. Figure 3.26 shows the observed and predicted distributions of the tag rates versus luminosity in JET20/50/70/100, and Figure 3.27 shows the observed and predicted distributions of the tag rates versus total number of tracks in the event for the SUMET sample. These distributions are the only ones that do not match very well. Any sample that has a very different underlying luminosity and/or number of total tracks will cause a bias in this prediction. However, in our case, since the luminosity used to make the matrix is very close to the luminosity for the analysis, it is safe to use this matrix with respect to luminosity differences. Also, since the average number of total tracks is very similar in the jet data and the W+jets data, it is also safe to use this matrix for

that dataset. Therefore, this matrix will accurately predict the number of negative tags in the signal sample.

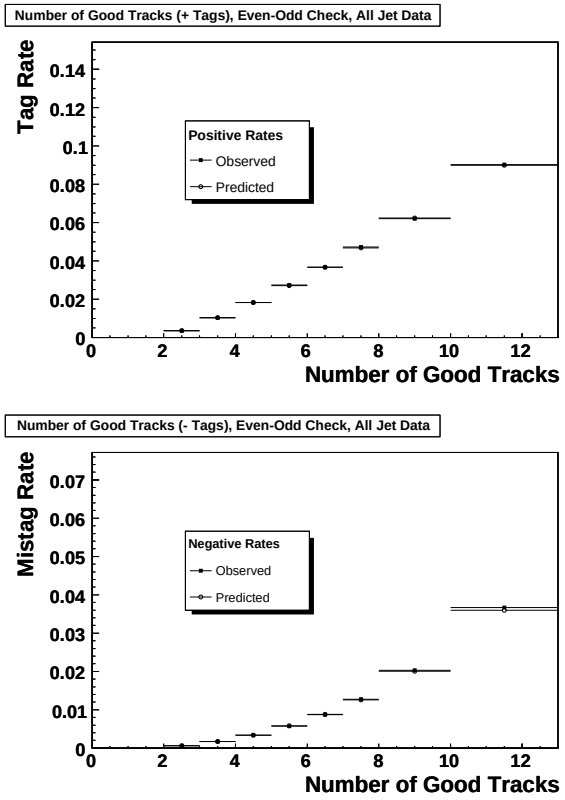

Figure 3.24: Observed (full squares) and predicted (open circles) tag rates versus Jet N_{good}, for all jet data cross checks where the "even" matrix is applied to the odd events of all jet data for the SecVtx tagger. The top plot is for positive tags, and the bottom plot is for negative tags.

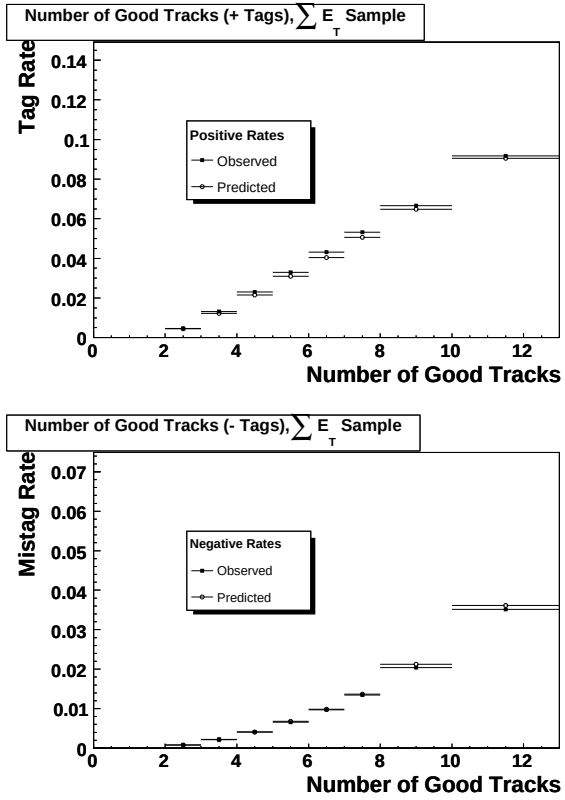

Figure 3.25: Observed (full squares) and predicted (open circles) tag rates versus Jet N_{good}, for $\sum E_T$ data cross check where the full matrix is applied to all events of the $\sum E_T$ sample. The top plot is for positive tags, and the bottom plot is for negative tags.

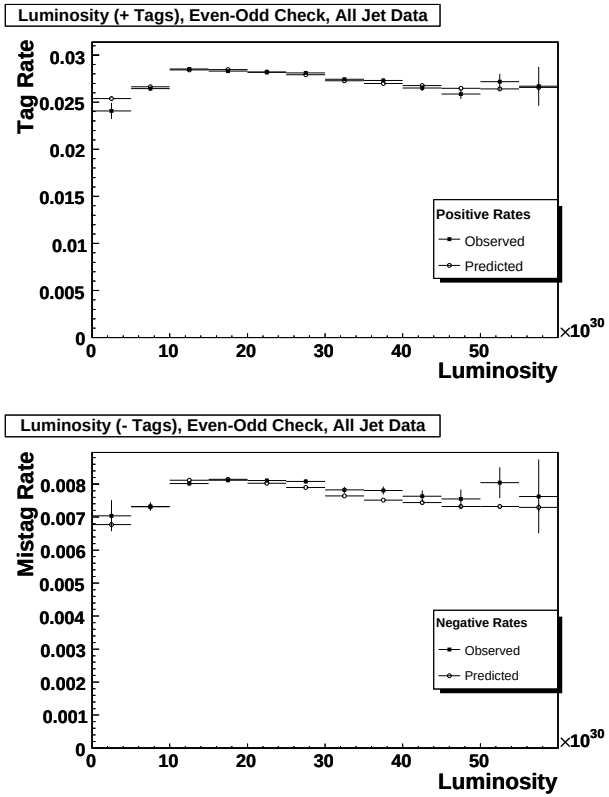

Figure 3.26: Observed (full squares) and predicted (open circles) tag rates versus instantaneous luminosity, for all jet data cross checks where the "even" matrix is applied to the odd events of all jet data for the SecVtx tagger. The top plot is for positive tags, and the bottom plot is for negative tags.

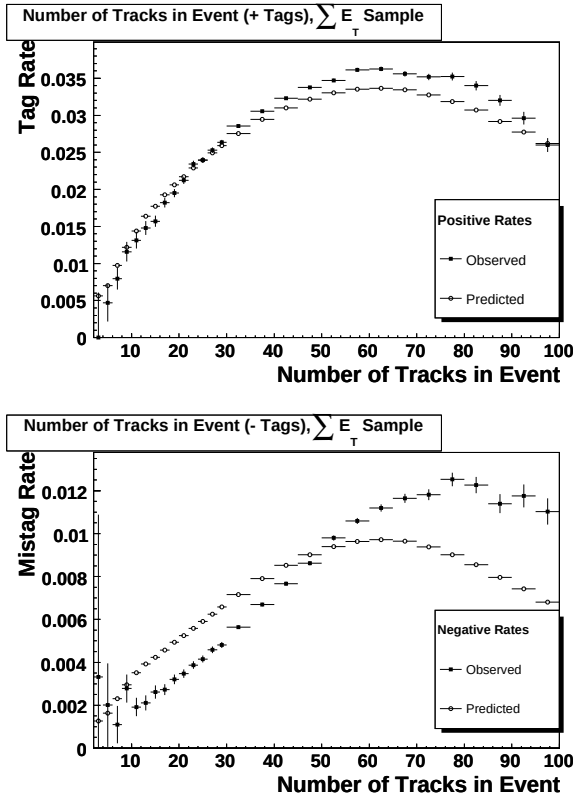

Figure 3.27: Observed (full squares) and predicted (open circles) tag rates versus number of tracks in the event, for $\sum E_T$ data cross check where the full matrix is applied to all events of the $\sum E_T$ sample. The top plot is for positive tags, and the bottom plot is for negative tags.

3.5.8 Cross Check: Checking $\sum E_T$

The matrix we currently use is sensitive to the total number of jets in the event (via the $\sum E_T$ variable). If a jet is gained or lost, the matrix will predict a different tag rate. Since the jet clustering algorithm and Monte Carlo simulation of the jet energy scale are imperfect, it is possible to gain or lose a jet in our signal sample, affecting the tag rates. It is thus necessary to obtain a systematic based on this effect.

To estimate this systematic, we scale the $\sum E_T$ of the event up and down by the average jet energy, and examine the observed and predicted rates. Table 3.12 shows the results of this cross-check.

The maximum difference we see in the tag rates for when we scale the event $\sum E_T$ is 6%, which would give us a systematic of 3% if we take half the difference. However, to be maximally conservative, we assign the same systematic as for the publication in [40] (4%).

3.5.9 Cross Check: Trigger Jet Bias

We have evaluated the systematic due to the fact that we use a triggered jet sample for our tag matrices. We have examined both "trigger" jets (i.e. the case where we look at the predicted and observed rates in the jet closest to the Level 2 calorimeter cluster that fired the jet trigger), and "non-trigger" jets (i.e. the case where we exclude the jet closest to the Level 2 trigger cluster).

We see a trigger jet bias of roughly 4% for the SecVtx tagger, and 3% for the loose tagger. The results are shown along with the rest of the cross checks in Table 3.12.

Check	Pos Obs	Pos Pred	**Pos Ratio**
Even-Odd, All Jet Data	0.027991 ± 0.00005	0.02798 ± 0.00005	**1.000 ± 0.003**
Even-Odd, JET20	0.01656 ± 0.00007	0.01691 ± 0.00006	**0.979 ± 0.005**
Even-Odd, JET50	0.02998 ± 0.00010	0.03009 ± 0.00008	**0.996 ± 0.004**
Even-Odd, JET70	0.03592 ± 0.00015	0.03561 ± 0.00009	**1.009 ± 0.005**
Even-Odd, JET100	0.04211 ± 0.00014	0.04137 ± 0.00015	**1.018 ± 0.005**
$\sum E_T$ Sample	0.03143 ± 0.00007	0.02999 ± 0.00007	**1.048 ± 0.003**
$\sum E_T$ Sample, Scale $\sum E_T \downarrow$	0.03143 ± 0.00007	0.02999 ± 0.00007	**1.048 ± 0.003**
$\sum E_T$ Sample, Scale $\sum E_T \uparrow$	0.03143 ± 0.00007	0.03072 ± 0.00009	**1.023 ± 0.004**
Trigger Jets	0.02721 ± 0.00008	0.02811 ± 0.00006	**0.968 ± 0.004**
Non-Trigger Jets	0.02861 ± 0.00007	0.02798 ± 0.00006	**1.023 ± 0.003**
Check	Neg Obs	Neg Pred	**Neg Ratio**
Even-Odd, All Jet Data	0.00799 ± 0.00003	0.00793 ± 0.00003	**1.008 ± 0.005**
Even-Odd, JET20	0.00312 ± 0.00003	0.00322 ± 0.00003	**0.968 ± 0.013**
Even-Odd, JET50	0.00833 ± 0.00005	0.00827 ± 0.00005	**1.007 ± 0.009**
Even-Odd, JET70	0.01134 ± 0.00008	0.01117 ± 0.00008	**1.016 ± 0.011**
Even-Odd, JET100	0.01490 ± 0.00009	0.01460 ± 0.00009	**1.020 ± 0.008**
$\sum E_T$ Sample	0.00804 ± 0.00003	0.00821 ± 0.00004	**0.980 ± 0.006**
$\sum E_T$ Sample, Scale $\sum E_T \downarrow$	0.00804 ± 0.00003	0.00821 ± 0.00004	**0.980 ± 0.006**
$\sum E_T$ Sample, Scale $\sum E_T \uparrow$	0.00804 ± 0.00003	0.00855 ± 0.00005	**0.940 ± 0.007**
Trigger Jets	0.00796 ± 0.00004	0.00811 ± 0.00004	**0.982 ± 0.007**
Non-Trigger Jets	0.00804 ± 0.00004	0.00784 ± 0.00004	**1.026 ± 0.007**

Table 3.12: Cross checks for tag matrices

3.5.10 Light Flavor Asymmetry

Due to the fact that we use the negative tag rate parameterization to estimate the mistags of SecVtx(which only accounts for the tags due to resolution), it is necessary to make corrections to the prediction to accurately model all light flavor tags. There are tags due to conversions and nuclear interactions and long lived light flavor hadrons like Λ and K_0^s. These types of tags will not be taken into account when using only the negative tag parameterization to estimate the light flavor tags.

The mistag matrix returns the quantity

$$R^- = \frac{N_{LF}^- + N_{HF}^-}{N_{LF}^{pre} + N_{HF}^{pre}} \tag{3.25}$$

In order to remove the heavy flavor from this expression, we derive two quantities,

$$\alpha = \frac{N_{LF}^+}{N_{LF}^- + N_{HF}^-} \tag{3.26}$$

$$\beta = \frac{N_{LF}^{pre} + N_{HF}^{pre}}{N_{LF}^{pre}} \tag{3.27}$$

$$\tag{3.28}$$

The first is the ratio of positive light flavor tags to all negative tags, and the second is the ratio of all pretags to light flavor pretags.

The product $R^-\alpha\beta$ gives the ratio

$$R^-\alpha\beta = \frac{N_{LF}^-}{N_{LF}^{pre}} \tag{3.29}$$

which is the quantity we are interested in. The remaining problem is to determine the quantities $N_{LF}^{\pm}$, $N_{HF}^{\pm}$, N_{LF}^{pre}, and N_{HF}^{pre}.

To do this, we fit the $c\tau$ distribution of tags in the various dijet data using templates from the corresponding Monte Carlo sample. The templates for for each are

quite different, and there is discriminating power available in this information. Figures 3.28(a)-3.28(d) show the templates and fits for the b, c, and light flavor hadrons, in JET20,50,70, and 100 data and Monte Carlo. We then parameterize the mistag asymmetry as a function of the $\sum E_T$ of the sample, as is done in the mistag matrix above. The correction is then applied jet-by-jet. Figure 3.29 shows the correction versus the $\sum E_T$ of the jet samples.

We assign an 18% systematic on this procedure. This is obtained by varying the heavy flavor content of the negative tags by a factor of 2 in each direction and examining the variation on the fit.

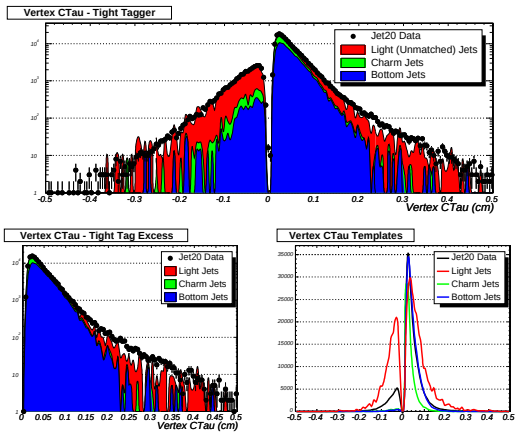

(a) $c\tau$ fits for JET20.

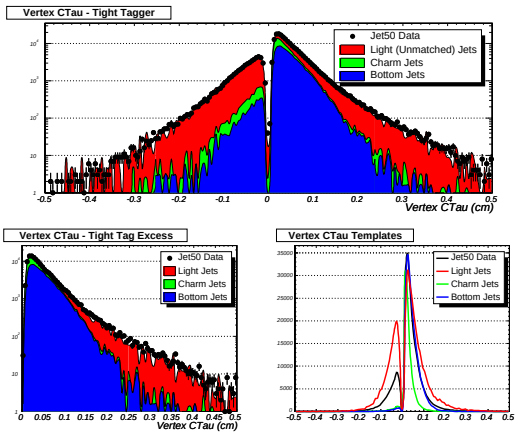

(b) $c\tau$ fits for JET50.

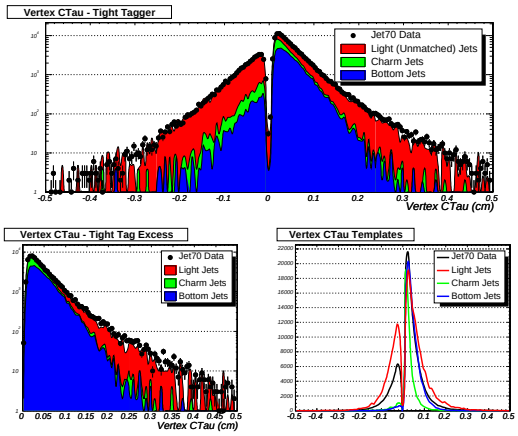

(c) $c\tau$ fits for JET70.

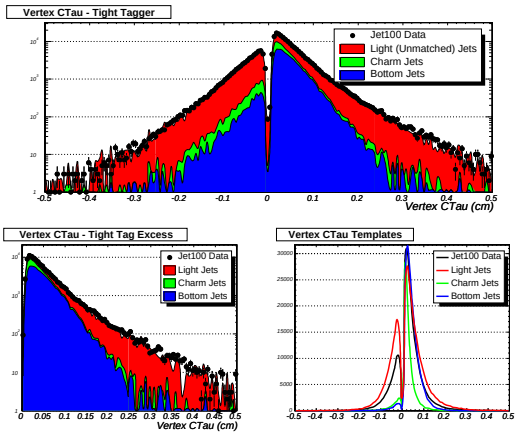

(d) $c\tau$ fits for JET100.

Figure 3.28: $c\tau$ fits for light flavor asymmetry. Blue is for b-jets, green is for c-jets, and red is for $udsg$-jets. Templates are derived from PYTHIA Monte Carlo.

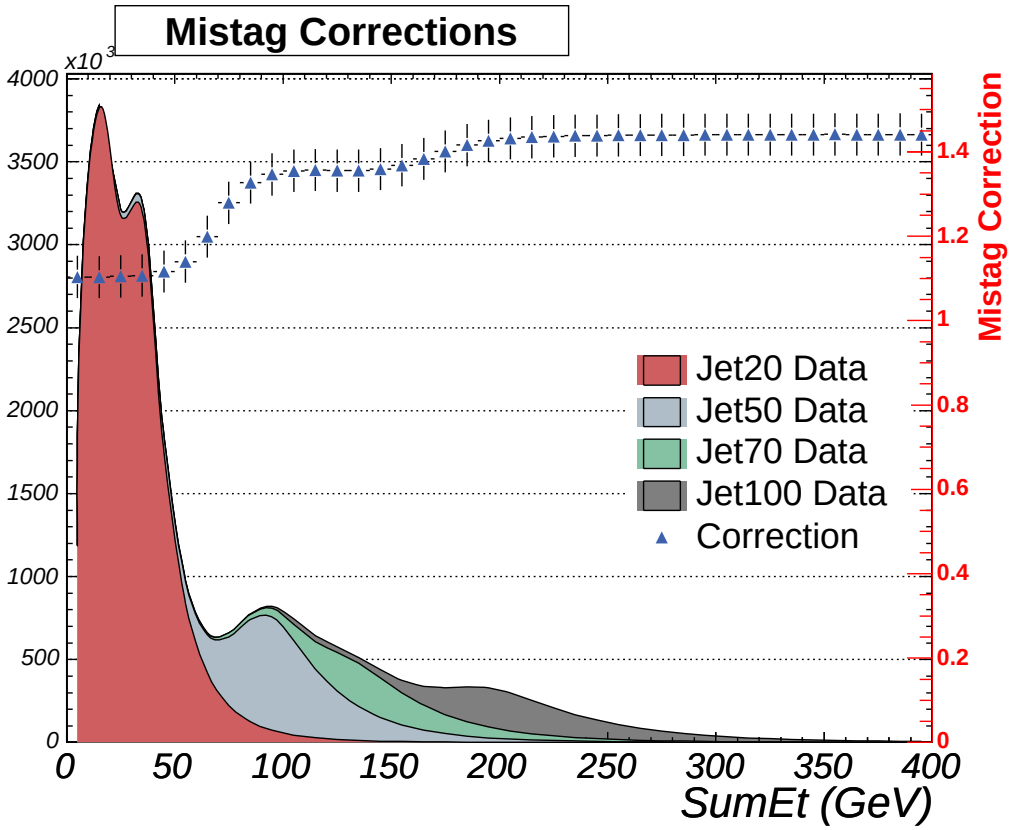

Figure 3.29: $\alpha\beta$ correction to mistag matrix as a function of $\sum E_T$. The left hand axis is the number of jets, while the right hand axis is the mistag correction $\alpha\beta$.

3.5.11 Systematic Uncertainties

The systematic uncertainties were estimated from the following sources:

- $\sum E_T$ **uncertainty:** Estimated as half of the difference between the matrix prediction and observation when we scale the $\sum E_T$ up and down by the average jet energy in the event.
- **Sample bias:** Obtained by applying the matrix to the $\sum E_T$ sample.
- **Trigger bias:** Obtained by applying the matrix to only trigger and only non-trigger jets in the jet samples.
- **Light flavor asymmetry:** This is obtained by changing the heavy flavor content in the negative tails of our $c\tau$ fits by a factor of two.

Table 3.12 summarizes the results of the cross checks.

Wherever the systematic effects in positive and negative tags disagree, we apply the larger systematic to both to be maximally conservative.

The systematic uncertainties are summarized in Table 3.13. We obtain 20% overall systematic for the negative tag rates.

Systematic	Tight	Loose
Sample bias	5%	4%
$\sum E_T^{jets}$ uncertainty	4%	4%
Trigger jet bias	4%	3%
Light flavor asymmetry	18%	18%
Total	**20%**	**20%**

Table 3.13: Systematic uncertainties assign to the tag rate matrix.

3.5.12 Summary

Table 3.12 shows the results of all the cross checks of the tag matrices. The maximum differences observed are the application of the matrix to the SUMET sample, and when the $\sum E_T$ of the event is scaled up and down by the average jet energy. The discrepancies shown in this table are included in the systematic uncertainties.

The light flavor asymmetry is also measured as a function of the event $\sum E_T$. The variation of the light flavor asymmetry is the dominant systematic uncertainty for the mistag estimate. The summary of systematic uncertainties is shown in Table 3.13.

3.6 Overall Efficiency and Negative Tag Rates

The overall efficiency to tag a fiducial b-jet in $t\bar{t}$ events is about 44%. The overall negative tag rate for jets in $t\bar{t}$ signal data is about 0.5%. Figures 3.30(a) and 3.30(b) show the SecVtx efficiency times scale factor in $t\bar{t}$ events versus jet E_T and η, respectively. Figures 3.30(c) and 3.30(d) show the SecVtx negative tag rates versus jet E_T and η, respectively (with no light flavor asymmetry corrections). Both the tight and loose versions of SecVtx are shown, although only the tight version (blue) is used in this analysis. The error bands for the efficiency are for the b-tagging data-to-Monte Carlo scale factor (SF). The jet E_T dependence of the errors is shown correctly. The error bands for the negative tag rate are the errors on the negative tag matrix only (not including light flavor asymmetry corrections or errors).

The efficiency rises as a function of jet E_T, and then eventually falls back off. This is because we have made cuts on the maximum vertex radius allowed, and

have disallowed vertices with 2-tracks to be within material regions. This effects the efficiency at high E_T because the b-hadrons are more boosted, and hence have a higher probability of reaching the material region. The efficiency is flat versus η for $\eta < 1.0$, and then falls off due to reduced COT coverage for high η.

The negative tag rates also rise as a function of jet E_T. However, because we only plot negative tags due to resolution, it does not have the same drop-off as the efficiency. Thus, the negative tag rate essentially plateaus at around 100 GeV. The negative tag rates also increase with jet η, and then fall off as silicon coverage decreases. The initial increase is due to the fact that as jet η increases, the tracks in the jet pass through more and more material, and the tracking algorithm becomes steadily worse due to multiple scattering. The result is an increase in the fake rate in that case.

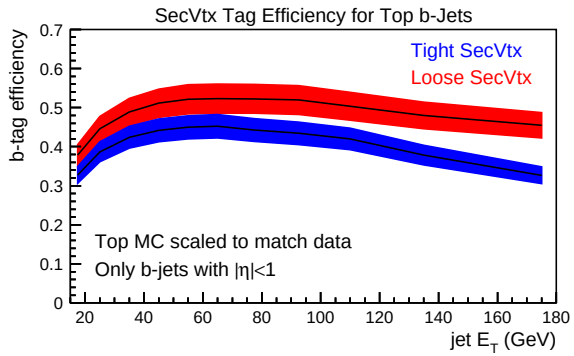

(a) SecVtx Efficiency Versus Jet E_T.

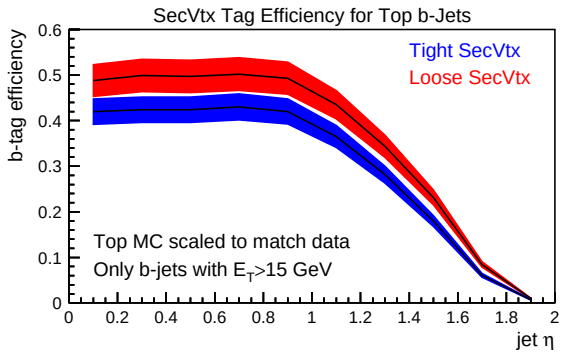

(b) SecVtx Efficiency Versus Jet η.

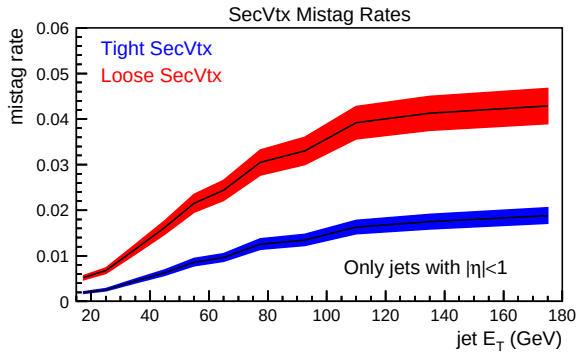

(c) SecVtx Negative Tag Rate Versus Jet E_T.

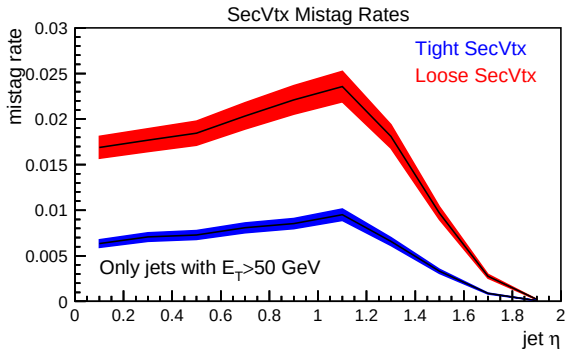

(d) SecVtx Negative Tag Rate Versus Jet η.

Figure 3.30: Summary plots for SecVtx tagger. The tight tagger (used in this analysis) is in blue, while the loose tagger is in red. The bands are systematic uncertainties.

Chapter 4

Measurement of $t\bar{t}$ Pair Production Cross Section

4.1 Analysis Overview

This analysis uses the decay chain

$$p\overline{p} \rightarrow t\bar{t} \rightarrow W^{+}bW^{-}\bar{b} \rightarrow \ell\nu b\bar{b}q\overline{q} \tag{4.1}$$

(where $l = e, \mu$) to measure the $t\bar{t}$ production cross section. We are thus looking for the experimental signature of

$$p\overline{p} \rightarrow \ell + \not{E}_T + \geq 3\ jets \tag{4.2}$$

where l is a muon or electron, $\not{E}_T$ is the missing E_T of the event, and at least one jet is tagged by SecVtx to contain heavy flavor. We require at least two jets are tagged for the double-tagged cross section measurement.

Because other physics processes mimic this signature, it is only possible to extract the $t\bar{t}$ cross section statistically. To do this, we measure (at the simplest level)

$$\sigma_{t\bar{t}} = \frac{N_{obs} - \widehat{N}_{bkg}}{BR(W^{\pm} \to \ell\nu + q\overline{q}) \cdot \mathcal{A} \cdot \epsilon \cdot \int \mathcal{L}dt} \tag{4.3}$$

where $BR(W^{\pm} \to \ell\nu + q\overline{q})$ is the branching ratio for the lepton plus jets channel using electrons and muons (24/81 theoretically, 29.2 $\pm$ 1.5 % experimentally, from Ref [6]), $\mathcal{A}$ is the geometrical acceptance, ϵ is the event efficiency, and $\int \mathcal{L}dt$ is the integrated luminosity. There is additional acceptance from τ sequential decays from $t\bar{t}$ that leak into our acceptance. That is modeled by selecting all events in $t\bar{t}$ Monte Carlo that pass our event selection.

We do not directly use Monte Carlo estimates of efficiencies because the overall simulation is not 100% accurate. Therefore, in order to estimate our acceptance, event selection efficiency, and b-tagging efficiency, it is necessary to use data-to-Monte Carlo *scale factors*. The scale factors we use are for the lepton identification and b-tagging, as well as for the jet energy scale. We measure the efficiencies for our event selection and b-tagging in the Monte Carlo, and then correct for the data expectation using externally measured scale factors.

The backgrounds that mimic the $\ell \not\!\!E_T\, jjbX$ signature are

- **W+ Jets**. This background consists of a real W boson produced in association with either quarks (from flavor excitation) or gluons. The gluon can split into a pair of heavy flavor quarks, producing *W + heavy flavor* events. Alternatively, the gluon or initial quark can hadronize into a jet which is mistagged, producing *W+ light flavor mistag* events. Figures 4.1(a) and 4.1(c) show the

Feynman diagrams for W+ jets production with heavy flavor and light flavor tags, respectively.

- **Non-W QCD Production**. This background arises when the event does not contain a real W boson. This can occur in two ways. The first is when a heavy flavor hadron decays semileptonically, and the resulting lepton and missing E_T pass the event selection. The second is when ordinary multijet QCD production produces a fake lepton plus missing E_T due to mis-measured jets. These two processes are shown in Figures 4.1(d) and 4.1(e), respectively.

- **Electroweak Boson Production**. These backgrounds occur when vector bosons are created in pairs, WW, WZ or ZZ. The WW background has two real W bosons. One can decay leptonically, and the other hadronically. The hadronic W daughters can then produce a b-tag. Similarly, the WZ background can have the W decay leptonically, while the Z can decay into heavy flavor quarks. The ZZ background can mimic the experimental signature if one Z decays leptonically and one leg is mis-reconstructed (faking a W boson) and the other decays into heavy flavor quarks. Also, it is possible for $Z \rightarrow \tau\tau$ to fake this signature because one τ can fake the W signature while the other τ is tagged. Figure 4.1(f) shows the diboson production for WW (WZ and ZZ are very similar).

- **Single Top Production**. Although this process contains real top quarks, it is a background to top pair production. If the W from the top decays leptonically, this process can mimic the experimental signature of pair production. Fig-

ure 4.1(g) shows the t-channel production of single top. There is an analogous s-channel diagram as well.

We present both an *optimized* and an *unoptimized* version of the analysis. The *optimized* version has additional kinematic cuts to improve signal to background.

Some of the estimates of background levels above depend on the amount of $t\bar{t}$ estimated to be in the signal. Particularly, the W+jets background estimates (both W+heavy flavor and W+light flavor) depend on the amount of $t\bar{t}$ present in the pretag sample. Similarly, the way we estimate the Non-W background (to be discussed below) also depends on the amount of $t\bar{t}$ in the pretag sample. Thus, in order to take this into account, we assume a cross section of 6.1 pb (the theoretical prediction for $m_{top} = 178\ GeV/c^2$), and measure the cross section. The measured cross section is then input back into the background estimate, and the cross section is remeasured. The process is repeated until the results are stable to $< 1\%$. We refer to this as the "iteration" procedure.

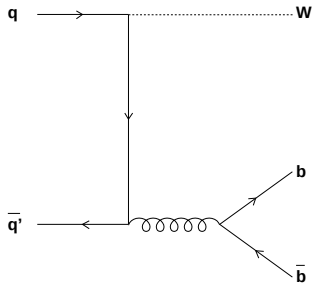

(a) W + heavy flavor jets

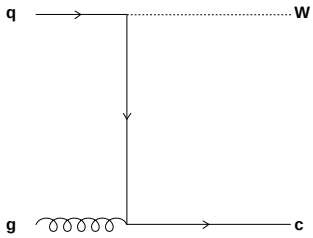

(b) W + heavy flavor jets, flavor excitation

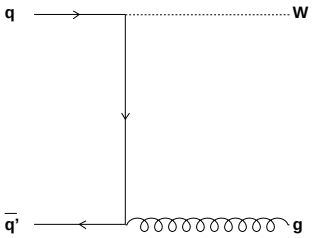

(c) W + light flavor jets

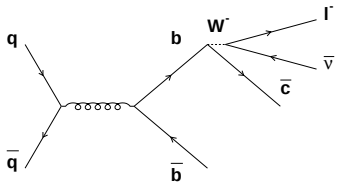

(d) Non-W QCD production from heavy flavor decay.

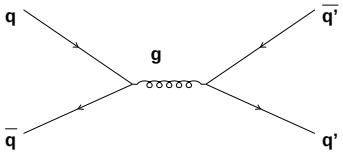

(e) Non-W QCD production from fake leptons.

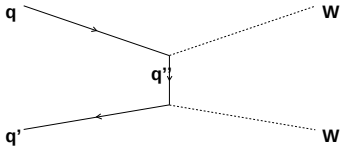

(f) Di-boson Production

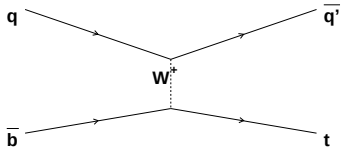

(g) Single top production, t-channel

Figure 4.1: Feynman diagrams for backgrounds to $t\bar{t}$ lepton plus jets production.

4.2 Data Sample and Event Selection

The data sample[1] is the 318 pb^{-1} collected until the September 2004 shutdown, covering runs 138425 (Feb 4, 2002) - 186598 (Aug 22, 2004), excluding the COT compromised data (runs 179057-182842). We use DQM Good Run List v7.0, including requirements on good silicon data, and ignoring CMX bits for runs before 150145. The integrated luminosity for this period is 318.5 ± 19.1 for CEM and CMUP, and 305.2 ± 18.3 for CMX, where a 1.9% correction has been applied. (See Chapter 2.2 for definitions of CEM, CMUP, and CMX detector elements).

We use datasets `bhel0d` (high p_T central electron triggered dataset) and `bhmu0d` (high p_T central muon triggered dataset) for the signal data for electrons and muons, respectively.

We require

- Jets $E_T > 15\ GeV$ and $|\eta_{detector}| < 1.0$, clustered with `JetClu` with a cone of 0.4, corrected to Level 4 with jet corrections version `jetCorr04b` (See Section 2.2.1 for details).
- One tight, isolated trigger lepton, with $|\eta| < 1.0$
- $\not\!\!E_T$ > 20.0 GeV (corrected to Level 4)
- Veto dileptons, Z bosons, conversions, cosmic rays
- $|\Delta z_{lepton-zvtx}| < 5.0$ cm

[1] See Glossary for jargon definitions.

- z_{vtx} found with `ZVertexModule` using the beamline as seed. The highest p_T z-vertex within 5.0 cm is selected.

- ≥ 1 or ≥ 2 positive tight SecVtx tags.

- Signal region defined as: ≥ 3 jets with $E_T > 15$ GeV (corrected at Level 4) and $|\eta_{detector}| < 2.0$

Event yields are shown in Table 4.1. We then divide the sample into pretags, ≥ 1 tag, and ≥ 2 tags based on SecVtx. The breakdown of events in the data sample are given in Table 4.2. (See Table 4.3 for a description of all entries in this table). Figure 4.2 shows the missing E_T, the δZ between the lepton and the primary vertex, the leptonic W transverse mass (M_T^W), and the scalar sum of transverse energies in the event (H_T). Section 4.2.1 outlines the specific lepton selection.

Data					
	1 jet	2 jets	3 jets	4 jets	$\geq$ 5 jets
CEM					
Pretag	17648	2846	469	115	19
$\geq$ 1+ Tag	249	142	59	39	8
$\geq$ 2+ Tag	0	10	11	7	1
$\geq$ 1− Tag	62	24	8	3	1
$\geq 1+-$ Tag	0	1	2	1	1
$\geq$ 2− Tag	0	0	0	0	0
CMUP					
Pretag	8514	1263	202	46	11
$\geq$ 1+ Tag	110	66	25	18	7
$\geq$ 2+ Tag	0	5	5	6	2
$\geq$ 1− Tag	27	12	2	1	0
$\geq 1+-$ Tag	0	0	0	0	0
$\geq$ 2− Tag	0	0	0	0	0
CMX					
Pretag	4466	682	98	18	6
$\geq$ 1+ Tag	73	34	11	6	4
$\geq$ 2+ Tag	0	0	1	3	0
$\geq$ 1− Tag	11	7	1	0	0
$\geq 1+-$ Tag	0	0	0	0	0
$\geq$ 2− Tag	0	0	0	0	0
Total					
Pretag	30628	4791	769	179	36
$\geq$ 1 Tag	432	242	95	63	19
$\geq$ 2 Tag	0	15	17	16	3
$\geq$ 1− Tag	100	43	11	4	1
$\geq 1+-$ Tag	0	1	2	1	1
$\geq$ 2− Tag	0	0	0	0	0

Table 4.1: Events Yields for $318.5 pb^{-1}$, for the *unoptimized* analysis.

Channel	0-jet	1-jet	2-jet	3-jet	4-jet	≥5-jet	Total
CEM							
Stage 0 INITIAL	557801	313245	230088	31576	4707	703	1138120
Stage 1 GOODRUN	557801	313245	230088	31576	4707	703	1138120
Stage 2 TRIGGER	286581	214598	184723	23046	3290	468	712706
Stage 3 ≥1TLEP	286581	210845	183236	22700	3229	455	707046
Stage 4 MET	179837	26552	7593	1868	392	87	216329
Stage 5 ISO	179837	18696	3159	549	130	23	202394
Stage 6 !DILEP	179701	18569	3101	527	128	22	202048
Stage 7 !Z	177993	17653	2848	469	115	20	199098
Stage 8 !CONV	177993	17653	2848	469	115	20	199098
Stage 9 !DIFFZ	177843	17648	2846	469	115	19	198940
Stage 10 KIN VETOS	0	17448	2780	197	95	18	20538
Stage 11 SI GOOD	0	17448	2780	197	95	18	20538
Stage 12 TAGGABLE	0	11643	2423	186	93	18	14363
Stage 13 ≥1+BTAG	0	246	137	40	34	8	465
Stage 14 ≥2+BTAG	0	0	10	10	6	1	27
Stage 15 ≥1-BTAG	0	61	23	4	3	1	92
Stage 16 ≥1+-BTAG	0	0	1	1	1	1	4
Stage 17 ≥2-BTAG	0	0	0	0	0	0	0
Stage 18 LTAGGABLE	0	12029	2455	187	93	18	14782
Stage 19 ≥1+LTAG	0	442	204	52	41	12	751
Stage 20 ≥2+LTAG	0	0	20	16	11	2	49
Stage 21 ≥1-LTAG	0	137	71	11	9	2	230
Stage 22 ≥1+-LTAG	0	0	3	3	3	2	11
Stage 23 ≥2-LTAG	0	0	0	0	0	0	0
CMUP							
Stage 0 INITIAL	557801	313245	230088	31576	4707	703	1138120
Stage 1 GOODRUN	557801	313245	230088	31576	4707	703	1138120
Stage 2 TRIGGER	150614	45689	15701	3013	485	85	215587
Stage 3 ≥1TLEP	150267	45471	15520	2966	468	81	214773
Stage 4 MET	111651	21748	8174	1896	308	58	143835
Stage 5 ISO	106975	9548	1419	230	49	12	118233
Stage 6 !DILEP	103508	9115	1348	212	48	12	114243
Stage 7 !Z	99009	8630	1280	207	46	11	109183
Stage 8 !COSMIC	93507	8612	1277	207	46	11	103660
Stage 9 !DIFFZ	91131	8514	1263	202	46	11	101167
Stage 10 KIN VETOS	0	8383	1219	86	34	10	9732
Stage 11 SI GOOD	0	8383	1219	86	34	10	9732
Stage 12 TAGGABLE	0	5481	1044	85	33	9	6652
Stage 13 ≥1+BTAG	0	108	61	14	18	6	207
Stage 14 ≥2+BTAG	0	0	5	4	6	2	17
Stage 15 ≥1-BTAG	0	25	10	2	1	0	38
Stage 16 ≥1+-BTAG	0	0	0	0	0	0	0
Stage 17 ≥2-BTAG	0	0	0	0	0	0	0
Stage 18 LTAGGABLE	0	5660	1057	85	33	9	6844
Stage 19 ≥1+LTAG	0	174	90	18	23	7	312
Stage 20 ≥2+LTAG	0	0	10	5	10	2	27
Stage 21 ≥1-LTAG	0	56	30	4	1	0	91
Stage 22 ≥1+-LTAG	0	0	1	0	0	0	1
Stage 23 ≥2-LTAG	0	0	1	1	0	0	2
CMX							
Stage 0 INITIAL	557801	313245	230088	31576	4707	703	1138120
Stage 1 GOODRUN	536748	302000	221601	30391	4540	684	1095964
Stage 2 TRIGGER	92725	28998	10548	1989	296	51	134607
Stage 3 ≥1TLEP	91042	28253	10140	1918	281	50	131684
Stage 4 MET	65140	13331	5116	1119	178	30	84914
Stage 5 ISO	61929	5107	790	117	21	6	67970
Stage 6 !DILEP	60352	4885	741	106	19	6	66109
Stage 7 !Z	58218	4659	710	104	18	6	63715
Stage 8 !COSMIC	57566	4655	710	103	18	6	63058
Stage 9 !DIFFZ	52061	4466	682	98	18	6	57331
Stage 10 KIN VETOS	0	4452	677	41	13	6	5189
Stage 11 SI GOOD	0	4452	677	41	13	6	5189
Stage 12 TAGGABLE	0	2985	581	37	13	6	3622
Stage 13 ≥1+BTAG	0	73	34	8	6	4	125
Stage 14 ≥2+BTAG	0	0	0	1	3	0	4
Stage 15 ≥1-BTAG	0	11	7	0	0	0	18
Stage 16 ≥1+-BTAG	0	0	0	0	0	0	0
Stage 17 ≥2-BTAG	0	0	0	0	0	0	0
Stage 18 LTAGGABLE	0	3076	591	38	13	6	3724
Stage 19 ≥1+LTAG	0	106	52	10	7	4	179
Stage 20 ≥2+LTAG	0	0	0	2	4	2	8
Stage 21 ≥1-LTAG	0	32	16	1	0	0	49
Stage 22 ≥1+-LTAG	0	0	2	0	0	0	2
Stage 23 ≥2-LTAG	0	0	0	0	0	0	0

Table 4.2: Event counts at each successive stage for the data sample. Note that the conversion veto is already applied in the tight lepton definition.

Cut	Description
Stage 0 INITIAL	Initial stage of event selection.
Stage 1a GOODRUN	Requirement of Good Run List without silicon detector requirement (data only).
Stage 1b OBSV	Requirement that event lie within $\|z_0\| < 60$ cm (MC only)
Stage 2 TRIGGER	Requirement that events pass trigger (data only).
Stage 3 ≥1TLEP	At least one tight lepton.
Stage 4 MET	$\not\!\!E_T > 20$ GeV
Stage 5 ISO	$iso < 0.1$
Stage 6 !DILEP	Dilepton veto. Require exactly one tight lepton.
Stage 7 !Z	Z-veto. Veto any event that has a lepton + track or lepton + jet forming the Z-mass.
Stage 8a !CONV	Conversion veto (electrons only).
Stage 8b !COSMIC	Cosmic veto (muons only).
Stage 9 !DIFFZ	$\|z_{lep} - z_{vtx}\| < 3$ cm
Stage 10 KIN VETOS	$H_T > 200$ GeV and $M_T^W > 20$ GeV/c^2.
Stage 11 SI GOOD	Requirement of Good Run List with silicon detector requirement (data only).
Stage 12 TAGGABLE	At least one jet taggable by tight SecVtx.
Stage 13 ≥1+BTAG	At least one jet tagged by tight SecVtx.
Stage 14 ≥2+BTAG	At least two jets tagged by tight SecVtx.
Stage 15 ≥1-BTAG	At least two jets negative tagged by tight SecVtx.
Stage 16 ≥1+-BTAG	At least one jet tagged and one jet negative tagged by tight SecVtx.
Stage 17 ≥2-BTAG	At least two jets negative tagged by tight SecVtx.
Stage 18 LTAGGABLE	At least one jet taggable by loose SecVtx.
Stage 19 ≥1+LTAG	At least one jet tagged by loose SecVtx.
Stage 20 ≥2+LTAG	At least two jets tagged by loose SecVtx.
Stage 21 ≥1-LTAG	At least two jets negative tagged by loose SecVtx.
Stage 22 ≥1+-LTAG	At least one jet tagged and one jet negative tagged by loose SecVtx.
Stage 23 ≥2-LTAG	At least two jets negative tagged by loose SecVtx.

Table 4.3: Definition of cuts used in Table 4.2.

4.2.1 Lepton Selection

To select leptons, we require exactly one tight, isolated, triggered lepton in the event.

- For electrons, we require
  - $E_T > 20$ GeV
  - $p_T > 10$ GeV/c
  - $|\eta| < 1.0$
  - $E_{HAD}/E_{EM} < 0.055 + 0.00045 * E$
  - $E/p < 2.0$ if $p_T < 50$ GeV
  - $|z_0| < 60$ cm
  - ≥ 3 COT Axial 5-hit superlayers
  - ≥ 2 COT Stereo 5-hit superlayers
  - $iso < 0.1$
  - $L_{shr} < 0.2$
  - $|\Delta z| < 3$ cm for CES strip cluster Δz
  - $-3.0 < Q\Delta X < 1.5$ cm for CES strip cluster Δx
  - Strip $\chi^2 < 10$
- For muons, we require
  - $p_T > 20$ GeV/c (corrected for curvature corrections due to non-uniform B-field)

- $|\eta| < 1.0$
- $E_{HAD} < 6.0 + max(0, 0.0280(p - 100\ GeV/c)$ GeV
- $E_{EM} < 2.0 + max(0, 0.0115(p - 100\ GeV/c)$ GeV
- $|z_0| < 60$ cm
- ≥ 3 COT Axial 5-hit superlayers
- ≥ 2 COT Stereo 5-hit superlayers
- $iso < 0.1$
- CMUP Muons:
  - $|\Delta x_{CMU}| < 3.0$ cm
  - $|\Delta x_{CMP}| < 5.0$ cm
  - CMUP fiduciality
- CMX Muons:
  - $|\Delta x_{CMX}| < 6.0$ cm
  - COT exit radius > 140 cm
  - CMX fiduciality

Figures 4.3-4.11 show the variables of the lepton selections along with their cut values.

The efficiency for these cuts is determined by examining isolated Z-events with two leptons. One leg is required to pass all the tight cuts, and the other is examined as an unbiased sample of leptons. The lepton ID cuts are then applied, and the efficiency is measured, using both lepton data, and PYTHIA Z Monte Carlo samples.

Systematic effects are of order 1%. See Ref [49, 50] for details and results. Table 4.5 shows a summary of the lepton ID quantities.

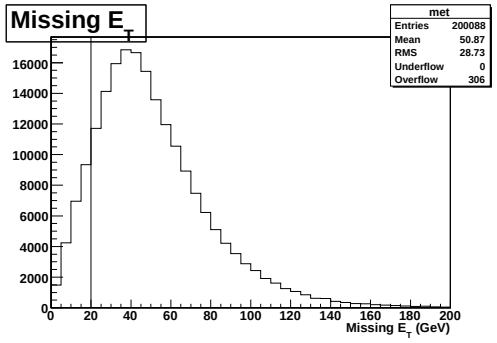

(a) $\not\!\!E_T$, (corrected for muon momentum).

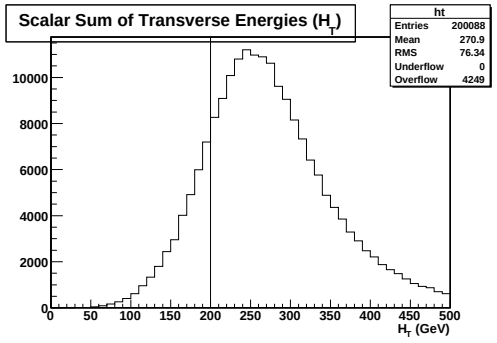

(b) Scalar sum of transverse energies

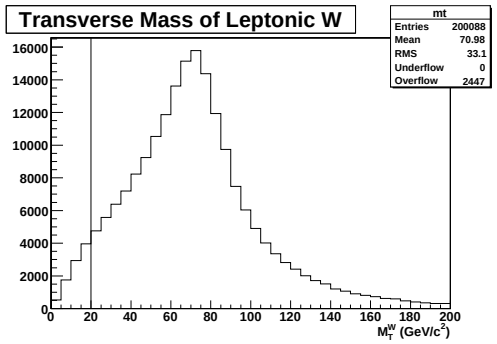

(c) W transverse mass

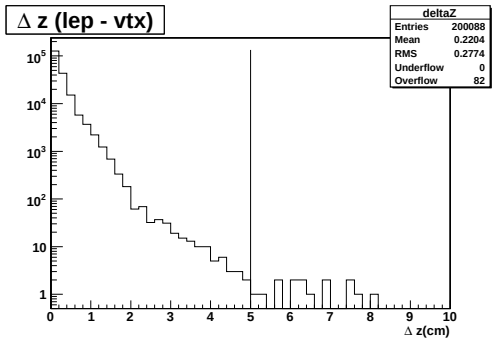

(d) Δz from lepton to primary vertex.

Figure 4.2: Kinematic distributions for lepton + jets events, taken from PYTHIA $t\bar{t}$ Monte Carlo with $m_{top} = 178$ GeV/c^2. This is done before any event selection.

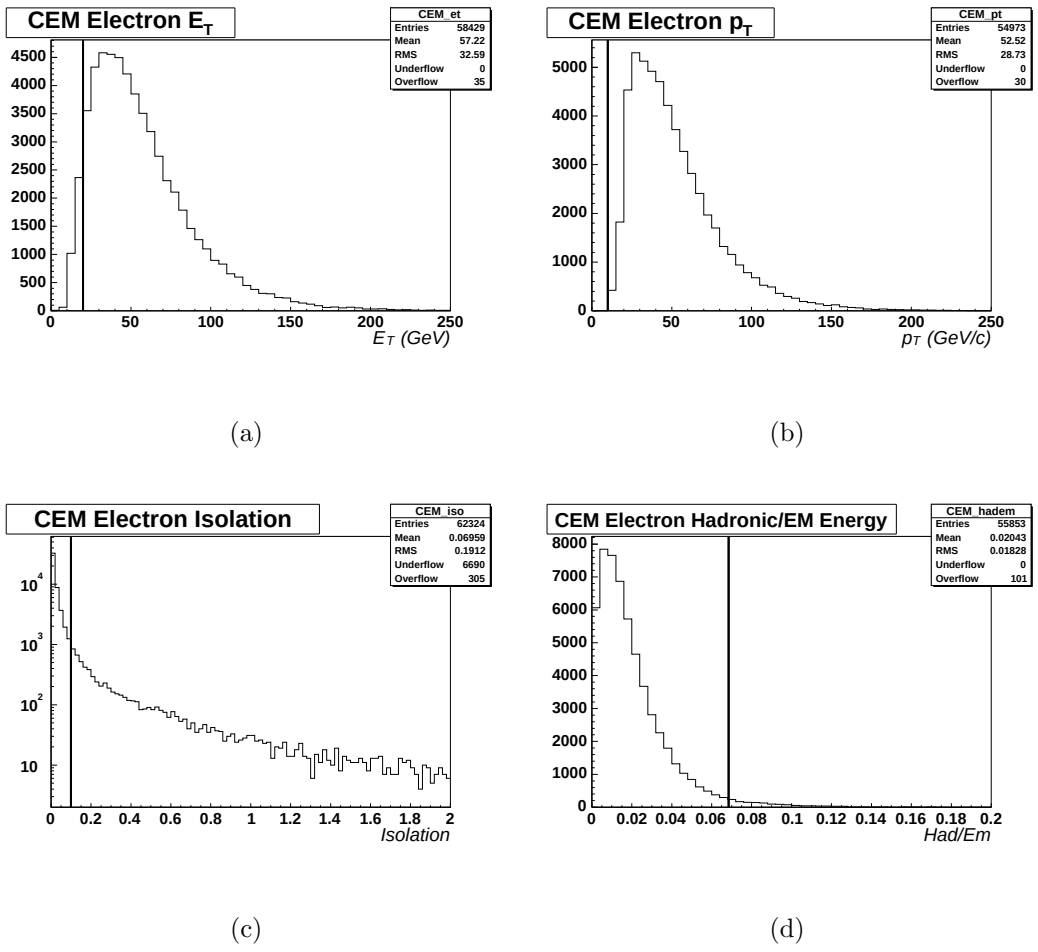

Figure 4.3: $N-1$ plots for lepton selection in lepton + jets events. Here, the plots are made applying all lepton cuts except the one being plotted. Taken from PYTHIA $t\bar{t}$ Monte Carlo with $m_{top} = 178$ GeV/c^2. No other event cuts are applied.

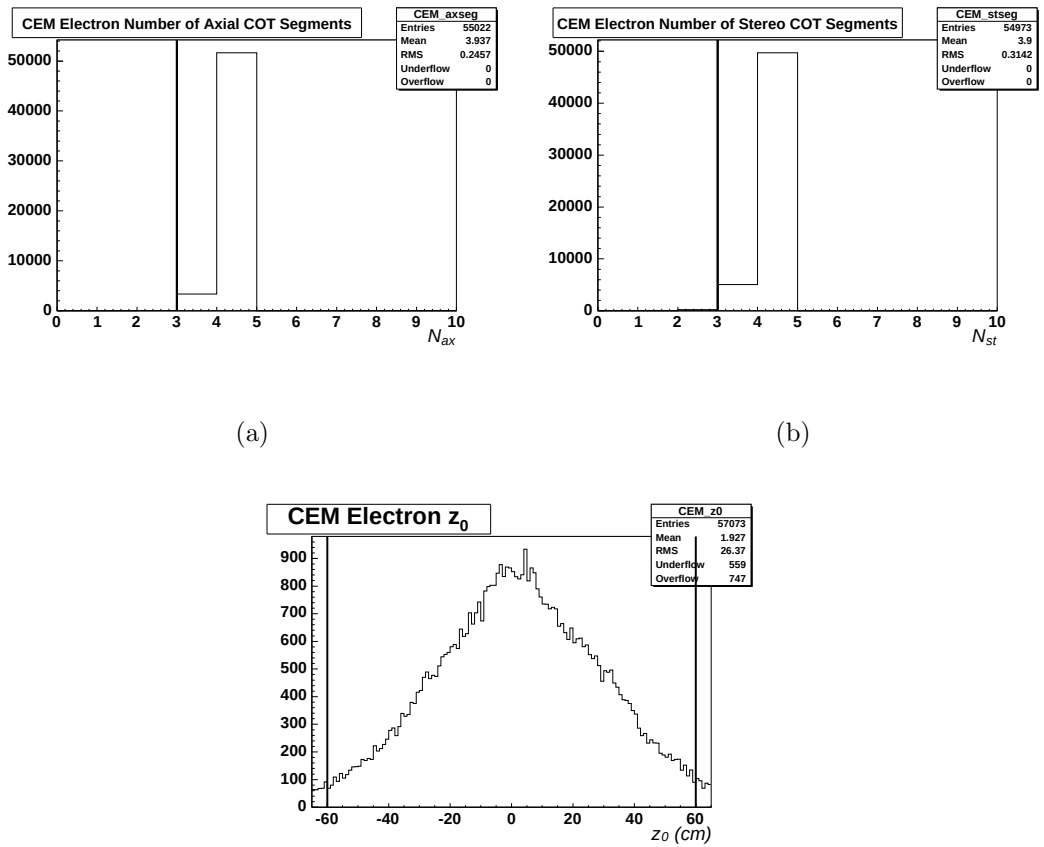

Figure 4.4: $N-1$ plots for lepton selection in lepton + jets events. Here, the plots are made applying all lepton cuts except the one being plotted. Taken from PYTHIA $t\bar{t}$ Monte Carlo with $m_{top} = 178$ GeV/c^2. No other event cuts are applied.

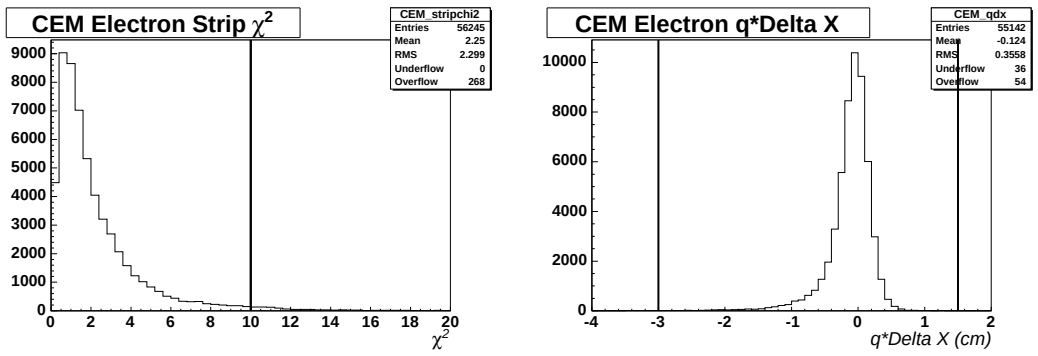

(a) (b)

(c)

Figure 4.5: $N-1$ plots for lepton selection in lepton + jets events. Here, the plots are made applying all lepton cuts except the one being plotted. Taken from PYTHIA $t\bar{t}$ Monte Carlo with $m_{top} = 178$ GeV/c^2. No other event cuts are applied.

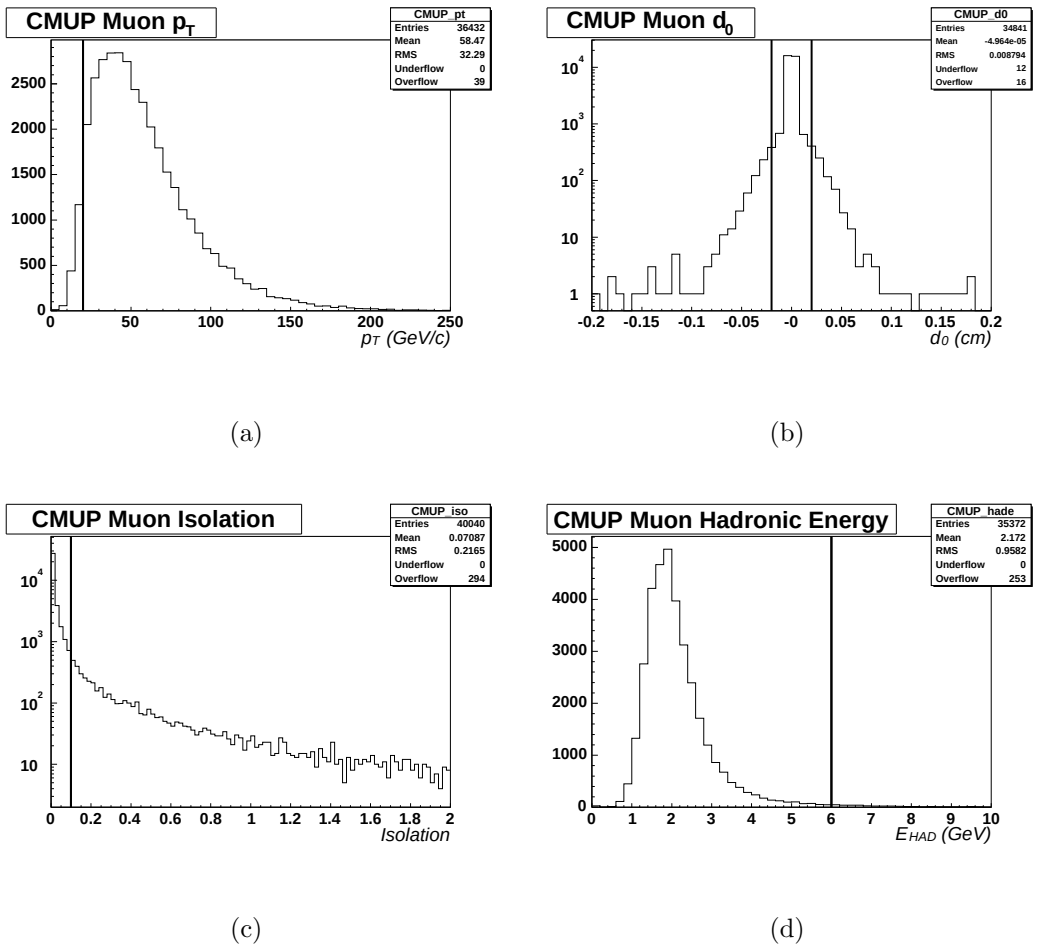

Figure 4.6: $N-1$ plots for lepton selection in lepton + jets events. Here, the plots are made applying all lepton cuts except the one being plotted. Taken from PYTHIA $t\bar{t}$ Monte Carlo with $m_{top} = 178$ GeV/c^2. No other event cuts are applied.

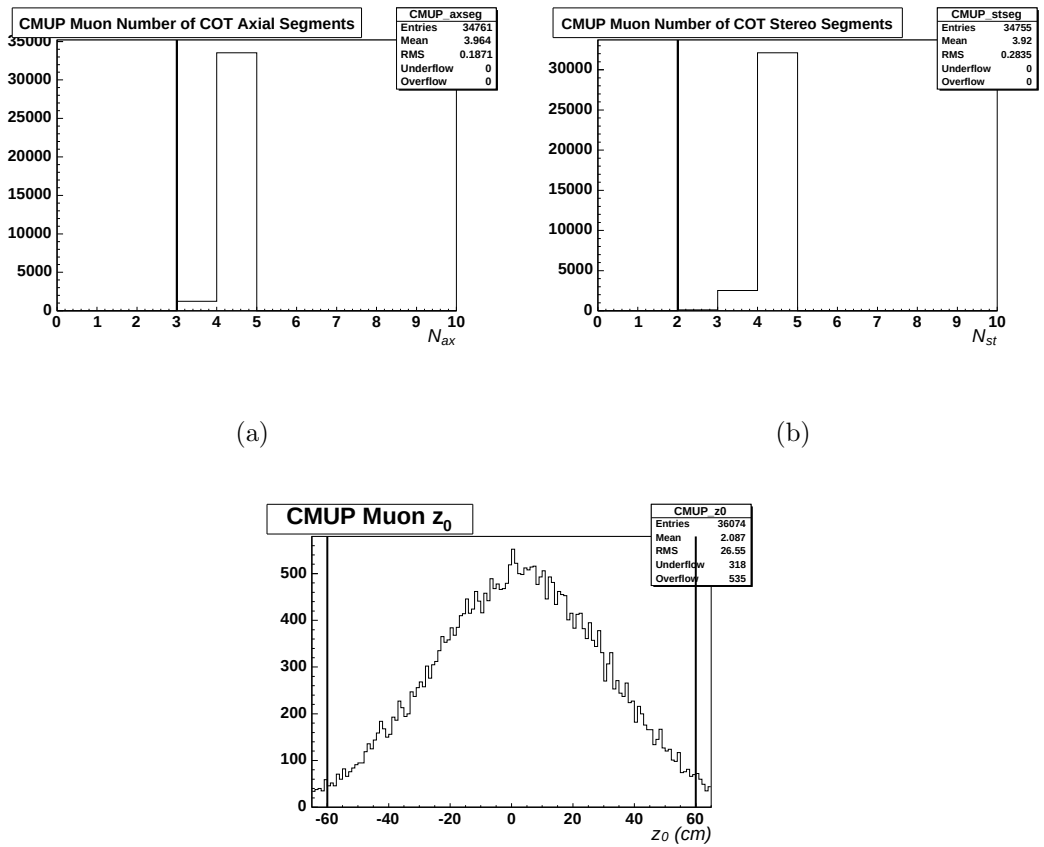

Figure 4.7: $N-1$ plots for lepton selection in lepton + jets events. Here, the plots are made applying all lepton cuts except the one being plotted. Taken from PYTHIA $t\bar{t}$ Monte Carlo with $m_{top} = 178$ GeV/c^2. No other event cuts are applied.

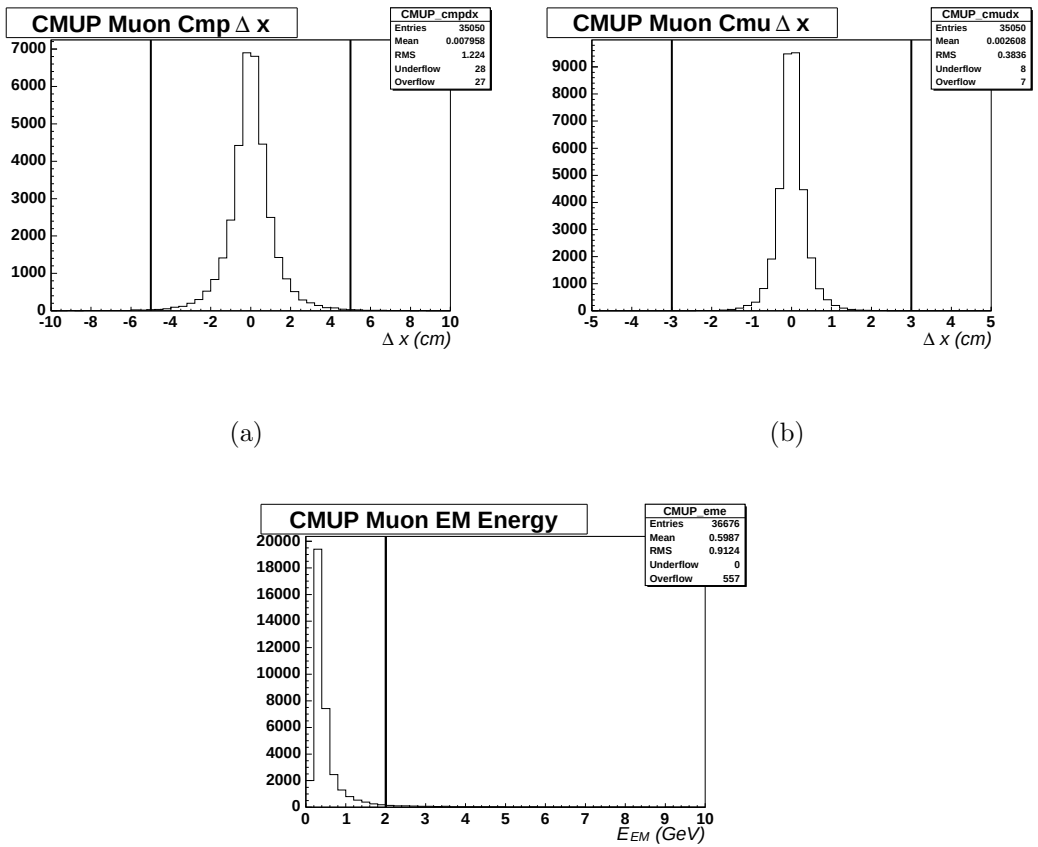

Figure 4.8: $N-1$ plots for lepton selection in lepton + jets events. Here, the plots are made applying all lepton cuts except the one being plotted. Taken from PYTHIA $t\bar{t}$ Monte Carlo with $m_{top} = 178$ GeV/c^2. No other event cuts are applied.

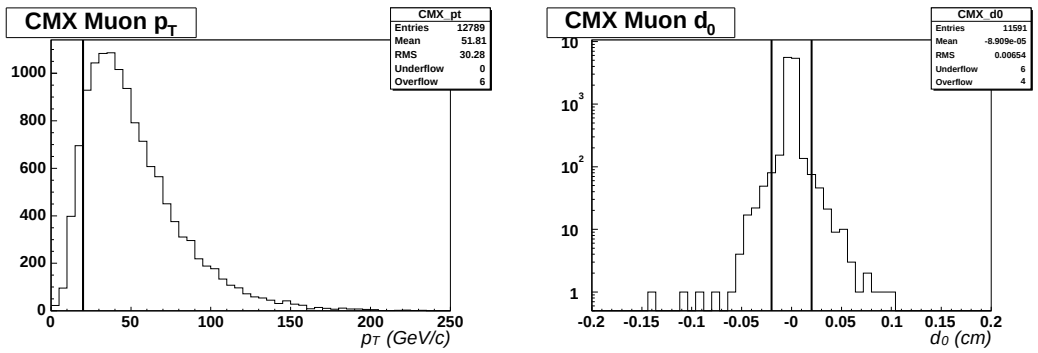

(a) (b)

(c) (d)

Figure 4.9: $N-1$ plots for lepton selection in lepton + jets events. Here, the plots are made applying all lepton cuts except the one being plotted. Taken from PYTHIA $t\bar{t}$ Monte Carlo with $m_{top} = 178$ GeV/c^2. No other event cuts are applied.

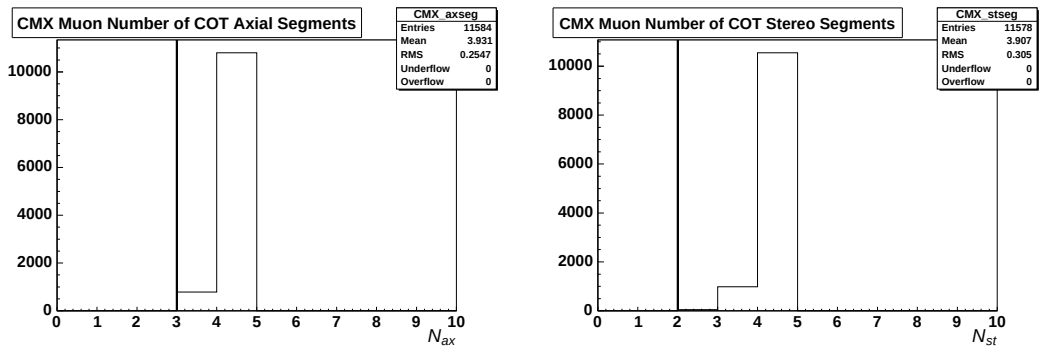

(a) (b)

(c)

Figure 4.10: $N-1$ plots for lepton selection in lepton + jets events. Here, the plots are made applying all lepton cuts except the one being plotted. Taken from PYTHIA $t\bar{t}$ Monte Carlo with $m_{top} = 178$ GeV/c^2. No other event cuts are applied.

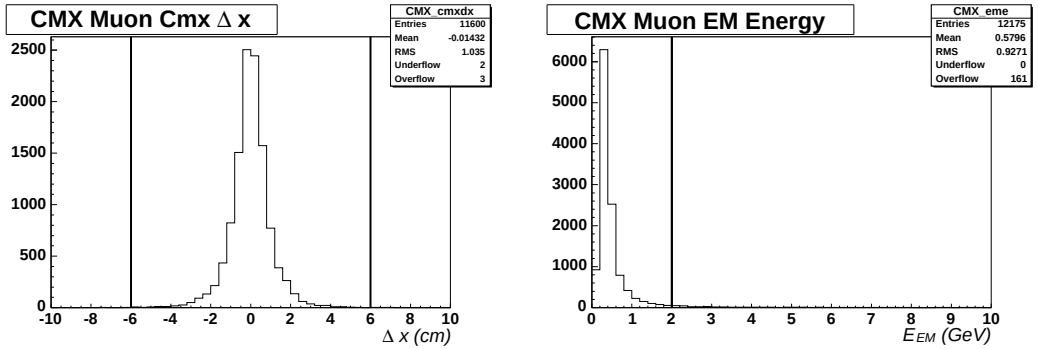

(a) (b)

Figure 4.11: $N-1$ plots for lepton selection in lepton + jets events. Here, the plots are made applying all lepton cuts except the one being plotted. Taken from PYTHIA $t\bar{t}$ Monte Carlo with $m_{top} = 178$ GeV/c^2. No other event cuts are applied.

4.3 Signal Estimate

We measure the top cross section using the formula

$$\sigma_{t\bar{t}} = \frac{N_{obs} - N_{bkg}}{BR(W \rightarrow \ell\nu)\,(\epsilon_{tag} * \Phi_e)\left(\epsilon_{pretag} \int \mathcal{L}dt\right)} \tag{4.4}$$

where N_{obs} is the number of observed tagged events in the $W+ \geq 3$ jet sample, N_{bkg} is the number of expected background events, ϵ_{tag} is the event tag rate in $t\bar{t}$ Monte Carlo, Φ_e is an "effective event scale factor" described in Section 4.3.2, ϵ_{pretag} is the pretag efficiency for $t\bar{t}$, and $\int \mathcal{L}dt$ is the integrated luminosity.

4.3.1 Pretag Acceptance $\times$ Efficiency

The pretag efficiency was estimated using a PYTHIA $t\bar{t}$ sample with $m_{top} = 178\ GeV/c^2$ (`ttopel`). Table 4.4 shows the breakdown of event counts after successive cuts in the $t\bar{t}$ Monte Carlo sample. Table 4.6 shows the acceptance times efficiencies for each lepton trigger type.

The acceptance times efficiency is determined by taking the number of events that pass the event selection (including the ≥ 3 jets cut) and dividing by the total number of events with $|z_0| < 60$ cm. This is to take into account a 5% discrepancy between the data and Monte Carlo in the number of events outside 60 cm. The efficiency of this cut (externally determined) is then applied with the appropriate systematic, shown in Table 4.5.

The lepton ID scale factors and trigger efficiencies, along with common systematics not evaluated in this note, are given in Table 4.5. The pretag acceptance times efficiency is given in Table 4.6.

We obtain a luminosity weighted pretag efficiency of

$$\epsilon_{pretag}^{t\bar{t}} \int \mathcal{L}dt = 23.6 \pm 2.1\ pb \tag{4.5}$$

4.3.2 $t\bar{t}$ Event Tagging Efficiency

We calculate the event tagging efficiency for our backgrounds by counting the number of events with ≥ 1 or ≥ 2 tags in the Monte Carlo, and then dividing by the number of pretag events.

$$\epsilon_{MC}^{tag} = \frac{N_{MC}^{tag}}{N_{MC}^{pre}} \tag{4.6}$$

In order to take the scale factor into account, we take the ratio of the event tag rates derived from the binomial expression for tagging N jets of flavor b, c, or p (for primary jets, i.e. uds quarks and gluons), given inputs from the b and c quark tagging efficiencies, and the mistag rate. The full expression for the combinatoric combination of tagging exactly N_{jet} jets N_{tag} times is

$$\begin{aligned}
\epsilon_{ev} = \sum_{n_b=0}^{N_{jet}} \sum_{n_c=0}^{N_{jet}} \sum_{n_p=0}^{N_{jet}} \{F_{n_b n_c n_p} \times \sum_{n_b^+=0}^{n_b} \sum_{n_c^+=0}^{n_c} \sum_{n_c^+=0}^{n_c} & \left[\binom{n_b}{n_b^+} \quad (\epsilon_b SF_b)^{n_b^+} (1-\epsilon_b SF_b)^{(n_b - n_b^+)} \right. \\
& \times \quad \binom{n_c}{n_c^+} \quad (\epsilon_c SF_c)^{n_c^+} (1-\epsilon_c SF_c)^{(n_c - n_c^+)} \\
& \times \quad \left. \binom{n_p}{n_p^+} \quad (M_p SF_p)^{n_p^+} (1-M_p SF_p)^{(n_p - n_p^+)} \right] \quad (4.7)
\end{aligned}$$

$$n_b + n_c + n_p = N_{jet} \tag{4.8}$$

$$n_b^+ + n_c^+ + n_p^+ = N_{tag} \tag{4.9}$$

$$\binom{r}{k} = \frac{r!}{(r-k)!k!} \tag{4.10}$$

where F_{bcp} is the fraction of events with b b-jet, c c-jets, and p p-jets, ϵ_b and ϵ_c are the Monte Carlo efficiencies for jets matched to b- and c-hadrons using Monte Carlo truth, M_p is the per-jet prediction of the mistag matrix applied to light quark jets in $t\bar{t}$ Monte Carlo, SF_b and SF_c are the scale factors for b and c-jets, and SF_p is the

ratio of predicted tag rates in data and Monte Carlo in JET50 events, multiplied by the light flavor asymmetry (1.37 ± 0.23) as described in Ref [41].

We then calculate the ratio of the event tagging efficiency with and without the b-tagging scale factors, which we denote by Φ_E:

$$\Phi_E = \frac{\epsilon_{ev}(\epsilon_b SF_b, \epsilon_c SF_c, M_p SF_p)}{\epsilon_{ev}(\epsilon_b, \epsilon_c, \epsilon_p)} \tag{4.11}$$

Subsequently, we multiply the event tag rate by Φ_E to obtain the event tag rate including the scale factor.

$$\epsilon_{DATA} = \epsilon_{MC} \times \Phi_E \tag{4.12}$$

Henceforth, all per-jet and event tagging efficiencies will be denoted in terms of ϵ (for the MC efficiency) multiplied by SF or Φ_E.

The heavy quark tagging efficiencies in $t\bar{t}$ are flat as a function of the number of jets. However, due to the different $\sum E_T$ in the different jet bins, the mistag matrix will predict a non-constant rate for the per-jet mistag rate in each jet bin, so the inputs to Equation 4.7 reflect that accordingly. The inputs we use are shown in Table 4.7. The calculation details are shown in Table 4.8, and the results are shown in Table 4.10.

Channel	0-jet	1-jet	2-jet	3-jet	4-jet	≥5-jet	Total
			CEM				
Stage 0 INITIAL	888	16286	90293	218306	327888	496382	1150043
Stage 1 OBSV	868	15789	87418	210316	315204	477050	1106645
Stage 2 TRIGGER	868	15789	87418	210316	315204	477050	1106645
Stage 3 ≥1TLEP	267	4694	20939	32232	29308	12254	99694
Stage 4 MET	248	4316	19126	29009	26134	10254	89087
Stage 5 ISO	248	4251	18401	26508	22516	6896	78820
Stage 6 !DILEP	138	2515	13107	24939	22117	6799	69615
Stage 7 !Z	127	2294	12198	23706	21479	6605	66409
Stage 8 !CONV	127	2294	12198	23706	21479	6605	66409
Stage 9 !DIFFZ	127	2294	12198	23706	21476	6604	66405
Stage 10 KIN VETOS	0	2249	11882	19809	20162	6382	60484
Stage 11 SI GOOD	0	2249	11882	19809	20162	6382	60484
Stage 12 TAGGABLE	0	1815	10950	18854	19402	6181	57202
Stage 13 ≥1+BTAG	0	824	6453	12383	13371	4267	37298
Stage 14 ≥2+BTAG	0	0	1309	3309	4158	1392	10168
Stage 15 ≥1-BTAG	0	18	209	436	427	198	1288
Stage 16 ≥1+-BTAG	0	0	67	198	225	123	613
Stage 17 ≥2-BTAG	0	0	1	4	4	4	13
Stage 18 LTAGGABLE	0	1855	11084	18978	19524	6218	57659
Stage 19 ≥1+LTAG	0	961	7418	13981	15040	4800	42200
Stage 20 ≥2+LTAG	0	0	1869	4664	5887	1976	14396
Stage 21 ≥1-LTAG	0	40	427	976	1044	463	2950
Stage 22 ≥1+-LTAG	0	0	161	541	664	321	1687
Stage 23 ≥2-LTAG	0	0	5	22	26	21	74
			CMUP				
Stage 0 INITIAL	888	16286	90293	218306	327888	496382	1150043
Stage 1 OBSV	868	15789	87418	210316	315204	477050	1106645
Stage 2 TRIGGER	868	15789	87418	210316	315204	477050	1106645
Stage 3 ≥1TLEP	188	3160	14047	21180	18780	6781	64136
Stage 4 MET	172	2922	12762	18958	16494	5946	57254
Stage 5 ISO	166	2770	11811	16780	14015	4247	49789
Stage 6 !DILEP	88	1596	8243	15789	13746	4195	43657
Stage 7 !Z	82	1485	7810	15332	13516	4132	42357
Stage 8 !COSMIC	82	1485	7810	15332	13516	4132	42357
Stage 9 !DIFFZ	82	1485	7809	15331	13510	4130	42347
Stage 10 KIN VETOS	0	1439	7493	12680	12514	3928	38054
Stage 11 SI GOOD	0	1439	7493	12680	12514	3928	38054
Stage 12 TAGGABLE	0	1147	6919	12044	12070	3798	35978
Stage 13 ≥1+BTAG	0	513	4082	7822	8315	2621	23353
Stage 14 ≥2+BTAG	0	0	852	2011	2626	871	6360
Stage 15 ≥1-BTAG	0	10	121	309	299	109	848
Stage 16 ≥1+-BTAG	0	0	36	135	161	69	401
Stage 17 ≥2-BTAG	0	0	0	1	2	2	5
Stage 18 LTAGGABLE	0	1180	7001	12136	12139	3820	36276
Stage 19 ≥1+LTAG	0	608	4691	8857	9312	2973	26441
Stage 20 ≥2+LTAG	0	0	1208	2906	3717	1226	9057
Stage 21 ≥1-LTAG	0	22	250	636	683	266	1857
Stage 22 ≥1+-LTAG	0	0	88	316	423	175	1002
Stage 23 ≥2-LTAG	0	0	2	7	18	6	33
			CMX				
Stage 0 INITIAL	888	16286	90293	218306	327888	496382	1150043
Stage 1 OBSV	868	15789	87418	210316	315204	477050	1106645
Stage 2 TRIGGER	868	15789	87418	210316	315204	477050	1106645
Stage 3 ≥1TLEP	70	1079	4807	7184	6278	2346	21764
Stage 4 MET	64	981	4376	6412	5519	2046	19398
Stage 5 ISO	61	921	3974	5638	4623	1444	16661
Stage 6 !DILEP	31	493	2718	5264	4543	1426	14475
Stage 7 !Z	28	460	2590	5099	4463	1408	14048
Stage 8 !COSMIC	28	460	2590	5099	4463	1408	14048
Stage 9 !DIFFZ	28	460	2588	5098	4463	1407	14044
Stage 10 KIN VETOS	0	456	2579	4275	4273	1389	12972
Stage 11 SI GOOD	0	456	2579	4275	4273	1389	12972
Stage 12 TAGGABLE	0	374	2415	4113	4136	1342	12380
Stage 13 ≥1+BTAG	0	163	1432	2703	2925	931	8154
Stage 14 ≥2+BTAG	0	0	292	690	948	307	2237
Stage 15 ≥1-BTAG	0	8	38	107	93	39	285
Stage 16 ≥1+-BTAG	0	0	10	43	58	24	135
Stage 17 ≥2-BTAG	0	0	0	0	2	1	3
Stage 18 LTAGGABLE	0	387	2442	4145	4153	1348	12475
Stage 19 ≥1+LTAG	0	192	1647	3055	3255	1059	9208
Stage 20 ≥2+LTAG	0	0	408	1004	1336	427	3175
Stage 21 ≥1-LTAG	0	10	90	199	244	100	643
Stage 22 ≥1+-LTAG	0	0	32	91	145	71	339
Stage 23 ≥2-LTAG	0	0	0	2	5	3	10

Table 4.4: Event counts at each successive stage for `ttopel` top Monte Carlo, with $m_{top} = 178\ GeV/c^2$. Note that the conversion veto is already applied in the tight lepton definition.

	Lepton ID and Trigger Quantities		
	CEM	CMUP	CMX
Lepton ID Eff SF	0.996 ± 0.005	0.874 ± 0.009	0.989 ± 0.006
Trigger Eff	0.962 ± 0.006	0.908 ± 0.005	0.965 ± 0.004
Total	0.959 ± 0.015	0.794 ± 0.015	0.954 ± 0.016
Luminosity (pb^{-1})	318.5 ± 19.1	318.5 ± 19.1	305.2 ± 18.3
z_0 Eff		0.951 ± 0.003	
Lepton Isolation Modeling		1.000 ± 0.050	

Table 4.5: Lepton ID scale factors and trigger efficiencies, plus z_0 efficiency and lepton isolation modeling systematic (to account for the extrapolation from isolated Z-samples to samples with jets). Taken from Ref [49, 50, 51].

$t\bar{t}$ Pretag Efficiency in ≥ 3 jets (ϵ_{pretag}) (%)					
Jet Multiplicity	1 jet	2 jets	3 jets	4 jets	≥ 5 jets
CEM MC estimate	0.21 ± 0.00	1.10 ± 0.01	2.14 ± 0.01	1.94 ± 0.01	0.60 ± 0.01
≥ 3 jet Average				4.68 ± 0.02	
CEM Data estimate				4.27 ± 0.29	
CMUP MC estimate	0.13 ± 0.00	0.71 ± 0.01	1.39 ± 0.01	1.22 ± 0.01	0.37 0.01
≥ 3 jet Average				2.98 ± 0.02	
CMUP Data estimate				2.25 ± 0.16	
CMX MC estimate	0.04 ± 0.00	0.24 ± 0.00	0.47 ± 0.01	0.41 ± 0.01	0.13 ± 0.00
≥ 3 jet Average				1.00 ± 0.01	
CMX Data estimate				0.91 ± 0.06	
$t\bar{t}$ Luminosity Weighted Denominator in ≥ 3 jets ($\epsilon_{pretag} \int \mathcal{L}dt$) (%)					
Total			23.6 ± 2.1 pb^{-1}		

Table 4.6: $t\bar{t}$ pretag efficiencies for the different trigger types, *before optimization*. The first line in each subsection is the Monte Carlo estimate of the efficiency. The second line gives the average in ≥ 3 jets. The third line gives the average in ≥ 3 jets, multiplied by the data-to-Monte Carlo scale factor to give the estimate of the efficiency in data. Numbers are given in percentage. Also shown is the luminosity weighted pretag denominator.

Quantity	1-jet	2-jet	3-jet	4-jet	≥ 5-jet	SF
ε_b	0.450	0.450	0.450	0.450	0.450	$SF = 0.909 \pm 0.060$
ε_c	0.098	0.098	0.098	0.098	0.098	$SF = 0.909 \pm 0.120$
M_p	0.004	0.005	0.006	0.006	0.007	$K\alpha\beta = 1.18 \pm 0.41$

Table 4.7: The inputs to the event efficiency calculation for the *unoptimized* analysis. The errors are negligible.

Njet = 1						
N_b	N_c	N_p	F_{bcp}	1-tag	2-tag	3-tag
0	0	1	0.1512	0.0003 ± 0.0001		
0	1	0	0.0322	0.0031 ± 0.0000		
1	0	0	0.8166	0.3648 ± 0.0008		
		Total		0.3683 ± 0.0010		
Njet = 2						
N_b	N_c	N_p	F_{bcp}	1-tag	2-tag	3-tag
0	0	2	0.0320	0.0002 ± 0.0000	0.0000 ± 0.0000	
0	1	1	0.0213	0.0021 ± 0.0000	0.0000 ± 0.0000	
0	2	0	0.0008	0.0001 ± 0.0000	0.0000 ± 0.0000	
1	0	1	0.3608	0.1613 ± 0.0004	0.0004 ± 0.0000	
1	1	0	0.0910	0.0416 ± 0.0002	0.0040 ± 0.0001	
2	0	0	0.4941	0.2442 ± 0.0001	0.0986 ± 0.0005	
		Total		0.4495 ± 0.0006	0.1030 ± 0.0005	
Njet = 3						
N_b	N_c	N_p	F_{bcp}	1-tag	2-tag	3-tag
0	0	3	0.0081	0.0001 ± 0.0000	0.0000 ± 0.0000	0.0000 ± 0.0000
0	1	2	0.0077	0.0008 ± 0.0000	0.0000 ± 0.0000	0.0000 ± 0.0000
0	2	1	0.0006	0.0001 ± 0.0000	0.0000 ± 0.0000	0.0000 ± 0.0000
0	3	0	0.0000	0.0000 ± 0.0000	0.0000 ± 0.0000	0.0000 ± 0.0000
1	0	2	0.1896	0.0848 ± 0.0002	0.0005 ± 0.0000	0.0000 ± 0.0000
1	1	1	0.1350	0.0617 ± 0.0003	0.0060 ± 0.0001	0.0000 ± 0.0000
1	2	0	0.0022	0.0010 ± 0.0000	0.0002 ± 0.0000	0.0000 ± 0.0000
2	0	1	0.5181	0.2558 ± 0.0001	0.1038 ± 0.0005	0.0003 ± 0.0000
2	1	0	0.1369	0.0652 ± 0.0002	0.0312 ± 0.0002	0.0027 ± 0.0000
3	0	0	0.0019	0.0008 ± 0.0000	0.0006 ± 0.0000	0.0002 ± 0.0000
		Total		0.4702 ± 0.0005	0.1424 ± 0.0007	0.0032 ± 0.0000
Njet = 4						
N_b	N_c	N_p	F_{bcp}	1-tag	2-tag	3-tag
0	0	4	0.0024	0.0000 ± 0.0000	0.0000 ± 0.0000	0.0000 ± 0.0000
0	1	3	0.0025	0.0003 ± 0.0000	0.0000 ± 0.0000	0.0000 ± 0.0000
0	2	2	0.0002	0.0000 ± 0.0000	0.0000 ± 0.0000	0.0000 ± 0.0000
0	3	1	0.0000	0.0000 ± 0.0000	0.0000 ± 0.0000	0.0000 ± 0.0000
0	4	0	0.0000	0.0000 ± 0.0000	0.0000 ± 0.0000	0.0000 ± 0.0000
1	0	3	0.0719	0.0322 ± 0.0001	0.0003 ± 0.0000	0.0000 ± 0.0000
1	1	2	0.0644	0.0295 ± 0.0001	0.0030 ± 0.0000	0.0000 ± 0.0000
1	2	1	0.0046	0.0021 ± 0.0000	0.0004 ± 0.0000	0.0000 ± 0.0000
1	3	0	0.0002	0.0001 ± 0.0000	0.0000 ± 0.0000	0.0000 ± 0.0000
2	0	2	0.4839	0.2386 ± 0.0001	0.0974 ± 0.0005	0.0006 ± 0.0000
2	1	1	0.3608	0.1715 ± 0.0004	0.0826 ± 0.0006	0.0072 ± 0.0001
2	2	0	0.0036	0.0016 ± 0.0000	0.0009 ± 0.0000	0.0001 ± 0.0000
3	0	1	0.0039	0.0016 ± 0.0000	0.0013 ± 0.0000	0.0003 ± 0.0000
3	1	0	0.0012	0.0005 ± 0.0000	0.0004 ± 0.0000	0.0001 ± 0.0000
4	0	0	0.0002	0.0001 ± 0.0000	0.0001 ± 0.0000	0.0000 ± 0.0000
		Total		0.4782 ± 0.0003	0.1864 ± 0.0008	0.0085 ± 0.0001
Njet = 5						
		Total		0.3833 ± 0.0003	0.1584 ± 0.0007	0.0097 ± 0.0001

Table 4.8: Calculation of event tagging efficiency for $t\bar{t}$ Monte Carlo for the *unoptimized* analysis.

$t\bar{t}$ Event Tagging Efficiency in MC (%)					
	1 jet	2 jets	3 jets	4 jets	$\geq$ 5 jets
$\epsilon_{\geq 1}$	36.81 ± 0.07	54.88 ± 0.31	61.34 ± 0.22	66.41 ± 0.22	67.00 ± 0.40
$\geq$ 3 jets avg				64.15 ± 0.15	
$\epsilon_{\geq 2}$	-	11.28 ± 0.20	15.55 ± 0.16	20.75 ± 0.19	21.83 ± 0.35
$\geq$ 3 jets avg				18.49 ± 0.12	

Table 4.9: Expected event tagging efficiencies in *Monte Carlo*. The average in ≥ 3 jets is also supplied. Calculated from Equation 4.7 with inputs from Table 4.7. See Table 4.8 for details on the calculation. Note: Scale factor *has not* been applied. This is for the *unoptimized* selection.

$t\bar{t}$ Event Tagging Efficiency in Data (%)					
	1 jet	2 jets	3 jets	4 jets	$\geq$ 5 jets
$\epsilon_{\geq 1} * \Phi_e$ (%)	33.51 ± 2.34	50.85 ± 2.88	57.19 ± 3.09	62.27 ± 3.17	63.07 ± 3.22
$\geq$ 3 jets avg				60.06 ± 3.13	
$\epsilon_{\geq 2} * \Phi_e$(%)	0.00 ± 0.00	9.38 ± 1.30	13.12 ± 1.80	17.66 ± 2.38	18.85 ± 2.52
$\geq$ 3 jets avg				15.73 ± 2.13	
$t\bar{t}$ Event Φ_E Factors (%)					
$\Phi_e^{\geq 1}$(%)	91.04 ± 6.13	92.65 ± 5.23	93.23 ± 5.03	93.76 ± 4.77	94.13 ± 4.78
$\geq$ 3 jets avg				93.62 ± 4.87	
$\Phi_e^{\geq 2}$(%)	0.00 ± 0.00	83.20 ± 11.40	84.35 ± 11.56	85.13 ± 11.44	86.36 ± 11.45
$\geq$ 3 jets avg				85.10 ± 11.48	

Table 4.10: Event tagging efficiencies in *data*. Also supplied are the ≥ 3 jets average. Calculated from Equation 4.7 with inputs from Table 4.7. See Table 4.8 for details on the calculation. Note: Scale factor *has* been applied. The values for Φ_E are also shown. This is for the *unoptimized* selection.

4.4 Backgrounds to $t\bar{t} \to \ell\nu b\bar{b}jjX$

4.4.1 Method 2 Backgrounds

There are four categories of backgrounds for the lepton plus jets channel.

- **Electroweak and Single Top**. These backgrounds are taken from Monte Carlo, scaled to theoretical cross sections.

- **Non-W Backgrounds**. This background is estimated from a study of $\not\!\!E_T$ vs lepton isolation in the data sample.

- **W+Heavy Flavor**. These backgrounds are estimated using the efficiency derived from Monte Carlo and the scale factor outlined in [32], plus the heavy flavor fractions in W plus jets events measured in Ref [40] scaled to the pretag data.

- **W+Light Flavor Mistags**. This background is estimated using the negative tag matrix outlined in Ref [42] and Section 3.5.3 applied to the pretag sample (corrected for other backgrounds), with the appropriate scaling for the asymmetry of the light flavor L_{2D} distribution.

Electroweak and Single Top

The electroweak and single top backgrounds are determined from the theoretical cross section and luminosity with the equation:

$$N_{exp}^{p\bar{p}\to X} = \sigma^{p\bar{p}\to X}\epsilon_{pretag}\epsilon_{tag}\int \mathcal{L}dt \tag{4.13}$$

where $\sigma^{p\bar{p}\to X}$ is the theoretical cross section, $\int \mathcal{L}dt$ is the integrated luminosity, ϵ_{pretag} is the pretag efficiency for the process, and ϵ_{tag} is the event tagging efficiency. The event tagging efficiency is determined in the same way as the $t\bar{t}$ expectation, using

$$\epsilon_{tag} = \epsilon_{tag}^{MC} \times \Phi_E \tag{4.14}$$

where ϵ_{tag}^{MC} is the event tag rate in Monte Carlo, and Φ_E is the "effective event scale factor" analogous to Equation 4.11.

The theoretical cross sections along with their uncertainties for the backgrounds considered are shown in Table 4.11, along with the theoretical prediction for the top quark.

Theoretical Cross Sections	
WW	13.25 ± 0.25 pb
WZ	3.96 ± 0.06 pb
ZZ	1.58 ± 0.02 pb
Single Top, s-channel	0.88 ± 0.05 pb
Single Top, t-channel	1.98 ± 0.08 pb
$t\bar{t}$	6.1 ± 0.7 pb
$Z \rightarrow \tau\tau$	13.0 ± 1.5 pb

Table 4.11: Theoretical cross sections and uncertainties for the electroweak and single top backgrounds, along with the theoretical cross section for $t\bar{t}$.

Non-W Backgrounds

The non-W backgrounds are estimated using the $\not\!\!E_T$ versus isolation method, where non-isolated leptons are used to estimate the background composition of isolated leptons. In order to calculate the scaling that should be used for the non-isolated leptons, low-$\not\!\!E_T$ regions of isolated and non-isolated leptons are used as a scaling. The regions are:

- Region A: isolation > 0.2 and $\not\!\!E_T < 15$ GeV
- Region B: isolation < 0.1 and $\not\!\!E_T < 15$ GeV
- Region C: isolation > 0.2 and $\not\!\!E_T > 20$ GeV
- Region D: isolation < 0.1 and $\not\!\!E_T > 20$ GeV (signal region)

The number of events in each region is given in Figure 4.12. We use the following formulas for the estimation of the number of Non-W events in Region D (the signal region).

$$F_{Non-W} = \frac{N_B^{pre}}{N_A^{pre}} \frac{N_C^{pre}}{N_D^{pre}} \quad (4.15)$$

$$N_{Non-W}^{pretags} = F_{Non-W} N_{pretags} \quad (4.16)$$

$$N_{\bar{N}on-W}^{\geq 1} : tag = \frac{N_B^+}{N_A^+} N_C^+ \quad (4.17)$$

$$N_{\bar{N}on-W}^{\geq 1} : pretag = N_{pretags} F_{Non-W} \frac{N_B^+}{N_B^{pre}} \quad (4.18)$$

$$N_{\bar{N}on-W}^{\geq 2} = N_{pretags} F_{Non-W} \frac{N_B^{++}}{N_B^{pre}} \quad (4.19)$$

where $N_{(A,B,C,D)}^{pre}$ is the number of pretagged events in regions (A,B,C,D), F_{Non-W} is the fraction of events in the pretag sample that we expect to come from non-W

backgrounds, $N^{+}_{(A,B,C)}$ is the number of single-tagged events in regions (A,B,C), and $N^{++}_{(A,B,C)}$ is the number of double-tagged events in regions (A,B,C).

For the ≥ 1 tag estimates, we take a weighted average of $N_{Non-W} : A$ (the "tag method") and $N_{Non-W} : B$ (the "pretag method"). We take F_{Non-W}, $\frac{N^{+}_{B}}{N^{+}_{A}}$, and $\frac{N^{++}_{B}}{N^{++}_{A}}$ to be the same in ≥ 3 jets to conserve statistics. We also combine the CMUP and CMX muons into one estimate for F_{Non-W}, $\frac{N^{+}_{B}}{N^{+}_{A}}$, and $\frac{N^{+}_{B}}{N^{+}_{A}}$. For the double tagged estimate, we use only the "pretag method" since the "tag method" suffers from very low statistics.

We remove $t\bar{t}$ from the various $\not\!\!E_T$ versus isolation regions, as shown in Table C.32. We use the theoretical prediction for the number of events in each region, and then include the cross section in our "iteration" procedure to calculate the final result.

Because of the very small statistics in the various regions for the Non-W double tags, we compute a Feldman-Cousins interval [43] for the number of Non-W events. That is, we compute

$$N^{Non-W}_{++} = N^{obs}_{++} - N^{t\bar{t}}_{++} \tag{4.20}$$

In this case, $t\bar{t}$ is the "background", and we wish to compute N^{Non-W}_{++}. We take the 68% C.L. interval for the Feldman-Cousins construction, and then take

$$N^{Non-W}_{++} = \left(\frac{N_{up} + N_{lo}}{2}\right) \pm \left(\frac{N_{up} - N_{lo}}{2}\right) \tag{4.21}$$

where N_{up} is the upper 68% limit, and N_{lo} is the lower 68% limit. That is, we take the center of the interval as our central value, plus half the interval as the uncertainty. We then compute the backgrounds using Equations 4.15, substituting N^{Non-W}_{++} for N_{++}.

Figure 4.13 shows the ratio of events in Regions B to A for single and double tags, for both electrons and muons. This ratio is constant for ≥ 3 jets, so we combine the ≥ 3 jet bins for one estimate of this quantity. Figure 4.14 shows the event tag rates versus $\not\!\!E_T$ for single and double tags, for the regions with $iso > 0.2$ and $iso < 0.1$. It is clear that although the tag rates versus $\not\!\!E_T$ are not constant for the $iso > 0.2$ regions because of biases from heavy flavor, the tag rates versus $\not\!\!E_T$ are constant for the $iso < 0.1$ region. Thus, we feel the tag rate in Region B (low $\not\!\!E_T$, $iso < 0.1$) is indicative of the tag rates in Region D for Non-W events.

The results of the Non-W background calculation are shown in Table 4.12. The derivation is shown in Table C.33.

Non-W					
	1 jet	2 jets	3 jets	4 jets	≥ 5 jets
Electrons					
F_{Non-W} (%)	10.08 ± 2.53	12.89 ± 3.27	12.43 ± 3.37		
N_+^B/N_+^A (%)	34.20 ± 1.23	26.08 ± 2.15	27.73 ± 4.50		
$N_+^{tagmethod}$	47.45 ± 16.27	22.31 ± 8.01	6.23 ± 2.78	2.07 ± 1.17	0.61 ± 0.54
R_+^B (%)	1.63 ± 0.33	3.50 ± 0.75	6.90 ± 1.80	10.68 ± 4.76	13.02 ± 15.34
$N_+^{pretagmethod}$	28.91 ± 9.32	12.82 ± 4.26	4.02 ± 1.52	1.53 ± 0.80	0.31 ± 0.37
R_{++}^B (%)	0.00 ± 0.00	0.03 ± 0.02	0.67 ± 0.39	3.28 ± 2.49	5.40 ± 5.81
$N_{++}^{pretagmethod}$	0.00 ± 0.00	0.10 ± 0.09	0.39 ± 0.25	0.47 ± 0.38	0.13 ± 0.14
Pretag	1778.22 ± 446.14	366.89 ± 93.13	58.31 ± 15.80	14.30 ± 3.87	2.36 ± 0.64
$\geq$ 1+ Tag	33.49 ± 8.04	14.91 ± 3.74	4.53 ± 1.33	1.70 ± 0.66	0.41 ± 0.31
$\geq$ 2+ Tag	0.00 ± 0.00	0.10 ± 0.09	0.39 ± 0.25	0.47 ± 0.38	0.13 ± 0.14
Muons					
F_{Non-W} (%)	3.75 ± 0.94	4.44 ± 1.15	6.90 ± 2.01		
N_+^B/N_+^A (%)	9.76 ± 0.68	8.82 ± 1.29	14.17 ± 4.30		
$N_+^{tagmethod}$	8.28 ± 2.93	4.30 ± 1.69	3.21 ± 1.68	1.48 ± 0.86	0.19 ± 0.22
R_+^B (%)	1.91 ± 0.40	5.27 ± 1.30	8.92 ± 3.64	28.26 ± 19.00	42.85 ± 96.97
$N_+^{pretagmethod}$	9.29 ± 3.05	4.55 ± 1.63	1.85 ± 0.93	1.25 ± 0.92	0.50 ± 1.15
R_{++}^B (%)	0.00 ± 0.00	0.22 ± 0.14	2.43 ± 1.63	6.71 ± 5.33	174.42 ± 235.07
$N_{++}^{pretagmethod}$	0.00 ± 0.00	0.19 ± 0.13	0.50 ± 0.37	0.30 ± 0.25	2.04 ± 2.83
Pretag	487.24 ± 122.62	86.33 ± 22.28	20.69 ± 6.04	4.41 ± 1.29	1.17 ± 0.34
$\geq$ 1+ Tag	8.76 ± 2.09	4.43 ± 1.17	2.17 ± 0.82	1.37 ± 0.62	0.20 ± 0.22
$\geq$ 2+ Tag	0.00 ± 0.00	0.19 ± 0.13	0.50 ± 0.37	0.30 ± 0.25	0.20 ± 2.83

Table 4.12: Results of Non-W background calculation. Derivation can be seen in Table C.33. The contribution from $t\bar{t}$ to Regions A,B,C has been removed to make the calculation. The theoretical prediction using 6.1 pb is used, and then iterated to 8.9 to construct this table. This is for the *unoptimized* analysis.

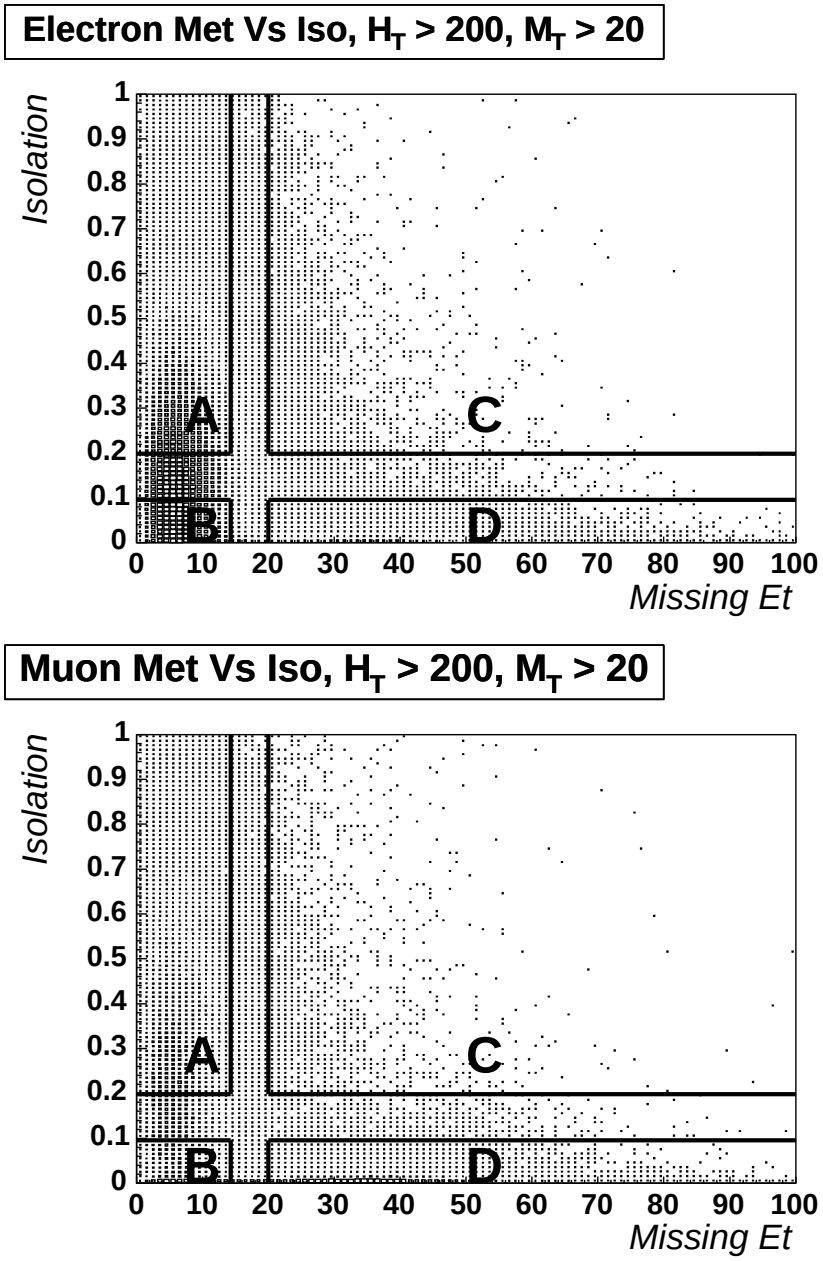

Figure 4.12: Pretag events (as defined in Section 4.3.1, minus the lepton isolation and $\not\!\!E_T$ cuts) in Regions A,B,C,D for electrons and muons. This is for the *unoptimized* analysis.

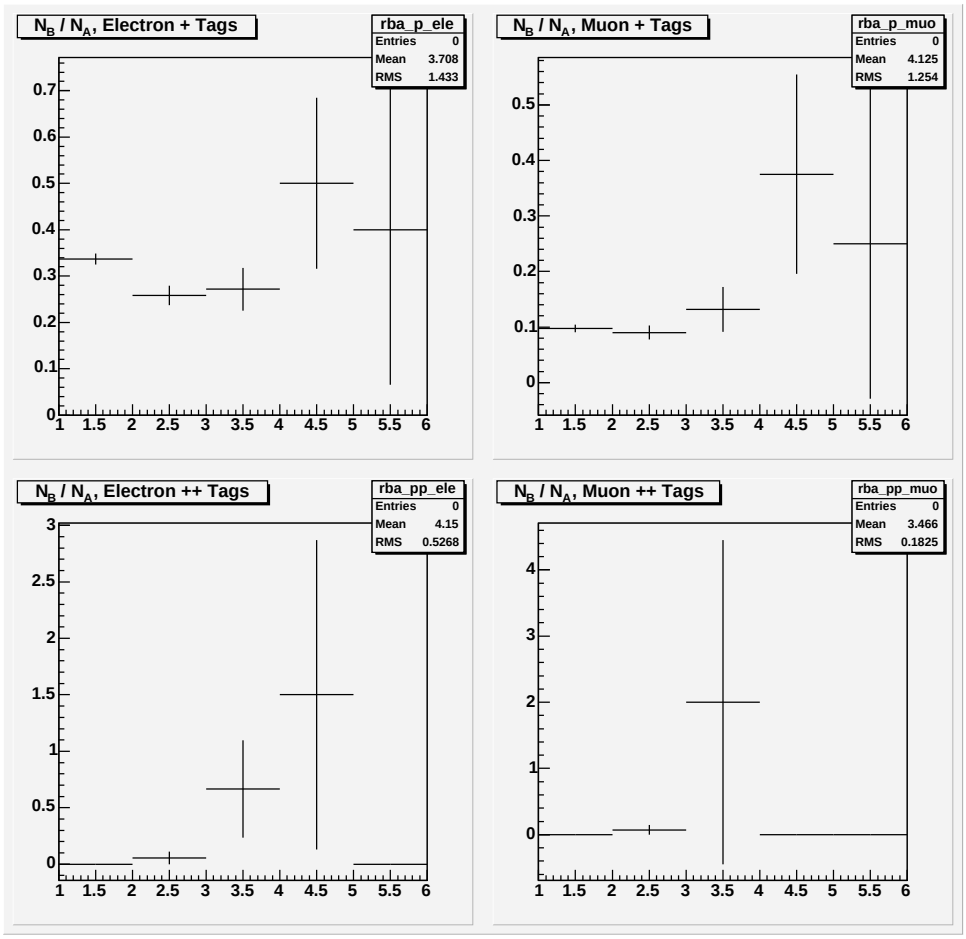

Figure 4.13: Ratio of events in regions B and A for electrons (left) and muons (right), for single (top) and double (bottom) tags. This is for the *unoptimized* analysis.

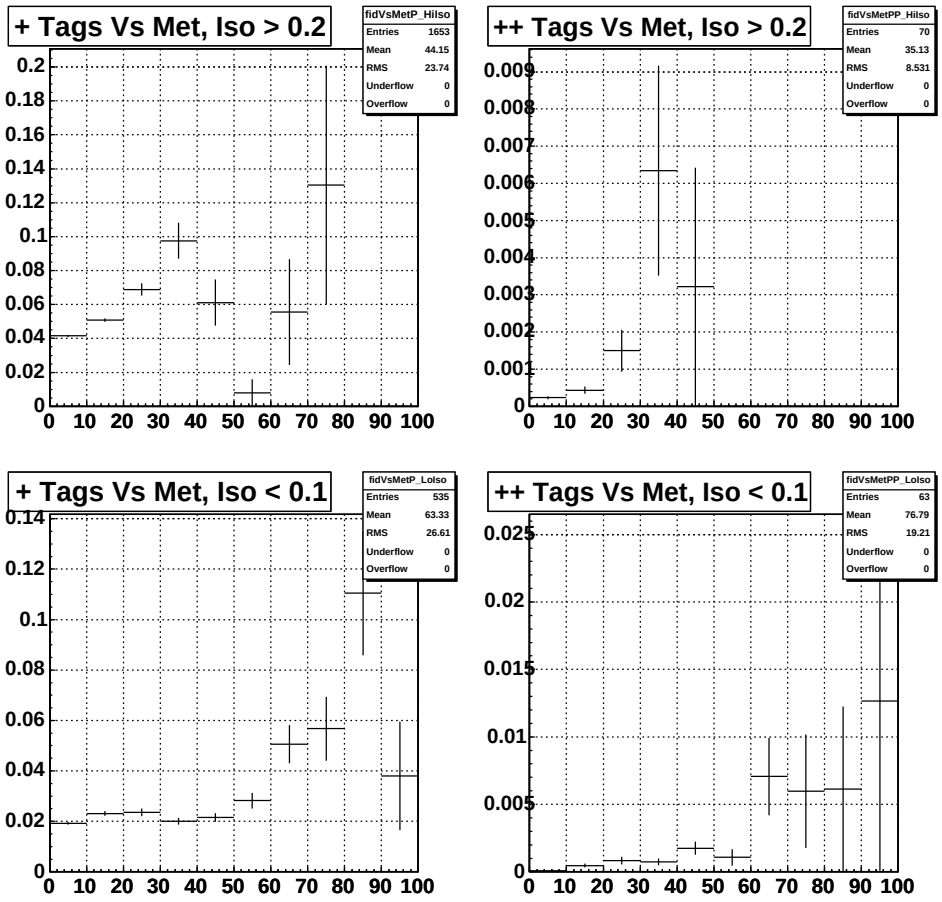

Figure 4.14: Event tag rates versus $\not\!\!E_T$ for single tags (left) and double tags (right), for $iso > 0.2$ (top) and $iso < 0.1$ (bottom). Although the tag rates versus $\not\!\!E_T$ are not constant for $iso > 0.2$ due to the presence of heavy flavor in the non-isolated lepton sample, the event tag rates versus $\not\!\!E_T$ are constant for the $iso < 0.1$ region. This is for the *unoptimized* analysis.

W+Heavy Flavor

Due to the technical problems outlined in Section 1.3.4, we cannot directly take the Monte Carlo prediction for the number of W+Jets events. We only have a leading order matrix element generator available. To mitigate this, we follow a standard prescription outlined in Run I, known as the Method 2 formulation (see Ref [44]).

The pretag sample is scaled by the fraction of events that contain heavy flavor jets (the *heavy flavor fraction*). This number is then multiplied by the tagging efficiencies measured in the ALPGEN $W + Q\overline{Q} + Np$ samples described in Ref [13]. We use the heavy flavor fractions determined by Ref [1], outlined in Table 4.13.

$$N_{W+HF} = (N_{pretag}(1 - F_{non-W}) - N_{EW,singletop} - N_{t\bar{t}})\,(f_{HF})(\epsilon_{tag})(\Phi_E) \qquad (4.22)$$

where N_{pretag} is the number of pretag events, F_{non-W} is the non-W fraction outlined in Section 4.4.1, $N_{(EW,SingleTop,t\bar{t})}$ is the number of electroweak, single top, and top pair events as outlined in Section 4.4.1, and f_{HF} is the heavy flavor fraction given in Ref [1].

We remove the contribution of Non-W pretag events, as well as the contributions from electroweak, single top, and $t\bar{t}$ to the pretag sample. This is the origin of the first term in Table 4.22. Table 4.14 shows the various components of this correction.

ϵ_{tag} is the *event tagging efficiency* in W+HF ALPGEN + HERWIG Monte Carlo ($\frac{N^{\geq 1+}}{N_{pre}}$ and $\frac{N^{\geq 2+}}{N_{pre}}$). We require tags to be within $\Delta R < 0.4$ of hadrons at the simulation level. The scale factor is taken into account by using the *per-jet* tagging efficiency, and calculating the event Φ_E factor analogously to Section 4.3.2.

We have used *exclusive matching* (see Section 1.3.4) for combining the different $W + Q\overline{Q} + Np$ backgrounds for the 1-3 jet bins. However, since we do not have

samples for $W + BB + 3p$ and $W + CC + 3p$, we take *inclusive matching*, where extra jets are allowed in the matching scheme, to cover the 4- and $\geq$ 5- jet bins. We require tags to be in reconstructed jets within $\Delta R < 0.4$ of a b or c hadron at the simulation level.

The tagging rates for the different samples are shown in Table 4.15. Figures 4.15-4.19 show the contributions to the N_{jet} spectrum from the various contributions of the $W + HF + Np$ samples, for pretags, ≥ 1 tags, and ≥ 2 tags. The lower left shows the ≥ 1 and ≥ 2 event tag rates.

The heavy flavor fractions are measured by calibrating the ALPGEN prediction of the heavy flavor fraction to control sample data, and then applying the same scaling to the W+jets data.

To perform the calibration (see Ref [1] for details), the $c\tau$ distribution of tags in JET20 data is fit as in Section 3.5.10 to determine the fraction of tags with b, c, and light flavor. The templates are taken from ALPGEN $2 \rightarrow 2$ scattering Monte Carlo passed through a parameterization of the JET20 dijet trigger.

After determining the heavy flavor composition of the tagged sample, the heavy flavor composition of the pre-tagged sample is then obtained by dividing by the b-tagging efficiency. The ratio of pretag heavy flavor fractions in data and Monte Carlo is then assumed to be the same in dijet production as it is in W+jets production. The ratio determined by Ref [1] is 1.5 ± 0.4.

We then scale the ALPGEN prediction of the heavy flavor fraction in W+jets by this ratio, and use that as the heavy flavor fraction in our sample. Table 4.13 shows the heavy flavor fractions versus the number of jets for our sample.

W + HF Fractions				
Jet Multiplicity	1 jet	2 jets	3 jets	$\geq$ 4 jets
$W + b\bar{b}, 1B$	1.0 ± 0.3	1.4 ± 0.4	2.0 ± 0.5	2.2 ± 0.6
$W + b\bar{b}, 2B$	-	1.4 ± 0.4	2.0 ± 0.5	2.6 ± 0.7
$W + c\bar{c}, 1C$	1.6 ± 0.4	2.4 ± 0.6	3.4 ± 0.9	3.6 ± 1.0
$W + c\bar{c}, 2C$	-	1.8 ± 0.5	2.7 ± 0.7	3.7 ± 1.0
$W + c, 1C$	4.3 ± 0.9	6.0 ± 1.3	6.3 ± 1.3	6.1 ± 1.3

Table 4.13: Heavy flavor fractions taken from Ref [1]. These are measured using template fits derived from ALPGEN $W+Q\overline{Q}+Np$ samples applied to the lepton+jets data. All numbers are quoted in percentage. This is for the *unoptimized* analysis.

Corrections to Pretag data					
	1 jet	2 jets	3 jets	4 jets	$\geq$ 5 jets
Data	30628	4791	769	179	36
Non-W	2265.47 ± 567.81	453.22 ± 114.65	79.00 ± 21.10	18.71 ± 5.00	3.53 ± 0.94
$t\bar{t}$ (8.9 pb)	9.20 ± 0.82	49.55 ± 4.40	96.66 ± 8.58	86.37 ± 7.67	26.63 ± 2.38
EW	157.32 ± 14.33	151.44 ± 13.67	31.54 ± 2.92	5.26 ± 0.47	0.82 ± 0.07
Single Top	18.71 ± 4.51	23.37 ± 5.04	4.54 ± 0.97	0.72 ± 0.16	0.09 ± 0.02
W+ Jets	28177 ± 584	4113 ± 134	557 ± 32	68 ± 13	5 ± 3

Table 4.14: Corrections to pretag data. The corrected pretag data is used in the W+HF estimate. Here the $t\bar{t}$ cross section is taken at the measured value of 8.9 pb. The level of $t\bar{t}$ is iterated to obtain the final result of the cross section. This is for the *unoptimized* analysis.

W+Heavy Flavor Tagging Efficiencies					
	1 jet	2 jets	3 jets	4 jets	$\geq$ 5 jets
WBB, 1B, 1 Tag	35.04 ± 2.35	37.93 ± 2.38	39.38 ± 4.08	42.76 ± 3.46	
WBB, 2B, 1 Tag	0.00 ± 0.00	57.86 ± 3.52	59.01 ± 4.28	60.50 ± 3.92	
WBB, 2B, 2 Tag	0.00 ± 0.00	14.10 ± 1.93	16.06 ± 2.42	17.45 ± 2.83	
WCC, 1C, 1 Tag	7.44 ± 1.04	8.78 ± 1.37	12.57 ± 2.33	10.53 ± 4.26	
WCC, 2C, 1 Tag	0.00 ± 0.00	15.48 ± 2.40	16.59 ± 3.48	23.32 ± 5.14	
WCC, 2C, 2 Tag	0.00 ± 0.00	0.36 ± 0.19	0.18 ± 0.12	0.00 ± 0.00	
WC, 1C, 1 Tag	8.19 ± 1.10	8.84 ± 1.23	9.53 ± 1.56	13.16 ± 2.56	

Table 4.15: Efficiencies of W+HF samples, derived from exclusive matching of ALPGEN + HERWIG Monte Carlo samples. The scale factor has been applied. All numbers are quoted in percentage. This is for the *unoptimized* analysis.

ALPGEN + HERWIG Generated Cross Sections	
Sample	Cross Section (pb)
$W \to \ell\nu + BB + 0p$	2.914 ± 0.003
$W \to \ell\nu + BB + 1p$	1.557 ± 0.002
$W \to \ell\nu + BB + 2p$	0.744 ± 0.001
$W \to \ell\nu + CC + 0p$	4.755 ± 0.006
$W \to \ell\nu + CC + 1p$	2.737 ± 0.005
$W \to \ell\nu + CC + 2p$	1.392 ± 0.002
$W \to \ell\nu + C + 0p$	21.67 ± 0.02
$W \to \ell\nu + C + 1p$	12.96 ± 0.02
$W \to \ell\nu + C + 2p$	5.397 ± 0.006
$W \to \ell\nu + C + 3p$	1.959 ± 0.002

Table 4.16: Generated cross sections used to combine the various $W + HF + Np$ samples. Taken from Ref [2].

W+Light Flavor Mistags

The W+Light Flavor single tag mistag background is estimated by applying the negative tag matrix outlined in [42] to the pretag sample (N^{-}_{pred}). We correct for the number of tagged light flavor events already counted in the Non-W, W+HF, and Monte Carlo derived backgrounds, as well as for the $t\bar{t}$ expectation, and apply a factor ($\alpha_{LF} \times \beta$) to account for the fact that the light flavor L_{2D} distribution of `SecVtx` is not symmetric, outlined in [41] and Section 3.5.10. This has a value of $\sim 1.37 \pm 0.23$, with a $\sum E_T$ dependence as shown in Figure 3.29.

The double mistags are calculated by running the mistag matrix over away jets in the ≥ 1 tag sample ($N^{pred}_{+,-}$). It is designed to represent the fake + fake background arising from $W + LF$. The Monte-Carlo derived backgrounds, Non-W background, $W + HF$ backgrounds, and the $t\bar{t}$ signal all have real + fake contributions in their respective ≥ 2 tag rate.

The equations used to calculate the mistags are

$$N^{W+LF}_{\geq 1} = N^{pred}_{-} \times \alpha_{LF}\beta \times \left(\frac{N_{pre} - N^{t\bar{t}}_{pre} - N^{NonW}_{pre} - N^{W+HF}_{pre} - N^{MC}_{pre}}{N_{pre}} \right) \quad (4.23)$$

$$N^{W+LF}_{\geq 2} = N^{pred}_{+,-} \times \alpha_{LF}\beta \times \left(\frac{N_{+} - N^{t\bar{t}}_{+} - N^{NonW}_{+} - N^{W+HF}_{+} - N^{MC}_{+}}{N_{+}} \right) \quad (4.24)$$

where N^{pred}_{-} is the predicted number of negatives tags using the matrix outlined in [42], $N^{pred}_{+,-}$ is the predicted number of negative tags in positively tagged events, $\alpha_{LF}\beta \sim 1.37 \pm 0.23$ is the light flavor asymmetry (again taken as $\sum E_T$ dependent), N^{X}_{pre} is the number of pretags expected from background type X, N^{X}_{+} is the number of tags expected from background type X, N_{pre} is the observed pretags, and N_{+} is the observed tagged events. We have counted light-flavor tags from other backgrounds in

their ≥ 1 and ≥ 2 tag estimates, and are not counted here.

Figures 4.20(a)-4.20(d) show the observed and predicted negative tags in the data sample versus number of jets, jet E_T, scalar sum of transverse energies (H_T) and transverse mass of the W (m_T^W). We see good predictions across all variables using this matrix, and gives us confidence that we have correctly predicted the $W + LF$ background.

Unoptimized Mistags					
	1 jet	2 jets	3 jets	4 jets	≥ 5 jets
Raw Tag Matrix Predictions					
(+) Pred	447.03 ± 5.18	169.45 ± 1.04	49.27 ± 0.65	18.45 ± 0.11	4.75 ± 0.08
(-) Pred	96.12 ± 4.98	41.51 ± 0.96	13.47 ± 0.63	5.25 ± 0.08	1.40 ± 0.05
(+,-) Pred	-	1.24 ± 0.15	1.40 ± 0.05	1.56 ± 0.08	0.54 ± 0.05
(-,-) Pred	-	0.00 ± 0.00	0.00 ± 0.00	0.00 ± 0.00	0.00 ± 0.00
Tag Matrix Predictions, Including $\alpha_{LF} \times \beta$					
(-) Pred $\times\alpha_{LF}\beta$	109.96 ± 4.98	52.51 ± 0.96	18.27 ± 0.63	7.35 ± 0.08	1.99 ± 0.05
(+,-) Pred $\times\alpha_{LF}\beta$	0.00 ± 0.00	1.62 ± 0.15	1.94 ± 0.05	2.19 ± 0.08	0.77 ± 0.05
Number of W+LF Mistags (corrected for $\sigma_{t\bar{t}} = 8.9\ pb$)					
≥ 1 Tag	94.05 ± 19.28	39.12 ± 7.86	11.05 ± 2.24	2.27 ± 0.45	0.22 ± 0.05
≥ 2 Tag	0.00 ± 0.00	0.54 ± 0.12	0.22 ± 0.05	0.06 ± 0.03	0.03 ± 0.05

Table 4.17: Raw mistag matrix prediction, prediction scaled to correct for light flavor asymmetry, and W+LF estimate removing other backgrounds (assuming $\sigma_{t\bar{t}} = 8.9$ pb). This is for the *unoptimized* analysis.

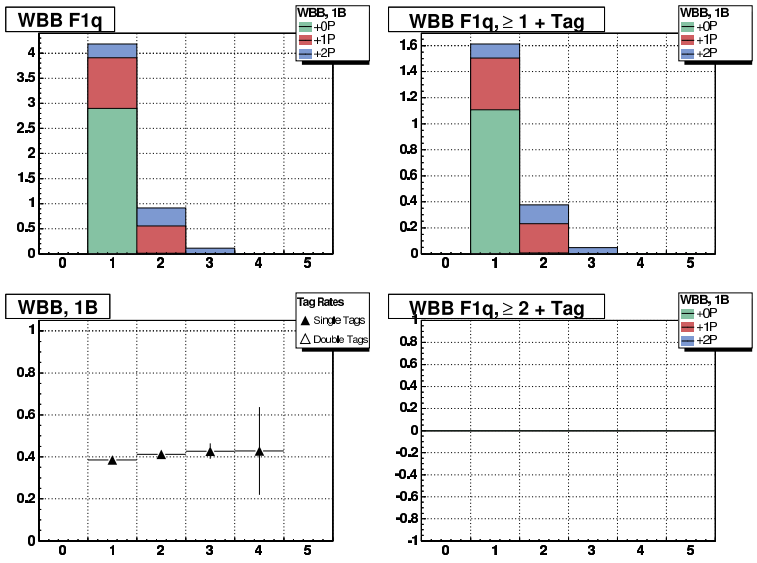

Figure 4.15: Number of events per pb^{-1} from the various $W+BB+Np$ samples, when there is 1 matched b-jet in the event. The upper left shows the pretags, the upper right shows the ≥ 1 tags, and the lower right shows the ≥ 2 tags. The lower left shows the event tag rates (ratio of right plots to pretagged plot). The cross sections used to weight the samples are given in Table 4.16. This is for the *unoptimized* analysis.

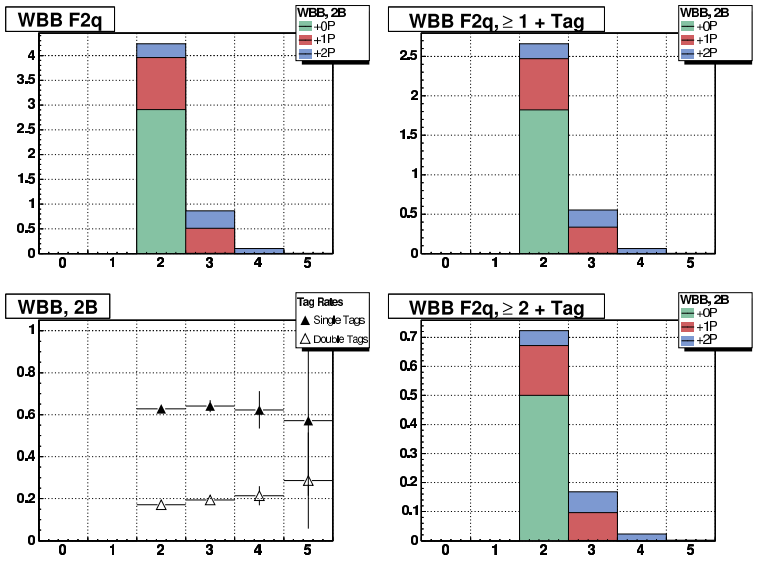

Figure 4.16: Number of events per pb^{-1} from the various $W+BB+Np$ samples, when there are 2 matched b-jets in the event. The upper left shows the pretags, the upper right shows the ≥ 1 tags, and the lower right shows the ≥ 2 tags. The lower left shows the event tag rates (ratio of right plots to pretagged plot). The cross sections used to weight the samples are given in Table 4.16. This is for the *unoptimized* analysis.

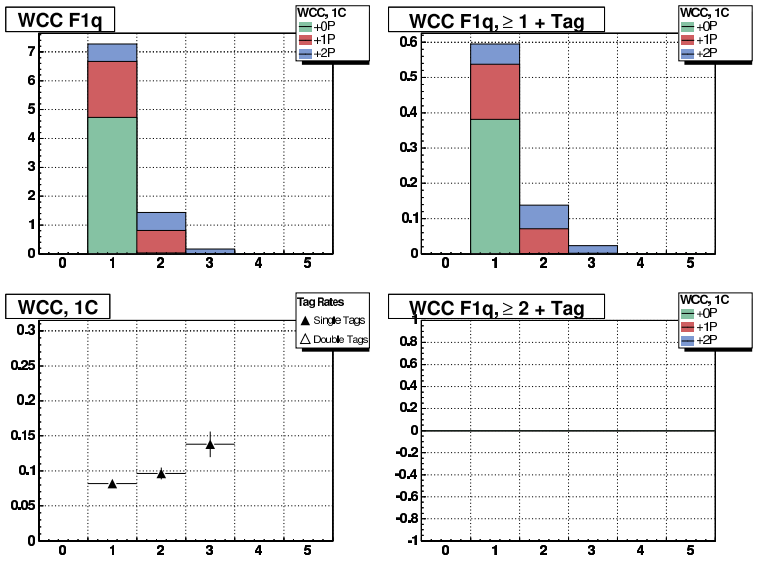

Figure 4.17: Number of events per pb^{-1} from the various $W+CC+Np$ samples, when there is 1 matched c-jet in the event. The upper left shows the pretags, the upper right shows the ≥ 1 tags, and the lower right shows the ≥ 2 tags. The lower left shows the event tag rates (ratio of right plots to pretagged plot). The cross sections used to weight the samples are given in Table 4.16. This is for the *unoptimized* analysis.

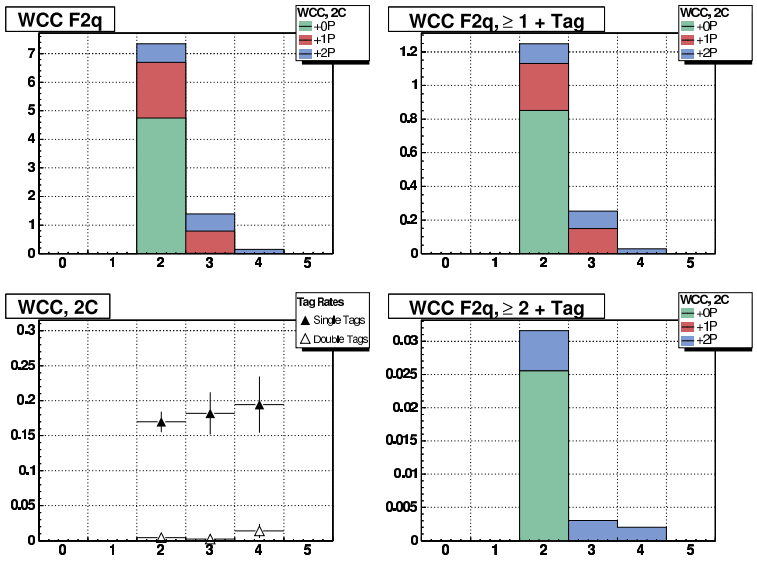

Figure 4.18: Number of events per pb^{-1} from the various $W+CC+Np$ samples, when there are 2 matched c-jets in the event. The upper left shows the pretags, the upper right shows the ≥ 1 tags, and the lower right shows the ≥ 2 tags. The lower left shows the event tag rates (ratio of right plots to pretagged plot). The cross sections used to weight the samples are given in Table 4.16. This is for the *unoptimized* analysis.

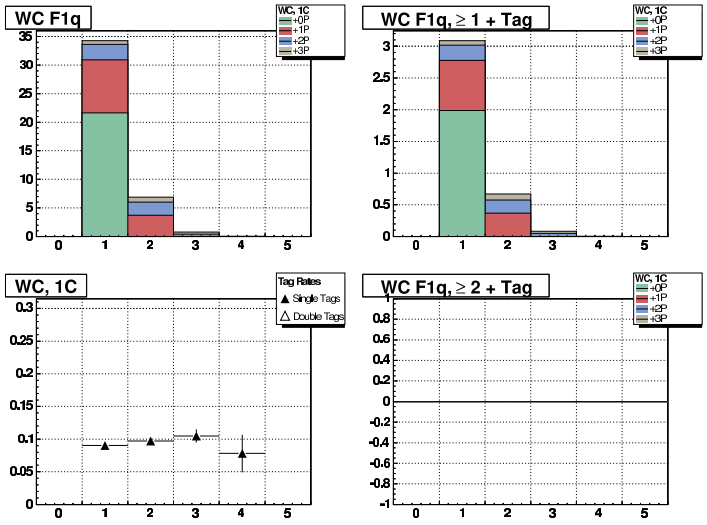

Figure 4.19: Number of events per pb^{-1} from the various $W + C + Np$ samples. The upper left shows the pretags, the upper right shows the ≥ 1 tags. The lower left shows the event tag rates (ratio of right plots to pretagged plot). The cross sections used to weight the samples are given in Table 4.16. This is for the *unoptimized* analysis.

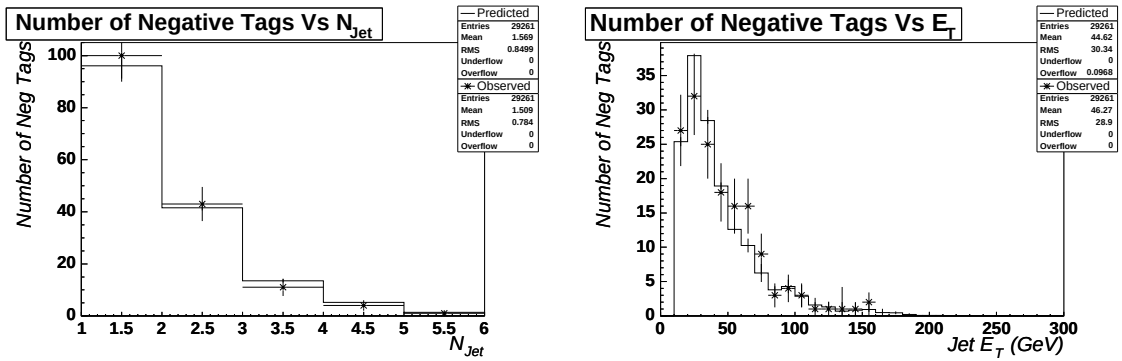

(a) (b)

(c) (d)

Figure 4.20: Observed (points) and predicted (histogram) negative tags in the pretag signal region (as described in Section 4.3.1) for the number of jets, jet E_T, H_T, and M_T^W. This is for the *unoptimized* analysis. Note that $\alpha\beta$ is not included.

4.5 Optimization

To optimize the cross section measurement, we wish to minimize the cross section uncertainty. To do so, we examine the cross section formula:

$$\sigma = \frac{N - B}{\epsilon \times L} \tag{4.25}$$

where N is the number observed, B is the background, ϵ is the event efficiency, and L is the integrated luminosity. The uncertainty on the cross section is therefore

$$\begin{aligned} \Delta\sigma^2 &= \left(\frac{\sqrt{N}}{N-B}\right)^2 + \left(\frac{\Delta B}{N-B}\right)^2 \\ &+ \left(\frac{\Delta\epsilon}{\epsilon}\right)^2 + \left(\frac{\Delta L}{L}\right)^2 \end{aligned} \tag{4.26}$$

Improvements in the uncertainties on the luminosity, the luminosity uncertainty, and the efficiency uncertainty are beyond the scope of this note, and can be considered fixed for the current discussion. Improvements in the efficiency uncertainty have been studied extensively in the `5.3.3_nt` analysis (see Ref [37] for the b-tagging scale factor, [20] for the jet energy scale, and [45] for the pretag efficiency). In the present discussion, we examine the effect of changing N and B only.

To examine this, we write $N = S + B$, where S is the expected number of $t\bar{t}$ events and B is the background. Then we rewrite Equation 4.26 in terms of S and S/B (without the efficiency and luminosity terms):

$$\Delta\sigma^2 = \left(\frac{\sqrt{N}}{N-B}\right)^2 + \left(\frac{\Delta B}{N-B}\right)^2 + \ldots \quad (4.27)$$

$$= \left(\frac{\sqrt{S+B}}{S}\right)^2 + \left(\frac{\Delta B}{S}\right)^2 + \ldots \quad (4.28)$$

$$= \left(\frac{\sqrt{S+B}}{S}\right)^2 + \left(\frac{\Delta B}{B}\right)^2 \left(\frac{B}{S}\right)^2 + \ldots \quad (4.29)$$

$$= \left(\frac{1}{\sqrt{S}}\right)^2 \left(\sqrt{1+\frac{B}{S}}\right)^2 + \left(\frac{\Delta B}{B}\right)^2 \left(\frac{B}{S}\right)^2 + \ldots \quad (4.30)$$

So we see the statistical term $(1/\sqrt{S})$ and the background uncertainty in Equation 4.30, modified by S/B. To improve the measurement, we can either increase S, increase S/B, or decrease $\Delta B/B$.

Increasing S has already been done for the `5.3.3_nt` release. The b-tagging efficiency has increased by 20% per-jet (see Ref [46]) over the `4.11.2` tagger, and of course the luminosity increased by a factor of 2. The remaining improvements are to reduce the uncertainty on the background or improve the signal to background ratio.

In order to examine the effects of this, we examine a toy model where we can increase S/B while reducing S by some amount. For illustration, we assume that if S/B is improved by 0.5, then S is decreased by 5%. Figure 4.21 shows the overall cross section relative uncertainty (including statistical uncertainty, uncertainty on the b-tag scale factor, the pretag efficiency, and the luminosity) versus the relative background uncertainty, for different configurations of S/B and S. The black curve is the nominal S/B, and the star on that line is the background uncertainty of the *unoptimized* analysis presented in 4.4.

We see that decreasing the background uncertainty by a factor of 2 has an equivalent impact as improving S/B from 1.5 to 2.5, and keeping the same relative back-

ground uncertainty, for instance.

We now explore ways to improve both S/B (Section 4.5.1) and $\Delta B/B$ (Section 4.9).

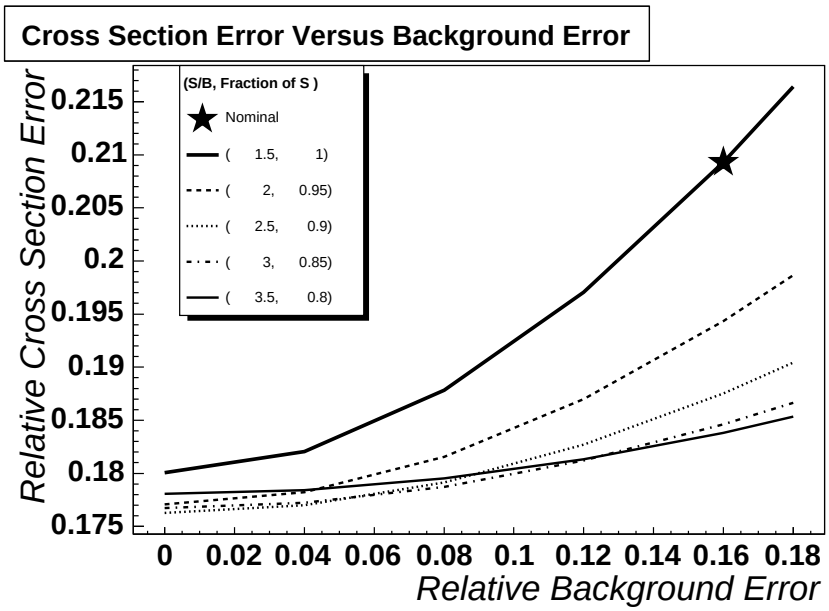

Figure 4.21: Cross section uncertainty as a function of the background uncertainty, for various ratios of S/B. Here, a simple model is used in that 5% of the signal is removed for every factor of 0.5 in S/B.

4.5.1 Improvement of S/B with Analysis Cuts

In order to find the optimal cuts for the analysis, we chose to maximize the statistical significance $\frac{S}{\sqrt{S+B}}$ (which minimizes the statistical uncertainty on the cross section). We will assume that the background uncertainties will remain the same throughout this part of the optimization.

Several variables were examined to optimize $\frac{S}{\sqrt{S+B}}$ that were thought to have discrimination. These include

- H_T
- $\not\!\!E_T$
- M_T^W
- Jet E_T of the leading jets
- Jet η of the leading jets
- Number of good tracks in the leading jets.

The estimated shapes of our various backgrounds in the following section is taken from the following estimates:

- **W+HF**: Taken from the $W+BB+1p$, $W+CC+1p$ and $W+C+2p$ samples, using no parton-jet matching (see Section 1.3.4).
- **W+LF**: Taken from the prediction of the mistag matrix.
- **Non-W**: Taken from the pretags in Region C ($\not\!\!E_T > 20\ GeV$, $iso > 0.2$).
- **EW + Single Top**: Taken from the MC, requiring ≥ 1 tag.
- **Top**: Taken from the MC, requiring ≥ 1 tag.

To examine our optimization, we take the extreme values of the theoretical range of predicted cross sections, 5 pb and 9 pb (see [47]), and show that the optimization does not strongly depend on the true cross section. Figures 4.22(a)-4.22(d) show the optimization of $S/\sqrt{S+B}$ for various event variables. The top plots in this group show the optimization for $\sigma = 5$ pb, and the bottom plots show the optimization for

$\sigma = 9$ pb. The red curve in each plot shows $S/\sqrt{S+B}$, with values delineated on the right hand axis. The contributions from $t\bar{t}$ are shown, as well as the contributions to several background species.

The variable with the most discrimination is the scalar sum of the transverse energies in the event, H_T. The average of the optimal points is $H_T > 200\ GeV$. While this is numerically the same value found for the optimization in [48], it is actually a different point because the jet energy scale has changed between that analysis and this one, by about 5%.

We have also examined the E_T and η of the leading three jets in the event. We only show plots for $\sigma = 5$ pb because the results are the same for 9 pb. So the $S/\sqrt{S+B}$ should be compared to Figure 4.22(a) with $\sigma = 5$ pb.

Figures 4.24(a)-4.24(b) show E_T on the top and η on the bottom for the leading jet. Figures 4.25(a)-4.25(b) show the same for the second leading jet, and 4.26(a)-4.26(b) show the same for the third leading jet.

There is an optimal point if we cut on the jet E_T. However, the $S/\sqrt{S+B}$ is not as large as by cutting on H_T. Thus, we use H_T as our optimizing variable, and $H_T > 200\ GeV$ as the optimal point.

There is one other aspect of the analysis we can improve upon. If we examine the transverse mass of the W boson in Figure 4.22(c), we see that the Non-W shape is different from the others. We examine this in the following section.

4.5.2 Non-W Background Reduction

Examining the transverse mass of the W boson in Figure 4.22(c), we see that the Non-W shape is different from the others. This is expected because the Non-W background is basically QCD dijets (including $b\bar{b}$ production) and mis-measured jets. One would expect a $b\bar{b}$ event to have a low M_T^W because the $l\nu$ invariant mass is small (because it comes from a virtual W boson).

The Non-W background is problematic for this analysis because there is heavy flavor contamination in the sideband regions. There are two possibilities to deal with this background. One is to estimate it better, and the other is to reduce it. The M_T^W distribution shows good discrimination, so we can attempt to remove it.

Examining Figures 4.22(c) and 4.22(d), it is clear that the analysis can benefit from cutting on transverse mass. The optimal point is 20 GeV/c^2.

One must also worry that the H_T and M_T^W cuts are not cutting away the same events. Figures 4.27 and 4.28 show H_T versus M_T^W for $t\bar{t}$ and the Non-W background, respectively. We can see that these two variables are not very correlated, and so we expect to gain by cutting on $M_T^W > 20\ GeV$ on top of the $H_T > 200\ GeV$ cut.

4.5.3 Examination of Other Variables

We have also examined several other variables to optimize the event selection. These include

- Missing E_T ($\not\!\!E_T$) (Figures 4.23(a)-4.23(b))
- Jet E_T of first, second and third jets (Figures 4.24(a),4.25(a),4.26(a))

- Jet η of first, second, and third jets (Figures 4.24(b),4.25(b),4.26(b))

While there is clear discrimination between signal and background in these variables, they are subsumed in the H_T variable. Once the H_T requirement is made, these variables have little additional power.

Since all of these distributions are included in the H_T variable, the discriminating power is already included.

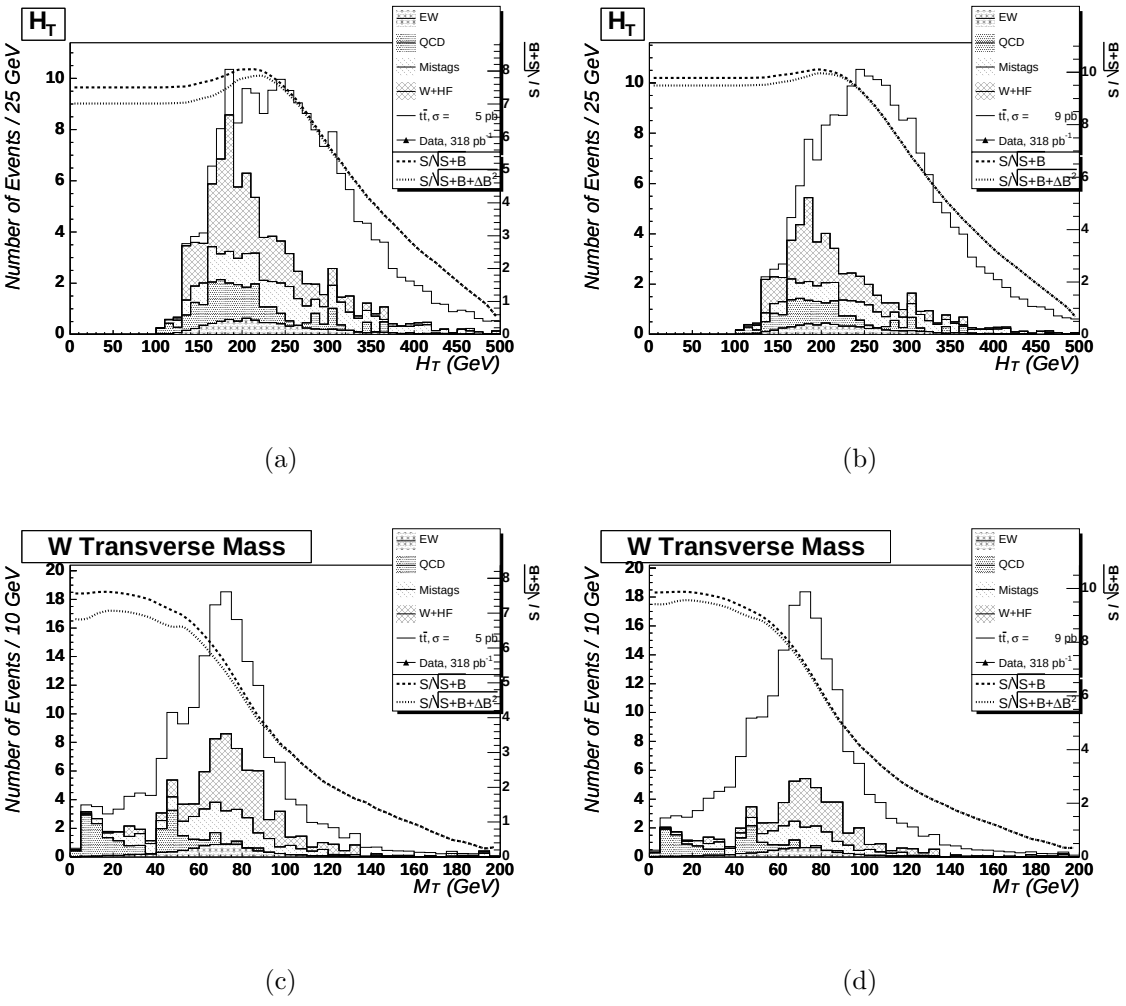

Figure 4.22: H_T and M_T^W distributions for various background contributions and the $t\bar{t}$ signal, shown at the limits of the theoretical calculation for the predicted cross section, 5-9 pb (left and right, respectively). The optimization curves of $S/\sqrt{S+B}$ and $S/\sqrt{S+B+\Delta B^2}$ dashed and dotted (respectively), and the axis of $S/\sqrt{S+B}$ is shown on the right. The histograms are stacked upon each other.

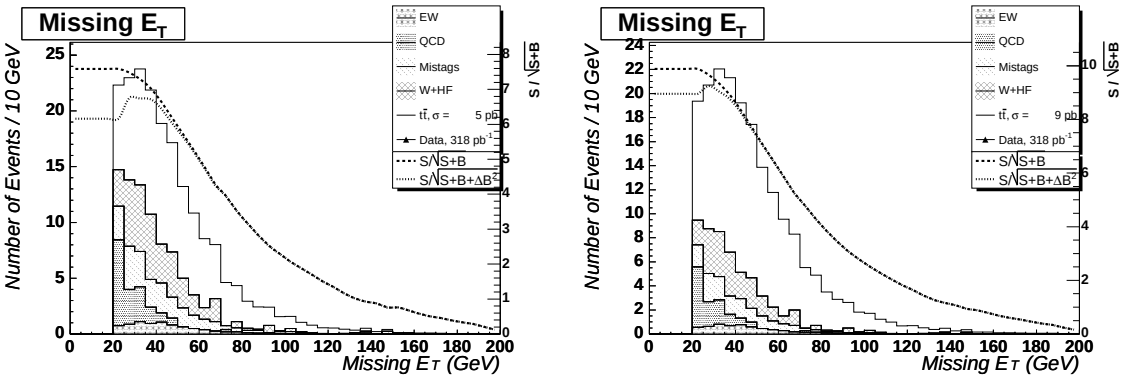

(a) (b)

Figure 4.23: $\not\!\!E_T$ distribution for various background contributions and the $t\bar{t}$ signal, shown at the limits of the theoretical calculation for the predicted cross section, 5-9 pb (left and right, respectively). The optimization curves of $S/\sqrt{S+B}$ and $S/\sqrt{S+B+\Delta B^2}$ dashed and dotted (respectively), and the axis of $S/\sqrt{S+B}$ is shown on the right. The histograms are stacked upon each other.

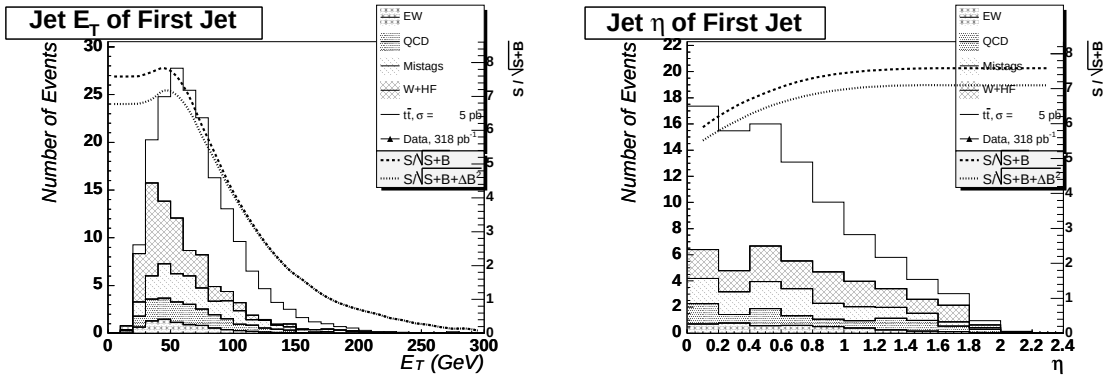

(a) (b)

Figure 4.24: First jet E_T and η distribution for various background contributions and the $t\bar{t}$ signal, shown at the lower limit of the theoretical calculation for the predicted cross section, 5 pb. The optimization curves of $S/\sqrt{S+B}$ and $S/\sqrt{S+B+\Delta B^2}$ dashed and dotted (respectively), and the axis of $S/\sqrt{S+B}$ is shown on the right. The histograms are stacked upon each other.

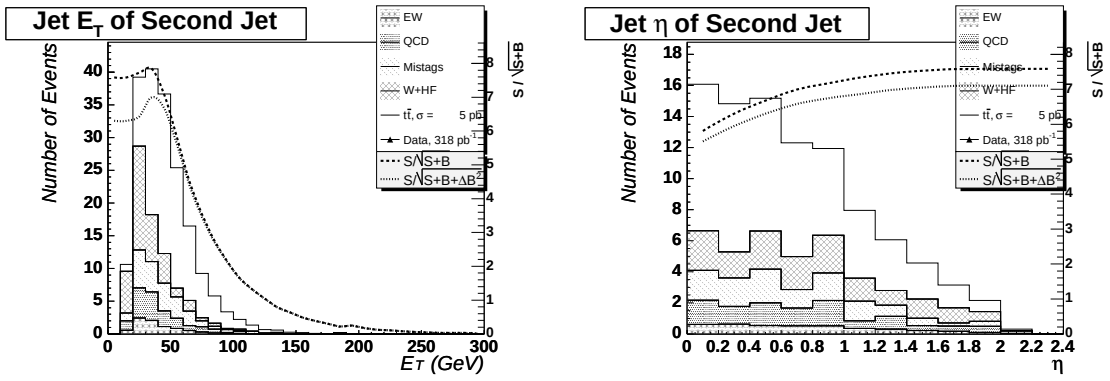

(a) (b)

Figure 4.25: Second jet E_T and η distribution for various background contributions and the $t\bar{t}$ signal, shown at the lower limit of the theoretical calculation for the predicted cross section, 5 pb. The optimization curves of $S/\sqrt{S+B}$ and $S/\sqrt{S+B+\Delta B^2}$ dashed and dotted (respectively), and the axis of $S/\sqrt{S+B}$ is shown on the right. The histograms are stacked upon each other.

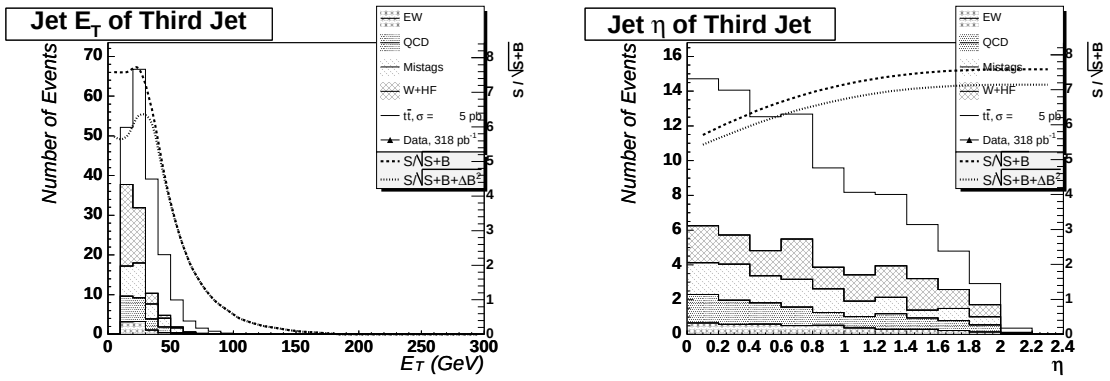

(a) (b)

Figure 4.26: Third jet E_T and η distribution for various background contributions and the $t\bar{t}$ signal, shown at the lower limit of the theoretical calculation for the predicted cross section, 5 pb. The optimization curves of $S/\sqrt{S+B}$ and $S/\sqrt{S+B+\Delta B^2}$ dashed and dotted (respectively), and the axis of $S/\sqrt{S+B}$ is shown on the right. The histograms are stacked upon each other.

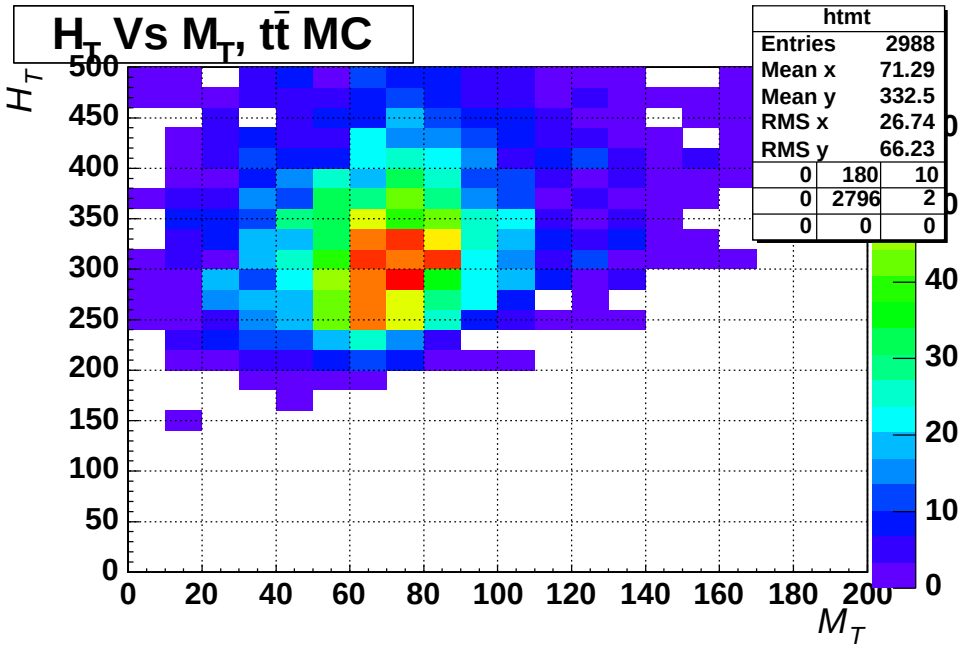

Figure 4.27: H_T versus M_T^W for $t\bar{t}$ Monte Carlo. This shows that H_T and M_T^W are not very correlated for the $t\bar{t}$ signal.

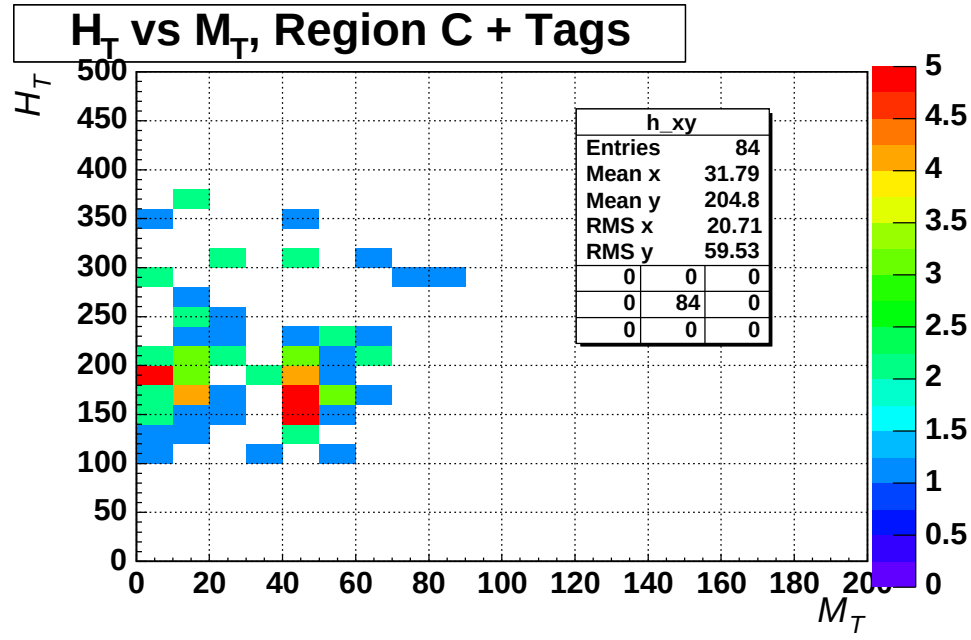

Figure 4.28: H_T versus M_T^W for the Non-W background, represented by the Region C positive tags. This shows that H_T and M_T^W are not very correlated for the Non-W background.

4.6 Optimized Measurement of $t\bar{t}$ Cross Section

4.6.1 Optimized Event Selection

We require the same base selection for the optimized measurement, with additional cuts on the scalar sum of event transverse energies (H_T) and the W leptonic transverse mass (M_T^W):

- Jets clustered with `JetClu` with a cone of 0.4, corrected to Level 4 with jet corrections version `jetCorr04b` (See Section 2.2.1 for details).
- One tight, isolated trigger lepton
- $\not\!\!E_T > 20.0$ GeV (corrected to Level 4)
- Dilepton, Z boson, conversion, cosmic veto
- $|\Delta z_{lepton-zvtx}| < 5.0$ cm
- z_{vtx} found with `ZVertexModule` using the beamline as seed.
- $H_T > 200$ GeV for $N_{jets} >= 3$
- $M_T^W > 20$ GeV/c^2
- ≥ 1 or ≥ 2 positive tight SecVtx tags.
- Signal region defined as: ≥ 3 jets with $E_T > 15$ GeV (at Level 4) and $|\eta_{detector}| < 2.0$

Event yields are shown in Table 4.18. We then divide the sample into pretags, ≥ 1 tag, and ≥ 2 tags based on SecVtx.

Data					
	1 jet	2 jets	3 jets	4 jets	$\geq$ 5 jets
CEM					
Pretag	17448	2780	197	95	18
$\geq$ 1+ Tag	246	137	40	34	8
$\geq$ 2+ Tag	0	10	10	6	1
$\geq$ 1− Tag	61	23	4	3	1
$\geq 1+-$ Tag	0	1	1	1	1
$\geq$ 2− Tag	0	0	0	0	0
CMUP					
Pretag	8383	1219	86	34	10
$\geq$ 1+ Tag	108	61	14	18	6
$\geq$ 2+ Tag	0	5	4	6	2
$\geq$ 1− Tag	25	10	2	1	0
$\geq 1+-$ Tag	0	0	0	0	0
$\geq$ 2− Tag	0	0	0	0	0
CMX					
Pretag	4452	677	41	13	6
$\geq$ 1+ Tag	73	34	8	6	4
$\geq$ 2+ Tag	0	0	1	3	0
$\geq$ 1− Tag	11	7	0	0	0
$\geq 1+-$ Tag	0	0	0	0	0
$\geq$ 2− Tag	0	0	0	0	0
Total					
Pretag	30283	4676	324	142	34
$\geq$ 1 Tag	427	232	62	58	18
$\geq$ 2 Tag	0	15	15	15	3
$\geq$ 1− Tag	97	40	6	4	1
$\geq 1+-$ Tag	0	1	1	1	1
$\geq$ 2− Tag	0	0	0	0	0

Table 4.18: Events Yields for $318.5 pb^{-1}$ for the *optimized* event selection.

4.6.2 Effect of Optimization on Signal Estimate

The H_T and M_T^W cuts will of course reduce the efficiency to have a top event in our sample. Table 4.19 compares the number of events before and after the cuts in $t\bar{t}$ Monte Carlo, and we see that there is an 8% decrease in the $t\bar{t}$ signal due to these cuts.

After the H_T and M_T^W cuts, the luminosity weighted pretag efficiency is

$$\epsilon_{pretag}^{t\bar{t}} \int \mathcal{L}dt = 21.2 \pm 2.0\ pb \tag{4.31}$$

Table 4.4 shows the breakdown of event counts after successive cuts in the `ttopel` $t\bar{t}$ Monte Carlo.

Table 4.19 shows the pretag efficiency times acceptance for both the optimized an unoptimized analyses.

$t\bar{t}$ Pretag Acceptance × Efficiency in ≥ 3 jets (ϵ_{pretag}) (%)		
	$H_T > 0$ GeV, $M_T^W > 0$ GeV/c^2	$H_T > 200$ GeV, $M_T^W > 20$ GeV/c^2
Total Number of Events	1106645	
CEM Pretags	51786	46353
CEM Acc	4.68 ± 0.02	4.21 ± 0.02
CEM Acc*SF	4.27 ± 0.31	3.84 ± 0.29
CMUP Pretags	32975	29126
CMUP Acc	2.98 ± 0.02	2.68 ± 0.02
CMUP Acc * SF	2.25 ± 0.17	2.02 ± 0.15
CMX Pretags	11116	10077
CMX Acc	1.00 ± 0.01	0.90 ± 0.01
CMX Acc * SF	0.91 ± 0.07	0.82 ± 0.06
$t\bar{t}$ Luminosity Weighted Denominator in ≥ 3 jets ($\epsilon_{pretag} \int \mathcal{L}dt$) (%)		
Total	23.6 ± 2.1 pb^{-1}	21.2 ± 2.0 pb^{-1}

Table 4.19: Comparison of pretagging rates before and after the $H_T > 200$ GeV and $M_T^W > 20$ GeV cuts in $t\bar{t}$ Monte Carlo. The H_T cut is only applied for ≥ 3 jets, but the M_T^W cut is applied everywhere. Also shown is the luminosity weighted denominator.

If we cut on the H_T of the event, we expect that in the tagging efficiency increases

because we are effectively cutting harder on the jet E_T (in conjunction with the other transverse energies), and so the average b-tag rate will increase. The heavy flavor fractions will also change due to the H_T cut, because events with heavy flavor can be affected differently than events with no heavy flavor, and so the ratio between them can change. We examine the effect on the $t\bar{t}$ event tagging rate in Table 4.20. The event tagging efficiency did increase slightly as expected, by about 1%.

$t\bar{t}$ Event Tagging Efficiency in Data						
		1 jet	2 jets	3 jets	4 jets	$\geq$ 5 jets
$H_T > 0$, $M_T^W > 0$	$\Phi_e^{\geq 1}$	91.0 ± 6.1	92.7 ± 5.2	93.2 ± 5.0	93.8 ± 4.8	94.1 ± 4.8
	$\geq$ 3 jets avg				93.6 ± 4.9	
	$\Phi_e^{\geq 2}$	-	83.2 ± 11.4	84.4 ± 11.6	85.1 ± 11.4	86.4 ± 11.5
	$\geq$ 3 jets avg				85.1 ± 11.5	
	$\epsilon_{\geq 1} * \Phi_E^1$	33.5 ± 2.3	50.9 ± 2.9	57.2 ± 3.1	62.3 ± 3.2	63.1 ± 3.2
	$\geq$ 3 jets avg				60.1 ± 3.1	
	$\epsilon_{\geq 2} * \Phi_E^2$	-	9.4 ± 1.3	13.1 ± 1.8	17.7 ± 2.4	18.9 ± 2.5
	$\geq$ 3 jets avg				15.7 ± 2.1	
$H_T > 200$, $M_T^W > 20$	$\Phi_e^{\geq 1}$	91.0 ± 6.1	92.7 ± 5.2	93.3 ± 5.0	93.8 ± 4.8	94.2 ± 4.8
	$\geq$ 3 jets avg				93.7 ± 4.8	
	$\Phi_e^{\geq 2}$	-	83.2 ± 11.4	84.6 ± 11.6	85.2 ± 11.4	86.4 ± 11.5
	$\geq$ 3 jets avg				85.3 ± 11.5	
	$\epsilon_{\geq 1} * \Phi_E^1$	33.4 ± 2.3	50.9 ± 2.9	58.3 ± 3.1	62.8 ± 3.2	63.2 ± 3.2
	$\geq$ 3 jets avg				60.9 ± 3.2	
	$\epsilon_{\geq 2} * \Phi_E^2$	-	9.4 ± 1.3	13.9 ± 1.9	18.0 ± 2.4	19.0 ± 2.5
	$\geq$ 3 jets avg				16.4 ± 2.2	

Table 4.20: Comparison of the event tagging rates before and after the $H_T > 200$ GeV and $M_T^W > 20$ GeV cuts. The H_T cut is only applied for ≥ 3 jets, but the M_T^W cut is applied everywhere. The values are given, along with their ≥ 3 jet average, in percentage.

4.6.3 Effect of Optimization on Background Estimate

W+HF

The W+HF background will be affected by applying the H_T cut. Since there is a real W in this background, the effect of the M_T^W cut will be minimal. Thus, the only effect that needs to be examined is the effect due to the H_T cut. Since the H_T cut is the same as in Ref [48], we can use the same heavy flavor fractions. We reproduce them in Table 4.21.

Since the event efficiency can change in the same way as the $t\bar{t}$, we also examine the effects of the H_T cut on the tagging efficiencies. Table 4.22 shows the efficiencies before and after the optimization cuts.

W + HF Fractions (%)						
Jet Multiplicity	1 jet	2 jets	3 jets		$\geq$ 4 jets	
			$H_T > 0$	$H_T > 200$	$H_T > 0$	$H_T > 200$
$W + b\bar{b}, 1B$	1.0 ± 0.3	1.4 ± 0.4	2.0 ± 0.5	2.4 ± 0.6	2.2 ± 0.6	2.2 ± 0.6
$W + b\bar{b}, 2B$	-	1.4 ± 0.4	2.0 ± 0.5	2.3 ± 0.6	2.6 ± 0.7	2.6 ± 0.7
$W + c\bar{c}, 1C$	1.6 ± 0.4	2.4 ± 0.6	3.4 ± 0.9	3.8 ± 1.0	3.6 ± 1.0	3.5 ± 1.0
$W + c\bar{c}, 2C$	-	1.8 ± 0.5	2.7 ± 0.7	2.9 ± 0.8	3.7 ± 1.0	3.7 ± 1.0
$W + c, 1C$	4.3 ± 0.9	6.0 ± 1.3	6.3 ± 1.3	6.0 ± 1.3	6.1 ± 1.3	5.9 ± 1.3

Table 4.21: Heavy flavor fractions taken from Ref [1] before and after optimization cuts. These are measured using template fits derived from ALPGEN $W + Q\overline{Q} + Np$ samples applied to the lepton+jets data. The H_T cut affects the heavy flavor fractions, but the M_T^W cut does not. Since we only apply the H_T cut for $N_{jets} \geq 3$, the fractions for $N_{jets} < 3$ are the same.

Non-W Background

The estimation of the Non-W background is effected by both the H_T and M_T^W cuts. They also have special consideration in this case. We only apply the H_T cut for events with $\not\!\!E_T > 20\ GeV$ because the lower $\not\!\!E_T$ regions will generally fail the H_T cut

W+Heavy Flavor Tagging Efficiencies (%)					
	1 jet	2 jets	3 jets	4 jets	$\geq$ 5 jets
$H_T > 0$ GeV, $M_T^W > 0$ GeV					
WBB, 1B, 1 Tag	35.04 ± 2.35	37.93 ± 2.38	39.38 ± 4.08	42.76 ± 3.46	
WBB, 2B, 1 Tag	0.00 ± 0.00	57.86 ± 3.52	59.01 ± 4.28	60.50 ± 3.92	
WBB, 2B, 2 Tag	0.00 ± 0.00	14.10 ± 1.93	16.06 ± 2.42	17.45 ± 2.83	
WCC, 1C, 1 Tag	7.44 ± 1.04	8.78 ± 1.37	12.57 ± 2.33	10.53 ± 4.26	
WCC, 2C, 1 Tag	0.00 ± 0.00	15.48 ± 2.40	16.59 ± 3.48	23.32 ± 5.14	
WCC, 2C, 2 Tag	0.00 ± 0.00	0.36 ± 0.19	0.18 ± 0.12	0.00 ± 0.00	
WC, 1C, 1 Tag	8.19 ± 1.10	8.84 ± 1.23	9.53 ± 1.56	13.16 ± 2.56	
$H_T > 200$ GeV, $M_T^W > 20$ GeV					
WBB, 1B, 1 Tag	34.94 ± 2.35	38.07 ± 2.34	45.77 ± 4.50	43.58 ± 3.65	
WBB, 2B, 1 Tag	0.00 ± 0.00	57.90 ± 3.51	62.78 ± 4.82	62.23 ± 4.06	
WBB, 2B, 2 Tag	0.00 ± 0.00	14.12 ± 1.93	18.17 ± 2.80	18.24 ± 3.02	
WCC, 1C, 1 Tag	7.40 ± 1.03	8.91 ± 1.38	13.63 ± 2.79	15.22 ± 5.99	
WCC, 2C, 1 Tag	0.00 ± 0.00	15.44 ± 2.39	18.71 ± 4.65	26.30 ± 6.33	
WCC, 2C, 2 Tag	0.00 ± 0.00	0.33 ± 0.18	0.15 ± 0.15	0.00 ± 0.00	
WC, 1C, 1 Tag	8.19 ± 1.10	8.86 ± 1.23	10.94 ± 2.10	14.37 ± 2.95	

Table 4.22: Efficiencies of W+HF samples before and after optimization cuts, derived from exclusive matching of ALPGEN + HERWIG Monte Carlo samples. The scale factor has been applied.

by construction. We do apply the M_T^W cut for $\not\!\!E_T < 20$ GeV, however. This changes the result by 30%, and so we take 30% as an additional systematic uncertainty on this method. It is important to apply the M_T^W cut for $\not\!\!E_T < 20$. The class of events that is being removed for high $\not\!\!E_T$ (i.e. those with $M_T^W < 20$) should not be used to scale the Region C tags to Region D. That is, we should remove the same class of events (i.e. those with $M_T^W < 20$) for all regions symmetrically.

Table 4.23 shows the Non-W background estimates for single and double tags after the optimization cuts.

W + Light Flavor

The H_T and M_T^W cuts reduce the sample size in all jet bins. Therefore, the tag rate parameterization predictions will also change over all jet bins. Table 4.24 shows

Non-W					
	1 jet	2 jets	3 jets	4 jets	$\geq$ 5 jets
Electrons					
F_{Non-W} (%)	9.21 ± 2.31	12.06 ± 3.08	7.44 ± 2.34		
N_+^B/N_+^A (%)	39.60 ± 1.93	34.14 ± 3.79	42.24 ± 8.64		
$N_+^{tagmethod}$	45.43 ± 15.75	17.27 ± 6.56	3.83 ± 2.13	0.71 ± 0.80	0.56 ± 0.65
R_+^B (%)	1.63 ± 0.33	3.29 ± 0.74	7.64 ± 2.17	13.75 ± 6.96	3.39 ± 11.42
$N_+^{pretagmethod}$	26.16 ± 8.47	11.04 ± 3.75	1.12 ± 0.48	0.97 ± 0.59	0.05 ± 0.15
R_{++}^B (%)	0.00 ± 0.00	0.04 ± 0.04	1.04 ± 0.60	5.43 ± 4.14	5.99 ± 6.49
$N_{++}^{pretagmethod}$	0.00 ± 0.00	0.14 ± 0.13	0.15 ± 0.10	0.38 ± 0.32	0.08 ± 0.09
Pretag	1607.56 ± 403.69	335.18 ± 85.63	14.66 ± 4.61	7.07 ± 2.22	1.34 ± 0.42
$\geq$ 1+ Tag	30.49 ± 7.41	12.58 ± 3.23	1.25 ± 0.47	0.88 ± 0.46	0.07 ± 0.15
$\geq$ 2+ Tag	0.00 ± 0.00	0.14 ± 0.13	0.15 ± 0.10	0.38 ± 0.32	0.07 ± 0.09
Muons					
F_{Non-W} (%)	3.20 ± 0.81	3.78 ± 1.00	2.80 ± 1.10		
N_+^B/N_+^A (%)	12.68 ± 1.29	12.59 ± 2.73	22.93 ± 9.71		
$N_+^{tagmethod}$	6.31 ± 2.36	3.38 ± 1.51	0.05 ± 0.33	-0.08 ± 0.24	0.10 ± 0.24
R_+^B (%)	1.75 ± 0.39	4.60 ± 1.34	9.92 ± 5.09	44.27 ± 45.90	42.95 ± 95.94
$N_+^{pretagmethod}$	7.19 ± 2.42	3.30 ± 1.30	0.35 ± 0.23	0.58 ± 0.65	0.19 ± 0.44
R_{++}^B (%)	0.00 ± 0.00	0.23 ± 0.17	4.40 ± 2.98	19.45 ± 18.00	172.44 ± 230.49
$N_{++}^{pretagmethod}$	0.00 ± 0.00	0.17 ± 0.13	0.16 ± 0.12	0.26 ± 0.26	0.77 ± 1.08
Pretag	410.61 ± 103.74	71.71 ± 18.95	3.55 ± 1.40	1.31 ± 0.52	0.45 ± 0.18
$\geq$ 1+ Tag	6.74 ± 1.66	3.33 ± 0.98	0.25 ± 0.17	0.00 ± 0.22	0.12 ± 0.21
$\geq$ 2+ Tag	0.00 ± 0.00	0.17 ± 0.13	0.16 ± 0.12	0.00 ± 0.26	0.12 ± 1.08

Table 4.23: Non-W background estimation for single and double tags, for $H_T > 200$ GeV and $M_T^W > 20$ GeV. Note that the H_T cut is only applied for $\not\!\!E_T > 20$ GeV because the loss of the 20 GeV causes most of the events to fail the H_T cut. $t\bar{t}$ is removed from the sideband regions in this table, after iterating to the measured cross section of 8.7. This is for the *optimized* analysis.

the summary of the $W + LF$ mistags for the optimized analysis.

W + LF Mistags					
	1 jet	2 jets	3 jets	4 jets	$\geq$ 5 jets
Raw Tag Matrix Predictions					
(+) Pred	440.36 ± 5.13	164.69 ± 1.02	26.06 ± 0.64	15.85 ± 0.10	4.51 ± 0.06
(-) Pred	94.43 ± 4.95	40.25 ± 0.94	7.80 ± 0.63	4.69 ± 0.07	1.32 ± 0.04
(+,-) Pred	0.00 ± 0.00	1.11 ± 0.15	1.07 ± 0.05	1.47 ± 0.08	0.52 ± 0.05
(-,-) Pred	0.00 ± 0.00	0.00 ± 0.00	0.00 ± 0.00	0.00 ± 0.00	0.00 ± 0.00
Tag Matrix Predictions, Including $\alpha_{LF} \times \beta$					
(-) Pred $\times\alpha_{LF}\beta$	107.95 ± 4.95	50.84 ± 0.94	10.84 ± 0.63	6.59 ± 0.07	1.87 ± 0.04
(+,-) Pred $\times\alpha_{LF}\beta$	0.00 ± 0.00	1.45 ± 0.15	1.50 ± 0.05	2.07 ± 0.08	0.74 ± 0.05
Number of W+LF Mistags (corrected for $\sigma_{t\bar{t}} = 8.7\ pb$)					
$\geq$ 1 Tag	93.08 ± 19.09	38.23 ± 7.68	5.80 ± 1.21	1.86 ± 0.37	0.28 ± 0.06
$\geq$ 2 Tag	0.00 ± 0.00	0.48 ± 0.11	0.10 ± 0.04	0.17 ± 0.04	0.05 ± 0.04

Table 4.24: Raw mistag matrix prediction, prediction scaled to correct for light flavor asymmetry, and W+LF estimate removing other backgrounds (assuming $\sigma_{t\bar{t}} = 8.7$ pb). This is for the *optimized* analysis.

4.7 Systematic Uncertainties

4.7.1 Background Systematics

The systematics on the various backgrounds come from several sources. The following uncertainties are derived elsewhere and we use the determined systematics:

- **Heavy flavor fractions**: This affects the W+HF backgrounds. The systematics on the heavy flavor fractions are taken to be the same as calculated in Ref [1]. There is an overall relative uncertainty of 26% on the heavy flavor fractions.

- ***B*-Tagging Scale Factor**: This affects the W+HF, electroweak, and single top backgrounds, as well as the signal prediction. We take the systematic from Ref [37]. There is an overall relative uncertainty of 6.6% on the scale factor.

- ***B*-Tagging Tag Matrices**: This affects the mistag background. We take the systematic from Ref [42]. There is an overall relative uncertainty of 8% from the matrix itself and 22% due to the light flavor asymmetry, for a total of 23% relative uncertainty on the mistag prediction.

- **Lepton ID Scale Factors**: This affects the electroweak and single top backgrounds, and the signal prediction. We take the systematic from Ref [45]. There is an overall relative uncertainty of 8% on the lepton ID scale factors.

The following uncertainties are specific to this analysis and are estimated here:

- **Jet energy scale**: The variation in jet energy scale affects the $t\bar{t}$ efficiency, the electroweak and single top backgrounds, and the W+HF background. We

use the procedure outlined in [20] to estimate the effect of the JES on these backgrounds.

- **Non-W Background Specific**: This background has an additional uncertainty due to the definition of the sideband regions. We vary the definition of the sideband regions, and take the average of the deviations as an additional systematic.

Non-W Background Systematics

The $\not\!\!E_T$ versus isolation method of determining the Non-W background carries a systematic due to the definition of the background regions. To determine the effect of this on the Non-W background estimate, we add the sideband regions into the main regions and re-calculate F_{Non-W}. The results of this variation can be found in Table 4.25. Specifically, we move the isolation region definition up and down by 0.1, and the $\not\!\!E_T$ region definition up and down by 10 GeV.

We see that the results of varying the isolation region up and down results in an average deviation of 23.5%, and that varying the $\not\!\!E_T$ region up and down results in an average deviation of 21.3%. We take 25% as our systematic for this effect. We take this to be the same for electrons and muons.

We also assign an additional 50% systematic on the Non-W double-tag estimate because of the use of the Feldman-Cousins prescription described in Section 4.4.1. Thus, the overall systematic on the Non-W double tags is 60%.

Variation	ΔF_{Non-W}, Ele (%)	ΔF_{Non-W}, Muo (%)	Average
Isolation Down 0.1	52%	16%	
Isolation Up 0.1	3%	23%	23.5%
$\not\!\!E_T$ Down 10 GeV	4%	19%	
$\not\!\!E_T$ Up 10 GeV	32%	30%	21.3%

Table 4.25: Effect of varying the $\not\!\!E_T$ versus isolation sidebands on the Non-W background. We take 25% as our overall systematic.

Overall Background Uncertainties

Table 4.26 describes the uncertainties on the various backgrounds and the $t\bar{t}$ signal, and how they are estimated.

Background Level Fractional Uncertainties			
	≥ 1 Tag	≥ 2 Tags	Estimated From
EW + Single Top	11%	16%	Lepton ID + modeling (6.7%), b-tag SF (6.6%), JES(3.9%), lum (6.0%)
W+HF	26%	28%	Matching (15%), ISR/FSR (10%), m_Q (6%) JES (5%), PDF (5%), Q^2 scale (4%), b-tag SF (6.6%)
Mistags	23%	23%	Mistag matrix (8%), light-flavor asymmetry (22%)
Non-W, Tag Method	25%	n/a	Vary sidebands (25%)
Non-W, Pretag Method	33%	60%	F_{Non-W} (25%), R_B (20%) small stats (double tags:50%)

Table 4.26: Background level uncertainties summary for the unoptimized analysis.

4.7.2 Jet Energy Scale

We use the procedure outlined in [20] to estimate the systematic due to the jet energy scale. We estimate the background levels varying the jet energy scale by $\pm 1\sigma$, and take the average deviation as a systematic on the result. The results are summarized below for each background.

Background Level Fractional Uncertainties			
	≥ 1	≥ 2	Estimated From
EW + Single Top	11%	16%	Lepton ID + modeling (7.4%), b-tag SF (6.6%), JES(4.3%), lum (6.0%)
W+HF	26%	28%	Matching (15%), ISR/FSR (10%), m_Q (6%) JES (5.0%), PDF (5%), Q^2 scale (4%), b-tag SF (6.6%)
Mistags	23%	23%	Mistag matrix (8%), light-flavor asymmetry (22%)
Non-W, Tag Method	39%	n/a	Vary sidebands (25%), apply M_T^W for $\not\!\!E_T < 20$ (30%)
Non-W, Pretag Method	44%	60%	F_{Non-W} (25%), R_B (20%) apply M_T^W for $\not\!\!E_T < 20$ (30%), small stats (double tags:50%)

Table 4.27: Background systematics summary for the optimized analysis.

Species	JES systematic
$t\bar{t}$	2.9%
EW + Single Top	2.9%
W+HF	5.0%

Table 4.28: Effect of varying the jet energy scale on $t\bar{t}$, electroweak and single top, and W+HF backgrounds. We apply the same systematic to the electroweak and single top as the $t\bar{t}$ acceptance. The effect of the jet energy scale on the W+HF background is taken from Ref [1].

$t\bar{t}$ Acceptance

We have calculated the jet energy scale systematic on the $t\bar{t}$ acceptance at different stages of the analysis. We use the total systematic function provided by the jet energy group. The effect of the jet energy scale on the $t\bar{t}$ expectation is 2.9%. Table 4.28 shows the effect of variation of the jet energy scale.

Backgrounds

- **W+HF**: The jet energy scale systematic is already included in the overall systematic for the heavy flavor fractions. Ref [1] estimates 5% systematic on

$W + b\bar{b}$ and $W + c\bar{c}$, and a 10% systematic on $W + c$.

- **Electroweak and Single Top**: The electroweak and single top backgrounds were assumed to have the same jet energy scale systematic as the $t\bar{t}$ signal expectation. We take the same 2.9% systematic on these backgrounds due to the jet energy scale.

4.7.3 B-Tag Efficiency

The uncertainty of the b-tagging efficiency is the same as the uncertainty on the b-tagging scale factor as described in Section 3.4.3. Because there are two b-jets possible in $t\bar{t}$ events, the impact of the b-tagging event efficiency is slightly less than the uncertainty on the per-jet efficiency. In order to see this, we imagine the only tags are on b-jets and write the event tagging efficiency as

$$\epsilon_{ev} = F_{1b}\epsilon + 2F_{2b}\epsilon(1-\epsilon) + F_{2b}\epsilon^2 \tag{4.32}$$

So the fractional uncertainty of the event efficiency due to the per-jet efficiency is

$$\frac{d\epsilon_{ev}}{\epsilon_{ev}} = \frac{d\epsilon}{\epsilon}\left[\frac{(F_{1b}+2F_{2b}) - 2F_{2b}\epsilon}{(F_{1b}+2F_{2b}) - F_{2b}\epsilon}\right] \tag{4.33}$$

As $F_{2b}\times\epsilon$ is positive, the quantity in brackets is strictly less than one, so the fractional uncertainty of the event tagging efficiency is less than the fractional uncertainty on the per-jet efficiency. The value depends on the fraction of events with $1b$ versus $2b$ and the per-jet efficiency. In our case, the total uncertainty on the per-jet efficiency is 6.6% (from the scale factor), and the total uncertainty on the event efficiency is 5.2%.

4.7.4 Lepton ID Scale Factors

The actual effect of the lepton ID scale factor is quite small. The lepton ID and trigger efficiencies are determined in $Z \to \ell^+\ell^-$ samples where one leg is required to pass tight cuts, and the other leg is considered a probe. The backgrounds to these samples are minuscule, and so an unbiased sample of leptons can be easily selected.

A much larger systematic uncertainty comes from applying the lepton ID scale factors to samples in which there are jets. When the leptons are close to jets (i.e. are non-isolated), it is not guaranteed that the lepton ID scale factors for isolated leptons applies directly.

The problem is that examining the lepton isolation versus the number of jets is a very statistically limited method of determining the scale factor. Instead, we examine the lepton ID scale factor in Z+1 jet events as a function of the distance to the nearest jet. As the results are statistically limited, we conservatively apply a 5% systematic due to this effect.

For full details, see References [49, 50, 51]

4.7.5 Luminosity

The luminosity uncertainty comes from two sources. Firstly, there is the intrinsic resolution of the Cerenkov luminosity counter. There is also an uncertainty due to the total inelastic $p\overline{p}$ cross section. These are approximately 5% and 3% uncertainties, respectively, resulting in a total uncertainty of 5.9% on the luminosity measurement.

4.7.6 Monte Carlo Uncertainties

There are several uncertainties on the acceptance times efficiency that arise from the Monte Carlo. These are not the same uncertainties as the theoretical prediction, but they come from the same places. The event selection efficiency can vary given the variation of several quantities. These quantities are the uncertainties due to initial and final state radiation, the parton distribution function, and the event model for $t\bar{t}$ production.

In order to take into account these uncertainties, the efficiency times acceptance is examined after varying these parameters, and the full differences are taken as systematic uncertainties. We now discuss each in detail.

4.7.7 Initial and Final State Radiation

As mentioned above, it is very difficult to get a good handle on the initial and final state radiation model to use. If there are different amounts of radiation in the event, the kinematics can change, and the acceptance can be affected.

We have performed the analysis in four different configurations, one each of varying Λ_{QCD} by 2.0 and 0.5 in ISR and FSR. We summed the differences of the different samples in quadrature to obtain the total uncertainty. Table 4.29 shows the results of the calculation on the pretag efficiency.

We assign a systematic of 2.0% due to changing the initial and final state radiation.

Sample	Change in Cross Section
Less ISR ($\Lambda_{QCD}/2.0$)	-1.5%
More ISR ($\Lambda_{QCD} * 2.0$)	-0.2%
Less FSR ($\Lambda_{QCD}/2.0$)	0.0%
More FSR ($\Lambda_{QCD} * 2.0$)	-0.9%
Quadrature Sum	1.8%

Table 4.29: Changes in cross section due to different initial and final state radiation configurations.

4.7.8 Parton Distribution Functions

The parton distribution function chosen for this analysis was the CTEQ parameterization outlined in [10, 11]. There are uncertainties associated with this parameterization, as well as other parameterizations that could change the kinematics of the event slightly, thus changing the acceptance.

In order to account for this, we re-weight the events that are already generated with the new PDF eigenvectors. The weight for each event is the ratio of the PDFs of the new set with the ratio of the old set. We then sum the weights to determine the effect on the cross section. We repeat this for the variations of the PDF we have used for the analysis, as well as performing the same for the MRST PDF set.

We determine that there is a 2.0% systematic uncertainty associated with our choice of PDF.

4.7.9 Event Model

The production models used for different Monte Carlo generators are based on different assumptions. Thus, there are small differences in the way processes can be produced (i.e. p_T and η distributions). Because of this, a systematic uncertainty

must be assigned to cover these differences.

We have chosen to use PYTHIA as our Monte Carlo generator for the signal sample. In order to deal with this systematic, we have also performed the analysis using the HERWIG generator. One caveat is that the branching ratios of $W \to \ell\nu$ are different between the two. In PYTHIA, the measured value of 0.108 is used, while in HERWIG, the theoretical value of 0.111 is used. Correcting for this difference, we see a change of 1.0% in our result. Thus, we assign a 1.0% systematic uncertainty for the Monte Carlo event model.

4.7.10 Summary of Systematic Uncertainties

A summary table showing all the uncertainties on the various components of the analysis and the effect on the $t\bar{t}$ cross section is given in Table 4.31.

4.8 Results

4.8.1 Unoptimized Background Summary

Table 4.32 shows the summary (from Tables C.4-C.10, C.11,C.12-C.14, and C.17) for the different components of the unoptimized analysis in the ≥ 3 jet bin. Note that the pretag efficiency for the W+HF backgrounds are calculated using:

$$\epsilon_{pretag} = \frac{N_{W+Jets} f_{HF}}{\sigma_{W+HF} \int \mathcal{L} dt} \tag{4.34}$$

where σ_{W+HF} is the sum of the 3+4 jet bin cross sections in Table 4.16. The other backgrounds use the cross sections given in Table 4.11, and the $t\bar{t}$ is taken at the measured value of the cross section.

	$H_T > 0$, $M_T > 0$			
Quantity	Variation in Quantity		Variation in $\sigma_{t\bar{t}}$	
Systematic	≥ 1 Tags	≥ 2 Tags	≥ 1 Tags	≥ 2 Tags
Lepton ID (CEM)	1.6		1.6	
Lepton ID (CMUP)	1.9		1.9	
Lepton ID (CMX)	1.7		1.7	
ISR/FSR	2.0		2.0	
PDF	2.0		2.0	
PYTHIA vs HERWIG	1.0		1.0	
Lepton Isolation	5.0		5.0	
JES	2.9		2.9	
b-tagging SF	6.6		5.2	13.5
$W + HF$	26	26	6.2	2.6
$W + LF$	20	66	2.2	0.5
EW and Single top	12	18	0.9	0.8
Non-W	30	60	2.7	12.0
Total Backgrounds			7.3	13.1
Luminosity	5.9		5.9	

Table 4.30: Uncertainty of each component used to compute $\sigma_{t\bar{t}}$, and effect on $\sigma_{t\bar{t}}$. All numbers are quoted in percentage. This is for the *unoptimized* analysis.

	$H_T > 200$, $M_T > 20$			
Quantity	Variation in Quantity		Variation in $\sigma_{t\bar{t}}$	
Systematic	≥ 1 Tags	≥ 2 Tags	≥ 1 Tags	≥ 2 Tags
Lepton ID (CEM)	1.6		1.6	
Lepton ID (CMUP)	1.9		1.9	
Lepton ID (CMX)	1.7		1.7	
ISR/FSR	2.0		2.0	
PDF	2.0		2.0	
PYTHIA vs HERWIG	1.0		1.0	
Lepton Isolation	5.0		5.0	
JES	4.3		4.3	
b-tagging SF	6.6		5.2	13.5
$W + HF$	26	26	3.8	1.5
$W + LF$	20	66	1.4	0.4
EW and Single top	12	18	0.6	0.5
Non-W	39	60	1.2	5.7
Total Backgrounds		4.4	5.4	5.0
Luminosity	5.9		5.9	

Table 4.31: Uncertainty of each component used to compute $\sigma_{t\bar{t}}$, and effect on $\sigma_{t\bar{t}}$. All numbers are quoted in percentage. This is for the *optimized* analysis.

	ϵ_{pretag}	$\epsilon_{\geq 1}$	$\epsilon_{\geq 2}$	N_{pre}	$N_{\geq 1}$	$N_{\geq 2}$
$t\bar{t}$ (8.9 pb)	7.47 ± 0.49	60.06 ± 3.13	15.73 ± 2.13	209.66 ± 18.51	125.85 ± 12.92	32.96 ± 5.33
$W + b\bar{b}$ (*)	3.52 ± 1.17	49.49 ± 2.84	8.21 ± 1.10	25.79 ± 8.58	12.76 ± 4.34	2.12 ± 0.78
$W + c\bar{c}$ (*)	2.99 ± 1.03	14.53 ± 1.87	0.07 ± 0.02	39.31 ± 13.51	5.71 ± 2.12	0.03 ± 0.01
$W + c$ (*)	1.69 ± 0.48	9.49 ± 1.25	0.00 ± 0.00	39.55 ± 11.20	3.75 ± 1.22	0.00 ± 0.00
$W + LF$	-	-	-	583.64± 51.55	13.54± 2.74	0.58 ± 0.15
Non-W	-	-	-	101.24± 27.98	10.38± 3.96	1.99 ± 4.31
Single top, t-channel	1.57 ± 0.11	51.78 ± 2.94	9.45 ± 1.33	3.27 ± 0.93	1.69 ± 0.49	0.31 ± 0.10
Single top, s-channel	2.26 ± 0.15	61.01 ± 3.15	15.73 ± 2.12	2.08 ± 0.20	1.27 ± 0.14	0.33 ± 0.06
WW	0.76 ± 0.05	5.32 ± 0.74	0.10 ± 0.05	31.30 ± 2.84	1.66 ± 0.31	0.03 ± 0.02
WZ	0.44 ± 0.03	15.04 ± 1.26	2.23 ± 0.41	5.51 ± 0.51	0.83 ± 0.11	0.12 ± 0.03
ZZ	0.09 ± 0.01	14.77 ± 2.03	2.32 ± 0.75	0.43 ± 0.04	0.06 ± 0.01	0.01 ± 0.00
$Z \to \tau\tau$	0.01 ± 0.00	6.28 ± 2.28	0.00 ± 0.00	0.38 ± 0.06	0.03 ± 0.01	0.00 ± 0.00

Table 4.32: Background summary for events in ≥ 3 jets for unoptimized analysis. Note that the W+HF backgrounds (denoted by *) use an effective cross section for the pretag efficiency. Also note that ≥ 2 numbers have been iterated to the same cross section as ≥ 1.

4.8.2 Unoptimized Results

The luminosity weighted pretag efficiency in ≥ 3 jets is

$$\epsilon_{pretag}^{t\bar{t}} \int \mathcal{L}dt = 23.6 \pm 2.1 \; pb^{-1} \tag{4.35}$$

The tag rate in ≥ 3 jets is

$$\epsilon_{\geq 1\; tag}^{t\bar{t}} = 60.06 \pm 3.13\% \tag{4.36}$$

$$\epsilon_{\geq 2\; tag}^{t\bar{t}} = 15.73 \pm 2.13\% \tag{4.37}$$

To obtain the cross section, we start the analysis assuming $\sigma = 6.1$ pb. We then iterate until the results are stable to $< 1\%$. The number of observed events is 171 for the single tags and 36 for the double tags. After iteration, the number of background events is

$$N_{bkg}^{\geq 1\; tag} = 51.70 \pm 9.11 \tag{4.38}$$

$$N_{bkg}^{\geq 2\; tag} = 5.61 \pm 3.98 \tag{4.39}$$

This gives unoptimized cross sections of

$$\sigma_{\geq 1} = 8.9 \pm 0.9(stat) \pm 1.1(sys) \; pb \tag{4.40}$$

$$\sigma_{\geq 2} = 8.2 \pm 1.6(stat) \pm 1.7(sys) \; pb \tag{4.41}$$

The Poisson asymmetric uncertainties of these cross sections are

$$\sigma_{\geq 1} = 8.9^{+1.0}_{-0.9}(stat)^{+1.2}_{-1.0}(sys) \; pb \tag{4.42}$$

$$\sigma_{\geq 2} = 8.2^{+1.7}_{-1.5}(stat)^{+2.0}_{-1.5}(sys) \; pb \tag{4.43}$$

Figures 4.30(a) and 4.30(b) show the likelihood curves with statistical uncertainty bands.

4.8.3 Optimized Background Summary

Table 4.33 shows the summary (from Tables C.19-C.26, C.27,C.28-C.30, and C.33) for the different components of the optimized analysis in the ≥ 3 jet bin. Note that the pretag efficiency for the W+HF backgrounds are calculated using:

$$\epsilon_{pretag} = \frac{N_{W+Jets} f_{HF}}{\sigma_{W+HF} \int \mathcal{L} dt} \tag{4.44}$$

where σ_{W+HF} is the sum of the 3+4 jet bin cross sections in Table 4.16. The other backgrounds use the cross sections given in Table 4.11, and the $t\bar{t}$ is taken at the measured value of the cross section.

	ϵ_{pretag}	$\epsilon_{\geq 1}$	$\epsilon_{\geq 2}$	N_{pre}	$N_{\geq 1}$	$N_{\geq 2}$
$t\bar{t}$ (8.7 pb)	6.71 ± 0.49	60.93 ± 3.15	16.37 ± 2.21	184.32 ± 17.29	112.25 ± 12.04	30.13 ± 4.96
$W + b\bar{b}$ (*)	1.71 ± 0.62	53.83 ± 3.08	9.06 ± 1.21	12.54 ± 4.52	6.75 ± 2.48	1.14 ± 0.45
$W + c\bar{c}$ (*)	1.37 ± 0.51	16.38 ± 2.09	0.05 ± 0.01	18.07 ± 6.76	2.96 ± 1.19	0.01 ± 0.00
$W + c$ (*)	0.68 ± 0.22	10.66 ± 1.41	0.00 ± 0.00	15.88 ± 5.06	1.69 ± 0.61	0.00 ± 0.00
$W + LF$	-	-	-	219.07± 31.86	7.94 ± 1.64	0.32 ± 0.12
Non-W	-	-	-	28.38 ± 9.35	2.58 ± 1.34	0.88 ± 1.71
Single top, t-channel	0.96 ± 0.07	54.78 ± 3.11	10.52 ± 1.51	2.01 ± 0.58	1.10 ± 0.32	0.21 ± 0.07
Single top, s-channel	1.52 ± 0.12	63.26 ± 3.28	17.27 ± 2.34	1.40 ± 0.15	0.88 ± 0.10	0.24 ± 0.04
WW	0.37 ± 0.03	6.45 ± 0.94	0.12 ± 0.08	15.23 ± 1.49	0.98 ± 0.20	0.02 ± 0.02
WZ	0.22 ± 0.02	17.04 ± 1.55	2.22 ± 0.49	2.80 ± 0.28	0.48 ± 0.07	0.06 ± 0.02
ZZ	0.05 ± 0.00	14.62 ± 2.52	2.01 ± 0.89	0.22 ± 0.02	0.03 ± 0.01	0.00 ± 0.00
$Z \to \tau\tau$	0.00 ± 0.00	8.64 ± 5.23	0.00 ± 0.00	0.08 ± 0.02	0.01 ± 0.01	0.00± 0.01

Table 4.33: Background summary for ≥ 3 jets for optimized analysis. Note that the W+HF backgrounds (denoted by *) use an effective cross section for the pretag efficiency.

4.8.4 Optimized Results

The luminosity weighted pretag efficiency in ≥ 3 jets using $H_T > 200$ GeV and $M_T^W > 20$ GeV/c^2 is

$$\epsilon_{pretag}^{t\bar{t}} \int \mathcal{L}dt = 21.2 \pm 2.0\ pb^{-1} \tag{4.45}$$

The tag rate in ≥ 3 jets is

$$\epsilon_{\geq 1\ tag}^{t\bar{t}} = 60.93 \pm 3.15\% \tag{4.46}$$

$$\epsilon_{\geq 2\ tag}^{t\bar{t}} = 16.37 \pm 2.21\% \tag{4.47}$$

To obtain the cross section, we start the analysis assuming $\sigma = 6.1$ pb. We then iterate until the results are stable to $< 1\%$. The number of observed events is 138 for the single tags and 33 for the double tags. After iteration, the number of background events is

$$N_{bkg}^{\geq 1\ tag} = 25.41 \pm 4.94 \tag{4.48}$$

$$N_{bkg}^{\geq 2\ tag} = 2.89 \pm 1.94 \tag{4.49}$$

This gives cross sections of

$$\sigma_{\geq 1} = 8.7 \pm 0.9(stat) \pm 1.0(sys)\ pb \tag{4.50}$$

$$\sigma_{\geq 2} = 8.7 \pm 1.7(stat) \pm 1.6(sys)\ pb \tag{4.51}$$

The results of the Method 2 background calculation are shown in Table 4.35, along with the prediction from $t\bar{t}$. The $t\bar{t}$ contribution is shown at the measured cross sections.

The Poisson asymmetric uncertainties of these cross sections are

$$\sigma_{\geq 1} = 8.7^{+0.9}_{-0.9}(stat)^{+1.2}_{-0.9}(sys)\ pb \quad (4.52)$$

$$\sigma_{\geq 2} = 8.7^{+1.8}_{-1.6}(stat)^{+1.9}_{-1.3}(sys)\ pb \quad (4.53)$$

Figures 4.30(c) and 4.30(d) show the likelihood curves with statistical uncertainty bands.

Unoptimized Event Counts					
Jet Multiplicity	1 jet	2 jets	3 jets	4 jets	$\geq$ 5 jets
Pretags					
Data	30628	4791	769	179	36
$t\bar{t}$ (8.9 pb)	9.20 ± 0.82	49.55 ± 4.40	96.66 ± 8.58	86.37 ± 7.67	26.63 ± 2.38
$\geq$ 1 Tags					
EW	4.47 ± 0.69	8.47 ± 1.25	2.10 ± 0.34	0.39 ± 0.08	0.10 ± 0.03
Single Top	6.86 ± 1.71	11.55 ± 2.42	2.50 ± 0.53	0.41 ± 0.09	0.06 ± 0.01
Non-W	42.25 ± 10.05	19.34 ± 4.77	6.70 ± 1.92	3.07 ± 1.06	0.61 ± 0.39
$W + LF$	94.05 ± 19.28	39.12 ± 7.86	11.05 ± 2.24	2.27 ± 0.45	0.22 ± 0.05
$W + c$	99.23 ± 26.61	21.06 ± 6.03	3.22 ± 0.98	0.51 ± 0.23	0.02 ± 0.02
$W + c\bar{c}$	33.52 ± 10.17	20.13 ± 6.60	4.88 ± 1.70	0.81 ± 0.40	0.02 ± 0.02
$W + b\bar{b}$	98.74 ± 32.37	55.13 ± 17.85	10.94 ± 3.44	1.70 ± 0.79	0.12 ± 0.12
$t\bar{t}$ (8.9 pb)	3.08 ± 0.35	25.19 ± 2.66	55.28 ± 5.74	53.78 ± 5.50	16.80 ± 1.73
Bkg	379.12 ± 72.53	174.80 ± 32.04	41.39 ± 6.84	9.16 ± 1.83	1.15 ± 0.43
Bkg + $t\bar{t}$	382.20 ± 72.53	199.99 ± 32.15	96.67 ± 8.93	62.94 ± 5.80	17.95 ± 1.78
Data	432	242	95	63	19
$\geq$ 2 Tags					
EW	-	0.42 ± 0.09	0.14 ± 0.04	0.02 ± 0.01	0.01 ± 0.01
Single Top	-	1.52 ± 0.29	0.53 ± 0.13	0.09 ± 0.03	0.02 ± 0.01
Non-W	-	0.29 ± 0.17	0.90 ± 0.50	0.78 ± 0.49	0.34 ± 2.64
$W + LF$	-	0.55 ± 0.12	0.30 ± 0.06	0.20 ± 0.04	0.08 ± 0.05
$W + HF$	-	8.39 ± 2.93	1.84 ± 0.62	0.34 ± 0.16	0.03 ± 0.02
$t\bar{t}$ (8.2 pb)	-	4.28 ± 0.70	11.68 ± 1.91	14.06 ± 2.27	4.63 ± 0.74
Bkg	-	11.17 ± 2.96	3.71 ± 0.82	1.42 ± 0.52	0.48 ± 2.64
Bkg + $t\bar{t}$	-	15.46 ± 3.04	15.39 ± 2.08	15.48 ± 2.33	5.11 ± 2.74
Data	-	15	17	16	3

Table 4.34: Method 2 background calculation summary for 318.5 pb^{-1} for the *unoptimized* analysis. Here the $t\bar{t}$ prediction is show for the measured cross sections of 8.9 pb and 8.2 pb for ≥ 1 and ≥ 2 tags, respectively. Taken from tables as described in Section 4.8.1.

Optimized Event Counts					
Jet Multiplicity	1 jet	2 jets	3 jets	4 jets	$\geq$ 5 jets
Pretags					
Data	30283	4676	324	142	34
$t\bar{t}$ (8.7 pb)	8.80 $\pm$ 0.83	47.13 $\pm$ 4.45	79.67 $\pm$ 7.51	79.48 $\pm$ 7.49	25.16 $\pm$ 2.39
$\geq$ 1 Tags					
EW	4.38 $\pm$ 0.69	8.28 $\pm$ 1.25	1.13 $\pm$ 0.20	0.28 $\pm$ 0.06	0.09 $\pm$ 0.03
Single Top	6.75 $\pm$ 1.70	11.31 $\pm$ 2.41	1.59 $\pm$ 0.34	0.34 $\pm$ 0.08	0.05 $\pm$ 0.01
Non-W	37.23 $\pm$ 8.96	15.91 $\pm$ 4.01	1.51 $\pm$ 0.54	0.88 $\pm$ 0.54	0.19 $\pm$ 0.26
$W + LF$	93.08 $\pm$ 19.09	38.23 $\pm$ 7.68	5.80 $\pm$ 1.21	1.86 $\pm$ 0.37	0.28 $\pm$ 0.06
$W + c$	98.90 $\pm$ 26.31	20.78 $\pm$ 5.90	1.28 $\pm$ 0.41	0.39 $\pm$ 0.18	0.03 $\pm$ 0.02
$W + c\bar{c}$	33.25 $\pm$ 10.02	19.92 $\pm$ 6.49	2.22 $\pm$ 0.81	0.72 $\pm$ 0.36	0.02 $\pm$ 0.02
$W + b\bar{b}$	98.13 $\pm$ 31.97	54.39 $\pm$ 17.49	5.32 $\pm$ 1.75	1.28 $\pm$ 0.61	0.15 $\pm$ 0.12
$t\bar{t}$ (8.7 pb)	2.94 $\pm$ 0.35	23.99 $\pm$ 2.64	46.47 $\pm$ 5.04	49.88 $\pm$ 5.34	15.89 $\pm$ 1.72
Bkg	371.71 $\pm$ 71.52	168.81 $\pm$ 31.33	18.84 $\pm$ 3.30	5.75 $\pm$ 1.34	0.82 $\pm$ 0.31
Bkg + $t\bar{t}$	374.65 $\pm$ 71.52	192.80 $\pm$ 31.44	65.31 $\pm$ 6.02	55.64 $\pm$ 5.51	16.71 $\pm$ 1.74
Data	427	232	62	58	18
$\geq$ 2 Tags					
EW	-	0.41 $\pm$ 0.08	0.06 $\pm$ 0.02	0.01 $\pm$ 0.01	0.01 $\pm$ 0.01
Single Top	-	1.48 $\pm$ 0.28	0.36 $\pm$ 0.09	0.08 $\pm$ 0.02	0.02 $\pm$ 0.01
Non-W	-	0.31 $\pm$ 0.20	0.31 $\pm$ 0.18	0.38 $\pm$ 0.44	0.19 $\pm$ 1.09
$W + LF$	-	0.48 $\pm$ 0.11	0.10 $\pm$ 0.04	0.17 $\pm$ 0.04	0.05 $\pm$ 0.04
$W + HF$	-	8.25 $\pm$ 2.86	0.89 $\pm$ 0.32	0.24 $\pm$ 0.12	0.02 $\pm$ 0.02
$t\bar{t}$ (8.7 pb)	-	4.42 $\pm$ 0.74	11.06 $\pm$ 1.84	14.28 $\pm$ 2.35	4.78 $\pm$ 0.78
Bkg	-	10.93 $\pm$ 2.89	1.71 $\pm$ 0.38	0.88 $\pm$ 0.46	0.29 $\pm$ 1.09
Bkg + $t\bar{t}$	-	15.35 $\pm$ 2.99	12.78 $\pm$ 1.88	15.16 $\pm$ 2.39	5.07 $\pm$ 1.35
Data	-	15	15	15	3

Table 4.35: Method 2 background calculation summary for 318.5 pb^{-1} for the *optimized* analysis. Here the $t\bar{t}$ prediction is shown for the measured cross section of 8.7 pb (single) and 8.7 pb (double). Taken from tables as described in Section 4.8.3.

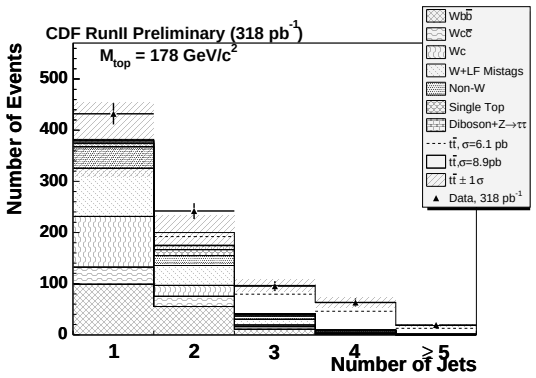

(a) Unoptimized, ≥ 1 Tag, $\sigma = 8.9$ pb

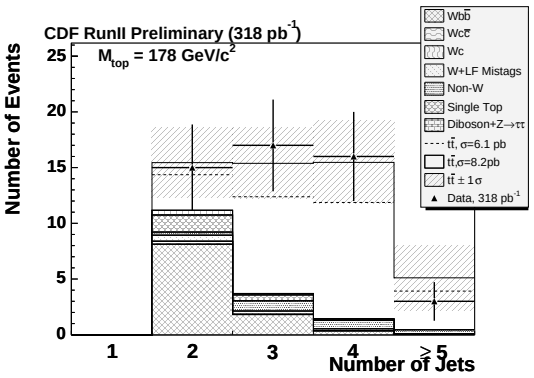

(b) Unoptimized, ≥ 2 Tag, $\sigma = 8.2$ pb

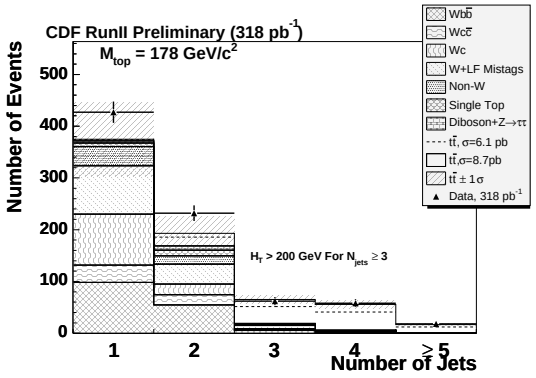

(c) Optimized, ≥ 1 Tag, $\sigma = 8.7$ pb

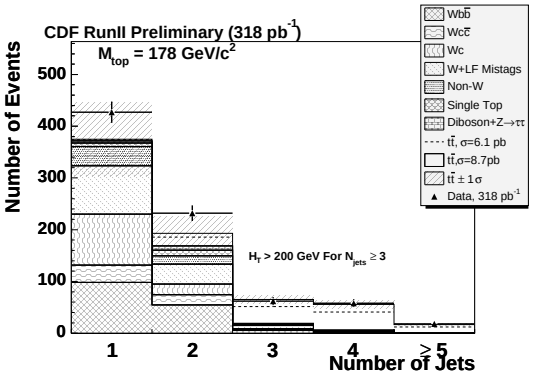

(d) Optimized, ≥ 2 Tag, $\sigma = 8.7$ pb

Figure 4.29: Number of jets for unoptimized and optimized analyses. $t\bar{t}$ cross sections are shown at the measured values in all cases. Total expectation is shown with 1σ error bands in diagonal hatching.

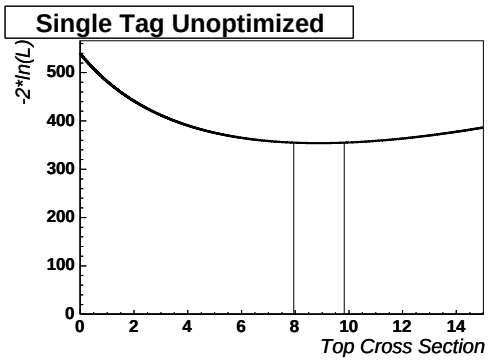

(a) Unoptimized, ≥ 1 Tag, $\sigma = 8.9$ pb

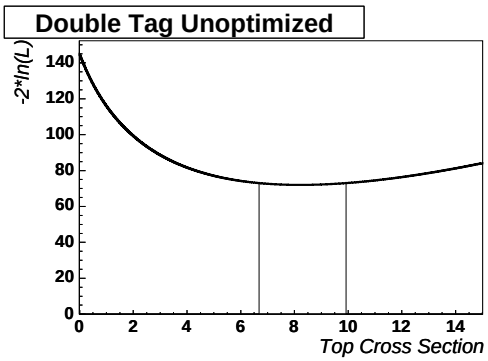

(b) Unoptimized, ≥ 2 Tag, $\sigma = 8.2$ pb

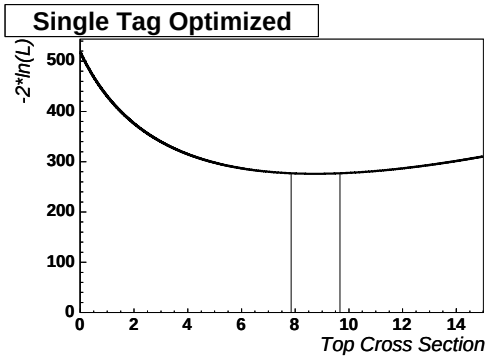

(c) Optimized, ≥ 1 Tag, $\sigma = 8.7$ pb

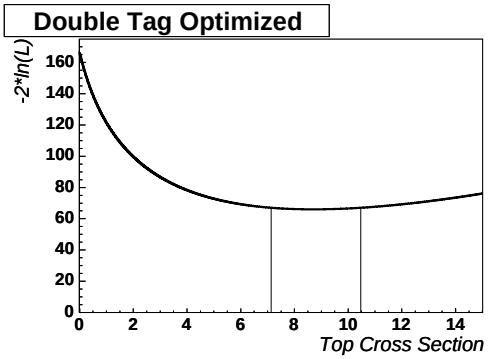

(d) Optimized, ≥ 2 Tag, $\sigma = 8.7$ pb

Figure 4.30: Likelihood curves for unoptimized and optimized analyses.

4.8.5 *A priori* Expectation

The *a priori* expectation of the variance of the $t\bar{t}$ cross sections can be determined by taking the expected background inputs for $\sigma = 6.1$ pb, and varying them within their Gaussian uncertainties. The final number of events per bin is then fluctuated in a Poisson distribution. We can then obtain the expected cross sections, and examine the ratio of $\sigma_{\geq 2}$ to $\sigma_{\geq 1}$.

Figure 4.31(a) shows the results of 10000 pseudoexperiments of the $t\bar{t}$ cross sections for ≥ 1 and ≥ 2 tags, assuming $\sigma = 6.1$ pb. It also shows the ratio $\sigma_{\geq 2}/\sigma_{\geq 1}$ to see what the possible spread is between the two measurements.

We see that the mean values of the expected experiments are at 6.1 pb, which is the input value. We also see that the average ratio is 1.0. Given this distribution, there is a probability of 6% that the cross section is 6.1 and we measure 8.7.

Figure 4.31(b) shows the results of 10000 similar pseudoexperiments of the $t\bar{t}$ cross sections for ≥ 1 and ≥ 2 tags, assuming $\sigma = 6.1$ pb. However, in this case, we have only selected experiments where the ≥ 1 cross section has fluctuated from 6.1 pb to > 8.7 pb. The probability of obtaining a ≥ 2 cross section of > 8.7 pb is still high, even given a fluctuation in the ≥ 1 cross section. The distribution of the ratio of $\geq 2/\geq 1$ is also shown.

4.8.6 Top Mass Dependence

Since we have quoted our cross section at a specific top mass (178 GeV/c^2), it is necessary to give the dependence on the assumed top mass input. In order to do this, we use HERWIG $t\bar{t}$ samples with top mass assumptions of 170,172.5,178,182.5, and

185. We then re-calculate our results using those assumed top masses. We then use a linear fit to interpolate to a given top mass. The way this is done is to calculate the effect on the overall event efficiency (pretag + tag) and assume that is a function of the input top mass, using the formula

$$\sigma(m) = \sigma(m_0)\frac{\epsilon(m_0)}{\alpha \times (m - m_0) + \epsilon(m_0)} \tag{4.54}$$

Table 4.37 shows the results of our efficiency calculations. Due to the differences between PYTHIA and HERWIG, we only use α from the HERWIG prediction and use ϵ from PYTHIA.

Our fit results are $\alpha_{\geq 1} = 0.000298 \pm 0.000061/GeV/c^2$, and $\alpha_{\geq 2} = 0.000091 \pm 0.000025/GeV/c^2$. They are shown in Figure 4.32(a). This gives

$$\sigma_{\geq 1} = 8.9 \pm 0.9(stat) \pm 1.0(sys)\ pb \tag{4.55}$$

and

$$\sigma_{\geq 2} = 8.9 \pm 1.6(stat) \pm 1.5(sys)\ pb \tag{4.56}$$

assuming $m_{top} = 175\ GeV/c^2$.

4.8.7 Comparison Of Gen5 Optimized Results with Gen4 Optimized Results

The major differences between this result and the Gen4 result outlined in [40] are as follows.

Primarily, we have used a new tagger. The previous tagger was optimized using poorer tracking algorithms and resolutions. It placed stringent requirements on the

quality of the input tracks, and used almost no final vertex selection. The current tagger was optimized using the current tracking algorithms. In general, the track selection was loosened, while the final vertex selection was tightened to reduce fakes. This resulted in an increase of about 20% in the per-jet b-tagging efficiency, leading to an increase of 50% in the double-tag efficiency.

Also, the Monte Carlo changed substantially, so the data-to-MC ratios for lepton ID have changed, as well as that for the b-tagging scale factor, and also the jet energy corrections.

Moreover, there are now two methods for evaluating the b-tagging scale factor, the electron and muon methods. The other major difference is in the Non-W background estimate and the usage of the $M_T^W > 20\ GeV/c^2$ cut, which reduces the background level and increases the systematic uncertainty.

The systematic for the light-flavor asymmetry is also increased in Gen5 relative to Gen4. The reason for this is that we feel there is a sample dependence of this correction that was not covered by the systematic in Gen4. We double the systematic to be conservative.

Table 4.36 shows the differences between Gen4 and Gen5 for the major parts of the analysis.

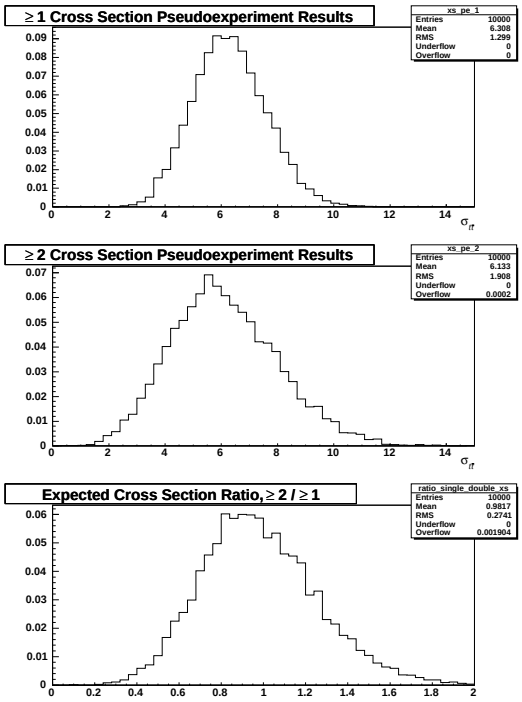

(a) *A priori* expectation for the distribution of cross sections for the ≥ 1 and ≥ 2 analyses, plus their ratio (2/1). The theoretical cross section taken here is 6.1 pb.

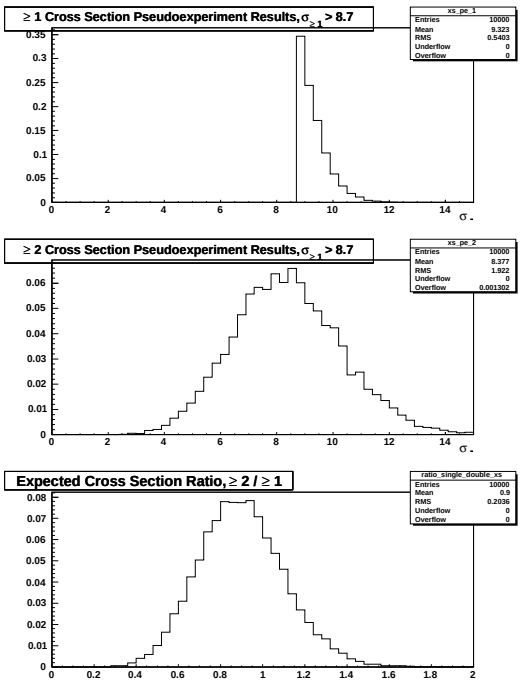

(b) *A priori* expectation for the distribution of cross sections for the ≥ 1 and ≥ 2 analyses, plus their ratio (2/1), when the ≥ 1 cross section is above 8.7 pb. The theoretical cross section taken here is 6.1 pb.

Figure 4.31: *A priori* expectations of cross section for the optimized analysis.

Quantity	Gen4	Gen5
CEM		
Lepton ID Scale Factor	0.931 ± 0.015	0.959 ± 0.015
Pre-tag Efficiency	4.1 ± 0.4%	3.8 ± 0.3%
CMUP		
Lepton ID Scale Factor	0.787 ± 0.016	0.784 ± 0.020
Pre-tag Efficiency	2.1 ± 0.2%	2.0 ± 0.2%
CMX		
Lepton ID Scale Factor	0.960 ± 0.018	0.941 ± 0.020
Pre-tag Efficiency	1.0 ± 0.8%	0.8 ± 0.1%
Common Systematics		
ISR/FSR	3.0%	2.0%
PDF	1.5%	2.0%
PYTHIA vs HERWIG	1.4%	1.0%
Lepton Isolation	5.0%	5.0%
Jet Energy Scale	4.9%	4.3%
B-Tagging Quantities		
≥ 1 Tag Eff	53.4 ± 3.2%	60.9 ± 3.2%
≥ 2 Tag Eff	11.0 ± 1.6%	16.4 ± 2.2%
Scale Factor	0.82 ± 0.06	0.909 ± 0.060
Mistag Matrix Sys	12%	22%
Background Level Systematics (≥ 1 Tag)		
W+Heavy Flavor	26%	26%
Mistags	12%	20%
Non-W	14%	39%
Monte Carlo Bkgs	18%	12%
Effect on $\sigma_{t\bar{t}}$ (≥ 1 Tag)		
W+Heavy Flavor	4.8%	3.8%
Mistags	2.6%	1.4%
Non-W	2.6%	1.2%
Monte Carlo Bkgs	3.2%	0.6%
Total Systematic Uncertainty on $\sigma_{t\bar{t}}$		
≥ 1 Tag	13.7%	11.4%
≥ 2 Tag	19.2%	17.2%

Table 4.36: Comparison of Gen4 and Gen5 results.

Top Mass Dependence of $\epsilon_{t\bar{t}}$			
m_{top}	ϵ_{pre} (%)	$\epsilon_{\geq 1\ tag}$ (%)	$\epsilon_{\geq 2\ tag}$ (%)
170	8.69 ± 0.10	64.90 ± 0.49	19.10 ± 0.40
172.5	8.69 ± 0.10	65.01 ± 0.34	19.36 ± 0.28
178	8.99 ± 0.06	65.08 ± 0.18	18.77 ± 0.15
182.5	9.15 ± 0.11	65.60 ± 0.33	19.19 ± 0.27
185	9.31 ± 0.11	64.93 ± 0.33	19.55 ± 0.27

Table 4.37: Monte Carlo top mass dependence of efficiencies. Uncertainties are MC statistical only. No scale factors are applied. Note that these efficiencies use the HERWIG generator, not the default PYTHIA generator.

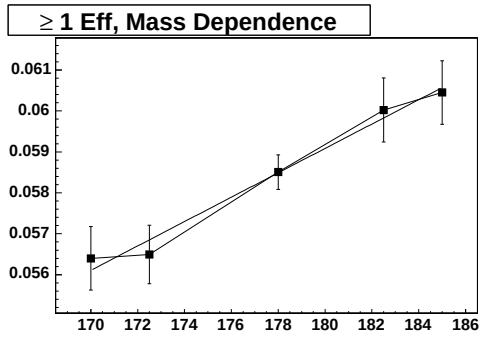

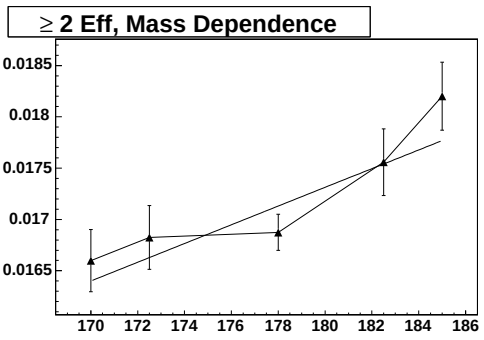

(a) Dependence of efficiency on top mass. Note HERWIG values are shown here. The straight lines are the fits.

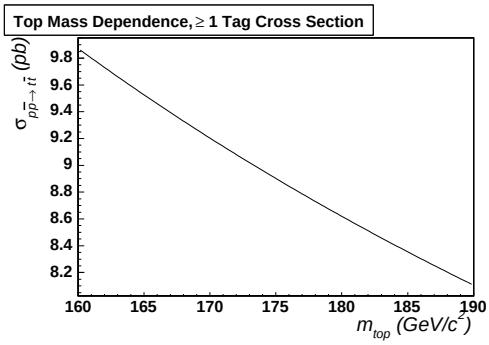

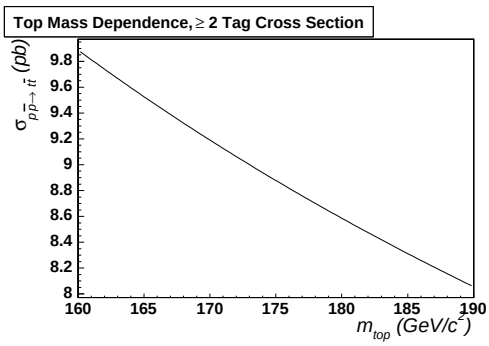

(b) Dependence of cross section on top mass.

Figure 4.32: Top mass dependencies.

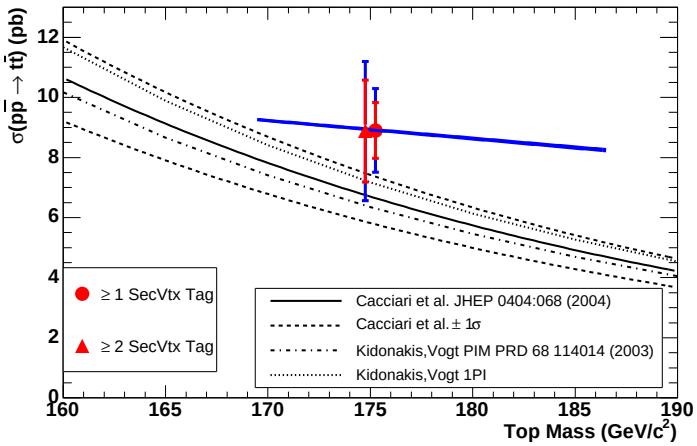

(a) Comparison of results with theory. The line shows the top mass dependence of the result.

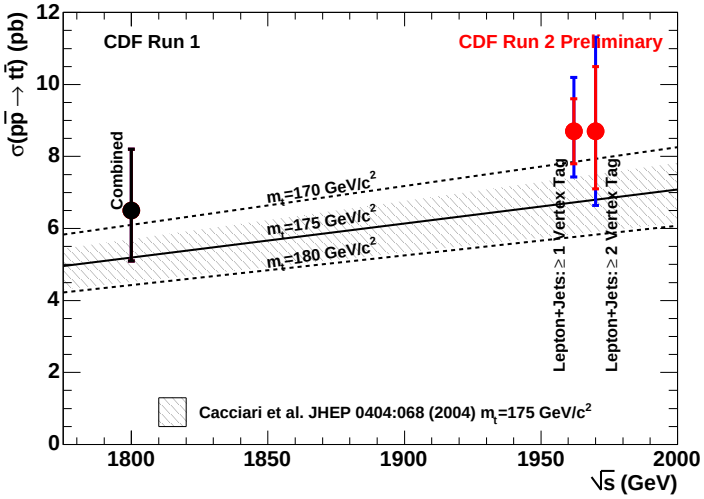

(b) Comparison of results with theory versus $\sqrt{s}$. The world average of Run I results is shown along with the optimized measurements of this analysis.

Figure 4.33: Comparisons of results with theory.

4.9 Improvement of Background Uncertainties with N_{jet} Spectrum Fitting

If we examine Figure 4.29(c), we notice that there are somewhat large uncertainties in the background estimation in the 1 and 2 jet bins. The data also seems to be slightly larger than the total background prediction, although it is within the quoted uncertainty.

Examining Table 4.27, we see that there are large uncertainties on the W+HF and Non-W backgrounds, while the mistag and "Monte Carlo derived" backgrounds like dibosons and single top have small uncertainties. However, the Non-W background in Figure 4.29(c) is very small compared to the W+HF backgrounds, and so the W+HF backgrounds contribute much more to the overall background uncertainty level.

Because of the observation that the uncertainty in the W+HF estimate is driving the overall background estimate in the 1- and 2-jet bins, combined with the size of the sample with > 300 pb^{-1}, it is feasible to fit for the W+HF background level using a likelihood fit to the N_{jet} spectrum.

If we assume that the *shape* of the N_{jet} spectrum is well-modeled in the Monte Carlo, but that it's overall *level* is not very well determined, we can assume the various background species will have an overall *fit factor* that will multiply the entire N_{jet} spectrum together. We can then use the information we obtain from a fit in the 1- and 2-jet bins to constrain the backgrounds in the $\geq$ 3-jet bins, and reduce our background uncertainty further, as can be seen in Equation 4.30.

In order to use all the information available, we will fit the N_{jet} spectrum bin-by-

bin, for $= 1$ and ≥ 2 tags simultaneously (i.e. we no longer examine ≥ 1 and ≥ 2). We also must take into account all the correlations between the various different backgrounds (for example, the correlation between the Non-W estimate and the mistag estimate due to the correction of $(1 - F_{Non-W})$ in the mistag matrix prediction).

We will also input the various background contributions and their estimated uncertainties (as shown in Table 4.27) and allow them all to fluctuate. We expect that only the heavy flavor fit factor will differ substantially from unity.

Before we tackle the complete likelihood with all backgrounds allowed to float independently, we first examine a likelihood with only the heavy flavor allowed to float, and all other backgrounds constrained to their values from Table 4.35.

4.9.1 Simple Example: Only Fit W+HF

The number of events expected in a given jet bin is given by the equation

$$N_{exp}^{jet}(\sigma_{t\bar{t}}, F_{HF}) = \sigma_{t\bar{t}}\mathrm{SF}\varepsilon_{MC}\int \mathcal{L}dt + N_{HF}^{pred}F_{HF} + \sum N_{other} \tag{4.57}$$

where

- $\sigma_{t\bar{t}}$ is the $t\bar{t}$ cross section
- F_{HF} is the *fit factor* by which the W+HF backgrounds (as shown in Table 4.35) should be multiplied
- ϵ_{MC} is the event efficiency in the Monte Carlo
- SF is the b-tagging scale factor
- $\int \mathcal{L}dt$ is the luminosity

- N_{HF}^{pred} is the W+HF prediction from method 2
- $\sum N_{other}$ is the sum of the other Method 2 backgrounds (constrained for the moment to the values shown in Table 4.35).

We then maximize the Poisson likelihood for single-tag data,

$$-2\ln\mathcal{L}(\sigma_{t\bar{t}}, F_{HF}) = 2N^i_{exp}(\sigma_{t\bar{t}}, F_{HF}) + 2\ln\Gamma(N^i_{obs}+1) - 2N^i_{obs}\ln N^i_{exp}(\sigma_{t\bar{t}}, F_{HF}). \quad (4.58)$$

We can then constrain the heavy flavor fit fraction to what is externally measured from Method 2 (see [1]) by including a Gaussian constraint on F_{HF}:

$$-2\ln\mathcal{L}(\sigma_{t\bar{t}}, F_{HF}) = 2N^i_{exp}(\sigma_{t\bar{t}}, F_{HF}) + 2\ln\Gamma(N^i_{obs}+1) - 2N^i_{obs}\ln N^i_{exp}(\sigma_{t\bar{t}}, F_{HF}) + \left(\frac{F_{HF}-1}{\sigma_{HF}}\right)^2. \quad (4.59)$$

It is now clear how to extend the likelihood to include all backgrounds and their uncertainties.

4.9.2 Full Likelihood

In the full likelihood expression, we fit each jet bin separately, and we also fit the $= 1$ and ≥ 2 tags simultaneously. We float the single and double mistags and Non-W backgrounds separately because of the correlations in these backgrounds with other backgrounds. We also include the b-tagging scale factor into the likelihood, because it correlates many of the different components of the fit.

The full expression we obtain is

$$\begin{aligned}
-2\ln\mathcal{L} &= -2\ln\mathcal{L}(\sigma_{t\bar{t}}, F_{EWK}, F_{Non-W}, F_{MT}, F_{HF}, F_{MT2}, F_{Non-W2}, F_{SF}) \\
&= 2\sum_{i\text{jets}}\sum_{1,2\text{tags}} [N^i_{exp}(\sigma_{t\bar{t}}, F_{EWK}, F_{Non-W}, F_{MT}, F_{HF}, F_{MT2}, F_{Non-W2}, F_{SF}) \\
&\quad -N^i_{obs}\ln N^i_{exp}(\sigma_{t\bar{t}}, F_{EWK}, F_{Non-W}, F_{MT}, F_{HF}, F_{MT2}, F_{Non-W2}, F_{SF}) \\
&\quad +\ln\Gamma(N^i_{obs}+1)] \\
&\quad +\left(\frac{F_{EWK}-1}{\sigma_{EWK}}\right)^2 + \left(\frac{F_{Non-W}-1}{\sigma_{Non-W}}\right)^2 + \left(\frac{F_{MT}-1}{\sigma_{MT}}\right)^2 \\
&\quad +\left(\frac{F_{HF}-1}{\sigma_{HF}}\right)^2 + \left(\frac{F_{MT2}-1}{\sigma_{MT2}}\right)^2 + \left(\frac{F_{Non-W2}-1}{\sigma_{Non-W2}}\right)^2 + \left(\frac{F_{SF}-1}{\sigma_{SF}}\right)^2 \qquad (4.60)
\end{aligned}$$

where

$$\begin{aligned}
N^i_{exp:1-tag} &= N^i_{exp}(\sigma_{t\bar{t}}, F_{EWK}, F_{Non-W}, F_{MT}, F_{HF}, F_{MT2}, F_{Non-W2}, F_{SF}) \qquad (4.61) \\
= \sigma_{t\bar{t}}(F_{SF})^{k1} &\times (\epsilon^{t\bar{t}}_{pre})(\epsilon^{t\bar{t}}_{1-tag})(SF)\int\mathcal{L}dt \\
+F_{EWK}(F_{SF})^{k1} &\times \sum_{bkg=EW,s.top}\sigma^{bkg}(\epsilon^{bkg}_{pre})(\epsilon^{bkg}_{1-tag})(SF)\int\mathcal{L}dt \\
+F_{Non-W} &\times N^{\geq 1}_{Non-W} \\
+F_{HF}(F_{SF})^{k1} &\times \left(\frac{N_{pre}-N^{NonW}_{pre}-F_{EWK}N^{EW,s.top}_{pre}-F_{t\bar{t}}N^{t\bar{t}}_{pre}}{N_{pre}-N^{NonW}_{pre}-N^{EW,s.top}_{pre}-N^{t\bar{t}}_{pre}}\right)(SF)(f_{HF})(\epsilon_{1-tag}) \\
+F_{MT} &\times \alpha\beta N^{pred}_{-}\left(\frac{N_{pre}-N^{NonW}_{pre}-F_{EWK}N^{EW,s.top}_{pre}-F_{t\bar{t}}N^{t\bar{t}}_{pre}-F_{WHF}N^{pre}_{WHF}}{N_{pre}-N^{NonW}_{pre}-N^{EW,s.top}_{pre}-N^{t\bar{t}}_{pre}-N^{pre}_{WHF}}\right) \\
N^i_{exp:2-tag} &= N^i_{exp}(\sigma_{t\bar{t}}, F_{EWK}, F_{Non-W}, F_{MT}, F_{HF}, F_{MT2}, F_{Non-W2}, F_{SF}) \qquad (4.62) \\
= \sigma_{t\bar{t}}(F_{SF})^{k2} &\times (\epsilon^{t\bar{t}}_{pre})(\epsilon^{t\bar{t}}_{2-tag})(SF)\int\mathcal{L}dt \\
+F_{EWK}(F_{SF})^{k2} &\times \sum_{bkg=EW,s.top}\sigma^{bkg}(\epsilon^{bkg}_{pre})(\epsilon^{bkg}_{2-tag})(SF)\int\mathcal{L}dt \\
+F_{Non-W2} &\times N^{\geq 1}_{Non-W} \\
+F_{HF}(F_{SF})^{k2} &\times \left(\frac{N_{pre}-N^{NonW}_{pre}-F_{EWK}N^{EW,s.top}_{pre}-F_{t\bar{t}}N^{t\bar{t}}_{pre}}{N_{pre}-N^{NonW}_{pre}-N^{EW,s.top}_{pre}-N^{t\bar{t}}_{pre}}\right)(SF)(f_{HF})(\epsilon_{2-tag}) \\
+F_{MT2} &\times \alpha_{LF}\beta N^{pred}_{+:-}\left(\frac{N_{pre}-N^{NonW}_{+}-F_{EWK}N^{EW,s.top}_{+}-F_{t\bar{t}}N^{t\bar{t}}_{+}-F_{WHF}N^{+}_{WHF}}{N_{pre}-N^{NonW}_{+}-N^{EW,s.top}_{+}-N^{t\bar{t}}_{+}-N^{+}_{WHF}}\right)
\end{aligned}$$

The fit factor for the scale factor (F_{SF}) comes into the expression raised to a power because there are more than one b-jets in the event. That is, if we consider

the efficiency to tag exactly one and exactly two b-jets given F_{1b} events with 1b and F_{2b} events with 2b's and no other species,

$$\begin{aligned} \epsilon_{1|1\vee 2} &= F_{1b}P(1|1) + 2F_{2b}P(1|2) + F_{2b}P(2|2) && (4.63)\\ &= F_{1b}\epsilon SF + 2F_{2b}\epsilon SF(1-\epsilon SF) + F_{2b}\epsilon^2 SF^2 && (4.64)\\ \epsilon_{2|2} &= P(2|2) && (4.65)\\ &= \epsilon^2 SF^2 && (4.66) \end{aligned}$$

where $P(i|j)$ is the probability to tag i b-jets given j b-jets total, $\epsilon_{1|1\vee 2}$ is the efficiency to tag 1 b-jet given 1 or 2 b-jets (given by F_{1b} and F_{2b}), and $\epsilon_{2|2}$ is the efficiency to tag 2 b-jets given 2 b-jets. In our case, $F_{1b} = 0.23$, $F_{2b} = 0.77$, $\epsilon = 0.44$ and $SF = 0.909$, and hence

$$\begin{aligned} k1 &= \frac{d\epsilon_{1|1\vee 2}}{dSF} = 0.51 && (4.67)\\ k2 &= \frac{d\epsilon_{2|2}}{dSF} = 2 && (4.68)\\ & && (4.69) \end{aligned}$$

The likelihood curve is given in Figure 4.34(c). The inputs and outputs of the likelihood are given in Table 4.38. All the input fit factors are sitting near their input values with the same uncertainty as input, except for the W+HF fit factor, as expected. The maximum likelihood of that fit factor is 1.16 ± 0.14. Also, examining the W+HF input value of 1.00 ± 0.30 and output value of 1.16 ± 0.14, we see that the fractional uncertainty was reduced from 30% to 12%. This improvement will be propagated into the signal region to obtain a better measurement of the cross section.

The correlations between the outputs of the likelihood are given in Table 4.39. The cross section is correlated strongly with the b-tagging scale factor and the heavy

flavor fit fraction. The cross section is not very correlated with the other backgrounds.

The fit results include the uncertainties due to the background uncertainty, the scale factor, and the statistical uncertainty. To this we must add the pretag and luminosity uncertainties. Combining everything, we obtain

$$\sigma_{t\bar{t}} = 8.90^{+0.91}_{-0.86}\,(stat)^{+1.02}_{-0.89}\,(bkg+sf) \pm 0.93\,(pretag+lum+shape)\;pb \quad (4.70)$$

$$= 8.90^{+0.91}_{-0.86}\,(stat)^{+1.28}_{-1.18}\,(sys)\;pb \quad (4.71)$$

$$= 8.90^{+1.57}_{-1.46}\,(stat+sys)\;pb \quad (4.72)$$

Figures 4.34(a) and 4.34(b) show the $= 1$ and ≥ 2 N_{jet} spectra including the fit results for the various components. Figures 4.35-4.42 show the results of pseudoexperiments to determine the sensitivity of the various fit factors in Table 4.38.

The distribution of the expected uncertainties on the $t\bar{t}$ cross section are shown in Figure 4.34(d). The measured values of 15.3% for the upper uncertainty and 13.9% for the lower uncertainties are also shown with blue arrows.

	Input	Output
F_{EWK}	1.00 ± 0.16	1.02 ± 0.16
F_{Non-W}	1.00 ± 0.33	1.08 ± 0.32
F_{MT1}	1.00 ± 0.12	1.08 ± 0.23
F_{HF}	1.00 ± 0.30	1.22 ± 0.13
F_{MT2}	1.00 ± 0.30	0.99 ± 0.30
F_{Non-W2}	1.00 ± 0.66	0.97 ± 0.66
F_{SF}	1.00 ± 0.06	1.00 ± 0.06

Table 4.38: Input values to likelihood fit factors, and values after maximization of the likelihood.

	$\sigma_{t\bar{t}}$	F_{EWK}	F_{Non-W}	F_{mistag}	F_{HF}	$F_{2-mistag}$	$F_{2-Non-W}$	F_{SF}
$\sigma_{t\bar{t}}$	1.000	-0.016	-0.006	-0.064	0.107	-0.003	-0.028	-0.513
F_{EWK}	-0.016	1.000	-0.004	-0.009	-0.063	-0.001	-0.000	-0.010
F_{Non-W}	-0.006	-0.004	1.000	-0.068	-0.343	0.002	0.004	0.007
F_{mistag}	-0.064	-0.009	-0.068	1.000	-0.641	0.003	0.010	0.033
F_{HF}	0.107	-0.063	-0.343	-0.641	1.000	-0.002	0.005	-0.299
$F_{2-mistag}$	-0.003	-0.001	0.002	0.003	-0.002	1.000	-0.001	-0.008
$F_{2-Non-W}$	-0.028	-0.000	0.004	0.010	0.005	-0.001	1.000	-0.042
F_{SF}	-0.513	-0.010	0.007	0.033	-0.299	-0.008	-0.042	1.000

Table 4.39: Correlation matrix for likelihood fit. It is clear that the backgrounds are not very correlated with the cross section. The only thing that is correlated is the scale factor, which is expected.

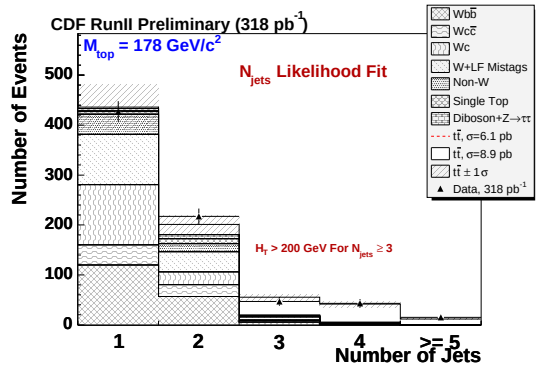

(a) Fit results for, $= 1$ Tag, $\sigma = 8.9$ pb

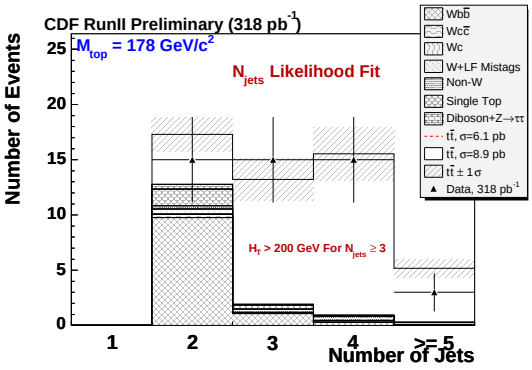

(b) Fit results for, ≥ 2 Tag, $\sigma = 8.9$ pb

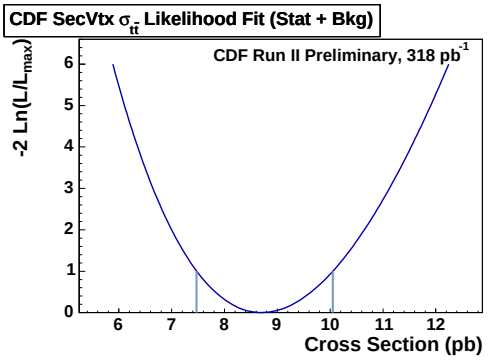

(c) Likelihood curve for N_{jets} fit.

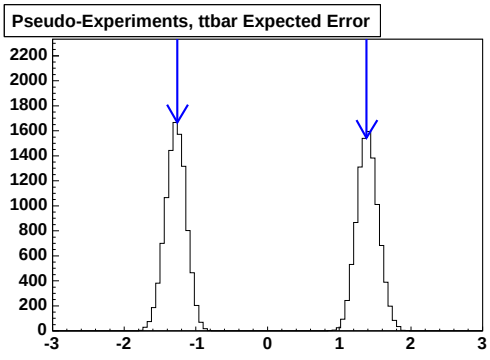

(d) Sensitivity of N_{jets} fit uncertainties.

Figure 4.34: Results of N_{jets} likelihood fit.

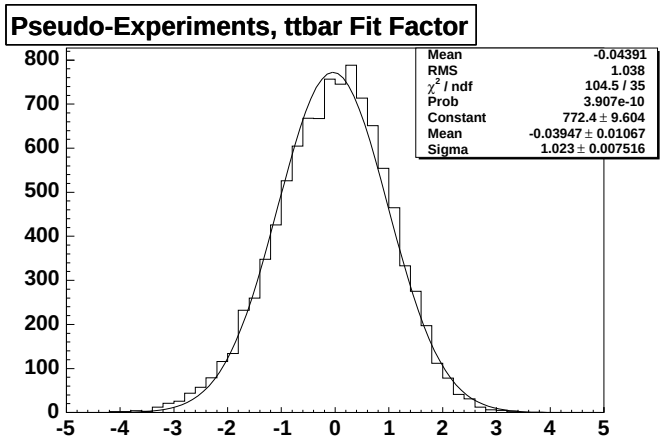

Figure 4.35: Sensitivity of the top cross section.

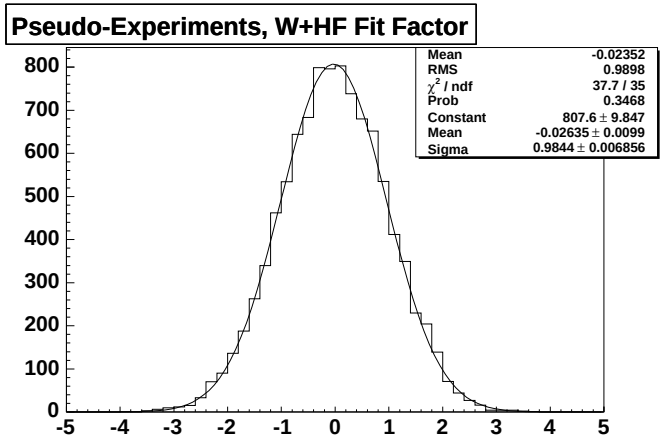

Figure 4.36: Sensitivity of the heavy flavor fraction.

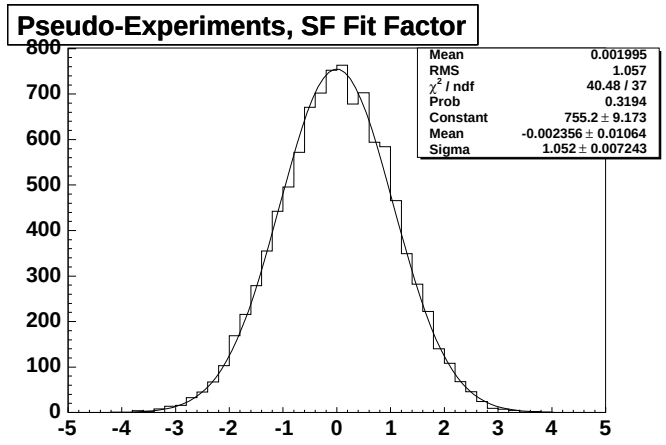

Figure 4.37: Sensitivity of the fit factor for the b-tagging scale factor.

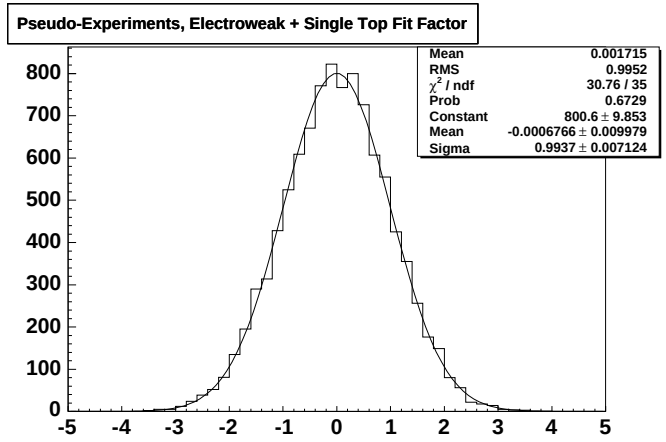

Figure 4.38: Sensitivity of the fit factor for the "Monte Carlo derived" backgrounds.

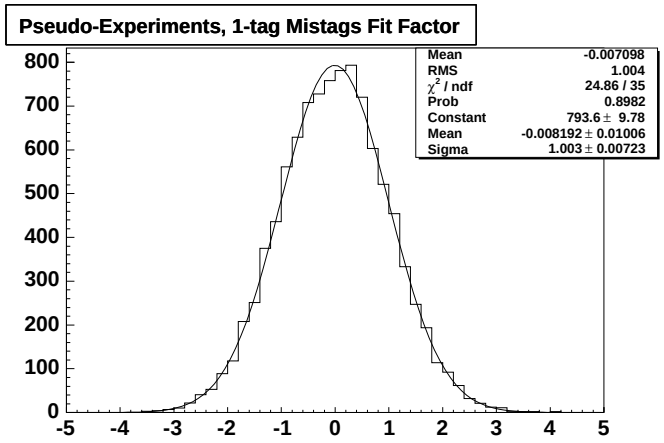

Figure 4.39: Sensitivity of the fit factor for the single mistag background.

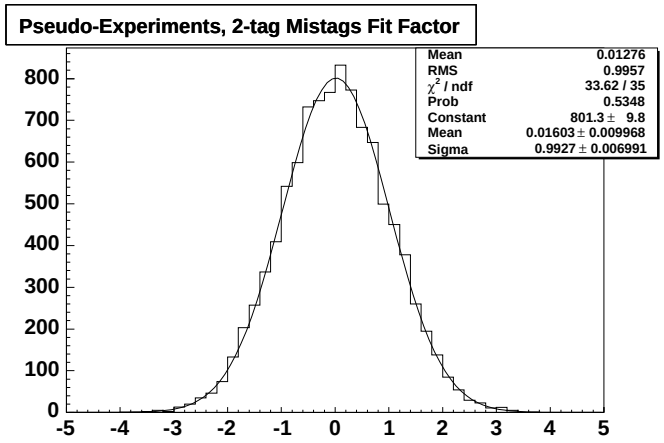

Figure 4.40: Sensitivity of the fit factor for the double mistag background.

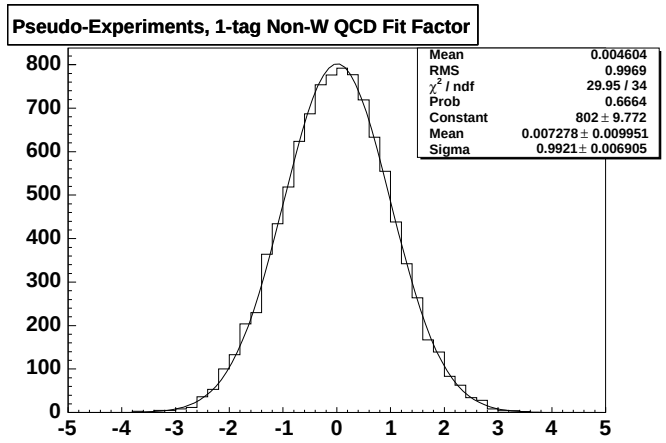

Figure 4.41: Sensitivity of the fit factor for the single Non-W background.

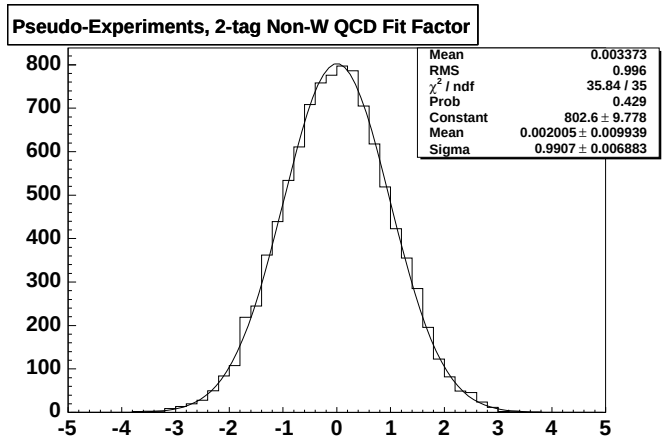

Figure 4.42: Sensitivity of the fit factor for the double Non-W background.

	N_{jets} Likelihood Fit	
Quantity	Variation in Quantity	Variation in $\sigma_{t\bar{t}}$
Lepton ID (CEM)	1.6	1.6
Lepton ID (CMUP)	1.9	1.9
Lepton ID (CMX)	1.7	1.7
ISR/FSR	2.0	2.0
PDF	2.0	2.0
PYTHIA vs HERWIG	1.0	1.0
Lepton Isolation	5.0	5.0
JES	4.3	5.0
b-tagging SF	6.6	5.0
Total Backgrounds		5.0
Shape Systematic		3.6
Luminosity	5.9	5.9

Table 4.40: Uncertainty of each component used to compute $\sigma_{t\bar{t}}$, and effect on $\sigma_{t\bar{t}}$. All numbers are quoted in percentage. This is for the N_{jets} spectrum fit.

4.10 Data Comparison Plots

Figures 4.43-4.58 show the comparison of the observed and predicted distributions for various kinematic and vertex variables. The shapes for the various background components are the same as in Section 4.5.1 for the kinematic variables. The $W + LF$ component of the tagged variables (such as vertex L_{2D} and tagged jet E_T) is taken from light flavor quarks in the $t\bar{t}$ Monte Carlo. The Non-W component of the tagged variables is taken from observed positive tags in the non-isolated, high $\not\!\!E_T$ region.

Excellent agreement is seen for all variables considered.

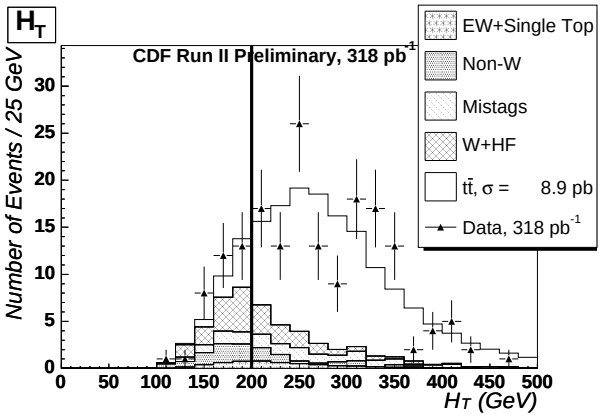

Figure 4.43: Observation and prediction of scalar sum of transverse energies (H_T), using the *unoptimized* measured cross section of 8.9 pb.

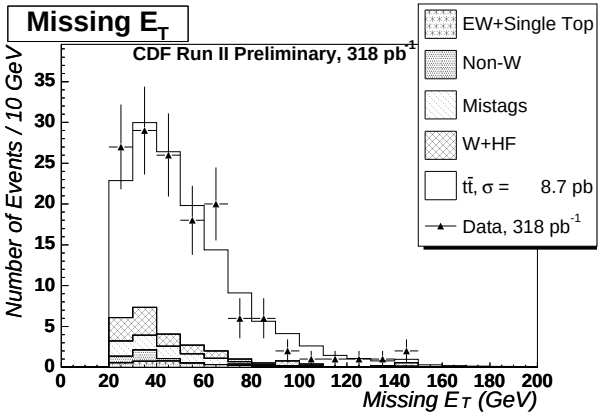

Figure 4.44: Observation and prediction of missing transverse energy ($\not\!\!E_T$), using the *optimized* measured cross section of 8.7 pb.

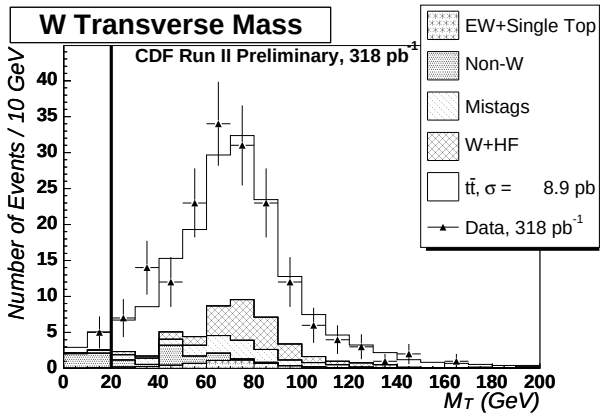

Figure 4.45: Observation and prediction of W transverse mass (M_T^W), using the *unoptimized* measured cross section of 8.9 pb.

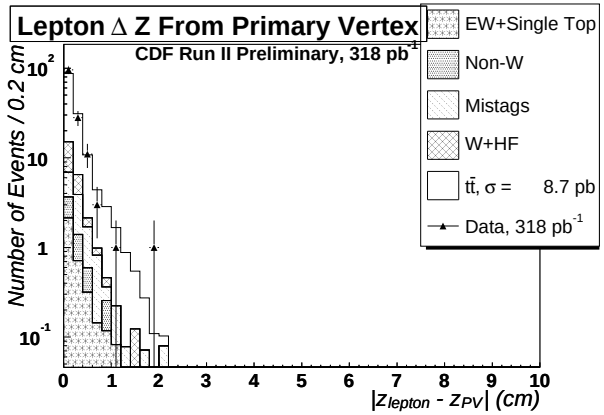

Figure 4.46: Observation and prediction of z-distance between lepton and primary vertex, using the *optimized* measured cross section of 8.7 pb.

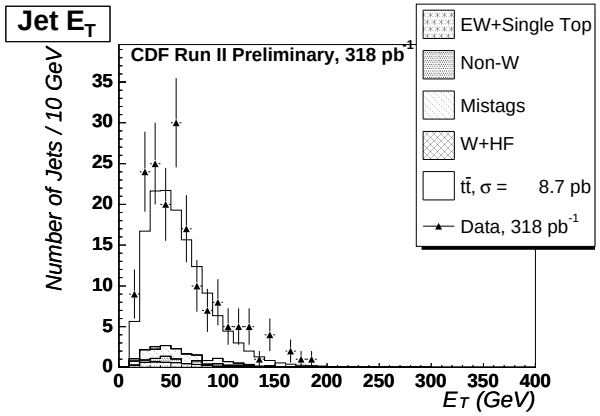

Figure 4.47: Observation and prediction of tagged jet E_T, using the *optimized* measured cross section of 8.7 pb.

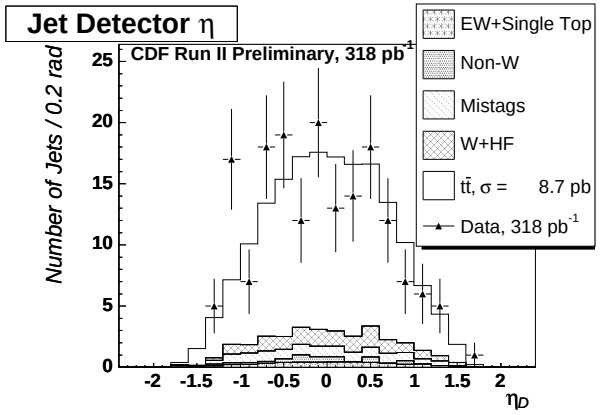

Figure 4.48: Observation and prediction of tagged jet η, using the *optimized* measured cross section of 8.7 pb.

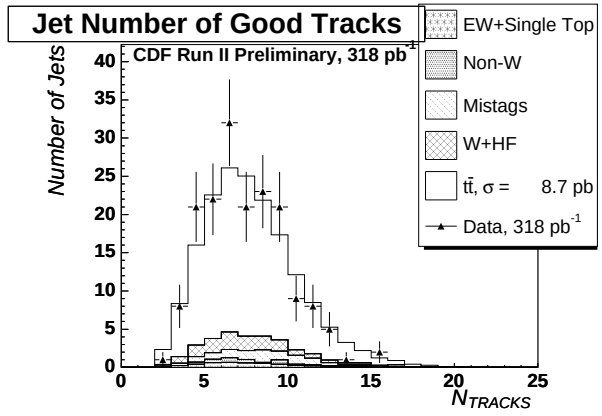

Figure 4.49: Observation and prediction of number of good tracks in tagged jets, using the *optimized* measured cross section of 8.7 pb.

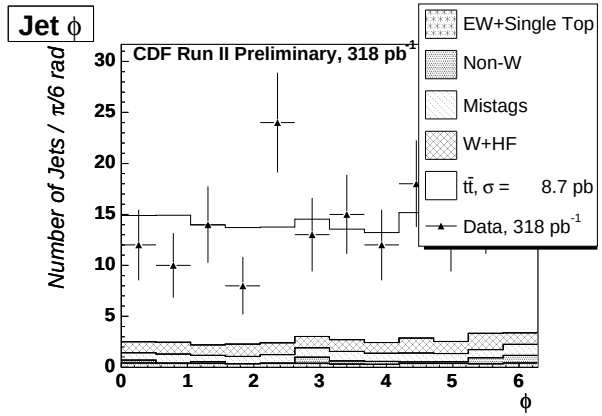

Figure 4.50: Observation and prediction of tagged jet ϕ, using the *optimized* measured cross section of 8.7 pb.

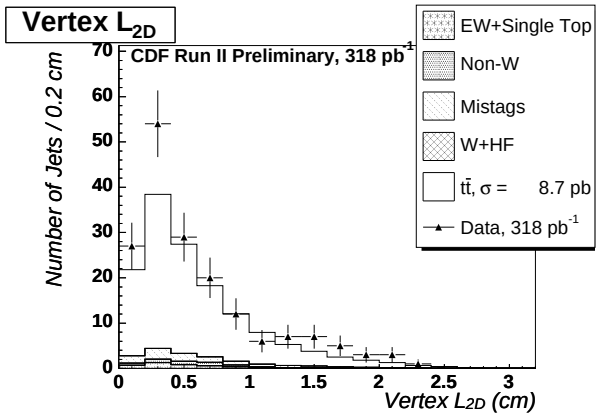

Figure 4.51: Observation and prediction of secondary vertex L_{xy}, using the *optimized* measured cross section of 8.7 pb.

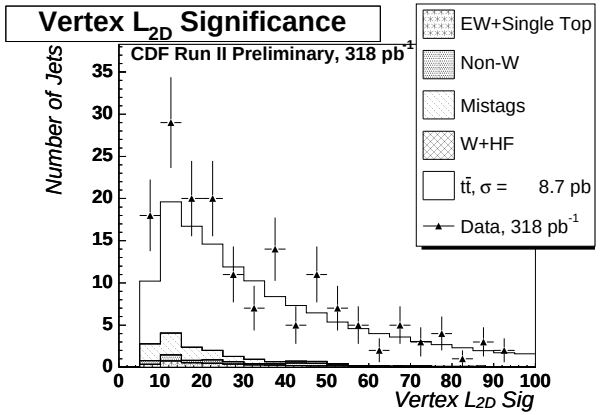

Figure 4.52: Observation and prediction of secondary vertex L_{xy} significance, using the *optimized* measured cross section of 8.7 pb.

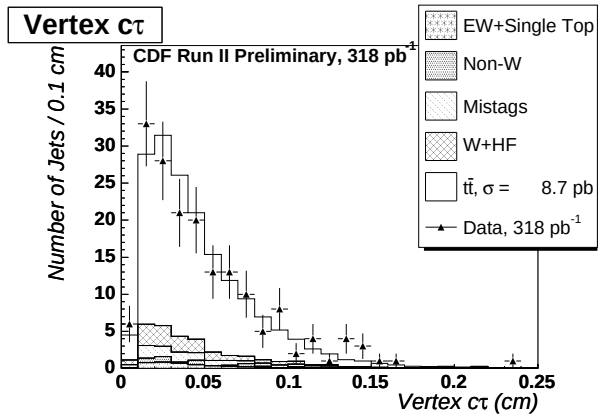

Figure 4.53: Observation and prediction of secondary vertex $c\tau$, using the *optimized* measured cross section of 8.7 pb.

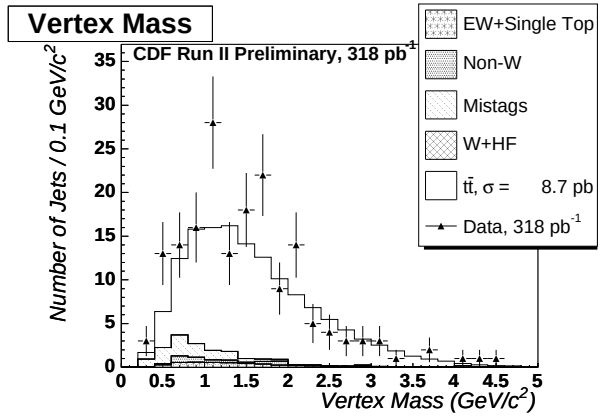

Figure 4.54: Observation and prediction of secondary vertex mass, using the *optimized* measured cross section of 8.7 pb.

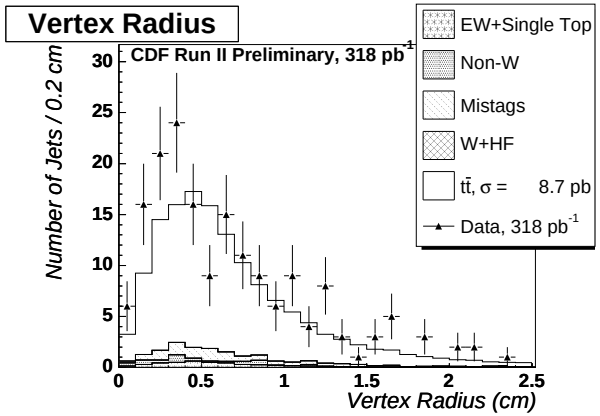

Figure 4.55: Observation and prediction of secondary vertex radius, using the *optimized* measured cross section of 8.7 pb.

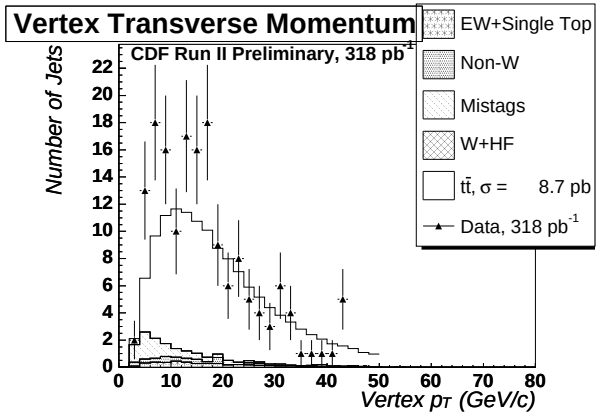

Figure 4.56: Observation and prediction of secondary vertex transverse momentum, using the *optimized* measured cross section of 8.7 pb.

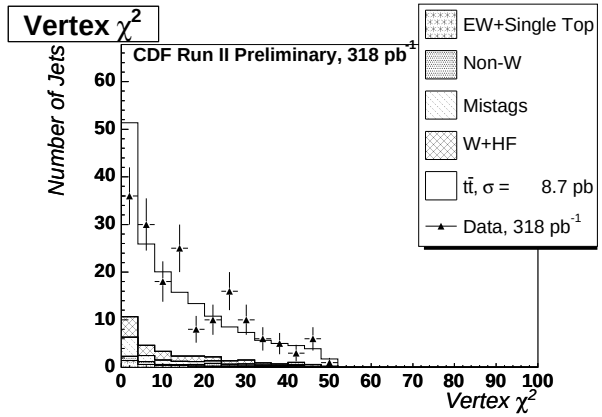

Figure 4.57: Observation and prediction of secondary vertex fit χ^2, using the *optimized* measured cross section of 8.7 pb.

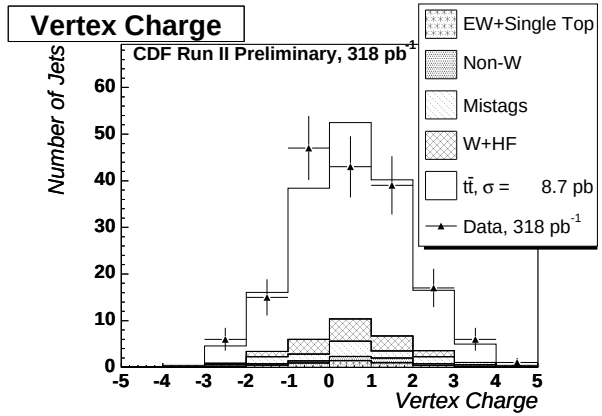

Figure 4.58: Observation and prediction of secondary vertex charge, using the *optimized* measured cross section of 8.7 pb.

4.11 Conclusions

We have presented a measurement of the $t\bar{t}$ production cross section with 318.5 pb^{-1} of data in the `5.3.3_nt` release. The unoptimized results are

$$\sigma_{\geq 1} = 8.9^{+1.0}_{-0.9}(stat)^{+1.2}_{-1.0}(sys)\ pb \tag{4.73}$$

$$\sigma_{\geq 2} = 8.2^{+1.7}_{-1.5}(stat)^{+2.0}_{-1.5}(sys)\ pb \tag{4.74}$$

For the optimized analysis with $H_T > 200$ GeV and $M_T^W > 20$ GeV, we obtain values of

$$\sigma_{\geq 1} = 8.7^{+0.9}_{-0.9}(stat)^{+1.2}_{-0.9}(sys)\ pb \tag{4.75}$$

$$\sigma_{\geq 2} = 8.7^{+1.8}_{-1.6}(stat)^{+1.9}_{-1.3}(sys)\ pb \tag{4.76}$$

We have also presented a measurement of the $t\bar{t}$ cross section by fitting the N_{jet} spectrum. We combine the $= 1$ and ≥ 2 tag cross sections to obtain

$$\sigma_{t\bar{t}} = 8.9^{+0.9}_{-0.9}(stat)^{+1.4}_{-1.3}(syst)\ pb. \tag{4.77}$$

Appendix A

Theoretical Appendices

A.1 Theoretical Overview

A.1.1 Gauge Symmetries

The Standard Model is based on intrinsic symmetries of the interactions between particles [52]. Once an internal symmetry is identified, the dynamics of the interaction can be derived using the group properties of that symmetry. The next section deals with the most accurate quantum field theory in the Standard Model, Quantum Electrodynamics. It is useful to examine this in some detail because it forms the basis of the other quantum field theories used to construct the Standard Model.

A.1.2 Quantum ElectroDynamics (QED)

Quantum electrodynamics (QED) is the most accurate theory in the Standard Model [53]. It describes the interactions of all charged particles, mediated by a gauge

boson called the *photon*. It has the simplest dynamics, and as such it is instructive to examine the theory in some detail.

The Lagrangian describing the interaction between charged particles is (see [9]):

$$\mathcal{L} = -\frac{1}{4}F_{\mu\nu}F^{\mu\nu} + \overline{\psi}\left(i\gamma^{\mu}D_{\mu} - m\right)\psi \tag{A.1}$$

where ψ is the field of the charged particle with mass m, γ^{μ} is the Dirac γ matrix, $F_{\mu\nu}$ is the electromagnetic field tensor

$$F_{\mu\nu} = \partial_{\mu}A_{\nu} - \partial_{\nu}A_{\mu} \tag{A.2}$$

and D_{μ} is the covariant derivative

$$D_{\mu} = \partial_{\mu} + ieA_{\mu}Q \tag{A.3}$$

Here, e is the charge of the particle, A_{μ} is the electromagnetic potential, and Q is the charge operator ($Q\psi = e\psi$).

The symmetry principle at work in QED is seen if we make the *local gauge transformation* (i.e. transform the field at every point in space and time)

$$\psi(x) \rightarrow e^{ie\Lambda(x)}\psi(x) \tag{A.4}$$

$$A_{\mu}(x) \rightarrow A_{\mu}(x) + \partial\Lambda(x)\partial x_{\mu} \tag{A.5}$$

After making these gauge transformations, the Lagrangian is unchanged. The phase factors $exp[i\Lambda(x)]$ belong to the symmetry group $U(1)$ of unitary transformations in one dimension. Note that without the photon field A_{μ}, the local gauge transformation would not leave the Lagrangian invariant. Thus, *requiring* local $U(1)$ gauge invariance *forces* the existence of the photon field and fixes the form of the Lagrangian.

Given the symmetry group and therefore the Lagrangian of the theory, it is now possible to calculate transition amplitudes. We will return to this after we consider the dynamics from an arbitrary symmetry group.

A.1.3 Generalization to Arbitrary Symmetries

If we examine some generic symmetry with generators T_i, satisfying the commutation relations

$$[T_i, T_j] = if_{ijk}T_k \tag{A.6}$$

where f_{ijk} are the structure constants for the symmetry group. For each linearly independent generator T_i, there is an associated gauge field W_i. The Lagrangian for a particle field ψ with gauge field W_i is then

$$\mathcal{L} = -\frac{1}{4}W_{i\mu\nu}W_i^{\mu\nu} + \overline{\psi}\left(i\gamma^\mu D_\mu - m\right)\psi \tag{A.7}$$

where

$$W_{i\mu\nu} = \partial_\mu W_{i\nu} - \partial_\nu W_{i\mu} - gf_{ijk}W_{j\mu}W_{k\nu} \tag{A.8}$$

$$D_\mu = \partial_\mu + igW_{i\mu}T_i \tag{A.9}$$

We see that Equations A.2 and A.3 are simple cases of these where the generators commute (i.e. $f_{ijk} = 0$). Such cases where the generators commute is called an *Abelian* gauge theory. Those cases where the generators do not commute are called *non-Abelian* gauge theories.

It can be shown [9] that this Lagrangian is invariant under the gauge transforma-

tions

$$\psi(x) \rightarrow [1 - ig\alpha_i(x)T_i]\,\psi(x) \tag{A.10}$$

$$W_{i\mu}(x) \rightarrow W_{i\mu}(x) + \partial_\mu\alpha_i(x) + gf_{ijk}\alpha_j(x)W_{k\mu}(x) \tag{A.11}$$

Again, it is possible to hypothesize the existence of a gauge boson given a symmetry principle and the requirement of gauge invariance. Thus, a prescription can be determined to construct a gauge theory given a specific symmetry principle. We will apply this to electroweak unification and strong interactions. However, a brief interlude into matrix element calculations and the Feynman Calculus is necessary and informative.

A.1.4 Relativistic Quantum Mechanical Amplitudes

In non-relativistic quantum mechanics, the probability of a given process to evolve from state $|i\rangle$ to $|f\rangle$ is equal to the transition matrix element squared, $P = |\mathcal{M}|^2$. The matrix element $\mathcal{M}$ is (see [8]):

$$\mathcal{M} = -i\int d^4x\langle f|\widehat{\mathcal{H}}_{int}(x,t)|i\rangle \tag{A.12}$$

where d^4x is the differential element of Lorentz space, $\langle f|$ is the final state and $|i\rangle$ is the initial state, and $\widehat{\mathcal{H}}_{int}(x,t)$ is the interaction Hamiltonian. In this sense, the interaction Hamiltonian "connects" the initial state to the final state. It is necessary to integrate over all possible connections between $|i\rangle$ and $\langle f|$ to find the total amplitude.

The different types of interaction transition amplitudes depend on the group properties of the interaction. These integrals are easily represented by "Feynman graphs" displaying the interactions. In these graphs, each particle is displayed by a line (wavy

for spin-1, with an arrow for spin $\frac{1}{2}$), and each interaction is represented by a vertex. Figure A.1 shows a 2→2 annihilation process via exchange of an intermediate gauge boson. The incoming particles are u and $\bar{u}$, the outgoing particles are v and $\bar{v}$, the propagator associated with the gauge boson is associated with some Green's function (a.k.a. *propagator*) P, and the interaction vertices are denoted by $i\sqrt{\alpha}\phi$, where α is the dimensionless coupling strength, and ϕ is some tensor that depends on the group properties. The matrix element for this process is then

$$\mathcal{M} = -i \int d^4x \left(\bar{u}(-i\sqrt{\alpha}\phi)u\right)(P)\left(\bar{v}(-i\sqrt{\alpha}\phi)v\right) \tag{A.13}$$

$$= i\alpha \int d^4x \left(\bar{u}(\phi)u\right)(P)\left(\bar{v}(\phi)v\right) \tag{A.14}$$

Given the propagator and the interaction transition amplitude for the interaction Hamiltonian, it is possible to evaluate this integral and hence calculate observable properties. The possible propagators in "natural" units are (see [7] for details):

1. Spin 0:

$$\frac{i}{q^2 - m^2} \tag{A.15}$$

2. Spin $\frac{1}{2}$:

$$\frac{i(\not{q} + m)}{q^2 - m^2} \tag{A.16}$$

3. Spin 1, massless:

$$\frac{-ig_{\mu\nu}}{q^2} \tag{A.17}$$

4. Spin 1, massive:

$$\frac{-i\left[g_{\mu\nu} - q_\mu q_\nu / m^2\right]}{q^2 - m^2} \tag{A.18}$$

Here, q is the 4-momentum of the propagating particle, $\not{q} = \gamma_\mu q^\mu$, and m is the mass of the propagator.

There are some intricacies involved when the particles have spin. Not only is it necessary to integrate over the kinematic phase space, it is also necessary to sum over all the spin configurations. Such a discussion is beyond the scope here, and we will simply state results when needed. See [8] for full details.

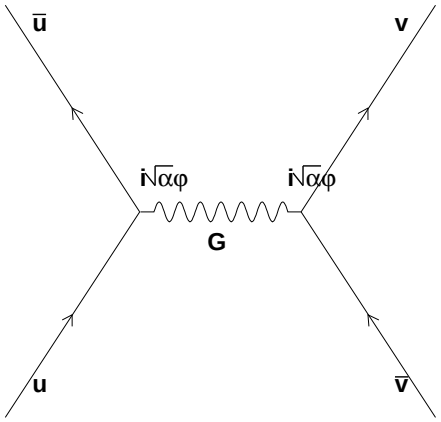

Figure A.1: Simple Feynman diagram to calculate matrix elements.

Because of the $U(1)$ symmetry underlying the electromagnetic interaction, there is only one vertex allowed. That is, only a charged particle can interact with a photon. Although any spin is allowed, we will focus on interactions with fermions (spin $\frac{1}{2}$). Figure A.2 shows the interaction vertex between a charged fermion like an electron, and a photon. The propagator is the photon propagator which is Equation A.17 and the vertex factor is $ie\gamma^\mu$.

The coupling strength of the electromagnetic interaction at low momentum trans-

fer is (putting in $\hbar$ and c to be clear):

$$\alpha_{EM} = \frac{ke^2}{\hbar c} = \frac{1}{137} \tag{A.19}$$

We now discuss the implications of having $\alpha < 1$ and $\alpha > 1$ in the next section.

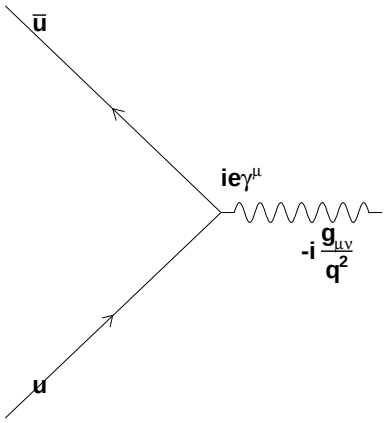

Figure A.2: Vertex between charged fermions and photons in quantum electrodynamics.

A.1.5 Renormalization

If we consider pair annihilation in QED as shown in Figure A.3, there are an infinite number of corrections to this diagram. Consider Figure A.4(a). Because the Feynman Calculus requires summation over all possible internal states, this diagrams (and infinitely many other) need to be calculated and summed.

The problem is that if we examine this loop diagram, the integral itself diverges logarithmically. That is, the matrix element for this is (see [7] for details):

$$\mathcal{M} = i\alpha \left(\bar{u}(\gamma^\mu)u\right) \left\{ \frac{g_{\mu\nu}}{q^2} \left(1 - \frac{\alpha}{3\pi} \left[\log \frac{\Lambda^2}{m^2} - f\left(\frac{-q^2}{m^2}\right) \right] \right) \right\} \left(\bar{v}(\gamma^\mu)v\right) \tag{A.20}$$

where we have introduced an arbitrary cutoff for the logarithmic divergence Λ, q^2 is the momentum transfer, and m is the mass of the fermion in the loop. We have defined

$$f(x) = 6 \int_0^1 z(1-z) \log 1 + xz(1-z) dz \tag{A.21}$$

which cannot be represented in closed form but is finite.

In order to accommodate this divergence, G. t'Hooft and M. Veltman [54, 55, 56] realized that what we measure in the laboratory (i.e. the fine structure constant $\frac{1}{137}$) is not equal to the α in equation A.20. Instead, we measure the quantity

$$\alpha_R = \alpha \sqrt{1 - \frac{\alpha}{3\pi} \left[\log \frac{M^2}{m^2} - f\left(\frac{-q^2}{m^2} \right) \right]} \tag{A.22}$$

Thus, the divergence is transferred to the *bare coupling constant* α, whereas we actually measure α_R as in Equation A.22. Thus, the "bare" coupling constant is effectively infinite. Notice also that α_R actually depends on the momentum transfer q^2. This means that the coupling constant will actually change with energy.

Of course, there are even higher-order loop diagrams to be considered, as in Figure A.4(b), and other diagrams as well. Fortunately, because $\alpha_{EM} < 1$, and each loop contributes another factor of α, this series will actually converge at some point. We can achieve any accuracy desired (limited only by computational considerations) because subsequent corrections are all smaller than the previous. All diagrams together create an infinite series instead of the finite sum shown in Equation A.22, but the terms get smaller and smaller.

When $\alpha < 1$, therefore, the theory is said to be *re normalizable*, i.e. the series in Equation A.22 converges. Problems arise when $\alpha > 1$, and the theory is said to

be *non-re normalizable*. Higher order diagrams contribute *more* to the total cross section than lower order diagrams. Hence, the theory is incalculable.

We shall see that quantum chromodynamics is non-re normalizable at longer length scales (i.e. small q^2). However, for short q^2 scales, the coupling gets weaker, and the theory becomes normalizable.

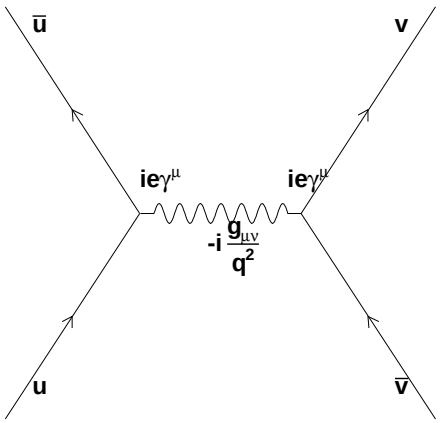

Figure A.3: QED diagram for tree level pair annihilation of charged particles.

A.1.6 Electroweak Unification

The first model of decays via the weak interaction were first formulated by Enrico Fermi in 1934. It was a pointlike theory that explained β decay very well. We now know that this theory was so successful because the mass of the electroweak propagator gauge bosons are very massive compared to the scale at which particles decay (except, interestingly, the top quark). Figure A.5 shows the decay of a particle via this pointlike interaction. The coupling strength is G. By measuring the lifetime

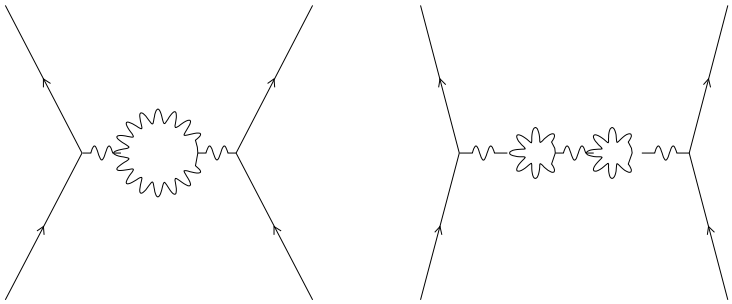

(a) (b)

Figure A.4: 1- and 2-loop diagrams for pair-annihilation of charged particles.

and mass of a particle very well, it is possible to know this factor very well. Currently, in natural units, $G = (1.16637 \pm 0.00001) \times 10^{-5}$ GeV^{-2} [6].

If we examine the propagator for a spin-1 particle where we assume $M \gg q$, i.e. that the mass of the propagator is much larger than the energies involved in the process, the propagator reduces to $1/M^2$, and so the interaction probability is g^2/M^2, where g is the coupling strength of the interaction. Given this fact, it is possible to obtain an order-of-magnitude estimate of the mass of the propagator given G. If we assume for the moment that the coupling strengths of the weak interaction and the electromagnetic interaction are the same (which turns out to be the case, as we shall see), then (in natural units):

$$G = \frac{g^2}{M^2} = \frac{e^2}{M^2} \tag{A.23}$$

$$M = \frac{e}{G^{1/2}} \sim 90\ GeV/c^2 \tag{A.24}$$

We shall see that this is remarkably close to the actual mass of the propagators of the

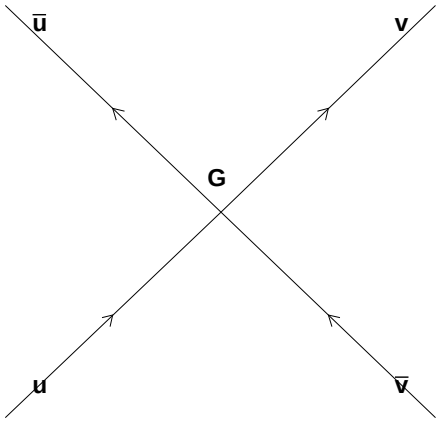

Figure A.5: Fermi's pointlike theory to calculate β-decay.

weak interaction. It is also suggestive that the electromagnetic and weak interactions could be unified into one force, if the weak interaction propagators have large masses. This, of course, turns out to be the case, as we shall see.

There are theoretical reasons why the Fermi theory does not work. At sufficiently high energies, the amplitude (hence the probability) for a transition is larger than 1, which is an inconsistency in the theory. It turns out that this can be solved by introducing the correct propagator.

We now turn to some phenomenology of the weak interactions. Firstly, in the mid-1950's, Lee and Yang (1956) predicted that parity was violated in the weak interactions (for details, see [8]). In 1957, Wu et. al. conclusively showed that the weak interaction violated parity by examining the angular distribution of decay products from polarized nuclei. That is, it turns out that right-handed particles (and left-handed antiparticles) do not participate in the weak interaction. This makes the

weak interaction somewhat strange, in that there are really two types of particles in the world for each that we observe in Table 1.1, a left-handed and a right-handed component, which have different dynamics. Also, it seems that the weak interaction only operates between specific particles. For example, a strange quark will decay into an up quark, but a strange quark decaying into a down quark has never been observed.

These two pieces of experimental phenomenology suggest that the weak interaction is somewhat more complicated than the electromagnetic. It seems to have doublets of coupling that operate only on the left-handed component of the particles. The simplest group that can satisfy this property is $SU(2)$, where the interactions are only between the left-handed components (for matter) and right-handed components (for antimatter).

Given this set of experimental observations, Glashow, Salam, and Weinberg formulated a theory of weak interactions that incorporated it with electrodynamics. The resulting work is known as *electroweak unification*. Essentially, they showed that it was possible to incorporate all the observed phenomena by using a symmetry principle in the electroweak sector. They assumed a gauge symmetry of $SU(2)_L \otimes U(1)_Y$, where $SU(2)_L$ is a symmetry in *weak isospin* (with quantum numbers denoted by I, z-components of weak isospin by I_3), and acts only on the left handed components of the particles, and $U(1)_Y$ is a symmetry analogous to the $U(1)$ symmetry of QED (with charge Q as the quantum number), but incorporates *weak hypercharge*, where $Y = 2(Q - I_3)$.

Each generator of the symmetry group (as mentioned above) gives rise to a gauge

boson. The three generators of the $SU(2)$ group are (in the 2-d representation)

$$T_1 = \frac{1}{2}\begin{pmatrix} 0 & 1 \\ 1 & 0 \end{pmatrix}, T_2 = \frac{1}{2}\begin{pmatrix} 0 & -i \\ i & 0 \end{pmatrix}, T_3 = \frac{1}{2}\begin{pmatrix} 1 & 0 \\ 0 & -1 \end{pmatrix} \tag{A.25}$$

where the T_i satisfy

$$[T_i, T_j] = i\epsilon_{ijk}T_k \tag{A.26}$$

and ϵ_{ijk} is the antisymmetric tensor that has the property $\epsilon_{ijk} = -\epsilon_{jik}$ and likewise for other permutations.

These generators give rise to three gauge bosons, plus one for the $U(1)_Y$ symmetry, W^1, W^2, W^3, and B^0. The Lagrangian for the $SU(2)_L \otimes U(1)_Y$ interaction is therefore

$$\mathcal{L} = -\frac{1}{4}\mathbf{W}^{\mu\nu} \cdot \mathbf{W}_{\mu\nu} - \frac{1}{4}B^{\mu\nu}B_{\mu\nu} + \bar{\psi}i\gamma^\mu D_\mu \psi \tag{A.27}$$

where the gauge fields are

$$W_{i\mu\nu} = \partial_\mu W_{i\nu} - \partial_\nu W_{i\mu} - g f_{ijk} W_{j\mu} W_{k\nu} \tag{A.28}$$

$$B_{\mu\nu} = \partial_\mu B_\nu - \partial_\nu B_\mu \tag{A.29}$$

and the covariant derivative is

$$\begin{aligned} D_\mu &= \partial_\mu + ig\mathbf{W}_\mu \cdot \mathbf{T} + ig'\frac{1}{2}YB_\mu \\ &= \partial_\mu + ig(W^+_\mu T^+ + W^-_\mu T^-) + igW_{3\mu}T_3 + ig'\frac{1}{2}YB_\mu \end{aligned} \tag{A.30}$$

In order to unify the electromagnetic and weak interactions, the neutral term in Eq A.30 must contain the electromagnetic coupling $ieQA$. Thus, the fields W^3 and B must combine linearly to form the physical γ and Z_0 bosons. The fields corresponding

to the four physical particles that are observed are

$$W_\mu^\pm(x) = \frac{1}{\sqrt{2}}(W_\mu^1(x) \pm iW_\mu^2(x)) \tag{A.31}$$

$$\begin{pmatrix} A_\mu(x) \\ Z_\mu(x) \end{pmatrix} = \begin{pmatrix} \cos\theta_W & -\sin\theta_W \\ \sin\theta_W & \cos\theta_W \end{pmatrix} \begin{pmatrix} W_\mu^3(x) \\ B_\mu^0(x) \end{pmatrix} \tag{A.32}$$

The parameter θ_W is called the "weak mixing angle" or "Weinberg angle". It is theoretically unconstrained and is a basic parameter of the theory. It's experimental value is $\sin\theta_W = 0.23120 \pm 0.00015$ [6]. We now rewrite the neutral term of Eq A.30 as

$$\begin{aligned} igW_3T_3 + ig'\frac{1}{2}YB &= iA\left[g\sin\theta_W T_3 + g'\cos\theta_W\frac{1}{2}Y\right] \\ &+ iZ\left[g\cos\theta_W T_3 - g'\sin\theta_W\frac{1}{2}Y\right] \end{aligned} \tag{A.33}$$

Given the definition $ieQ = ie(T_3 + \frac{1}{2}Y)$, we need

$$g = \frac{e}{\sin\theta_W} \tag{A.34}$$

$$g' = \frac{e}{\cos\theta_W} \tag{A.35}$$

Thus, it is possible to combine the electromagnetic and weak interactions into a *single* gauge theory with a mixing parameter θ_W.

Each particle in the Standard Model has an associated quantum number for weak isospin and weak hypercharge. Table A.1 shows the quantum numbers for the various particles in the Standard Model. Note that all the "up-type" quarks and "down-type" quarks share the same quantum numbers for the electroweak interaction.

Due to the fact that the generators of $SU(2)$ do not commute, there are self-interactions between the gauge bosons. Figures A.6(a)-A.6(c) show the interactions

between the W and Z bosons and the fermions and Figures A.6(d)-A.6(i) show the vertices of the self-interactions between the W and Z bosons and the photon. Once these vertices are known, it is possible to calculate their associated amplitudes as in Section A.1.4.

	I	I_3	Y	Q
$\begin{pmatrix} \nu_L \\ e_L \end{pmatrix}$	$\begin{pmatrix} 1/2 \\ 1/2 \end{pmatrix}$	$\begin{pmatrix} 1/2 \\ -1/2 \end{pmatrix}$	$\begin{pmatrix} -1 \\ -1 \end{pmatrix}$	$\begin{pmatrix} 0 \\ 1 \end{pmatrix}$
e_R	0	0	2	1
$\begin{pmatrix} u_L \\ d_L \end{pmatrix}$	$\begin{pmatrix} 1/2 \\ 1/2 \end{pmatrix}$	$\begin{pmatrix} 1/2 \\ -1/2 \end{pmatrix}$	$\begin{pmatrix} 1/3 \\ 1/3 \end{pmatrix}$	$\begin{pmatrix} +2/3 \\ -1/3 \end{pmatrix}$
u_R	0	0	$4/3$	$-2/3$
d_R	0	0	$-2/3$	$+1/3$

Table A.1: $SU(2)_L \otimes U(1)_Y$ quantum numbers of the fermions and gauge bosons.

There is an additional phenomenological complication with the weak interaction. While the leptons seem to have coupling only between each charged lepton and it's associated neutrino, the quarks have no such phenomenology. Cabibbo noticed in 1963 [57] that hadronic transitions with $\Delta S = 1$ were four times less likely than hadronic transitions with $\Delta S = 0$, and thus hypothesized that the charged current interaction was

$$J_\mu^{hadronic} = J_\mu^{\Delta S=0} \cos\theta_C + J_\mu^{\Delta S=1} \sin\theta_C \tag{A.36}$$

where θ_C is a parameter known as the Cabibbo mixing angle. In 1973, Kobayashi and Maskawa [58] extended this concept to incorporate the three known quarks at the time (u,d,s), as well as the yet-to-be discovered partner of the strange quark (the charm quark), and then went on to postulate the existence of a *third* family of quarks (as-yet unobserved). This was in response to the discovery of CP-violation in the

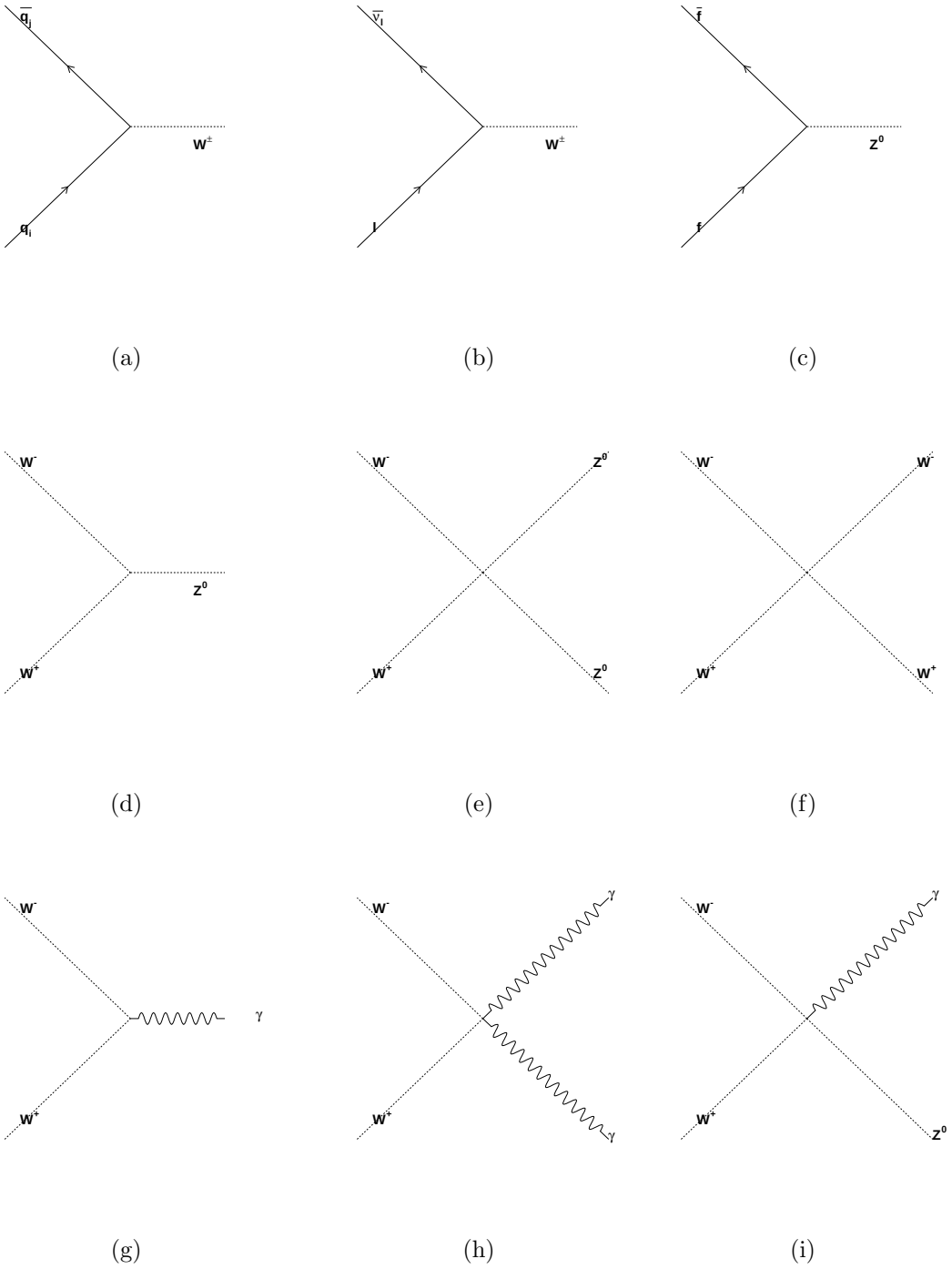

Figure A.6: Electroweak vertices between fermions and self-interaction terms.

neutral kaon system [59]. In order to be allowed in the Standard Model, the mixing between the quarks had to include three generations.

Kobayashi and Maskawa proposed that the observed quarks (i.e. the particles in eigenstates of the strong interaction) were composed of a linear combination of quarks in the weak eigenstates:

$$\begin{pmatrix} d' \\ s' \\ b' \end{pmatrix} = \begin{pmatrix} V_{ud} & V_{us} & V_{ub} \\ V_{cd} & V_{cs} & V_{cb} \\ V_{td} & V_{ts} & V_{tb} \end{pmatrix} \begin{pmatrix} d \\ s \\ b \end{pmatrix} \tag{A.37}$$

This means that any given up-type quark i can couple to any down-type quark j, with amplitude V_{ij}. The matrix V_{ij} is nearly diagonal. That is, most of the coupling is between (u, d), (c, s), and (t, b). Because V_{tb} is much larger than V_{td} and V_{ts}, we will look for top decays into bottom quarks.

A.1.7 Electroweak Symmetry Breaking

There is a problem with the formulation presented in this chapter. It requires all the gauge boson fields and all the fermion fields to be *massless*. We know from experiment that this is not the case. The W and Z bosons are massive, while the photon is massless, and all the fermion fields have mass. The problem can be solved by the introduction of a gauge field that *spontaneously breaks the* $SU(2)_L \otimes U(1)_Y$ *symmetry* thus giving mass to the vector bosons and the fermions in the theory.

There are many different ways of achieving *spontaneous electroweak symmetry breaking* (SEWSB, or EWSB). All involve adding fields to the theory that give mass to particles via interactions. As yet, no such particle has been observed.

The simplest "existence proof" model of a gauge field giving rise to mass terms of the other gauge bosons is the so-called *Higgs mechanism* [7]. For clarity, we shall work with a theory of a fictitious universe with a $U(1)$ symmetry only, however, the principles apply to any symmetry group. This theory introduces a complex field

$$\phi = \phi_1 + i\phi_2 \tag{A.38}$$

The Lagrangian to be associated is

$$\mathcal{L} = \frac{1}{2}(D_\mu\phi)^*(D^\mu\phi) + \frac{1}{2}\mu^2(\phi^*\phi) - \frac{1}{4}\lambda^2(\phi^*\phi)^2 \tag{A.39}$$

Figure A.7(a) shows a schematic of this potential, and A.7(b) shows the projection around the z-axis. The minimum of this potential occurs when $\sqrt{\phi_1^2 + \phi_2^2} = \mu/\lambda$.

The implications of this potential is that the vacuum expectation value (vev) is *not* at zero field. There is a non-zero expectation value in the ground state. In fact, there are an infinite number of ground states (around the circle with $\sqrt{\phi_1^2 + \phi_2^2} = \mu/\lambda$).

This field obeys a $U(1)$ symmetry relation when the field traverses the valley in Figure A.7(a). This causes the gauge field to be invariant under operations

$$\phi \rightarrow e^{i\theta(x)}\phi \tag{A.40}$$

This, of course, requires a massless gauge field A^μ, which sets the form of the covariant derivative to be

$$D_\mu = \partial_\mu + iqA_\mu \tag{A.41}$$

Defining fields

$$\eta = \phi_1 - \mu/\lambda, \xi = \phi_2 \tag{A.42}$$

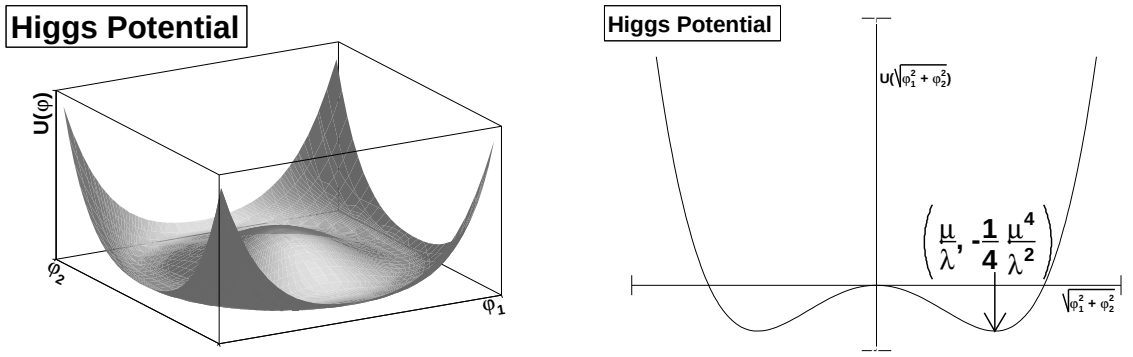

(a) (b)

Figure A.7: Higgs mechanism potential and projection around the z axis.

the Lagrangian in Equation A.39 becomes

$$\begin{aligned}
\mathcal{L} &= \left[\frac{1}{2}(\partial_\mu\eta)(\partial^\mu\eta)\right] + \left[\frac{1}{2}(\partial_\mu\xi)(\partial^\mu\xi)\right] \\
&+ \left[-\frac{1}{16\pi}F_{\mu\nu}F^{\mu\nu} + \frac{1}{2}q^2\left(\frac{\mu}{\lambda}\right)^2 A_\mu A^\mu\right] - 2iq\left(\frac{\mu}{\lambda}\right)(\partial_\mu\xi)A^\mu \\
&+ \left\{q\left[\eta(\partial_\mu\xi) - \xi(\partial_\mu\eta)\right]A^\mu + q^2\frac{\mu}{\lambda}\eta(A_\mu A^\mu) + \frac{1}{2}q^2(\xi^2+\eta^2)(A_\mu A^\mu)\right. \\
&- \left.\lambda\mu(\eta^3+\eta\xi^2) - \frac{1}{4}\lambda^2(\eta^4+2\eta^2\xi^2+\xi^4)\right\} + \left(\frac{\mu^2}{2\lambda}\right)
\end{aligned} \tag{A.43}$$

The first line describes two scalar particles, η (with mass $\sqrt{2}m$) and ξ (which is massless). The second line describes the gauge field A^μ, but it has acquired a mass

$$m_A = 2\sqrt{\pi}\left(\frac{q\mu}{\lambda}\right) \tag{A.44}$$

Without loss of generality, we now choose a gauge where ϕ_2 is real. This is done by setting $\theta(x)$ in Equation A.40 is equal to

$$\theta = -\tan^{-1}(\phi_2/\phi_1) \tag{A.45}$$

The Lagrangian now becomes

$$\begin{aligned}\mathcal{L} &= \left[\frac{1}{2}(\partial_\mu\eta)(\partial^\mu\eta)\right] + \left[-\frac{1}{16\pi}F_{\mu\nu}F^{\mu\nu} + \frac{1}{2}q^2\left(\frac{\mu}{\lambda}\right)^2 A_\mu A^\mu\right] \\ &+ \left\{q^2\frac{\mu}{\lambda}\eta(A_\mu A^\mu) + \frac{1}{2}q^2\eta^2(A_\mu A^\mu) - \lambda\mu\eta^3 - \frac{1}{4}\lambda^2\eta^4\right\} \\ &+ \left(\frac{\mu^2}{2\lambda}\right) \end{aligned} \tag{A.46}$$

In this case, we are left with only one scalar field η, and the other field ξ has disappeared. It's degree of freedom has become a longitudinal component for the gauge field A^μ (thus giving it a mass). In QFT's parlance, it is said to have been *eaten* by the gauge field. Notice that the physical implications do not depend on the gauge choice made in Equation A.45. It simply makes the dynamics manifest in the Lagrangian.

Thus, it is possible to introduce *spontaneous electroweak symmetry breaking* and give some gauge fields longitudinal polarization (i.e. mass) without upsetting the underlying theory. This particular example has been a $U(1)$ symmetry, but the principles are the same for the $SU(2)_L \otimes U(1)_Y$ symmetry in the SM. In that case, one introduces a complex *doublet* of gauge bosons

$$\begin{pmatrix} \phi \\ \eta^\dagger \end{pmatrix} \tag{A.47}$$

which carries four degrees of freedom. Three of those degrees of freedom become the longitudinal components of the W and Z bosons (hence giving them mass), and the last degree of freedom becomes another massive scalar particle similar to η in the example above. This field is called the *Higgs boson*. The photon remains massless in the theory, as is seen from experiments.

The graphical interpretation is that if we examine Figure A.7(a), the massless

field moves along the "valley" of the potential, while the massive field oscillates up and down the "hills" of the potential.

It is also possible to use the Higgs mechanism to give all the fermions masses. However, it requires the introduction of a parameter for each fermion in the theory that is completely unconstrained theoretically.

That is, for each fermion f, a term is added to the Lagrangian that has the form

$$\mathcal{L}_{Yukawa} = -\frac{1}{\sqrt{2}}\lambda_f H f \bar{f} \tag{A.48}$$

$$\equiv -(\sqrt{2}G_F)^{\frac{1}{2}} m_f H f \bar{f} \tag{A.49}$$

The Yukawa couplings λ_f are unconstrained (and hence are the masses).

A.1.8 Quantum Chromodynamics (QCD)

The final piece of the Standard Model is quantum chromodynamics (QCD), which deals with the strong interaction that holds the nucleus together. The underlying structure was proposed by Gell-Mann and Zweig in 1964 [60]. They hypothesized that the plethora of hadrons visible at the time were actually arranged in specific patterns because there were underlying constituents ("quarks") that combined together to form hadrons. Gell-Mann and Zweig postulated that there was an $SU(3)$ symmetry governing the combination of quarks, and the hadrons were combinations of the 3 and $\bar{3}$ generators (u, d, s and $\bar{u}, \bar{d}, \bar{s}$).

At the time, only three quarks were necessary to explain all the observable particles at the time (up, down, and strange). The discovery of the charm, bottom, and top quarks would come later.

The phenomenology of this theory was that all baryons were composed of three quarks, and all mesons were composed of a quark-antiquark pair. While the spectrum of particles was accurately predicted, two inconsistencies remained with this theory. Firstly, there were no observations of free quarks. Second, it appeared that the quark model violated the Pauli exclusion principle. The Λ^{++}, for example, was supposedly composed of 3 up quarks in the same state, which is not possible for spin-$\frac{1}{2}$ particles.

The second dilemma was solved shortly thereafter by O.W. Greenberg [61]. He hypothesized that there was an internal quantum number for the strong interaction, color, analogous to electric charge, but the $SU(3)$ equivalent. There are three colors (and three anticolors), commonly referred to as red, blue, and green. Greenberg hypothesized that all observable particles are color-neutral. This solves the problem with particles like Λ^{++}, because it is composed of three up-quarks, one in each color state, and so is still color-neutral. This color $SU(3)$ symmetry is actually the correct symmetry of the strong interaction, and is referred to as $SU(3)_C$. There are eight generators of $SU(3)$, and these show up as eight different gauge bosons. They are all completely symmetric in every way (except their color charge) since there is no symmetry breaking principle for the strong interaction. Thus, they are all given the name "gluon".

The first dilemma is somewhat more difficult to solve. The fact that free quarks have never been observed was given the name "confinement". That is, it was assumed that there was some mechanism that confined quarks to lie within hadrons.

In 1974, D. Gross, H. D. Politzer, and F. Wilczek proposed a solution to this problem, colloquially called *asymptotic freedom* [62, 63, 64, 65]. They proposed that

unlike QED (as described in Section A.1.5), the strong interaction gets stronger at *long* distances, and weaker at *short* distances. Therefore, in the asymptotic regime of infinite momentum transfer, the quarks would be completely free.

This is accomplished using the QCD analogue of Equation A.22. In this case, the coupling strength decreases with increasing energy, the opposite of QED [7]:

$$\alpha_s(|q^2|) = \frac{\alpha_s \mu^2}{1 + (\alpha_s(\mu^2)/12\pi)(11n - 2f)\log\left(|q^2|/\mu^2\right)} \tag{A.50}$$

where n is the number of colors (3 for the SM) and f is the number of flavors (6 in the SM). If $11n > 2f$, the theory has antiscreening. This equation is only valid for $|q^2| \gg \mu^2$.

Notice that we cannot simply expand the running coupling starting from low-q^2 scales. That is precisely where the theory breaks down. Instead, we introduce a minimum scale for the QCD interaction. Introducing the variable

$$\log \Lambda^2 = \log \mu^2 - 12\pi / \left[(11n - 2f)\alpha_s(\mu^2)\right] \tag{A.51}$$

the running coupling constant becomes

$$\alpha_s(|q^2|) = \frac{12\pi}{(11n - 2f)\log\left(|q^2|/\Lambda^2\right)} \tag{A.52}$$

Λ is in principle calculable, but it is difficult to measure experimentally. It seems to be roughly $100 - 500\ MeV/c$.

Once this regime in QCD where the coupling strength is weak ($\alpha_s < 1$), calculating quantum mechanical amplitudes is much the same as QED as described in Section A.1.4. The group properties are slightly different as they are with the $SU(2)_L$ case for the weak interactions, but the essential properties of the Feynman Calculus are the same.

Figures A.8(a) shows the interaction of a fermion with the gluon field. Again, as with $SU(2)_L$, the generators of the $SU(3)_C$ group do not commute, and as such there will be interactions between the generators (the 8 gluons). Figures A.8(b) and A.8(c) show the 3 gluon vertex, and the 4 gluon vertex, respectively.

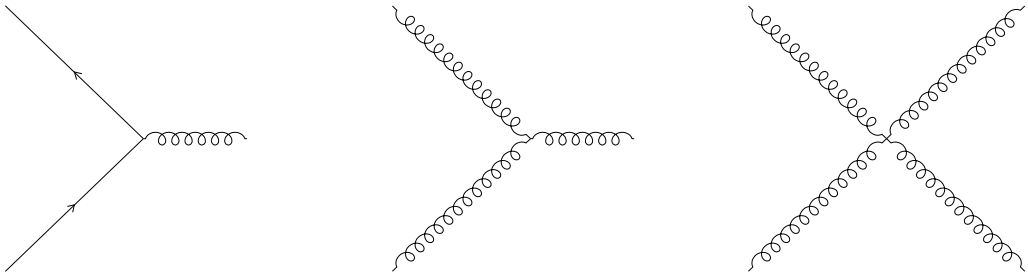

(a) (b) (c)

Figure A.8: QCD vertices between fermions and gluons.

Appendix B

B-Tagging Appendices

B.1 Detailed calculation of (SF)

B.1.1 Definitions

- $\boxed{N}$ refers to the number of data events in a certain (tag) category; the category is indicated by superscripts and subscripts.
- $\boxed{F}$ refers to the fraction of data events of a certain (flavor) type; this type is indicated by superscripts and subscripts.
- $\boxed{N_{\mathrm{mc}}}$ and $\boxed{F_{\mathrm{mc}}}$ are correspondingly defined for Monte Carlo events.
- $\boxed{N_{\mathrm{conv}}}$ and $\boxed{F_{\mathrm{conv}}}$ are correspondingly defined for events where the electron has an opposite sign conversion partner.

Following the notation in CDF6786, superscripts refer to the tag or flavor of the electron jet and subscripts refer to the tag or flavor of the away jet. An omitted

superscript or subscript implies no requirement on that jet; or equivalently, a sum over all possible superscripts and subscripts on that quantity. Hence $\boxed{F}^{H} \equiv \boxed{F}^{H}_{L} + \boxed{F}^{H}_{H}$ and $\boxed{N}_{+} \equiv \boxed{N}^{+}_{+} + \boxed{N}^{-}_{+} + \boxed{N}^{0}_{+}$.

- $(\epsilon^{+H}, \epsilon^{-H})$ are positive and negative tagging efficiencies for heavy flavor electron jets in data.
- $(\epsilon^{+}{}_{H}, \epsilon^{-}{}_{H})$ are positive and negative tagging efficiencies for heavy flavor away jets in data.
- $(\epsilon^{+L}, \epsilon^{-L})$ are positive and negative tagging efficiencies for light flavor electron jets in data.
- $(\epsilon^{+}{}_{L}, \epsilon^{-}{}_{L})$ are positive and negative tagging efficiencies for light flavor away jets in data.
- $(\mathfrak{e}^{+}, \mathfrak{e}^{-})$, with appropriate indices, are the Monte Carlo counterparts of the above quantities.
- $\alpha \equiv (\epsilon^{+L}/\epsilon^{-L})$ is a factor designed to account for the asymmetry in light flavor L_{xy} distributions, as described in CDF6906.
- $\beta \equiv (\epsilon^{+}{}_{L}/\epsilon^{-}{}_{L})$ is the corresponding factor for electron jets.
- (e^{H}, e^{L}) are the probabilities that an opposite sign conversion is found in a (heavy,light) flavor e-jet.

B.1.2 Calculation

From the basic equations for any event with an A tag on the e-jet and a B tag on the a-jet,

$$\boxed{N}^A_B = \boxed{N} \sum_{i,j=(H,L)} (\epsilon^A)^i (\epsilon^B)_j \boxed{F}^i_j \tag{B.1}$$

$$1 = \sum_{i,j=(H,L)} \boxed{F}^i_j \tag{B.2}$$

we can write

$$\boxed{N}_+ = \boxed{N}\left(\epsilon^+{}_H \boxed{F}_H + \epsilon^+{}_L \boxed{F}_L\right) \tag{B.3}$$

$$\boxed{N}_- = \boxed{N}\left(\epsilon^-{}_H \boxed{F}_H + (\epsilon^+{}_L/\alpha) \boxed{F}_L\right) \tag{B.4}$$

$$\text{hence } \boxed{N}_+ - \alpha \boxed{N}_- = \boxed{N}(\epsilon^+{}_H - \alpha\epsilon^-{}_H)\boxed{F}_H. \tag{B.5}$$

for away jet tags, and

$$\boxed{N}^+ = \boxed{N}\left(\epsilon^{+H} \boxed{F}^H + \epsilon^{+L} \boxed{F}^L\right) \tag{B.6}$$

$$\boxed{N}^- = \boxed{N}\left(\epsilon^{-H} \boxed{F}^H + (\epsilon^{+L}/\alpha) \boxed{F}^L\right) \tag{B.7}$$

$$\text{hence } \boxed{N}^+ - \beta \boxed{N}^- = \boxed{N}(\epsilon^{+H} - \beta\epsilon^{-H})\boxed{F}^H. \tag{B.8}$$

for electron jet tags. Here, α is the ratio $\epsilon^+{}_L/\epsilon^-{}_L$, believed to be independent of the electron jet characteristics. We define a similar quantity, $\beta = \epsilon^{+L}/\epsilon^{-L}$, for the e-jet. In Run I, both α and β were 1.0; recent studies suggest that they are larger in Run II due to material interactions [35] and long-lived particles.

Similarly, for double-tagged events,

$$\begin{aligned}
\boxed{N}^{+}_{+} &= \boxed{N}\Big(\epsilon^{+}{}_{H}(\epsilon^{+H}\boxed{F}^{H}_{H} + \epsilon^{+L}\boxed{F}^{L}_{H}) + \epsilon^{+}{}_{L}(\epsilon^{+H}\boxed{F}^{H}_{L} + \epsilon^{+L}\boxed{F}^{L}_{L})\Big) \\
\boxed{N}^{+}_{-} &= \boxed{N}\Big(\epsilon^{-}{}_{H}(\epsilon^{+H}\boxed{F}^{H}_{H} + \epsilon^{+L}\boxed{F}^{L}_{H}) + (\epsilon^{+}{}_{L}/\alpha)(\epsilon^{+H}\boxed{F}^{H}_{L} + \epsilon^{+L}\boxed{F}^{L}_{L})\Big) \\
\text{hence } \boxed{N}^{+}_{+} - \alpha\boxed{N}^{+}_{-} &= \boxed{N}(\epsilon^{+}{}_{H} - \alpha\epsilon^{-}{}_{H})(\epsilon^{+H}\boxed{F}^{H}_{H} + \epsilon^{+L}\boxed{F}^{L}_{H}) \qquad \text{(B.9)} \\
\boxed{N}^{-}_{+} &= \boxed{N}\Big(\epsilon^{+}{}_{H}(\epsilon^{-H}\boxed{F}^{H}_{H} + (\epsilon^{+L}/\beta)\boxed{F}^{L}_{H}) + \epsilon^{+}{}_{L}(\epsilon^{-H}\boxed{F}^{H}_{L} + (\epsilon^{+L}/\beta)\boxed{F}^{L}_{L})\Big) \\
\boxed{N}^{-}_{-} &= \boxed{N}\Big(\epsilon^{-}{}_{H}(\epsilon^{-H}\boxed{F}^{H}_{H} + (\epsilon^{+L}/\beta)\boxed{F}^{L}_{H}) + (\epsilon^{+}{}_{L}/\alpha)(\epsilon^{-H}\boxed{F}^{H}_{L} + (\epsilon^{+L}/\beta)\boxed{F}^{L}_{L})\Big) \\
\text{hence } \boxed{N}^{-}_{+} - \alpha\boxed{N}^{-}_{-} &= \boxed{N}(\epsilon^{+}{}_{H} - \alpha\epsilon^{-}{}_{H})(\epsilon^{-H}\boxed{F}^{H}_{H} + (\epsilon^{+L}/\beta)\boxed{F}^{L}_{H}). \qquad \text{(B.10)}
\end{aligned}$$

Then

$$(\boxed{N}^{+}_{+} - \alpha\boxed{N}^{+}_{-}) - \beta(\boxed{N}^{-}_{+} - \alpha\boxed{N}^{-}_{-}) = \boxed{N}(\epsilon^{+}{}_{H} - \alpha\epsilon^{-}{}_{H})(\epsilon^{+H} - \beta\epsilon^{-H})\boxed{F}^{H}_{H} \qquad \text{(B.11)}$$

and, dividing by Equation B.5,

$$\frac{(\boxed{N}^{+}_{+} - \alpha\boxed{N}^{+}_{-}) - \beta(\boxed{N}^{-}_{+} - \alpha\boxed{N}^{-}_{-})}{\boxed{N}_{+} - \alpha\boxed{N}_{-}} = (\epsilon^{+H} - \beta\epsilon^{-H})\frac{\boxed{F}^{H}_{H}}{\boxed{F}_{H}}. \qquad \text{(B.12)}$$

The fraction $\dfrac{\boxed{F}^{H}_{H}}{\boxed{F}_{H}}$ can be rewritten $(1 - \dfrac{\boxed{F}^{L}_{H}}{\boxed{F}_{H}})$ using Equation B.2, so

$$\frac{(\boxed{N}^{+}_{+} - \alpha\boxed{N}^{+}_{-}) - \beta(\boxed{N}^{-}_{+} - \alpha\boxed{N}^{-}_{-})}{(\boxed{N}_{+} - \alpha\boxed{N}_{-})(1 - \dfrac{\boxed{F}^{L}_{H}}{\boxed{F}_{H}})} = (\epsilon^{+H} - \beta\epsilon^{-H}) \qquad \text{(B.13)}$$

We can determine the only remaining unknown quantity, $(\boxed{N}_{+} - \alpha\boxed{N}_{-})(\boxed{F}^{L}_{H}/\boxed{F}_{H})$, by using the rate of identified conversions to distinguish between light and heavy flavor e-jets. If the conversion finder is uncorrelated with SecVtx, then the probability to find that the electron is a conversion in a given event only depends on the flavor of

the electron jet.

$$\boxed{N_{\rm conv}} = \boxed{N}(e^H\boxed{F}^H + e^L\boxed{F}^L) \quad \text{(B.14)}$$

$$\boxed{N_{\rm conv}}^+ = \boxed{N}(e^H\epsilon^{+H}\boxed{F}^H + e^L(\epsilon^{+L})\boxed{F}^L)$$

$$\boxed{N_{\rm conv}}^- = \boxed{N}(e^H\epsilon^{-H}\boxed{F}^H + e^L(\epsilon^{+L}/\beta)\boxed{F}^L) \text{ so}$$

$$\boxed{N_{\rm conv}}^+ - \beta\boxed{N_{\rm conv}}^- = \boxed{N}(e^H(\epsilon^{+H} - \beta\epsilon^{-H})\boxed{F}^H) \quad \text{(B.15)}$$

Similarly

$$\boxed{N_{\rm conv}}_+ = \boxed{N}(e^H(\epsilon^+{}_H\boxed{F}^H_H + \epsilon^+{}_L\boxed{F}^H_L) + e^L(\epsilon^+{}_H\boxed{F}^L_H + \epsilon^+{}_L\boxed{F}^L_L) \quad \text{(B.16)}$$

$$\boxed{N_{\rm conv}}_- = \boxed{N}(e^H(\epsilon^-{}_H\boxed{F}^H_H + (\epsilon^+{}_L/\alpha)\boxed{F}^H_L) + e^L(\epsilon^-{}_H\boxed{F}^L_H + (\epsilon^+{}_L/\alpha)\boxed{F}^L_L) \text{ so}$$

$$\boxed{N_{\rm conv}}_+ - \alpha\boxed{N_{\rm conv}}_- = \boxed{N}(e^H(\epsilon^+{}_H - \alpha\epsilon^-{}_H)\boxed{F}^H_H + e^L(\epsilon^+{}_H - \alpha\epsilon^-{}_H)\boxed{F}^L_H) \quad \text{(B.17)}$$

Now, by Equation B.5,

$$e^H(\boxed{N}_+ - \alpha\boxed{N}_-) = \boxed{N}(e^H(\epsilon^+{}_H - \alpha\epsilon^-{}_H)\boxed{F}^H_H + e^H(\epsilon^+{}_H - \alpha\epsilon^-{}_H)\boxed{F}^L_H). \quad \text{(B.18)}$$

Subtracting Equations B.17 and B.18,

$$\boxed{N_{\rm conv}}_+ - \alpha\boxed{N_{\rm conv}}_- - e^H(\boxed{N}_+ - \alpha\boxed{N}_-) = \boxed{N}(e^L - e^H)(\epsilon^+{}_H - \alpha\epsilon^-{}_H)\boxed{F}^L_H \quad \text{(B.19)}$$

Since quite obviously $e^H\boxed{N} = \boxed{N}\,(e^H\boxed{F}^H + e^H\boxed{F}^L)$, using Equation B.14

$$\boxed{N_{\rm conv}} - e^H\boxed{N} = \boxed{N}(e^L - e^H)\boxed{F}^L \quad \text{(B.20)}$$

and, using this to divide Equation B.19

$$\frac{\boxed{N_{\rm conv}}_+ - \alpha\boxed{N_{\rm conv}}_- - e^H(\boxed{N}_+ - \alpha\boxed{N}_-)}{\boxed{N_{\rm conv}} - e^H\boxed{N}} = (\epsilon^+{}_H - \alpha\epsilon^-{}_H)\frac{\boxed{F}^L_H}{\boxed{F}^L} \quad \text{(B.21)}$$

e^H is easily found from Equation B.15, since the left-hand side is $e^H(\boxed{N}^+ - \beta\boxed{N}^-)$. Hence

$$\frac{\boxed{N_{\rm conv}}_+ - \alpha\boxed{N_{\rm conv}}_- - \left(\frac{\boxed{N_{\rm conv}}^+ - \beta\boxed{N_{\rm conv}}^-}{\boxed{N}^+ - \beta\boxed{N}^-}\right)(\boxed{N}_+ - \alpha\boxed{N}_-)}{\boxed{N_{\rm conv}} - \left(\frac{\boxed{N_{\rm conv}}^+ - \beta\boxed{N_{\rm conv}}^-}{\boxed{N}^+ - \beta\boxed{N}^-}\right)\boxed{N}} = (\epsilon^+{}_H - \alpha\epsilon^-{}_H)\frac{\boxed{F}^L_H}{\boxed{F}^L} \tag{B.22}$$

or

$$\frac{(\boxed{N_{\rm conv}}_+ - \alpha\boxed{N_{\rm conv}}_-)(\boxed{N}^+ - \beta\boxed{N}^-) - (\boxed{N_{\rm conv}}^+ - \beta\boxed{N_{\rm conv}}^-)(\boxed{N}_+ - \alpha\boxed{N}_-)}{\boxed{N_{\rm conv}}(\boxed{N}^+ - \beta\boxed{N}^-) - \boxed{N}(\boxed{N_{\rm conv}}^+ - \beta\boxed{N_{\rm conv}}^-)} = (\epsilon^+{}_H - \alpha\epsilon^-{}_H)\frac{\boxed{F}^L_H}{\boxed{F}^L}. \tag{B.23}$$

We write, for simplicity,

$$\frac{(\boxed{N_{\rm conv}}_+ - \alpha\boxed{N_{\rm conv}}_-)(\boxed{N}^+ - \beta\boxed{N}^-) - (\boxed{N_{\rm conv}}^+ - \beta\boxed{N_{\rm conv}}^-)(\boxed{N}_+ - \alpha\boxed{N}_-)}{\boxed{N_{\rm conv}}(\boxed{N}^+ - \beta\boxed{N}^-) - \boxed{N}(\boxed{N_{\rm conv}}^+ - \beta\boxed{N_{\rm conv}}^-)} \equiv \chi. \tag{B.24}$$

(some algebra)

$$\boxed{N}\boxed{F}^L\chi = (\boxed{N}_+ - \alpha\boxed{N}_-)\frac{\boxed{F}^L_H}{\boxed{F}_H}$$

But from Equation B.2, $\boxed{F}^L = (1 - \boxed{F}^H)$, so

$$\boxed{N}(1 - \boxed{F}^H)\chi = (\boxed{N}_+ - \alpha\boxed{N}_-)\frac{\boxed{F}^L_H}{\boxed{F}_H} \tag{B.25}$$

Combining these, and applying the definition of the scale factor,

$$\frac{(\boxed{N}^+_+ - \alpha\boxed{N}^+_-) - \beta(\boxed{N}^-_+ - \alpha\boxed{N}^-_-)}{(\boxed{N}_+ - \alpha\boxed{N}_-) - \boxed{N}(1 - \boxed{F}^H)\chi} = (SF)(\mathfrak{z}^{+H} - \beta\mathfrak{z}^{-H}) \tag{B.26}$$

From definitions (see Equation B.8) we can also write

$$(SF) = \frac{\boxed{N}^+ - \beta\boxed{N}^-}{\boxed{N}\boxed{F}^H} \div \frac{\boxed{N_{\rm mc}}^+ - \beta\boxed{N_{\rm mc}}^-}{\boxed{N_{\rm mc}}\boxed{F_{\rm mc}}^H}. \tag{B.27}$$

or

$$\boxed{F}^{H} = \frac{\boxed{N}^{+} - \beta\boxed{N}^{-}}{\boxed{N}(SF)} \frac{\boxed{N_{\rm mc}}\boxed{F_{\rm mc}}^{H}}{\boxed{N_{\rm mc}}^{+} - \beta\boxed{N_{\rm mc}}^{-}}. \tag{B.28}$$

Substituting $\boxed{F}^{H}$ into Equation B.26,

$$\frac{(\boxed{N}_{+}^{+} - \alpha\boxed{N}_{-}^{+}) - \beta(\boxed{N}_{+}^{-} - \alpha\boxed{N}_{-}^{-})}{(\boxed{N}_{+} - \alpha\boxed{N}_{-}) - \left(\boxed{N} - \frac{\boxed{N}^{+} - \beta\boxed{N}^{-}}{(SF)} \frac{\boxed{N_{\rm mc}}\boxed{F_{\rm mc}}^{H}}{\boxed{N_{\rm mc}}^{+} - \beta\boxed{N_{\rm mc}}^{-}}\right)\chi} = (SF)(\mathfrak{z}^{+H} - \beta\mathfrak{z}^{-H}) \tag{B.29}$$

we can rearrange this expression to solve for (SF)

$$(SF) = \frac{\frac{(\boxed{N}_{+}^{+} - \alpha\boxed{N}_{-}^{+}) - \beta(\boxed{N}_{+}^{-} - \alpha\boxed{N}_{-}^{-})}{(\mathfrak{z}^{+H} - \beta\mathfrak{z}^{-H})} - \chi\frac{(\boxed{N}^{+} - \boxed{N}^{-})}{\boxed{N_{\rm mc}}^{+} - \beta\boxed{N_{\rm mc}}^{-}}(\boxed{N_{\rm mc}}\boxed{F_{\rm mc}}^{H}).}{(\boxed{N}_{+} - \alpha\boxed{N}_{-}) - \boxed{N}\chi} \tag{B.30}$$

with

$$\chi \equiv \frac{(\boxed{N}^{+} - \beta\boxed{N}^{-})(\boxed{N_{\rm conv}}_{+} - \alpha\boxed{N_{\rm conv}}_{-}) - (\boxed{N}_{+} - \alpha\boxed{N}_{-})(\boxed{N_{\rm conv}}^{+} - \beta\boxed{N_{\rm conv}}^{-})}{\boxed{N_{\rm conv}}(\boxed{N}^{+} - \beta\boxed{N}^{-}) - \boxed{N}(\boxed{N_{\rm conv}}^{+} - \beta\boxed{N_{\rm conv}}^{-})} \tag{B.31}$$

and

$$(\mathfrak{z}^{+H} - \beta\mathfrak{z}^{-H}) = \frac{(\boxed{N_{\rm mc}}_{+}^{+} - \alpha\boxed{N_{\rm mc}}_{-}^{+}) - \beta(\boxed{N_{\rm mc}}_{+}^{-} - \alpha\boxed{N_{\rm mc}}_{-}^{-})}{(\boxed{N_{\rm mc}}_{+} - \alpha\boxed{N_{\rm mc}}_{-})(1 - \boxed{F_{\rm mc}}_{H}^{L}/\boxed{F_{\rm mc}}_{H})}.$$

Appendix C

Analysis Appendices

C.1 Events at Each Cut Stage for $t\bar{t}$ MC For Each Channel

Channel	evqqbb	mvqqbb	tvqqbb	evevbb	mvmvbb	tvtvbb	evmvbb	evtvbb	mvtvbb	qqqqbb
CEM										
Stage 0 Initial	168044	167958	167694	13446	13312	13587	26963	26950	27170	524919
Stage 1 Obsv	161714	161679	161329	12981	12824	13099	25931	25942	26094	505052
Stage 2 Trigger	161714	161679	161329	12981	12824	13099	25931	25942	26094	505052
Stage 3 $\geq$1tlep	61468	639	5437	8087	50	875	10023	10433	877	1805
Stage 4 Met	55280	588	4665	7430	47	792	9248	9578	795	664
Stage 5 Iso	49102	156	3793	6940	20	683	8559	8807	688	72
Stage 5 $\geq$3jets	43666	125	3376	2966	1	283	1604	3699	128	72
Stage 6 !Dilep	43336	97	3351	2427	0	263	721	3521	67	72
Stage 7 !Z	42435	96	3297	1834	0	243	616	3146	57	66
Stage 8 !Conv	42435	96	3297	1834	0	243	616	3146	57	66
Stage 9 !Diffz	42431	96	3297	1834	0	243	616	3146	57	66
Stage 10 Kin Veto	38767	72	2594	1584	0	162	494	2589	39	52
Stage 11 Si Good	38767	72	2594	1584	0	162	494	2589	39	52
Stage 12 Tgb	37245	68	2491	1487	0	150	459	2453	35	49
Stage 13 $\geq$1+Btag	25066	40	1664	1036	0	110	328	1730	25	22
Stage 14 $\geq$2+Btag	7388	14	488	289	0	32	108	527	7	6
Stage 15 $\geq$1-Btag	885	4	69	33	0	1	9	54	3	3
Stage 16 $\geq$1+-Btag	457	3	36	12	0	1	4	30	1	2
Stage 17 $\geq$2-Btag	11	0	1	0	0	0	0	0	0	0
Stage 18 Ltgb	37467	69	2504	1500	0	151	468	2475	35	51
Stage 19 $\geq$1+Ltag	28247	45	1864	1157	0	122	371	1959	26	30
Stage 20 $\geq$2+Ltag	10447	16	698	405	0	49	146	744	11	11
Stage 21 $\geq$1-Ltag	2100	5	159	68	0	7	18	118	4	4
Stage 22 $\geq$1+-Ltag	1294	3	97	33	0	7	11	77	1	3
Stage 23 $\geq$2-Ltag	58	2	4	2	0	0	0	2	0	1
CMUP										
Stage 0 Initial	168044	167958	167694	13446	13312	13587	26963	26950	27170	524919
Stage 1 Obsv	161714	161679	161329	12981	12824	13099	25931	25942	26094	505052
Stage 2 Trigger	161714	161679	161329	12981	12824	13099	25931	25942	26094	505052
Stage 3 $\geq$1tlep	313	39640	3339	16	5556	574	6419	526	6791	962
Stage 4 Met	272	35095	2917	13	5145	515	5836	481	6196	784
Stage 5 Iso	10	30724	2341	0	4854	451	5313	419	5671	6
Stage 5 $\geq$3jets	7	27260	2096	0	921	194	2097	160	2301	6
Stage 6 !Dilep	6	27051	2087	0	491	183	1609	119	2178	6
Stage 7 !Z	6	26746	2075	0	432	175	1423	105	2012	6
Stage 8 !Cosmic	6	26746	2075	0	432	175	1423	105	2012	6
Stage 9 !Diffz	6	26737	2075	0	432	175	1423	105	2012	6
Stage 10 Kin Veto	5	24232	1481	0	334	113	1230	68	1655	4
Stage 11 Si Good	5	24232	1481	0	334	113	1230	68	1655	4
Stage 12 Tgb	5	23301	1406	0	316	102	1151	65	1562	4
Stage 13 $\geq$1+Btag	3	15594	942	0	227	71	795	45	1077	4
Stage 14 $\geq$2+Btag	0	4586	271	0	66	22	226	11	325	1
Stage 15 $\geq$1-Btag	0	606	30	0	4	3	31	1	42	0
Stage 16 $\geq$1+-Btag	0	309	14	0	3	1	17	1	20	0
Stage 17 $\geq$2-Btag	0	5	0	0	0	0	0	0	0	0
Stage 18 Ltgb	5	23447	1413	0	319	106	1163	66	1572	4
Stage 19 $\geq$1+Ltag	3	17587	1067	0	250	74	894	50	1213	4
Stage 20 $\geq$2+Ltag	0	6570	377	0	90	29	318	17	446	2
Stage 21 $\geq$1-Ltag	0	1350	84	0	12	6	57	2	74	0
Stage 22 $\geq$1+-Ltag	0	778	48	0	5	1	35	2	45	0
Stage 23 $\geq$2-Ltag	0	31	0	0	0	0	0	0	0	0
CMX										
Stage 0 Initial	168044	167958	167694	13446	13312	13587	26963	26950	27170	524919
Stage 1 Obsv	161714	161679	161329	12981	12824	13099	25931	25942	26094	505052
Stage 2 Trigger	161714	161679	161329	12981	12824	13099	25931	25942	26094	505052
Stage 3 $\geq$1tlep	146	13221	1133	12	1981	143	2146	183	2331	468
Stage 4 Met	128	11725	963	10	1831	126	1964	160	2125	366
Stage 5 Iso	1	10273	739	0	1691	105	1771	141	1938	2
Stage 5 $\geq$3jets	0	9122	654	0	321	52	711	52	791	2
Stage 6 !Dilep	0	9068	651	0	143	48	534	34	753	2
Stage 7 !Z	0	8974	644	0	124	46	457	32	691	2
Stage 8 !Cosmic	0	8974	644	0	124	46	457	32	691	2
Stage 9 !Diffz	0	8972	644	0	124	46	457	32	691	2
Stage 10 Kin Veto	0	8242	579	0	104	29	408	27	546	2
Stage 11 Si Good	0	8242	579	0	104	29	408	27	546	2
Stage 12 Tgb	0	7968	554	0	100	28	390	24	525	2
Stage 13 $\geq$1+Btag	0	5434	370	0	78	22	271	15	367	2
Stage 14 $\geq$2+Btag	0	1636	88	0	24	7	79	3	107	1
Stage 15 $\geq$1-Btag	0	199	11	0	3	2	9	1	14	0
Stage 16 $\geq$1+-Btag	0	108	7	0	2	1	3	0	4	0
Stage 17 $\geq$2-Btag	0	3	0	0	0	0	0	0	0	0
Stage 18 Ltgb	0	8008	556	0	102	28	393	24	533	2
Stage 19 $\geq$1+Ltag	0	6104	429	0	81	24	301	18	410	2
Stage 20 $\geq$2+Ltag	0	2317	139	0	35	10	101	4	160	1
Stage 21 $\geq$1-Ltag	0	467	25	0	5	2	14	2	28	0
Stage 22 $\geq$1+-Ltag	0	267	17	0	3	1	6	1	12	0
Stage 23 $\geq$2-Ltag	0	10	0	0	0	0	0	0	0	0

Table C.1: Event counts at each successive stage for `ttopel` Top Monte Carlo, with $M_{Top} = 178\ Gev/C^2$, for the ≥ 3 jet bin for each decay type.

Channel	evqqbb	mvqqbb	tvqqbb	evevbb	mvmvbb	tvtvbb	evmvbb	evtvbb	mvtvbb	qqqqbb
CEM										
Stage 0 Initial	168044	167958	167694	13446	13312	13587	26963	26950	27170	524919
Stage 1 Obsv	161714	161679	161329	12981	12824	13099	25931	25942	26094	505052
Stage 2 Trigger	161714	161679	161329	12981	12824	13099	25931	25942	26094	505052
Stage 3 $\geq$1tlep	61468	639	5437	8087	50	875	10023	10433	877	1805
Stage 4 Met	55280	588	4665	7430	47	792	9248	9578	795	664
Stage 5 Iso	49102	156	3793	6940	20	683	8559	8807	688	72
Stage 5 $\geq$4jets	25645	63	1965	610	1	65	234	748	20	61
Stage 6 !Dilep	25462	54	1954	491	0	61	110	713	10	61
Stage 7 !Z	24911	54	1921	376	0	55	90	615	7	55
Stage 8 !Conv	24911	54	1921	376	0	55	90	615	7	55
Stage 9 !Diffz	24907	54	1921	376	0	55	90	615	7	55
Stage 10 Kin Veto	23795	41	1615	352	0	48	82	559	5	47
Stage 11 Si Good	23795	41	1615	352	0	48	82	559	5	47
Stage 12 Tgb	22952	38	1551	334	0	47	74	538	5	44
Stage 13 $\geq$1+Btag	15831	22	1070	238	0	35	47	369	4	22
Stage 14 $\geq$2+Btag	5008	9	321	66	0	9	14	117	0	6
Stage 15 $\geq$1-Btag	553	2	43	7	0	1	2	13	1	3
Stage 16 $\geq$1+-Btag	311	2	23	3	0	1	0	5	1	2
Stage 17 $\geq$2-Btag	8	0	0	0	0	0	0	0	0	0
Stage 18 Ltgb	23088	38	1563	337	0	47	76	542	5	46
Stage 19 $\geq$1+Ltag	17829	26	1172	261	0	38	60	422	4	28
Stage 20 $\geq$2+Ltag	7081	9	466	98	0	16	21	160	1	11
Stage 21 $\geq$1-Ltag	1341	2	107	17	0	1	6	28	1	4
Stage 22 $\geq$1+-Ltag	884	2	65	9	0	1	4	16	1	3
Stage 23 $\geq$2-Ltag	40	1	2	1	0	0	0	2	0	1
CMUP										
Stage 0 Initial	168044	167958	167694	13446	13312	13587	26963	26950	27170	524919
Stage 1 Obsv	161714	161679	161329	12981	12824	13099	25931	25942	26094	505052
Stage 2 Trigger	161714	161679	161329	12981	12824	13099	25931	25942	26094	505052
Stage 3 $\geq$1tlep	313	39640	3339	16	5556	574	6419	526	6791	962
Stage 4 Met	272	35095	2917	13	5145	515	5836	481	6196	784
Stage 5 Iso	10	30724	2341	0	4854	451	5313	419	5671	6
Stage 5 $\geq$4jets	5	15965	1186	0	178	38	410	25	449	6
Stage 6 !Dilep	5	15840	1181	0	95	36	335	18	425	6
Stage 7 !Z	5	15650	1176	0	87	33	290	17	384	6
Stage 8 !Cosmic	5	15650	1176	0	87	33	290	17	384	6
Stage 9 !Diffz	5	15642	1176	0	87	33	290	17	384	6
Stage 10 Kin Veto	4	14815	891	0	76	26	265	14	347	4
Stage 11 Si Good	4	14815	891	0	76	26	265	14	347	4
Stage 12 Tgb	4	14318	854	0	75	25	247	14	327	4
Stage 13 $\geq$1+Btag	2	9868	586	0	59	19	165	12	221	4
Stage 14 $\geq$2+Btag	0	3156	194	0	15	5	52	5	69	1
Stage 15 $\geq$1-Btag	0	364	22	0	0	1	9	0	12	0
Stage 16 $\geq$1+-Btag	0	204	11	0	0	1	7	0	7	0
Stage 17 $\geq$2-Btag	0	4	0	0	0	0	0	0	0	0
Stage 18 Ltgb	4	14402	856	0	75	26	250	14	328	4
Stage 19 $\geq$1+Ltag	2	11092	658	0	65	21	184	12	247	4
Stage 20 $\geq$2+Ltag	0	4479	258	0	22	8	72	8	94	2
Stage 21 $\geq$1-Ltag	0	861	53	0	1	2	14	0	18	0
Stage 22 $\geq$1+-Ltag	0	541	32	0	0	1	10	0	14	0
Stage 23 $\geq$2-Ltag	0	24	0	0	0	0	0	0	0	0
CMX										
Stage 0 Initial	168044	167958	167694	13446	13312	13587	26963	26950	27170	524919
Stage 1 Obsv	161714	161679	161329	12981	12824	13099	25931	25942	26094	505052
Stage 2 Trigger	161714	161679	161329	12981	12824	13099	25931	25942	26094	505052
Stage 3 $\geq$1tlep	146	13221	1133	12	1981	143	2146	183	2331	468
Stage 4 Met	128	11725	963	10	1831	126	1964	160	2125	366
Stage 5 Iso	1	10273	739	0	1691	105	1771	141	1938	2
Stage 5 $\geq$4jets	0	5311	377	0	50	10	145	9	163	2
Stage 6 !Dilep	0	5279	375	0	24	10	113	8	158	2
Stage 7 !Z	0	5225	368	0	23	9	93	8	143	2
Stage 8 !Cosmic	0	5225	368	0	23	9	93	8	143	2
Stage 9 !Diffz	0	5224	368	0	23	9	93	8	143	2
Stage 10 Kin Veto	0	5060	351	0	21	8	85	8	127	2
Stage 11 Si Good	0	5060	351	0	21	8	85	8	127	2
Stage 12 Tgb	0	4898	336	0	21	8	85	7	121	2
Stage 13 $\geq$1+Btag	0	3438	234	0	16	6	65	5	90	2
Stage 14 $\geq$2+Btag	0	1137	61	0	4	3	20	1	28	1
Stage 15 $\geq$1-Btag	0	114	8	0	2	1	3	0	4	0
Stage 16 $\geq$1+-Btag	0	71	6	0	2	1	2	0	0	0
Stage 17 $\geq$2-Btag	0	3	0	0	0	0	0	0	0	0
Stage 18 Ltgb	0	4919	336	0	21	8	85	7	123	2
Stage 19 $\geq$1+Ltag	0	3848	268	0	17	7	71	5	96	2
Stage 20 $\geq$2+Ltag	0	1593	94	0	7	3	27	1	37	1
Stage 21 $\geq$1-Ltag	0	306	18	0	4	1	4	1	10	0
Stage 22 $\geq$1+-Ltag	0	188	16	0	3	1	3	1	4	0
Stage 23 $\geq$2-Ltag	0	8	0	0	0	0	0	0	0	0

Table C.2: Event counts at each successive stage for `ttopel` top Monte Carlo, with $m_{top} = 178\ GeV/c^2$, for the ≥ 4 jet bin for each decay type.

C.2 Unoptimized Summary Tables

Corrections to Pretag data					
	1 jet	2 jets	3 jets	4 jets	$\geq$ 5 jets
Data	30628.00 ± 0.00	4791.00 ± 0.00	769.00 ± 0.00	179.00 ± 0.00	36.00 ± 0.00
Non-W	2265.47 ± 567.81	453.22 ± 114.65	79.00 ± 21.10	18.71 ± 5.00	3.53 ± 0.94
$t\bar{t}$ (8.9 pb)	9.20 ± 0.82	49.55 ± 4.40	96.66 ± 8.58	86.37 ± 7.67	26.63 ± 2.38
EW	157.32 ± 14.33	151.44 ± 13.67	31.54 ± 2.92	5.26 ± 0.47	0.82 ± 0.07
Single Top	18.71 ± 4.51	23.37 ± 5.04	4.54 ± 0.97	0.72 ± 0.16	0.09 ± 0.02
Data, Corrected	28177.30 ± 584.08	4113.43 ± 134.29	557.27 ± 32.49	67.94 ± 13.03	4.92 ± 3.37

Table C.3: Corrections to pretag data for the W+HF background estimate. After an initial measurement, the $t\bar{t}$ cross section is input back into this calculation, and the process is iterated until the result is stable to 1%. These numbers are for the *unoptimized* analysis.

The tables are arranged in the following format.

- ϵ_{q-jet} is the MC efficiency to tag a q-flavor jet.
- $\epsilon_{q-jet}SF$ is the MC efficiency times the b-tag scale factor.
- Φ_E is the event scale factor.
- $\epsilon_{\geq 1,2}$ are the $\geq 1, 2$ event tagging efficiencies, respectively.
- ϵ_{pretag} is the pretag efficiency in the Monte Carlo
- $\epsilon_{pretag} * SF$ is the pretag efficiency times the pretag scale factors.
- "Pretag" is the number of pretag event counts.
- "$\geq$ 1+ Tag" is the number of tagged event counts.
- "$\geq$ 2+ Tag" is the number of double-tagged event counts.

$t\bar{t}$ (8.9 pb), $\sigma \int \mathcal{L}dt = 2835 \pm 369$					
	1 jet	2 jets	3 jets	4 jets	$\geq$ 5 jets
$\epsilon_{b-jet}(\%)$	44.43 ± 0.79	44.80 ± 0.26	44.80 ± 0.17	44.77 ± 0.17	43.83 ± 0.31
$\epsilon_{c-jet}(\%)$	10.97 ± 2.51	10.40 ± 0.57	10.07 ± 0.25	9.36 ± 0.21	9.80 ± 0.35
$\epsilon_{b-jet} * SF(\%)$	40.39 ± 2.76	40.72 ± 2.70	40.72 ± 2.69	40.70 ± 2.69	39.84 ± 2.64
$\epsilon_{c-jet} * SF(\%)$	9.97 ± 2.63	9.45 ± 1.35	9.15 ± 1.23	8.51 ± 1.14	8.91 ± 1.22
$\Phi_e^{\geq 1}(\%)$	91.04 ± 6.13	92.65 ± 5.23	93.23 ± 5.03	93.76 ± 4.77	94.13 ± 4.78
$\Phi_e^{\geq 2}(\%)$	0.00 ± 0.00	83.20 ± 11.40	84.35 ± 11.56	85.13 ± 11.44	86.36 ± 11.45
$\epsilon_{\geq 1}(\%)$	36.81 ± 0.70	54.88 ± 0.31	61.34 ± 0.22	66.41 ± 0.22	67.00 ± 0.40
$\epsilon_{\geq 2}$ (%)	0.00 ± 0.00	11.28 ± 0.20	15.55 ± 0.16	20.75 ± 0.19	21.83 ± 0.35
$\epsilon_{\geq 1} * \Phi_e$ (%)	33.51 ± 2.34	50.85 ± 2.88	57.19 ± 3.09	62.27 ± 3.17	63.07 ± 3.22
$\epsilon_{\geq 2} * \Phi_e(\%)$	0.00 ± 0.00	9.38 ± 1.30	13.12 ± 1.80	17.66 ± 2.38	18.85 ± 2.52
$\epsilon_{bjet}(\%)$				44.65 ± 0.11	
$\epsilon_{cjet}(\%)$				9.68 ± 0.15	
$\epsilon_{bjet} * SF(\%)$				40.59 ± 2.68	
$\epsilon_{cjet} * SF(\%)$				8.80 ± 1.17	
$\epsilon_{\geq 1}(\%)$				64.15 ± 0.15	
$\epsilon_{\geq 2}(\%)$				18.49 ± 0.12	
$\Phi_E^1(\%)$				93.62 ± 4.87	
$\Phi_E^2(\%)$				85.10 ± 11.48	
$\epsilon_{\geq 1}(\%) * \Phi_E^1$				60.06 ± 3.13	
$\epsilon_{\geq 2}(\%) * \Phi_E^2$				15.73 ± 2.13	
CEM					
$\epsilon_{pretag}(\%)$	0.21 ± 0.00	1.10 ± 0.01	2.14 ± 0.01	1.94 ± 0.01	0.60 ± 0.01
$\epsilon_{pretag} * SF(\%)$	0.19 ± 0.01	1.00 ± 0.07	1.95 ± 0.13	1.77 ± 0.12	0.55 ± 0.04
$\epsilon_{pretag}(\%)$				4.68 ± 0.02	
$\epsilon_{pretag} * SF(\%)$				4.27 ± 0.29	
Pretag Counts	5.43 ± 0.48	28.44 ± 2.55	55.32 ± 4.95	50.15 ± 4.49	15.51 ± 1.41
$\geq$ 1+ Tag Counts	1.82 ± 0.21	14.46 ± 1.54	31.64 ± 3.31	31.23 ± 3.22	9.78 ± 1.02
$\geq$ 2+ Tag Counts	0.00 ± 0.00	2.67 ± 0.44	7.26 ± 1.19	8.86 ± 1.43	2.92 ± 0.47
CMUP					
$\epsilon_{pretag}(\%)$	0.13 ± 0.00	0.71 ± 0.01	1.39 ± 0.01	1.22 ± 0.01	0.37 ± 0.01
$\epsilon_{pretag} * SF(\%)$	0.10 ± 0.01	0.54 ± 0.04	1.05 ± 0.07	0.92 ± 0.06	0.28 ± 0.02
$\epsilon_{pretag}(\%)$				2.98 ± 0.02	
$\epsilon_{pretag} * SF(\%)$				2.25 ± 0.15	
Pretag Counts	2.78 ± 0.25	15.20 ± 1.38	29.75 ± 2.68	26.11 ± 2.36	7.92 ± 0.74
$\geq$ 1+ Tag Counts	0.93 ± 0.11	7.73 ± 0.83	17.01 ± 1.79	16.26 ± 1.69	4.99 ± 0.53
$\geq$ 2+ Tag Counts	0.00 ± 0.00	1.43 ± 0.24	3.90 ± 0.64	4.61 ± 0.75	1.49 ± 0.24
CMX					
$\epsilon_{pretag}(\%)$	0.04 ± 0.00	0.24 ± 0.00	0.47 ± 0.01	0.41 ± 0.01	0.13 ± 0.00
$\epsilon_{pretag} * SF(\%)$	0.04 ± 0.00	0.22 ± 0.01	0.43 ± 0.03	0.37 ± 0.03	0.12 ± 0.01
$\epsilon_{pretag}(\%)$				1.00 ± 0.01	
$\epsilon_{pretag} * SF(\%)$				0.91 ± 0.06	
Pretag Counts	0.99 ± 0.09	5.91 ± 0.53	11.58 ± 1.07	10.10 ± 0.94	3.20 ± 0.29
$\geq$ 1+ Tag Counts	0.33 ± 0.04	3.01 ± 0.32	6.62 ± 0.71	6.29 ± 0.67	2.02 ± 0.21
$\geq$ 2+ Tag Counts	0.00 ± 0.00	0.56 ± 0.09	1.52 ± 0.25	1.78 ± 0.29	0.60 ± 0.10
Total					
Pretag	9.20 ± 0.82	49.55 ± 4.40	96.66 ± 8.58	86.37 ± 7.67	26.63 ± 2.38
$\geq$ 1 Tag Counts	3.08 ± 0.35	25.19 ± 2.66	55.28 ± 5.74	53.78 ± 5.50	16.80 ± 1.73
$\geq$ 2 Tag Counts	0.00 ± 0.00	4.65 ± 0.76	12.68 ± 2.07	15.26 ± 2.46	5.02 ± 0.81

Table C.4: Summary table for $t\bar{t}$. These numbers are for the *unoptimized* analysis.

WW, $\sigma \int \mathcal{L}dt = 4220 \pm 253$					
	1 jet	2 jets	3 jets	4 jets	$\geq$ 5 jets
ϵ_{b-jet}(%)	41.94 ± 8.86	37.86 ± 4.78	43.33 ± 5.22	25.93 ± 8.43	25.00 ± 12.50
ϵ_{c-jet}(%)	7.71 ± 0.47	8.46 ± 0.33	8.09 ± 0.67	7.36 ± 1.51	9.09 ± 3.88
$\epsilon_{b-jet} * SF$(%)	38.12 ± 8.44	34.41 ± 4.90	39.39 ± 5.41	23.57 ± 7.82	22.73 ± 11.46
$\epsilon_{c-jet} * SF$(%)	7.01 ± 1.02	7.69 ± 1.06	7.35 ± 1.15	6.69 ± 1.63	8.26 ± 3.69
$\Phi_e^{\geq 1}$(%)	90.90 ± 12.18	90.92 ± 12.09	91.07 ± 11.53	91.41 ± 10.99	92.16 ± 9.48
$\Phi_e^{\geq 2}$(%)	0.00 ± 0.00	82.63 ± 18.39	82.64 ± 17.97	82.75 ± 17.58	83.16 ± 16.70
$\epsilon_{\geq 1}$(%)	2.06 ± 0.11	4.42 ± 0.16	5.68 ± 0.39	5.75 ± 0.96	11.83 ± 3.35
$\epsilon_{\geq 2}$ (%)	0.00 ± 0.00	0.04 ± 0.01	0.12 ± 0.06	0.00 ± 0.00	1.08 ± 1.07
$\epsilon_{\geq 1} * \Phi_e$ (%)	1.87 ± 0.27	4.02 ± 0.55	5.17 ± 0.75	5.26 ± 1.08	10.90 ± 3.28
$\epsilon_{\geq 2} * \Phi_e$(%)	0.00 ± 0.00	0.03 ± 0.01	0.10 ± 0.05	0.00 ± 0.00	0.90 ± 0.91
ϵ_{bjet}(%)				37.98 ± 4.27	
ϵ_{cjet}(%)				8.01 ± 0.61	
$\epsilon_{bjet} * SF$(%)				34.52 ± 4.50	
$\epsilon_{cjet} * SF$(%)				7.28 ± 1.11	
$\epsilon_{\geq 1}$(%)				5.83 ± 0.36	
$\epsilon_{\geq 2}$(%)				0.12 ± 0.05	
Φ_E^1(%)				91.19 ± 11.31	
Φ_E^2(%)				82.80 ± 17.54	
$\epsilon_{\geq 1}$(%) $* \Phi_E^1$				5.32 ± 0.74	
$\epsilon_{\geq 2}$(%) $* \Phi_E^2$				0.10 ± 0.05	
CEM					
ϵ_{pretag}(%)	1.93 ± 0.02	1.92 ± 0.02	0.39 ± 0.01	0.06 ± 0.00	0.01 ± 0.00
$\epsilon_{pretag} * SF$(%)	1.76 ± 0.12	1.75 ± 0.12	0.36 ± 0.03	0.05 ± 0.00	0.01 ± 0.00
ϵ_{pretag}(%)				0.47 ± 0.01	
$\epsilon_{pretag} * SF$(%)				0.43 ± 0.03	
Pretag Counts	74.28 ± 6.83	73.90 ± 6.79	15.01 ± 1.42	2.31 ± 0.21	0.38 ± 0.04
$\geq$ 1+ Tag Counts	1.39 ± 0.24	2.97 ± 0.49	0.78 ± 0.13	0.12 ± 0.03	0.04 ± 0.01
$\geq$ 2+ Tag Counts	0.00 ± 0.00	0.02 ± 0.01	0.01 ± 0.01	0.00 ± 0.00	0.00 ± 0.00
CMUP					
ϵ_{pretag}(%)	1.20 ± 0.02	1.14 ± 0.02	0.25 ± 0.01	0.04 ± 0.00	0.01 ± 0.00
$\epsilon_{pretag} * SF$(%)	0.91 ± 0.06	0.86 ± 0.06	0.19 ± 0.01	0.03 ± 0.00	0.01 ± 0.00
ϵ_{pretag}(%)				0.29 ± 0.01	
$\epsilon_{pretag} * SF$(%)				0.22 ± 0.02	
Pretag Counts	38.24 ± 3.57	36.33 ± 3.40	7.97 ± 0.80	1.27 ± 0.12	0.32 ± 0.03
$\geq$ 1+ Tag Counts	0.72 ± 0.12	1.46 ± 0.24	0.41 ± 0.07	0.07 ± 0.02	0.03 ± 0.01
$\geq$ 2+ Tag Counts	0.00 ± 0.00	0.01 ± 0.00	0.01 ± 0.00	0.00 ± 0.00	0.00 ± 0.00
CMX					
ϵ_{pretag}(%)	0.49 ± 0.01	0.46 ± 0.01	0.09 ± 0.00	0.02 ± 0.00	0.00 ± 0.00
$\epsilon_{pretag} * SF$(%)	0.44 ± 0.03	0.42 ± 0.03	0.08 ± 0.01	0.02 ± 0.00	0.00 ± 0.00
ϵ_{pretag}(%)				0.12 ± 0.01	
$\epsilon_{pretag} * SF$(%)				0.11 ± 0.01	
Pretag Counts	17.98 ± 1.69	16.88 ± 1.59	3.30 ± 0.30	0.73 ± 0.07	0.00 ± 0.00
$\geq$ 1+ Tag Counts	0.34 ± 0.06	0.68 ± 0.11	0.17 ± 0.03	0.04 ± 0.01	0.00 ± 0.00
$\geq$ 2+ Tag Counts	0.00 ± 0.00	0.01 ± 0.00	0.00 ± 0.00	0.00 ± 0.00	0.00 ± 0.00
Total					
Pretag	130.50 ± 11.72	127.10 ± 11.42	26.28 ± 2.40	4.32 ± 0.39	0.70 ± 0.06
$\geq$ 1 Tag Counts	2.44 ± 0.42	5.11 ± 0.84	1.36 ± 0.23	0.23 ± 0.05	0.08 ± 0.02
$\geq$ 2 Tag Counts	0.00 ± 0.00	0.04 ± 0.01	0.03 ± 0.01	0.00 ± 0.00	0.01 ± 0.01

Table C.5: Summary table for WW. See Section C.2 for a description of the variables. These numbers are for the *unoptimized* analysis.

WZ, $\sigma \int \mathcal{L}dt = 1261 \pm 77$					
	1 jet	2 jets	3 jets	4 jets	$\geq$ 5 jets
ϵ_{b-jet}(%)	41.08 ± 1.09	40.68 ± 0.81	38.97 ± 1.75	37.42 ± 3.89	47.83 ± 10.42
ϵ_{c-jet}(%)	7.41 ± 0.77	9.24 ± 0.56	9.05 ± 1.07	9.22 ± 2.44	11.76 ± 5.53
$\epsilon_{b-jet} * SF$(%)	37.34 ± 2.66	36.98 ± 2.55	35.42 ± 2.83	34.01 ± 4.19	43.48 ± 9.90
$\epsilon_{c-jet} * SF$(%)	6.74 ± 1.13	8.40 ± 1.22	8.23 ± 1.46	8.38 ± 2.48	10.69 ± 5.22
$\Phi_e^{\geq 1}$(%)	90.90 ± 6.86	92.08 ± 6.38	92.29 ± 6.51	92.37 ± 6.40	92.38 ± 7.33
$\Phi_e^{\geq 2}$(%)	0.00 ± 0.00	82.63 ± 11.68	82.83 ± 11.61	83.00 ± 11.71	82.79 ± 12.13
$\epsilon_{\geq 1}$(%)	10.77 ± 0.33	16.02 ± 0.37	15.81 ± 0.79	18.47 ± 1.99	19.12 ± 4.77
$\epsilon_{\geq 2}$ (%)	0.00 ± 0.00	2.03 ± 0.14	2.69 ± 0.35	2.37 ± 0.78	4.41 ± 2.49
$\epsilon_{\geq 1} * \Phi_e$ (%)	9.79 ± 0.80	14.75 ± 1.08	14.59 ± 1.26	17.06 ± 2.19	17.66 ± 4.62
$\epsilon_{\geq 2} * \Phi_e$(%)	0.00 ± 0.00	1.68 ± 0.26	2.23 ± 0.43	1.97 ± 0.70	3.65 ± 2.13
ϵ_{bjet}(%)				38.94 ± 1.58	
ϵ_{cjet}(%)				9.18 ± 0.97	
$\epsilon_{bjet} * SF$(%)				35.40 ± 2.74	
$\epsilon_{cjet} * SF$(%)				8.34 ± 1.41	
$\epsilon_{\geq 1}$(%)				16.29 ± 0.73	
$\epsilon_{\geq 2}$(%)				2.69 ± 0.32	
Φ_E^1(%)				92.31 ± 6.51	
Φ_E^2(%)				82.87 ± 11.65	
$\epsilon_{\geq 1}$(%) $* \Phi_E^1$				15.04 ± 1.26	
$\epsilon_{\geq 2}$(%) $* \Phi_E^2$				2.23 ± 0.41	
CEM					
ϵ_{pretag}(%)	0.95 ± 0.02	1.08 ± 0.02	0.23 ± 0.01	0.04 ± 0.00	0.01 ± 0.00
$\epsilon_{pretag} * SF$(%)	0.87 ± 0.06	0.98 ± 0.07	0.21 ± 0.02	0.04 ± 0.00	0.01 ± 0.00
ϵ_{pretag}(%)				0.27 ± 0.01	
$\epsilon_{pretag} * SF$(%)				0.25 ± 0.02	
Pretag Counts	10.93 ± 1.02	12.42 ± 1.15	2.65 ± 0.27	0.46 ± 0.04	0.12 ± 0.01
$\geq$ 1+ Tag Counts	1.07 ± 0.13	1.83 ± 0.22	0.39 ± 0.05	0.08 ± 0.01	0.02 ± 0.01
$\geq$ 2+ Tag Counts	0.00 ± 0.00	0.21 ± 0.04	0.06 ± 0.01	0.01 ± 0.00	0.00 ± 0.00
CMUP					
ϵ_{pretag}(%)	0.59 ± 0.01	0.65 ± 0.01	0.13 ± 0.01	0.03 ± 0.00	0.00 ± 0.00
$\epsilon_{pretag} * SF$(%)	0.45 ± 0.03	0.49 ± 0.03	0.10 ± 0.01	0.02 ± 0.00	0.00 ± 0.00
ϵ_{pretag}(%)				0.17 ± 0.01	
$\epsilon_{pretag} * SF$(%)				0.13 ± 0.01	
Pretag Counts	5.62 ± 0.52	6.19 ± 0.57	1.24 ± 0.15	0.29 ± 0.03	0.00 ± 0.00
$\geq$ 1+ Tag Counts	0.55 ± 0.07	0.91 ± 0.11	0.18 ± 0.03	0.05 ± 0.01	0.00 ± 0.00
$\geq$ 2+ Tag Counts	0.00 ± 0.00	0.10 ± 0.02	0.03 ± 0.01	0.01 ± 0.00	0.00 ± 0.00
CMX					
ϵ_{pretag}(%)	0.22 ± 0.01	0.26 ± 0.01	0.06 ± 0.00	0.01 ± 0.00	0.00 ± 0.00
$\epsilon_{pretag} * SF$(%)	0.20 ± 0.02	0.24 ± 0.02	0.05 ± 0.00	0.01 ± 0.00	0.00 ± 0.00
ϵ_{pretag}(%)				0.07 ± 0.00	
$\epsilon_{pretag} * SF$(%)				0.06 ± 0.00	
Pretag Counts	2.41 ± 0.24	2.85 ± 0.28	0.66 ± 0.06	0.11 ± 0.01	0.00 ± 0.00
$\geq$ 1+ Tag Counts	0.24 ± 0.03	0.42 ± 0.05	0.10 ± 0.01	0.02 ± 0.00	0.00 ± 0.00
$\geq$ 2+ Tag Counts	0.00 ± 0.00	0.05 ± 0.01	0.01 ± 0.00	0.00 ± 0.00	0.00 ± 0.00
Total					
Pretag	18.96 ± 1.71	21.46 ± 1.93	4.54 ± 0.43	0.86 ± 0.08	0.12 ± 0.01
$\geq$ 1 Tag Counts	1.86 ± 0.23	3.17 ± 0.37	0.66 ± 0.09	0.15 ± 0.02	0.02 ± 0.01
$\geq$ 2 Tag Counts	0.00 ± 0.00	0.36 ± 0.07	0.10 ± 0.02	0.02 ± 0.01	0.00 ± 0.00

Table C.6: Summary table for WZ. See Section C.2 for a description of the variables. These numbers are for the *unoptimized* analysis.

ZZ, $\sigma \int \mathcal{L}dt = 503 \pm 30$					
	1 jet	2 jets	3 jets	4 jets	$\geq$ 5 jets
ϵ_{b-jet}(%)	29.76 ± 4.99	46.10 ± 2.90	42.19 ± 4.37	33.33 ± 8.61	44.44 ± 16.56
ϵ_{c-jet}(%)	8.70 ± 2.94	8.15 ± 1.79	8.49 ± 2.71	5.88 ± 4.04	0.00 ± 0.00
$\epsilon_{b-jet} * SF$(%)	27.05 ± 4.87	41.90 ± 3.82	38.35 ± 4.71	30.30 ± 8.08	40.40 ± 15.29
$\epsilon_{c-jet} * SF$(%)	7.91 ± 2.87	7.41 ± 1.90	7.72 ± 2.67	5.34 ± 3.74	0.00 ± 0.00
$\Phi_e^{\geq 1}$(%)	90.90 ± 9.46	92.37 ± 8.05	92.52 ± 8.10	92.68 ± 8.26	92.81 ± 6.50
$\Phi_e^{\geq 2}$(%)	0.00 ± 0.00	82.63 ± 14.28	82.96 ± 14.15	82.96 ± 14.38	82.63 ± 14.06
$\epsilon_{\geq 1}$(%)	4.78 ± 0.75	15.78 ± 1.25	16.01 ± 1.94	15.73 ± 3.86	15.79 ± 8.37
$\epsilon_{\geq 2}$ (%)	0.00 ± 0.00	3.53 ± 0.63	3.09 ± 0.92	1.12 ± 1.12	5.26 ± 5.12
$\epsilon_{\geq 1} * \Phi_e$ (%)	4.35 ± 0.82	14.58 ± 1.72	14.81 ± 2.21	14.58 ± 3.81	14.65 ± 7.84
$\epsilon_{\geq 2} * \Phi_e$(%)	0.00 ± 0.00	2.92 ± 0.72	2.56 ± 0.88	0.93 ± 0.94	4.35 ± 4.29
ϵ_{bjet}(%)				40.72 ± 3.80	
ϵ_{cjet}(%)				7.53 ± 2.18	
$\epsilon_{bjet} * SF$(%)				37.01 ± 4.23	
$\epsilon_{cjet} * SF$(%)				6.84 ± 2.18	
$\epsilon_{\geq 1}$(%)				15.95 ± 1.70	
$\epsilon_{\geq 2}$(%)				2.80 ± 0.77	
Φ_E^1(%)				92.58 ± 8.02	
Φ_E^2(%)				82.93 ± 14.20	
$\epsilon_{\geq 1}$(%) $* \Phi_E^1$				14.77 ± 2.03	
$\epsilon_{\geq 2}$(%) $* \Phi_E^2$				2.32 ± 0.75	
CEM					
ϵ_{pretag}(%)	0.07 ± 0.00	0.07 ± 0.00	0.04 ± 0.00	0.01 ± 0.00	0.00 ± 0.00
$\epsilon_{pretag} * SF$(%)	0.06 ± 0.00	0.06 ± 0.00	0.04 ± 0.00	0.01 ± 0.00	0.00 ± 0.00
ϵ_{pretag}(%)				0.05 ± 0.00	
$\epsilon_{pretag} * SF$(%)				0.05 ± 0.00	
Pretag Counts	0.32 ± 0.03	0.32 ± 0.03	0.18 ± 0.02	0.05 ± 0.00	0.00 ± 0.00
$\geq$ 1+ Tag Counts	0.01 ± 0.00	0.05 ± 0.01	0.03 ± 0.00	0.01 ± 0.00	0.00 ± 0.00
$\geq$ 2+ Tag Counts	0.00 ± 0.00	0.01 ± 0.00	0.00 ± 0.00	0.00 ± 0.00	0.00 ± 0.00
CMUP					
ϵ_{pretag}(%)	0.08 ± 0.00	0.08 ± 0.00	0.03 ± 0.00	0.01 ± 0.00	0.00 ± 0.00
$\epsilon_{pretag} * SF$(%)	0.06 ± 0.00	0.06 ± 0.00	0.02 ± 0.00	0.01 ± 0.00	0.00 ± 0.00
ϵ_{pretag}(%)				0.04 ± 0.00	
$\epsilon_{pretag} * SF$(%)				0.03 ± 0.00	
Pretag Counts	0.30 ± 0.03	0.30 ± 0.03	0.11 ± 0.01	0.04 ± 0.00	0.00 ± 0.00
$\geq$ 1+ Tag Counts	0.01 ± 0.00	0.04 ± 0.01	0.02 ± 0.00	0.01 ± 0.00	0.00 ± 0.00
$\geq$ 2+ Tag Counts	0.00 ± 0.00	0.01 ± 0.00	0.00 ± 0.00	0.00 ± 0.00	0.00 ± 0.00
CMX					
ϵ_{pretag}(%)	0.03 ± 0.00	0.03 ± 0.00	0.01 ± 0.00	0.00 ± 0.00	0.00 ± 0.00
$\epsilon_{pretag} * SF$(%)	0.03 ± 0.00	0.03 ± 0.00	0.01 ± 0.00	0.00 ± 0.00	0.00 ± 0.00
ϵ_{pretag}(%)				0.01 ± 0.00	
$\epsilon_{pretag} * SF$(%)				0.01 ± 0.00	
Pretag Counts	0.13 ± 0.01	0.13 ± 0.01	0.04 ± 0.00	0.00 ± 0.00	0.00 ± 0.00
$\geq$ 1+ Tag Counts	0.01 ± 0.00	0.02 ± 0.00	0.01 ± 0.00	0.00 ± 0.00	0.00 ± 0.00
$\geq$ 2+ Tag Counts	0.00 ± 0.00	0.00 ± 0.00	0.00 ± 0.00	0.00 ± 0.00	0.00 ± 0.00
Total					
Pretag	0.76 ± 0.07	0.76 ± 0.07	0.34 ± 0.03	0.08 ± 0.01	0.00 ± 0.00
$\geq$ 1 Tag Counts	0.03 ± 0.01	0.11 ± 0.02	0.05 ± 0.01	0.01 ± 0.00	0.00 ± 0.00
$\geq$ 2 Tag Counts	0.00 ± 0.00	0.02 ± 0.01	0.01 ± 0.00	0.00 ± 0.00	0.00 ± 0.00

Table C.7: Summary table for ZZ. See Section C.2 for a description of the variables. These numbers are for the *unoptimized* analysis.

$Z \to \tau\tau$, $\sigma \int \mathcal{L}dt = 4141 \pm 537$					
	1 jet	2 jets	3 jets	4 jets	$\geq$ 5 jets
ϵ_{b-jet}(%)	52.00 ± 9.99	41.67 ± 10.06	33.33 ± 15.71	0.00 ± 0.00	0.00 ± 0.00
ϵ_{c-jet}(%)	6.12 ± 3.42	8.70 ± 4.15	5.88 ± 5.71	0.00 ± 0.00	0.00 ± 0.00
$\epsilon_{b-jet} * SF$(%)	47.27 ± 9.60	37.88 ± 9.48	30.30 ± 14.42	0.00 ± 0.00	0.00 ± 0.00
$\epsilon_{c-jet} * SF$(%)	5.56 ± 3.19	7.91 ± 3.91	5.34 ± 5.24	0.00 ± 0.00	0.00 ± 0.00
$\Phi_e^{\geq 1}$(%)	90.90 ± 18.90	91.42 ± 18.28	92.44 ± 17.24	90.90 ± 33.24	0.00 ± 0.00
$\Phi_e^{\geq 2}$(%)	0.00 ± 0.00	82.63 ± 27.42	82.63 ± 27.03	0.00 ± 0.00	0.00 ± 0.00
$\epsilon_{\geq 1}$(%)	2.06 ± 0.30	4.53 ± 0.78	7.75 ± 2.35	0.00 ± 0.00	0.00 ± 0.00
$\epsilon_{\geq 2}$ (%)	0.00 ± 0.00	0.00 ± 0.00	0.00 ± 0.00	0.00 ± 0.00	0.00 ± 0.00
$\epsilon_{\geq 1} * \Phi_e$ (%)	1.87 ± 0.48	4.14 ± 1.09	7.16 ± 2.55	0.00 ± 0.00	0.00 ± 0.00
$\epsilon_{\geq 2} * \Phi_e$(%)	0.00 ± 0.00	0.00 ± 0.00	0.00 ± 0.00	0.00 ± 0.00	0.00 ± 0.00
ϵ_{bjet}(%)				33.33 ± 15.71	
ϵ_{cjet}(%)				5.00 ± 4.87	
$\epsilon_{bjet} * SF$(%)				30.30 ± 14.42	
$\epsilon_{cjet} * SF$(%)				4.55 ± 4.47	
$\epsilon_{\geq 1}$(%)				6.80 ± 2.08	
$\epsilon_{\geq 2}$(%)				0.00 ± 0.00	
Φ_E^1(%)				92.35 ± 18.19	
Φ_E^2(%)				82.63 ± 27.03	
$\epsilon_{\geq 1}$(%) $* \Phi_E^1$				6.28 ± 2.28	
$\epsilon_{\geq 2}$(%) $* \Phi_E^2$				0.00 ± 0.00	
CEM					
ϵ_{pretag}(%)	0.11 ± 0.00	0.03 ± 0.00	0.01 ± 0.00	0.00 ± 0.00	0.00 ± 0.00
$\epsilon_{pretag} * SF$(%)	0.10 ± 0.01	0.03 ± 0.00	0.01 ± 0.00	0.00 ± 0.00	0.00 ± 0.00
ϵ_{pretag}(%)				0.01 ± 0.00	
$\epsilon_{pretag} * SF$(%)				0.01 ± 0.00	
Pretag Counts	4.15 ± 0.61	1.13 ± 0.17	0.38 ± 0.06	0.00 ± 0.00	0.00 ± 0.00
$\geq$ 1+ Tag Counts	0.08 ± 0.02	0.05 ± 0.01	0.03 ± 0.01	0.00 ± 0.00	0.00 ± 0.00
$\geq$ 2+ Tag Counts	0.00 ± 0.00	0.00 ± 0.00	0.00 ± 0.00	0.00 ± 0.00	0.00 ± 0.00
CMUP					
ϵ_{pretag}(%)	0.06 ± 0.00	0.02 ± 0.00	0.00 ± 0.00	0.00 ± 0.00	0.00 ± 0.00
$\epsilon_{pretag} * SF$(%)	0.05 ± 0.00	0.02 ± 0.00	0.00 ± 0.00	0.00 ± 0.00	0.00 ± 0.00
ϵ_{pretag}(%)				0.00 ± 0.00	
$\epsilon_{pretag} * SF$(%)				0.00 ± 0.00	
Pretag Counts	1.88 ± 0.27	0.63 ± 0.09	0.00 ± 0.00	0.00 ± 0.00	0.00 ± 0.00
$\geq$ 1+ Tag Counts	0.04 ± 0.01	0.03 ± 0.01	0.00 ± 0.00	0.00 ± 0.00	0.00 ± 0.00
$\geq$ 2+ Tag Counts	0.00 ± 0.00	0.00 ± 0.00	0.00 ± 0.00	0.00 ± 0.00	0.00 ± 0.00
CMX					
ϵ_{pretag}(%)	0.03 ± 0.00	0.01 ± 0.00	0.00 ± 0.00	0.00 ± 0.00	0.00 ± 0.00
$\epsilon_{pretag} * SF$(%)	0.03 ± 0.00	0.01 ± 0.00	0.00 ± 0.00	0.00 ± 0.00	0.00 ± 0.00
ϵ_{pretag}(%)				0.00 ± 0.00	
$\epsilon_{pretag} * SF$(%)				0.00 ± 0.00	
Pretag Counts	1.08 ± 0.16	0.36 ± 0.05	0.00 ± 0.00	0.00 ± 0.00	0.00 ± 0.00
$\geq$ 1+ Tag Counts	0.02 ± 0.01	0.01 ± 0.00	0.00 ± 0.00	0.00 ± 0.00	0.00 ± 0.00
$\geq$ 2+ Tag Counts	0.00 ± 0.00	0.00 ± 0.00	0.00 ± 0.00	0.00 ± 0.00	0.00 ± 0.00
Total					
Pretag	7.11 ± 0.83	2.12 ± 0.24	0.38 ± 0.06	0.00 ± 0.00	0.00 ± 0.00
$\geq$ 1 Tag Counts	0.13 ± 0.04	0.09 ± 0.03	0.03 ± 0.01	0.00 ± 0.00	0.00 ± 0.00
$\geq$ 2 Tag Counts	0.00 ± 0.00	0.00 ± 0.00	0.00 ± 0.00	0.00 ± 0.00	0.00 ± 0.00

Table C.8: Summary table for $Z \to \tau\tau$. See Section C.2 for a description of the variables. These numbers are for the *unoptimized* analysis.

Single top, t-channel, $\sigma \int \mathcal{L}dt = 280 \pm 23$					
	1 jet	2 jets	3 jets	4 jets	$\geq$ 5 jets
$\epsilon_{b-jet}(\%)$	46.35 ± 0.40	45.89 ± 0.36	43.80 ± 0.71	41.43 ± 1.61	44.16 ± 4.00
$\epsilon_{c-jet}(\%)$	7.69 ± 1.91	6.85 ± 0.85	9.05 ± 1.98	11.11 ± 4.28	0.00 ± 0.00
$\epsilon_{b-jet} * SF(\%)$	42.13 ± 2.80	41.71 ± 2.77	39.81 ± 2.71	37.66 ± 2.88	40.14 ± 4.50
$\epsilon_{c-jet} * SF(\%)$	6.99 ± 1.97	6.23 ± 1.13	8.23 ± 2.10	10.10 ± 4.11	0.00 ± 0.00
$\Phi_e^{\geq 1}(\%)$	90.90 ± 6.04	91.22 ± 5.86	92.41 ± 5.16	93.00 ± 4.85	93.28 ± 4.77
$\Phi_e^{\geq 2}(\%)$	0.00 ± 0.00	82.63 ± 11.55	82.69 ± 11.05	82.83 ± 10.99	83.03 ± 10.84
$\epsilon_{\geq 1}(\%)$	39.59 ± 0.37	47.05 ± 0.37	55.19 ± 0.86	59.47 ± 2.13	64.20 ± 5.33
$\epsilon_{\geq 2}$ (%)	0.00 ± 0.00	1.80 ± 0.10	10.68 ± 0.53	14.82 ± 1.54	19.75 ± 4.42
$\epsilon_{\geq 1} * \Phi_e$ (%)	35.99 ± 2.41	42.92 ± 2.78	51.00 ± 2.96	55.31 ± 3.50	59.89 ± 5.84
$\epsilon_{\geq 2} * \Phi_e(\%)$	0.00 ± 0.00	1.49 ± 0.22	8.83 ± 1.26	12.28 ± 2.07	16.40 ± 4.25
$\epsilon_{bjet}(\%)$				43.44 ± 0.64	
$\epsilon_{cjet}(\%)$				9.12 ± 1.74	
$\epsilon_{bjet} * SF(\%)$				39.49 ± 2.67	
$\epsilon_{cjet} * SF(\%)$				8.29 ± 1.92	
$\epsilon_{\geq 1}(\%)$				55.95 ± 0.79	
$\epsilon_{\geq 2}(\%)$				11.42 ± 0.51	
$\Phi_E^1(\%)$				92.55 ± 5.09	
$\Phi_E^2(\%)$				82.74 ± 11.03	
$\epsilon_{\geq 1}(\%) * \Phi_E^1$				51.78 ± 2.94	
$\epsilon_{>2}(\%) * \Phi_E^2$				9.45 ± 1.33	
CEM					
$\epsilon_{pretag}(\%)$	4.43 ± 0.05	4.55 ± 0.05	0.86 ± 0.02	0.13 ± 0.01	0.02 ± 0.00
$\epsilon_{pretag} * SF(\%)$	4.04 ± 0.27	4.15 ± 0.28	0.78 ± 0.06	0.12 ± 0.01	0.02 ± 0.00
$\epsilon_{pretag}(\%)$				1.01 ± 0.02	
$\epsilon_{pretag} * SF(\%)$				0.92 ± 0.06	
Pretag Counts	8.49 ± 3.52	8.72 ± 3.61	1.65 ± 0.68	0.25 ± 0.10	0.04 ± 0.02
$\geq$ 1+ Tag Counts	3.06 ± 1.28	3.74 ± 1.57	0.84 ± 0.35	0.14 ± 0.06	0.02 ± 0.01
$\geq$ 2+ Tag Counts	0.00 ± 0.00	0.13 ± 0.06	0.15 ± 0.06	0.03 ± 0.01	0.01 ± 0.00
CMUP					
$\epsilon_{pretag}(\%)$	2.59 ± 0.04	2.72 ± 0.04	0.50 ± 0.02	0.09 ± 0.01	0.01 ± 0.00
$\epsilon_{pretag} * SF(\%)$	1.96 ± 0.14	2.05 ± 0.14	0.38 ± 0.03	0.07 ± 0.01	0.01 ± 0.00
$\epsilon_{pretag}(\%)$				0.59 ± 0.02	
$\epsilon_{pretag} * SF(\%)$				0.45 ± 0.03	
Pretag Counts	4.11 ± 1.70	4.32 ± 1.79	0.79 ± 0.33	0.14 ± 0.06	0.02 ± 0.01
$\geq$ 1+ Tag Counts	1.48 ± 0.62	1.85 ± 0.78	0.40 ± 0.17	0.08 ± 0.03	0.01 ± 0.00
$\geq$ 2+ Tag Counts	0.00 ± 0.00	0.06 ± 0.03	0.07 ± 0.03	0.02 ± 0.01	0.00 ± 0.00
CMX					
$\epsilon_{pretag}(\%)$	0.95 ± 0.02	0.91 ± 0.02	0.18 ± 0.01	0.03 ± 0.00	0.00 ± 0.00
$\epsilon_{pretag} * SF(\%)$	0.86 ± 0.06	0.83 ± 0.06	0.16 ± 0.01	0.03 ± 0.00	0.00 ± 0.00
$\epsilon_{pretag}(\%)$				0.21 ± 0.01	
$\epsilon_{pretag} * SF(\%)$				0.19 ± 0.02	
Pretag Counts	1.74 ± 0.72	1.66 ± 0.69	0.33 ± 0.14	0.05 ± 0.02	0.00 ± 0.00
$\geq$ 1+ Tag Counts	0.62 ± 0.26	0.71 ± 0.30	0.17 ± 0.07	0.03 ± 0.01	0.00 ± 0.00
$\geq$ 2+ Tag Counts	0.00 ± 0.00	0.02 ± 0.01	0.03 ± 0.01	0.01 ± 0.00	0.00 ± 0.00
Total					
Pretag	14.34 ± 4.08	14.70 ± 4.20	2.77 ± 0.79	0.45 ± 0.13	0.05 ± 0.02
$\geq$ 1 Tag Counts	5.16 ± 1.51	6.31 ± 1.85	1.41 ± 0.41	0.25 ± 0.07	0.03 ± 0.01
$\geq$ 2 Tag Counts	0.00 ± 0.00	0.22 ± 0.07	0.24 ± 0.08	0.05 ± 0.02	0.01 ± 0.00

Table C.9: Summary table for single top (t-channel). See Section C.2 for a description of the variables. These numbers are for the *unoptimized* analysis.

Single top, s-channel, $\sigma \int \mathcal{L}dt = 631 \pm 45$					
	1 jet	2 jets	3 jets	4 jets	$\geq$ 5 jets
$\epsilon_{b-jet}(\%)$	44.87 ± 0.47	44.40 ± 0.24	44.04 ± 0.53	41.35 ± 1.34	38.76 ± 3.37
$\epsilon_{c-jet}(\%)$	0.00 ± 0.00	5.95 ± 1.83	10.81 ± 2.08	3.64 ± 2.52	0.00 ± 0.00
$\epsilon_{b-jet} * SF(\%)$	40.79 ± 2.73	40.36 ± 2.67	40.03 ± 2.69	37.59 ± 2.76	35.23 ± 3.85
$\epsilon_{c-jet} * SF(\%)$	0.00 ± 0.00	5.41 ± 1.81	9.83 ± 2.29	3.31 ± 2.33	0.00 ± 0.00
$\Phi_e^{\geq 1}(\%)$	90.90 ± 6.02	93.06 ± 4.73	93.17 ± 4.73	93.20 ± 4.74	93.39 ± 4.85
$\Phi_e^{\geq 2}(\%)$	0.00 ± 0.00	82.63 ± 10.95	82.78 ± 10.93	82.89 ± 10.92	83.38 ± 10.70
$\epsilon_{\geq 1}(\%)$	42.81 ± 0.45	64.91 ± 0.31	65.77 ± 0.70	64.09 ± 1.81	62.14 ± 4.78
$\epsilon_{\geq 2}$ (%)	0.00 ± 0.00	18.18 ± 0.25	19.38 ± 0.58	16.45 ± 1.40	18.45 ± 3.82
$\epsilon_{\geq 1} * \Phi_e$ (%)	38.91 ± 2.61	60.41 ± 3.08	61.28 ± 3.18	59.73 ± 3.47	58.03 ± 5.39
$\epsilon_{\geq 2} * \Phi_e(\%)$	0.00 ± 0.00	15.02 ± 2.00	16.04 ± 2.17	13.64 ± 2.14	15.38 ± 3.75
$\epsilon_{bjet}(\%)$				43.58 ± 0.49	
$\epsilon_{cjet}(\%)$				8.78 ± 1.65	
$\epsilon_{bjet} * SF(\%)$				39.61 ± 2.65	
$\epsilon_{cjet} * SF(\%)$				7.98 ± 1.83	
$\epsilon_{\geq 1}(\%)$				65.48 ± 0.64	
$\epsilon_{\geq 2}(\%)$				18.99 ± 0.53	
$\Phi_E^1(\%)$				93.18 ± 4.73	
$\Phi_E^2(\%)$				82.81 ± 10.92	
$\epsilon_{\geq 1}(\%) * \Phi_E^1$				61.01 ± 3.15	
$\epsilon_{>2}(\%) * \Phi_E^2$				15.73 ± 2.12	
CEM					
$\epsilon_{pretag}(\%)$	3.08 ± 0.04	6.08 ± 0.06	1.25 ± 0.03	0.19 ± 0.01	0.03 ± 0.00
$\epsilon_{pretag} * SF(\%)$	2.81 ± 0.19	5.55 ± 0.38	1.14 ± 0.08	0.17 ± 0.01	0.03 ± 0.00
$\epsilon_{pretag}(\%)$				1.47 ± 0.03	
$\epsilon_{pretag} * SF(\%)$				1.34 ± 0.09	
Pretag Counts	2.62 ± 0.28	5.18 ± 0.55	1.06 ± 0.12	0.16 ± 0.02	0.03 ± 0.00
$\geq$ 1+ Tag Counts	1.02 ± 0.13	3.13 ± 0.37	0.65 ± 0.08	0.10 ± 0.01	0.01 ± 0.00
$\geq$ 2+ Tag Counts	0.00 ± 0.00	0.78 ± 0.13	0.17 ± 0.03	0.02 ± 0.00	0.00 ± 0.00
CMUP					
$\epsilon_{pretag}(\%)$	1.74 ± 0.03	3.55 ± 0.04	0.73 ± 0.02	0.11 ± 0.01	0.01 ± 0.00
$\epsilon_{pretag} * SF(\%)$	1.31 ± 0.09	2.68 ± 0.18	0.55 ± 0.04	0.08 ± 0.01	0.01 ± 0.00
$\epsilon_{pretag}(\%)$				0.86 ± 0.02	
$\epsilon_{pretag} * SF(\%)$				0.65 ± 0.05	
Pretag Counts	1.23 ± 0.13	2.50 ± 0.27	0.51 ± 0.06	0.08 ± 0.01	0.01 ± 0.00
$\geq$ 1+ Tag Counts	0.48 ± 0.06	1.51 ± 0.18	0.32 ± 0.04	0.05 ± 0.01	0.00 ± 0.00
$\geq$ 2+ Tag Counts	0.00 ± 0.00	0.38 ± 0.06	0.08 ± 0.01	0.01 ± 0.00	0.00 ± 0.00
CMX					
$\epsilon_{pretag}(\%)$	0.64 ± 0.02	1.21 ± 0.03	0.23 ± 0.01	0.04 ± 0.00	0.01 ± 0.00
$\epsilon_{pretag} * SF(\%)$	0.58 ± 0.04	1.10 ± 0.08	0.21 ± 0.02	0.04 ± 0.00	0.01 ± 0.00
$\epsilon_{pretag}(\%)$				0.28 ± 0.01	
$\epsilon_{pretag} * SF(\%)$				0.25 ± 0.02	
Pretag Counts	0.52 ± 0.06	0.98 ± 0.11	0.19 ± 0.02	0.03 ± 0.00	0.01 ± 0.00
$\geq$ 1+ Tag Counts	0.20 ± 0.03	0.59 ± 0.07	0.11 ± 0.01	0.02 ± 0.00	0.00 ± 0.00
$\geq$ 2+ Tag Counts	0.00 ± 0.00	0.15 ± 0.03	0.03 ± 0.01	0.00 ± 0.00	0.00 ± 0.00
Total					
Pretag	4.37 ± 0.42	8.67 ± 0.84	1.77 ± 0.17	0.27 ± 0.03	0.04 ± 0.00
$\geq$ 1 Tag Counts	1.70 ± 0.20	5.24 ± 0.57	1.08 ± 0.12	0.16 ± 0.02	0.02 ± 0.00
$\geq$ 2 Tag Counts	0.00 ± 0.00	1.30 ± 0.21	0.28 ± 0.05	0.04 ± 0.01	0.01 ± 0.00

Table C.10: Summary table for single top (s-channel). See Section C.2 for a description of the variables. These numbers are for the *unoptimized* analysis.

W + LF Mistags					
	1 jet	2 jets	3 jets	4 jets	$\geq$ 5 jets
Raw Tag Matrix Predictions					
(+) Pred	447.03 ± 5.18	169.45 ± 1.04	49.27 ± 0.65	18.45 ± 0.11	4.75 ± 0.08
(-) Pred	96.12 ± 4.98	41.51 ± 0.96	13.47 ± 0.63	5.25 ± 0.08	1.40 ± 0.05
(+,-) Pred	-	1.24 ± 0.15	1.40 ± 0.05	1.56 ± 0.08	0.54 ± 0.05
(-,-) Pred	-	0.00 ± 0.00	0.00 ± 0.00	0.00 ± 0.00	0.00 ± 0.00
Tag Matrix Predictions, Including $\alpha_{LF} \times \beta$					
(-) Pred $\times\alpha_{LF}\beta$	109.96 ± 4.98	52.51 ± 0.96	18.27 ± 0.63	7.35 ± 0.08	1.99 ± 0.05
(+,-) Pred $\times\alpha_{LF}\beta$	0.00 ± 0.00	1.62 ± 0.15	1.94 ± 0.05	2.19 ± 0.08	0.77 ± 0.05
Number of W+LF Mistags (corrected for $\sigma_{t\bar{t}} = 8.9\ pb$)					
$\geq$ 1 Tag Counts	94.05 ± 19.28	39.12 ± 7.86	11.05 ± 2.24	2.27 ± 0.45	0.22 ± 0.05
$\geq$ 2 Tag Counts	0.00 ± 0.00	0.54 ± 0.12	0.22 ± 0.05	0.06 ± 0.03	0.03 ± 0.05

Table C.11: Raw mistag matrix prediction, prediction scaled to correct for light flavor asymmetry, and W+LF estimate removing other backgrounds (assuming $\sigma_{t\bar{t}} = 8.9$ pb). This is for the *unoptimized* analysis.

$W + c$					
	1 jet	2 jets	3 jets	4 jets	$\geq$ 5 jets
F_{1c} (%)	4.30 ± 0.90	6.00 ± 1.30	6.30 ± 1.30	6.10 ± 1.30	
WC, 1C, 1 Tag (%)	8.19 ± 1.10	8.84 ± 1.23	9.53 ± 1.56	13.16 ± 2.56	
$\Phi_e^{\geq 1}$(%)	90.90 ± 12.00	90.90 ± 12.00	90.90 ± 12.00	90.90 ± 12.00	
$\epsilon_{\geq 1} * \Phi_e * F_{HF}$ (%)	0.35 ± 0.09	0.51 ± 0.13	0.58 ± 0.14	0.75 ± 0.19	
Total					
Pretag	1211.62 ± 278.66	246.81 ± 61.48	35.11 ± 9.26	4.14 ± 1.67	0.30 ± 0.27
$\geq$ 1 Tag Counts	99.23 ± 26.61	21.06 ± 6.03	3.22 ± 0.98	0.51 ± 0.23	0.02 ± 0.02
$\geq$ 2 Tag Counts	0.00 ± 0.00	0.00 ± 0.00	0.00 ± 0.00	0.00 ± 0.00	0.00 ± 0.00

Table C.12: Summary table for the W+C background. F_{ic} is the heavy flavor fraction measured from [1], and the efficiencies given are the event tag rates in Monte Carlo. Φ_E is the ratio of event efficiencies with and without the b-tagging scale factor using the full binomial expression.

$W + c\bar{c}$					
	1 jet	2 jets	3 jets	4 jets	$\geq$ 5 jets
F_{1c} (%)	1.60 ± 0.40	2.40 ± 0.60	3.40 ± 0.90	3.60 ± 1.00	
F_{2c} (%)	0.00 ± 0.00	1.80 ± 0.50	2.70 ± 0.70	3.70 ± 1.00	
WCC, 1C, 1 Tag (%)	7.44 ± 1.04	8.78 ± 1.37	12.57 ± 2.33	10.53 ± 4.26	
WCC, 2C, 1 Tag (%)	0.00 ± 0.00	15.48 ± 2.40	16.59 ± 3.48	23.32 ± 5.14	
WCC, 2C, 2 Tag (%)	0.00 ± 0.00	0.36 ± 0.19	0.18 ± 0.12	0.00 ± 0.00	
$\Phi_e^{\geq 1}$(%)	90.90 ± 12.00	91.15 ± 11.70	91.13 ± 11.73	91.23 ± 11.61	
$\Phi_e^{\geq 2}$(%)	0.00 ± 0.00	82.63 ± 21.82	82.63 ± 21.82	0.00 ± 0.00	
$\epsilon_{\geq 1} * \Phi_e * F_{HF}$ (%)	0.12 ± 0.03	0.49 ± 0.14	0.88 ± 0.26	1.20 ± 0.36	
$\epsilon_{\geq 2} * \Phi_e * F_{HF}$(%)	0.00 ± 0.00	0.01 ± 0.00	0.00 ± 0.00	0.00 ± 0.00	
Total					
Pretag	450.84 ± 122.03	172.76 ± 50.85	33.99 ± 10.87	4.96 ± 2.30	0.36 ± 0.34
$\geq$ 1 Tag Counts	33.52 ± 10.17	20.13 ± 6.60	4.88 ± 1.70	0.81 ± 0.40	0.02 ± 0.02
$\geq$ 2 Tag Counts	0.00 ± 0.00	0.26 ± 0.11	0.03 ± 0.01	0.00 ± 0.00	0.00 ± 0.00

Table C.13: Summary table for the W+CC background. F_{ic} is the heavy flavor fraction measured from [1], and the efficiencies given are the event tag rates in Monte Carlo. Φ_E is the ratio of event efficiencies with and without the b-tagging scale factor using the full binomial expression.

$W + b\bar{b}$					
	1 jet	2 jets	3 jets	4 jets	$\geq$ 5 jets
F_{1b}(%)	1.00 ± 0.30	1.40 ± 0.40	2.00 ± 0.50	2.20 ± 0.60	
F_{2b}(%)	0.00 ± 0.00	1.40 ± 0.40	2.00 ± 0.50	2.60 ± 0.70	
WBB, 1B, 1 Tag (%)	35.04 ± 2.35	37.93 ± 2.38	39.38 ± 4.08	42.76 ± 3.46	
WBB, 2B, 1 Tag (%)	0.00 ± 0.00	57.86 ± 3.52	59.01 ± 4.28	60.50 ± 3.92	
WBB, 2B, 2 Tag (%)	0.00 ± 0.00	14.10 ± 1.93	16.06 ± 2.42	17.45 ± 2.83	
$\Phi_e^{\geq 1}$(%)	90.90 ± 6.00	92.18 ± 5.24	92.11 ± 5.28	92.27 ± 5.18	
$\Phi_e^{\geq 2}$(%)	0.00 ± 0.00	82.63 ± 10.91	82.78 ± 11.06	83.08 ± 11.37	
$\epsilon_{\geq 1} * \Phi_e * F_{HF}$ (%)	0.35 ± 0.11	1.34 ± 0.39	1.96 ± 0.50	2.50 ± 0.69	
$\epsilon_{\geq 2} * \Phi_e * F_{HF}$(%)	0.00 ± 0.00	0.20 ± 0.06	0.32 ± 0.09	0.45 ± 0.14	
Total					
Pretag	281.77 ± 90.36	115.18 ± 36.64	22.29 ± 6.85	3.26 ± 1.51	0.24 ± 0.23
$\geq$ 1 Tag Counts	98.74 ± 32.37	55.13 ± 17.85	10.94 ± 3.44	1.70 ± 0.79	0.12 ± 0.12
$\geq$ 2 Tag Counts	0.00 ± 0.00	8.12 ± 2.82	1.79 ± 0.61	0.31 ± 0.15	0.02 ± 0.02

Table C.14: Summary table for the W+BB background. F_{ib} is the heavy flavor fraction measured from [1], and the efficiencies given are the event tag rates in Monte Carlo. Φ_E is the ratio of event efficiencies with and without the b-tagging scale factor using the full binomial expression.

Non-W : Raw Counts					
	1 jet	2 jets	3 jets	4 jets	$\geq$ 5 jets
Electrons					
N_A^{pre}	101832	12862	1773	189	30
N_B^{pre}	63472	5328	612	87	11
N_C^{pre}	2853	889	175	37	9
N_D^{pre}	17643	2845	468	114	19
N_A^{+}	3017	714	161	23	5
N_B^{+}	1032	187	44	11	2
N_C^{+}	139	87	25	9	3
N_D^{+}	249	141	58	39	8
N_A^{++}	0	18	6	2	1
N_B^{++}	0	1	4	3	0
N_C^{++}	0	3	3	1	0
N_D^{++}	0	9	11	7	1
F_{Non-W} (%)	10.08 $\pm$ 2.53	12.94 $\pm$ 3.28	13.11 $\pm$ 3.48		
N_+^B/N_+^A (%)	34.21 $\pm$ 1.23	26.19 $\pm$ 2.15	30.16 $\pm$ 4.56		
$N_+^{tagmethod}$	47.55 $\pm$ 16.29	22.79 $\pm$ 8.12	7.54 $\pm$ 3.12	2.71 $\pm$ 1.34	0.90 $\pm$ 0.62
R_+^B (%)	1.63 $\pm$ 0.33	3.51 $\pm$ 0.75	7.19 $\pm$ 1.82	12.64 $\pm$ 4.77	18.18 $\pm$ 14.44
$N_+^{pretagmethod}$	28.92 $\pm$ 9.32	12.93 $\pm$ 4.28	4.42 $\pm$ 1.62	1.91 $\pm$ 0.88	0.45 $\pm$ 0.38
R_{++}^B (%)	0.00 $\pm$ 0.00	0.02 $\pm$ 0.02	0.65 $\pm$ 0.35	3.45 $\pm$ 2.14	0.00 $\pm$ 0.00
$N_{++}^{pretagmethod}$	0.00 $\pm$ 0.00	0.07 $\pm$ 0.07	0.40 $\pm$ 0.24	0.52 $\pm$ 0.35	0.00 $\pm$ 0.00
Muons					
N_A^{pre}	39078	5565	709	90	19
N_B^{pre}	12008	976	119	18	2
N_C^{pre}	1586	489	128	32	8
N_D^{pre}	12977	1919	297	63	16
N_A^{+}	2345	583	89	15	4
N_B^{+}	229	52	12	6	1
N_C^{+}	85	50	25	12	2
N_D^{+}	182	100	36	24	11
N_A^{++}	0	13	1	0	0
N_B^{++}	0	1	2	0	1
N_C^{++}	0	3	2	1	1
N_D^{++}	0	5	6	9	2
F_{Non-W} (%)	3.76 $\pm$ 0.94	4.47 $\pm$ 1.15	7.59 $\pm$ 2.14		
N_+^B/N_+^A (%)	9.77 $\pm$ 0.68	8.92 $\pm$ 1.29	17.59 $\pm$ 4.38		
$N_+^{tagmethod}$	8.30 $\pm$ 2.94	4.46 $\pm$ 1.73	4.40 $\pm$ 2.02	2.11 $\pm$ 1.06	0.35 $\pm$ 0.29
R_+^B (%)	1.91 $\pm$ 0.40	5.33 $\pm$ 1.31	10.08 $\pm$ 3.66	33.33 $\pm$ 17.07	50.00 $\pm$ 62.05
$N_+^{pretagmethod}$	9.30 $\pm$ 3.05	4.63 $\pm$ 1.65	2.30 $\pm$ 1.06	1.62 $\pm$ 0.95	0.65 $\pm$ 0.82
R_{++}^B (%)	0.00 $\pm$ 0.00	0.10 $\pm$ 0.10	1.68 $\pm$ 1.24	0.00 $\pm$ 0.00	50.00 $\pm$ 62.05
$N_{++}^{pretagmethod}$	0.00 $\pm$ 0.00	0.09 $\pm$ 0.09	0.38 $\pm$ 0.30	0.00 $\pm$ 0.00	0.65 $\pm$ 0.82
Electrons					
Pretag Counts	1778.78 $\pm$ 446.23	368.39 $\pm$ 93.37	61.47 $\pm$ 16.33	15.07 $\pm$ 4.00	2.49 $\pm$ 0.66
$\geq$ 1+ Tag Counts	33.52 $\pm$ 8.04	15.07 $\pm$ 3.77	5.08 $\pm$ 1.43	2.15 $\pm$ 0.73	0.58 $\pm$ 0.32
$\geq$ 2+ Tag Counts	0.00 $\pm$ 0.00	0.07 $\pm$ 0.07	0.40 $\pm$ 0.24	0.52 $\pm$ 0.35	0.00 $\pm$ 0.00
Muons					
Pretag Counts	487.46 $\pm$ 122.66	86.92 $\pm$ 22.38	22.78 $\pm$ 6.42	4.86 $\pm$ 1.37	1.29 $\pm$ 0.36
$\geq$ 1+ Tag Counts	8.78 $\pm$ 2.09	4.55 $\pm$ 1.19	2.75 $\pm$ 0.94	1.84 $\pm$ 0.70	0.38 $\pm$ 0.27
$\geq$ 2+ Tag Counts	0.00 $\pm$ 0.00	0.09 $\pm$ 0.09	0.38 $\pm$ 0.30	0.00 $\pm$ 0.00	0.38 $\pm$ 0.82

Table C.15: Raw event counts for Non-W backgrounds. These numbers are for the *unoptimized* analysis.

$t\bar{t}$ (8.9 pb)					
	1 jet	2 jets	3 jets	4 jets	$\geq$ 5 jets
Electrons					
N_A^{pre}	0.03 ± 0.00	0.18 ± 0.02	0.51 ± 0.05	0.69 ± 0.06	0.64 ± 0.06
N_B^{pre}	0.28 ± 0.02	1.52 ± 0.14	3.55 ± 0.32	3.30 ± 0.30	1.14 ± 0.10
N_C^{pre}	0.88 ± 0.08	3.40 ± 0.30	4.96 ± 0.44	2.83 ± 0.25	1.38 ± 0.13
N_D^{pre}	5.43 ± 0.48	28.44 ± 2.55	55.32 ± 4.95	50.15 ± 4.49	15.51 ± 1.41
N_A^{+}	0.01 ± 0.00	0.08 ± 0.01	0.22 ± 0.02	0.27 ± 0.03	0.26 ± 0.03
N_B^{+}	0.09 ± 0.01	0.81 ± 0.09	2.03 ± 0.21	2.06 ± 0.21	0.72 ± 0.07
N_C^{+}	0.28 ± 0.03	1.47 ± 0.16	2.55 ± 0.27	1.54 ± 0.16	0.79 ± 0.08
N_D^{+}	1.82 ± 0.21	14.46 ± 1.54	31.64 ± 3.31	31.23 ± 3.22	9.78 ± 1.02
N_A^{++}	0.00 ± 0.00	0.01 ± 0.00	0.03 ± 0.01	0.03 ± 0.00	0.03 ± 0.01
N_B^{++}	0.00 ± 0.00	0.17 ± 0.03	0.50 ± 0.08	0.57 ± 0.09	0.22 ± 0.03
N_C^{++}	0.00 ± 0.00	0.13 ± 0.02	0.51 ± 0.08	0.35 ± 0.06	0.15 ± 0.02
N_D^{++}	0.00 ± 0.00	2.67 ± 0.44	7.26 ± 1.19	8.86 ± 1.43	2.92 ± 0.47
Muons					
N_A^{pre}	0.02 ± 0.00	0.17 ± 0.02	0.46 ± 0.04	0.64 ± 0.06	0.49 ± 0.04
N_B^{pre}	0.17 ± 0.01	1.22 ± 0.11	2.76 ± 0.25	2.77 ± 0.25	0.79 ± 0.07
N_C^{pre}	0.70 ± 0.06	2.75 ± 0.25	4.49 ± 0.40	2.83 ± 0.25	1.13 ± 0.10
N_D^{pre}	3.77 ± 0.34	21.11 ± 1.89	41.33 ± 3.70	36.22 ± 3.24	11.12 ± 1.01
N_A^{+}	0.01 ± 0.00	0.08 ± 0.01	0.21 ± 0.02	0.30 ± 0.03	0.23 ± 0.02
N_B^{+}	0.05 ± 0.01	0.60 ± 0.06	1.63 ± 0.17	1.70 ± 0.17	0.48 ± 0.05
N_C^{+}	0.23 ± 0.03	1.23 ± 0.13	2.37 ± 0.25	1.58 ± 0.16	0.64 ± 0.07
N_D^{+}	1.26 ± 0.14	10.73 ± 1.14	23.64 ± 2.47	22.55 ± 2.32	7.02 ± 0.73
N_A^{++}	0.00 ± 0.00	0.01 ± 0.00	0.04 ± 0.01	0.04 ± 0.01	0.02 ± 0.00
N_B^{++}	0.00 ± 0.00	0.11 ± 0.02	0.43 ± 0.07	0.51 ± 0.08	0.15 ± 0.02
N_C^{++}	0.00 ± 0.00	0.17 ± 0.03	0.49 ± 0.08	0.33 ± 0.05	0.16 ± 0.03
N_D^{++}	0.00 ± 0.00	1.98 ± 0.33	5.42 ± 0.89	6.40 ± 1.03	2.10 ± 0.34

Table C.16: Expectation of $t\bar{t}$ in Non-W sideband regions. These numbers are for the *unoptimized* analysis.

Non-W					
	1 jet	2 jets	3 jets	4 jets	$\geq$ 5 jets
Electrons					
N_A^{pre}	101831.97 ± 319.11	12861.82 ± 113.41	1772.49 ± 42.11	188.31 ± 13.75	29.36 ± 5.48
N_B^{pre}	63471.72 ± 251.94	5326.48 ± 72.99	608.45 ± 24.74	83.70 ± 9.33	9.86 ± 3.32
N_C^{pre}	2852.12 ± 53.41	885.60 ± 29.82	170.04 ± 13.24	34.17 ± 6.09	7.62 ± 3.00
N_D^{pre}	17643.00 ± 132.83	2845.00 ± 53.34	468.00 ± 21.63	114.00 ± 10.68	19.00 ± 4.36
N_A^{+}	3016.99 ± 54.93	713.92 ± 26.72	160.78 ± 12.69	22.73 ± 4.80	4.74 ± 2.24
N_B^{+}	1031.91 ± 32.12	186.19 ± 13.68	41.97 ± 6.64	8.94 ± 3.32	1.28 ± 1.42
N_C^{+}	138.72 ± 11.79	85.53 ± 9.33	22.45 ± 5.01	7.46 ± 3.00	2.21 ± 1.73
N_D^{+}	247.18 ± 15.78	126.54 ± 11.97	26.36 ± 8.30	7.77 ± 7.02	-1.78 ± 3.01
N_A^{++}	0.00 ± 0.00	18.30 ± 4.50	6.52 ± 2.73	2.47 ± 1.75	1.54 ± 1.19
N_B^{++}	0.00 ± 0.00	1.40 ± 1.18	4.06 ± 2.22	2.75 ± 1.98	0.53 ± 0.53
N_C^{++}	0.00 ± 0.00	3.10 ± 2.08	2.80 ± 2.00	1.22 ± 1.18	0.56 ± 0.56
N_D^{++}	0.00 ± 0.00	6.90 ± 3.23	4.32 ± 3.24	0.88 ± 0.88	0.24 ± 0.24
F_{Non-W} (%)	10.08 ± 2.53	12.89 ± 3.27	12.43 ± 3.37		
N_+^B/N_+^A (%)	34.20 ± 1.23	26.08 ± 2.15	27.73 ± 4.50		
$N_+^{tagmethod}$	47.45 ± 16.27	22.31 ± 8.01	6.23 ± 2.78	2.07 ± 1.17	0.61 ± 0.54
R_+^B (%)	1.63 ± 0.33	3.50 ± 0.75	6.90 ± 1.80	10.68 ± 4.76	13.02 ± 15.34
$N_+^{pretagmethod}$	28.91 ± 9.32	12.82 ± 4.26	4.02 ± 1.52	1.53 ± 0.80	0.31 ± 0.37
R_{++}^B (%)	0.00 ± 0.00	0.03 ± 0.02	0.67 ± 0.39	3.28 ± 2.49	5.40 ± 5.81
$N_{++}^{pretagmethod}$	0.00 ± 0.00	0.10 ± 0.09	0.39 ± 0.25	0.47 ± 0.38	0.13 ± 0.14
Muons					
N_A^{pre}	39077.98 ± 197.68	5564.83 ± 74.60	708.54 ± 26.63	89.36 ± 9.49	18.51 ± 4.36
N_B^{pre}	12007.83 ± 109.58	974.78 ± 31.24	116.24 ± 10.91	15.23 ± 4.25	1.21 ± 1.42
N_C^{pre}	1585.30 ± 39.82	486.25 ± 22.11	123.51 ± 11.32	29.17 ± 5.66	6.87 ± 2.83
N_D^{pre}	12977.00 ± 113.92	1919.00 ± 43.81	297.00 ± 17.23	63.00 ± 7.94	16.00 ± 4.00
N_A^{+}	2344.99 ± 48.43	582.92 ± 24.15	88.79 ± 9.43	14.70 ± 3.87	3.77 ± 2.00
N_B^{+}	228.95 ± 15.13	51.40 ± 7.21	10.37 ± 3.47	4.30 ± 2.46	0.52 ± 1.00
N_C^{+}	84.77 ± 9.22	48.77 ± 7.07	22.63 ± 5.01	10.42 ± 3.47	1.36 ± 1.42
N_D^{+}	180.74 ± 13.49	89.27 ± 10.06	12.36 ± 6.49	1.45 ± 5.42	3.98 ± 3.40
N_A^{++}	0.00 ± 0.00	13.49 ± 4.09	2.17 ± 1.34	1.26 ± 0.89	1.27 ± 0.90
N_B^{++}	0.00 ± 0.00	2.12 ± 1.33	2.83 ± 1.79	1.02 ± 0.73	2.12 ± 1.32
N_C^{++}	0.00 ± 0.00	3.91 ± 2.11	2.66 ± 1.67	1.92 ± 1.33	2.07 ± 1.33
N_D^{++}	0.00 ± 0.00	4.27 ± 2.53	2.60 ± 2.06	4.21 ± 2.85	1.76 ± 1.43
F_{Non-W} (%)	3.75 ± 0.94	4.44 ± 1.15	6.90 ± 2.01		
N_+^B/N_+^A (%)	9.76 ± 0.68	8.82 ± 1.29	14.17 ± 4.30		
$N_+^{tagmethod}$	8.28 ± 2.93	4.30 ± 1.69	3.21 ± 1.68	1.48 ± 0.86	0.19 ± 0.22
R_+^B (%)	1.91 ± 0.40	5.27 ± 1.30	8.92 ± 3.64	28.26 ± 19.00	42.85 ± 96.97
$N_+^{pretagmethod}$	9.29 ± 3.05	4.55 ± 1.63	1.85 ± 0.93	1.25 ± 0.92	0.50 ± 1.15
R_{++}^B (%)	0.00 ± 0.00	0.22 ± 0.14	2.43 ± 1.63	6.71 ± 5.33	174.42 ± 235.07
$N_{++}^{pretagmethod}$	0.00 ± 0.00	0.19 ± 0.13	0.50 ± 0.37	0.30 ± 0.25	2.04 ± 2.83
Electrons					
Pretag Counts	1778.22 ± 446.14	366.89 ± 93.13	58.31 ± 15.80	14.30 ± 3.87	2.36 ± 0.64
$\geq$ 1+ Tag Counts	33.49 ± 8.04	14.91 ± 3.74	4.53 ± 1.33	1.70 ± 0.66	0.41 ± 0.31
$\geq$ 2+ Tag Counts	0.00 ± 0.00	0.10 ± 0.09	0.39 ± 0.25	0.47 ± 0.38	0.13 ± 0.14
Muons					
Pretag Counts	487.24 ± 122.62	86.33 ± 22.28	20.69 ± 6.04	4.41 ± 1.29	1.17 ± 0.34
$\geq$ 1+ Tag Counts	8.76 ± 2.09	4.43 ± 1.17	2.17 ± 0.82	1.37 ± 0.62	0.20 ± 0.22
$\geq$ 2+ Tag Counts	0.00 ± 0.00	0.19 ± 0.13	0.50 ± 0.37	0.30 ± 0.25	0.20 ± 2.83

Table C.17: Non-W expectation, removing $t\bar{t}$. These numbers are for the *unoptimized* analysis.

C.3 Optimized Summary Tables

Corrections to Pretag data					
	1 jet	2 jets	3 jets	4 jets	$\geq$ 5 jets
Data	30283.00 ± 0.00	4676.00 ± 0.00	324.00 ± 0.00	142.00 ± 0.00	34.00 ± 0.00
Non-W	2018.18 ± 506.23	406.89 ± 103.52	18.21 ± 5.57	8.38 ± 2.57	1.79 ± 0.55
$t\bar{t}$ (8.7 pb)	8.80 ± 0.83	47.13 ± 4.45	79.67 ± 7.51	79.48 ± 7.49	25.16 ± 2.39
EW	154.17 ± 14.85	148.47 ± 14.20	13.81 ± 1.40	3.77 ± 0.36	0.76 ± 0.07
Single Top	18.44 ± 4.49	22.89 ± 5.01	2.74 ± 0.58	0.58 ± 0.13	0.09 ± 0.02
Data, Corrected	28083.42 ± 523.16	4050.62 ± 123.78	209.57 ± 14.18	49.79 ± 10.21	6.20 ± 2.96

Table C.18: Corrections to pretag data for the W+HF background estimate. After an initial measurement, the $t\bar{t}$ cross section is input back into this calculation, and the process is iterated until the result is stable to 1%. These numbers are for the *optimized* analysis.

The tables are arranged in the following format.

- ϵ_{q-jet} is the MC efficiency to tag a q-flavor jet.
- $\epsilon_{q-jet}SF$ is the MC efficiency times the b-tag scale factor.
- Φ_E is the event scale factor.
- $\epsilon_{\geq 1,2}$ are the $\geq 1, 2$ event tagging efficiencies, respectively.
- $\epsilon_{pretag}(\%)$ is the pretag efficiency in the Monte Carlo
- $\epsilon_{pretag} * SF$ is the pretag efficiency times the pretag scale factors.
- "Pretag" is the number of pretag event counts.
- "$\geq$ 1+ Tag" is the number of tagged event counts.
- "$\geq$ 2+ Tag" is the number of double-tagged event counts.

$t\bar{t}$ (8.7 pb), $\sigma \int \mathcal{L}dt = 2770 \pm 360$					
	1 jet	2 jets	3 jets	4 jets	$\geq$ 5 jets
$\epsilon_{b-jet}(\%)$	44.44 ± 0.80	44.85 ± 0.26	45.37 ± 0.19	45.07 ± 0.18	43.91 ± 0.31
$\epsilon_{c-jet}(\%)$	10.39 ± 2.46	10.37 ± 0.57	10.23 ± 0.28	9.46 ± 0.21	9.77 ± 0.36
$\epsilon_{b-jet} * SF(\%)$	40.40 ± 2.76	40.77 ± 2.70	41.24 ± 2.73	40.97 ± 2.71	39.91 ± 2.65
$\epsilon_{c-jet} * SF(\%)$	9.44 ± 2.56	9.43 ± 1.35	9.30 ± 1.25	8.60 ± 1.15	8.88 ± 1.22
$\Phi_e^{\geq 1}(\%)$	91.04 ± 6.14	92.67 ± 5.22	93.34 ± 5.00	93.81 ± 4.76	94.17 ± 4.77
$\Phi_e^{\geq 2}(\%)$	0.00 ± 0.00	83.21 ± 11.41	84.57 ± 11.59	85.22 ± 11.44	86.43 ± 11.45
$\epsilon_{\geq 1}(\%)$	36.72 ± 0.70	54.92 ± 0.32	62.49 ± 0.24	66.90 ± 0.23	67.07 ± 0.41
$\epsilon_{\geq 2}$ (%)	0.00 ± 0.00	11.28 ± 0.20	16.42 ± 0.18	21.08 ± 0.20	22.00 ± 0.36
$\epsilon_{\geq 1} * \Phi_e$ (%)	33.43 ± 2.34	50.89 ± 2.88	58.33 ± 3.13	62.76 ± 3.19	63.16 ± 3.22
$\epsilon_{\geq 2} * \Phi_e(\%)$	0.00 ± 0.00	9.39 ± 1.30	13.89 ± 1.91	17.96 ± 2.42	19.01 ± 2.54
$\epsilon_{bjet}(\%)$				45.03 ± 0.12	
$\epsilon_{cjet}(\%)$				9.76 ± 0.15	
$\epsilon_{bjet} * SF(\%)$				40.93 ± 2.70	
$\epsilon_{cjet} * SF(\%)$				8.87 ± 1.18	
$\epsilon_{\geq 1}(\%)$				65.02 ± 0.15	
$\epsilon_{\geq 2}(\%)$				19.20 ± 0.13	
$\Phi_E^1(\%)$				93.71 ± 4.84	
$\Phi_E^2(\%)$				85.25 ± 11.49	
$\epsilon_{\geq 1}(\%) * \Phi_E^1$				60.93 ± 3.15	
$\epsilon_{\geq 2}(\%) * \Phi_E^2$				16.37 ± 2.21	
CEM					
$\epsilon_{pretag}(\%)$	0.21 ± 0.00	1.07 ± 0.01	1.80 ± 0.01	1.83 ± 0.01	0.58 ± 0.01
$\epsilon_{Pretag} * SF$	0.19 ± 0.01	0.98 ± 0.07	1.65 ± 0.12	1.67 ± 0.12	0.53 ± 0.04
$\epsilon_{pretag}(\%)$				4.21 ± 0.02	
$\epsilon_{pretag} * SF(\%)$				3.84 ± 0.29	
Pretag Counts	5.19 ± 0.49	27.05 ± 2.58	45.60 ± 4.33	46.15 ± 4.39	14.65 ± 1.41
$\geq$ 1+ Tag Counts	1.74 ± 0.20	13.77 ± 1.53	26.60 ± 2.90	28.97 ± 3.12	9.26 ± 1.01
$\geq$ 2+ Tag Counts	0.00 ± 0.00	2.54 ± 0.43	6.33 ± 1.06	8.29 ± 1.37	2.79 ± 0.46
CMUP					
$\epsilon_{pretag}(\%)$	0.13 ± 0.00	0.69 ± 0.01	1.17 ± 0.01	1.15 ± 0.01	0.36 ± 0.01
$\epsilon_{Pretag} * SF$	0.10 ± 0.01	0.52 ± 0.04	0.89 ± 0.07	0.87 ± 0.07	0.27 ± 0.02
$\epsilon_{pretag}(\%)$				2.68 ± 0.02	
$\epsilon_{pretag} * SF(\%)$				2.02 ± 0.15	
Pretag Counts	2.66 ± 0.25	14.45 ± 1.40	24.52 ± 2.35	24.03 ± 2.30	7.48 ± 0.75
$\geq$ 1+ Tag Counts	0.89 ± 0.11	7.36 ± 0.82	14.30 ± 1.57	15.08 ± 1.64	4.73 ± 0.53
$\geq$ 2+ Tag Counts	0.00 ± 0.00	1.36 ± 0.23	3.41 ± 0.57	4.32 ± 0.71	1.42 ± 0.24
CMX					
$\epsilon_{pretag}(\%)$	0.04 ± 0.00	0.23 ± 0.00	0.40 ± 0.01	0.39 ± 0.01	0.13 ± 0.00
$\epsilon_{Pretag} * SF$	0.04 ± 0.00	0.21 ± 0.02	0.36 ± 0.03	0.35 ± 0.03	0.11 ± 0.01
$\epsilon_{pretag}(\%)$				0.90 ± 0.01	
$\epsilon_{pretag} * SF(\%)$				0.82 ± 0.06	
Pretag Counts	0.94 ± 0.09	5.63 ± 0.53	9.55 ± 0.93	9.30 ± 0.91	3.03 ± 0.29
$\geq$ 1+ Tag Counts	0.32 ± 0.04	2.86 ± 0.32	5.57 ± 0.62	5.84 ± 0.65	1.91 ± 0.21
$\geq$ 2+ Tag Counts	0.00 ± 0.00	0.53 ± 0.09	1.33 ± 0.22	1.67 ± 0.28	0.58 ± 0.09
Total					
Pretag	8.80 ± 0.83	47.13 ± 4.45	79.67 ± 7.51	79.48 ± 7.49	25.16 ± 2.39
$\geq$ 1 Tag Counts	2.94 ± 0.35	23.99 ± 2.64	46.47 ± 5.04	49.88 ± 5.34	15.89 ± 1.72
$\geq$ 2 Tag Counts	0.00 ± 0.00	4.42 ± 0.74	11.06 ± 1.84	14.28 ± 2.35	4.78 ± 0.78

Table C.19: Summary table for $t\bar{t}$. These numbers are for the *optimized* analysis.

Data					
	1 jet	2 jets	3 jets	4 jets	$\geq$ 5 jets
CEM					
Pretag Counts	17448	2780	197	95	18
$\geq$ 1+ Tag Counts	246	137	40	34	8
$\geq$ 2+ Tag Counts	0	10	10	6	1
$\geq$ 1− Tag Counts	61	23	4	3	1
$\geq 1+-$ Tag Counts	0	1	1	1	1
$\geq$ 2− Tag Counts	0	0	0	0	0
CMUP					
Pretag Counts	8383	1219	86	34	10
$\geq$ 1+ Tag Counts	108	61	14	18	6
$\geq$ 2+ Tag Counts	0	5	4	6	2
$\geq$ 1− Tag Counts	25	10	2	1	0
$\geq 1+-$ Tag Counts	0	0	0	0	0
$\geq$ 2− Tag Counts	0	0	0	0	0
CMX					
Pretag Counts	4452	677	41	13	6
$\geq$ 1+ Tag Counts	73	34	8	6	4
$\geq$ 2+ Tag Counts	0	0	1	3	0
$\geq$ 1− Tag Counts	11	7	0	0	0
$\geq 1+-$ Tag Counts	0	0	0	0	0
$\geq$ 2− Tag Counts	0	0	0	0	0
Total					
Pretag	30283	4676	324	142	34
$\geq$ 1 Tag Counts	427	232	62	58	18
$\geq$ 2 Tag Counts	0	15	15	15	3
$\geq$ 1− Tag Counts	97	40	6	4	1
$\geq 1+-$ Tag Counts	0	1	1	1	1
$\geq$ 2− Tag Counts	0	0	0	0	0

Table C.20: Event yields for 318.5 pb^{-1}. These numbers are for the *optimized* analysis.

WW, $\sigma \int \mathcal{L}dt = 2835 \pm 369$					
	1 jet	2 jets	3 jets	4 jets	$\geq$ 5 jets
ϵ_{b-jet}(%)	41.94 ± 8.86	37.25 ± 4.79	54.00 ± 7.05	33.33 ± 11.11	30.00 ± 14.49
ϵ_{c-jet}(%)	7.74 ± 0.47	8.43 ± 0.33	9.31 ± 1.10	7.00 ± 1.80	8.33 ± 3.99
$\epsilon_{b-jet} * SF$(%)	38.12 ± 8.44	33.86 ± 4.89	49.09 ± 7.18	30.30 ± 10.30	27.27 ± 13.29
$\epsilon_{c-jet} * SF$(%)	7.04 ± 1.02	7.66 ± 1.06	8.46 ± 1.50	6.36 ± 1.84	7.57 ± 3.76
$\Phi_e^{\geq 1}$(%)	90.90 ± 12.21	90.93 ± 12.12	91.13 ± 11.39	91.51 ± 10.98	92.23 ± 9.54
$\Phi_e^{\geq 2}$(%)	0.00 ± 0.00	82.63 ± 18.57	82.65 ± 17.98	82.79 ± 17.88	83.08 ± 17.17
$\epsilon_{\geq 1}$(%)	2.06 ± 0.11	4.41 ± 0.16	7.20 ± 0.66	5.65 ± 1.12	11.63 ± 3.46
$\epsilon_{\geq 2}$ (%)	0.00 ± 0.00	0.04 ± 0.01	0.13 ± 0.09	0.00 ± 0.00	1.16 ± 1.16
$\epsilon_{\geq 1} * \Phi_e$ (%)	1.87 ± 0.27	4.01 ± 0.55	6.56 ± 1.02	5.17 ± 1.20	10.73 ± 3.38
$\epsilon_{\geq 2} * \Phi_e$(%)	0.00 ± 0.00	0.03 ± 0.01	0.11 ± 0.08	0.00 ± 0.00	0.96 ± 0.98
ϵ_{bjet}(%)				46.15 ± 5.64	
ϵ_{cjet}(%)				8.77 ± 0.92	
$\epsilon_{bjet} * SF$(%)				41.95 ± 5.83	
$\epsilon_{cjet} * SF$(%)				7.97 ± 1.34	
$\epsilon_{\geq 1}$(%)				7.06 ± 0.57	
$\epsilon_{\geq 2}$(%)				0.15 ± 0.09	
Φ_E^1(%)				91.33 ± 11.12	
Φ_E^2(%)				82.82 ± 17.72	
$\epsilon_{\geq 1}$(%) $* \Phi_E^1$				6.45 ± 0.94	
$\epsilon_{\geq 2}$(%) $* \Phi_E^2$				0.12 ± 0.08	
CEM					
ϵ_{pretag}(%)	1.91 ± 0.02	1.89 ± 0.02	0.17 ± 0.01	0.04 ± 0.00	0.01 ± 0.00
$\epsilon_{Pretag} * SF$	1.74 ± 0.13	1.73 ± 0.13	0.16 ± 0.01	0.04 ± 0.00	0.01 ± 0.00
ϵ_{pretag}(%)				0.23 ± 0.01	
$\epsilon_{pretag} * SF$(%)				0.21 ± 0.02	
Pretag Counts	73.58 ± 7.16	72.88 ± 7.09	6.55 ± 0.70	1.66 ± 0.17	0.36 ± 0.04
$\geq$ 1+ Tag Counts	1.38 ± 0.24	2.92 ± 0.49	0.43 ± 0.08	0.09 ± 0.02	0.04 ± 0.01
$\geq$ 2+ Tag Counts	0.00 ± 0.00	0.02 ± 0.01	0.01 ± 0.01	0.00 ± 0.00	0.00 ± 0.00
CMUP					
ϵ_{pretag}(%)	1.19 ± 0.02	1.12 ± 0.02	0.11 ± 0.00	0.03 ± 0.00	0.01 ± 0.00
$\epsilon_{Pretag} * SF$	0.90 ± 0.07	0.85 ± 0.07	0.08 ± 0.01	0.02 ± 0.00	0.01 ± 0.00
ϵ_{pretag}(%)				0.14 ± 0.01	
$\epsilon_{pretag} * SF$(%)				0.11 ± 0.01	
Pretag Counts	37.88 ± 3.74	35.83 ± 3.55	3.48 ± 0.40	0.92 ± 0.09	0.29 ± 0.03
$\geq$ 1+ Tag Counts	0.71 ± 0.12	1.44 ± 0.24	0.23 ± 0.04	0.05 ± 0.01	0.03 ± 0.01
$\geq$ 2+ Tag Counts	0.00 ± 0.00	0.01 ± 0.00	0.00 ± 0.00	0.00 ± 0.00	0.00 ± 0.00
CMX					
ϵ_{pretag}(%)	0.49 ± 0.01	0.45 ± 0.01	0.04 ± 0.00	0.01 ± 0.00	0.00 ± 0.00
$\epsilon_{Pretag} * SF$	0.44 ± 0.03	0.41 ± 0.03	0.04 ± 0.00	0.01 ± 0.00	0.00 ± 0.00
ϵ_{pretag}(%)				0.06 ± 0.00	
$\epsilon_{pretag} * SF$(%)				0.05 ± 0.01	
Pretag Counts	17.81 ± 1.77	16.64 ± 1.66	1.44 ± 0.14	0.53 ± 0.05	0.00 ± 0.00
$\geq$ 1+ Tag Counts	0.33 ± 0.06	0.67 ± 0.11	0.09 ± 0.02	0.03 ± 0.01	0.00 ± 0.00
$\geq$ 2+ Tag Counts	0.00 ± 0.00	0.01 ± 0.00	0.00 ± 0.00	0.00 ± 0.00	0.00 ± 0.00
Total					
Pretag	129.26 ± 12.32	125.35 ± 11.95	11.48 ± 1.15	3.10 ± 0.30	0.65 ± 0.06
$\geq$ 1 Tag Counts	2.42 ± 0.42	5.03 ± 0.84	0.75 ± 0.14	0.16 ± 0.04	0.07 ± 0.02
$\geq$ 2 Tag Counts	0.00 ± 0.00	0.04 ± 0.01	0.01 ± 0.01	0.00 ± 0.00	0.01 ± 0.01

Table C.21: Summary table for WW. See Section C.3 for a description of the variables. These numbers are for the *optimized* analysis.

WZ, $\sigma \int \mathcal{L}dt = 2835 \pm 369$					
	1 jet	2 jets	3 jets	4 jets	$\geq$ 5 jets
ϵ_{b-jet}(%)	41.05 ± 1.10	40.49 ± 0.81	39.47 ± 2.52	39.29 ± 4.61	47.83 ± 10.42
ϵ_{c-jet}(%)	7.42 ± 0.78	9.31 ± 0.57	12.62 ± 1.89	11.43 ± 3.10	12.90 ± 6.02
$\epsilon_{b-jet} * SF$(%)	37.31 ± 2.66	36.81 ± 2.54	35.88 ± 3.29	35.71 ± 4.81	43.48 ± 9.90
$\epsilon_{c-jet} * SF$(%)	6.74 ± 1.14	8.46 ± 1.23	11.47 ± 2.29	10.39 ± 3.13	11.73 ± 5.69
$\Phi_e^{\geq 1}$(%)	90.90 ± 6.90	92.08 ± 6.43	92.31 ± 6.45	92.42 ± 6.47	92.42 ± 7.22
$\Phi_e^{\geq 2}$(%)	0.00 ± 0.00	82.63 ± 11.74	82.84 ± 11.58	83.05 ± 11.78	82.80 ± 12.15
$\epsilon_{\geq 1}$(%)	10.79 ± 0.33	16.03 ± 0.37	17.84 ± 1.23	20.15 ± 2.43	20.63 ± 5.10
$\epsilon_{\geq 2}$ (%)	0.00 ± 0.00	2.00 ± 0.14	2.58 ± 0.51	2.56 ± 0.96	4.76 ± 2.68
$\epsilon_{\geq 1} * \Phi_e$ (%)	9.81 ± 0.80	14.76 ± 1.09	16.47 ± 1.62	18.62 ± 2.60	19.07 ± 4.94
$\epsilon_{\geq 2} * \Phi_e$(%)	0.00 ± 0.00	1.65 ± 0.26	2.14 ± 0.52	2.13 ± 0.85	3.94 ± 2.29
ϵ_{bjet}(%)				39.80 ± 2.17	
ϵ_{cjet}(%)				12.36 ± 1.56	
$\epsilon_{bjet} * SF$(%)				36.18 ± 3.10	
$\epsilon_{cjet} * SF$(%)				11.24 ± 2.05	
$\epsilon_{\geq 1}$(%)				18.45 ± 1.07	
$\epsilon_{\geq 2}$(%)				2.68 ± 0.45	
Φ_E^1(%)				92.35 ± 6.50	
Φ_E^2(%)				82.90 ± 11.67	
$\epsilon_{\geq 1}$(%) $* \Phi_E^1$				17.04 ± 1.55	
$\epsilon_{\geq 2}$(%) $* \Phi_E^2$				2.22 ± 0.49	
CEM					
ϵ_{pretag}(%)	0.93 ± 0.02	1.06 ± 0.02	0.11 ± 0.01	0.03 ± 0.00	0.01 ± 0.00
$\epsilon_{Pretag} * SF$	0.85 ± 0.07	0.97 ± 0.07	0.10 ± 0.01	0.03 ± 0.00	0.01 ± 0.00
ϵ_{pretag}(%)				0.14 ± 0.01	
$\epsilon_{pretag} * SF$(%)				0.13 ± 0.01	
Pretag Counts	10.74 ± 1.06	12.17 ± 1.19	1.21 ± 0.14	0.33 ± 0.03	0.11 ± 0.01
$\geq$ 1+ Tag Counts	1.05 ± 0.13	1.80 ± 0.22	0.20 ± 0.03	0.06 ± 0.01	0.02 ± 0.01
$\geq$ 2+ Tag Counts	0.00 ± 0.00	0.20 ± 0.04	0.03 ± 0.01	0.01 ± 0.00	0.00 ± 0.00
CMUP					
ϵ_{pretag}(%)	0.58 ± 0.01	0.64 ± 0.01	0.06 ± 0.00	0.02 ± 0.00	0.00 ± 0.00
$\epsilon_{Pretag} * SF$	0.44 ± 0.03	0.48 ± 0.04	0.04 ± 0.01	0.02 ± 0.00	0.00 ± 0.00
ϵ_{pretag}(%)				0.09 ± 0.01	
$\epsilon_{pretag} * SF$(%)				0.07 ± 0.01	
Pretag Counts	5.52 ± 0.54	6.07 ± 0.59	0.57 ± 0.08	0.21 ± 0.02	0.00 ± 0.00
$\geq$ 1+ Tag Counts	0.54 ± 0.07	0.90 ± 0.11	0.09 ± 0.02	0.04 ± 0.01	0.00 ± 0.00
$\geq$ 2+ Tag Counts	0.00 ± 0.00	0.10 ± 0.02	0.01 ± 0.00	0.00 ± 0.00	0.00 ± 0.00
CMX					
ϵ_{pretag}(%)	0.22 ± 0.01	0.25 ± 0.01	0.03 ± 0.00	0.01 ± 0.00	0.00 ± 0.00
$\epsilon_{Pretag} * SF$	0.20 ± 0.02	0.23 ± 0.02	0.02 ± 0.00	0.01 ± 0.00	0.00 ± 0.00
ϵ_{pretag}(%)				0.04 ± 0.00	
$\epsilon_{pretag} * SF$(%)				0.03 ± 0.00	
Pretag Counts	2.37 ± 0.25	2.79 ± 0.29	0.30 ± 0.03	0.08 ± 0.01	0.00 ± 0.00
$\geq$ 1+ Tag Counts	0.23 ± 0.03	0.41 ± 0.05	0.05 ± 0.01	0.01 ± 0.00	0.00 ± 0.00
$\geq$ 2+ Tag Counts	0.00 ± 0.00	0.05 ± 0.01	0.01 ± 0.00	0.00 ± 0.00	0.00 ± 0.00
Total					
Pretag	18.63 ± 1.79	21.03 ± 2.01	2.08 ± 0.22	0.62 ± 0.06	0.11 ± 0.01
$\geq$ 1 Tag Counts	1.83 ± 0.23	3.10 ± 0.37	0.34 ± 0.05	0.11 ± 0.02	0.02 ± 0.01
$\geq$ 2 Tag Counts	0.00 ± 0.00	0.35 ± 0.06	0.04 ± 0.01	0.01 ± 0.01	0.00 ± 0.00

Table C.22: Summary table for WZ. See Section C.3 for a description of the variables. These numbers are for the *optimized* analysis.

ZZ, $\sigma \int \mathcal{L}dt = 2835 \pm 369$					
	1 jet	2 jets	3 jets	4 jets	$\geq$ 5 jets
ϵ_{b-jet}(%)	30.12 ± 5.04	46.86 ± 3.03	40.98 ± 6.30	33.33 ± 10.29	28.57 ± 17.07
ϵ_{c-jet}(%)	9.30 ± 3.13	7.01 ± 1.75	9.26 ± 3.94	10.53 ± 7.04	0.00 ± 0.00
$\epsilon_{b-jet} * SF$(%)	27.38 ± 4.92	42.60 ± 3.94	37.25 ± 6.23	30.30 ± 9.56	25.97 ± 15.61
$\epsilon_{c-jet} * SF$(%)	8.45 ± 3.06	6.37 ± 1.80	8.42 ± 3.75	9.57 ± 6.52	0.00 ± 0.00
$\Phi_e^{\geq 1}$(%)	90.90 ± 9.84	92.39 ± 8.44	92.50 ± 8.57	92.73 ± 8.34	92.79 ± 6.51
$\Phi_e^{\geq 2}$(%)	0.00 ± 0.00	82.63 ± 14.88	82.86 ± 14.94	82.75 ± 15.02	82.63 ± 14.77
$\epsilon_{\geq 1}$(%)	4.98 ± 0.78	15.56 ± 1.29	14.84 ± 2.63	20.41 ± 5.76	12.50 ± 8.27
$\epsilon_{\geq 2}$ (%)	0.00 ± 0.00	3.57 ± 0.66	2.75 ± 1.21	2.04 ± 2.02	0.00 ± 0.00
$\epsilon_{\geq 1} * \Phi_e$ (%)	4.53 ± 0.86	14.38 ± 1.77	13.73 ± 2.75	18.93 ± 5.61	11.60 ± 7.72
$\epsilon_{\geq 2} * \Phi_e$(%)	0.00 ± 0.00	2.95 ± 0.76	2.28 ± 1.08	1.69 ± 1.70	0.00 ± 0.00
ϵ_{bjet}(%)				38.20 ± 5.15	
ϵ_{cjet}(%)				8.97 ± 3.24	
$\epsilon_{bjet} * SF$(%)				34.72 ± 5.21	
$\epsilon_{cjet} * SF$(%)				8.15 ± 3.14	
$\epsilon_{\geq 1}$(%)				15.79 ± 2.32	
$\epsilon_{\geq 2}$(%)				2.43 ± 0.98	
Φ_E^1(%)				92.59 ± 8.29	
Φ_E^2(%)				82.80 ± 14.94	
$\epsilon_{\geq 1}$(%) $* \Phi_E^1$				14.62 ± 2.52	
$\epsilon_{\geq 2}$(%) $* \Phi_E^2$				2.01 ± 0.89	
CEM					
ϵ_{pretag}(%)	0.07 ± 0.00	0.06 ± 0.00	0.02 ± 0.00	0.01 ± 0.00	0.00 ± 0.00
$\epsilon_{Pretag} * SF$	0.06 ± 0.00	0.06 ± 0.00	0.02 ± 0.00	0.01 ± 0.00	0.00 ± 0.00
ϵ_{pretag}(%)				0.03 ± 0.00	
$\epsilon_{pretag} * SF$(%)				0.02 ± 0.00	
Pretag Counts	0.31 ± 0.03	0.30 ± 0.03	0.09 ± 0.01	0.03 ± 0.00	0.00 ± 0.00
$\geq$ 1+ Tag Counts	0.01 ± 0.00	0.04 ± 0.01	0.01 ± 0.00	0.00 ± 0.00	0.00 ± 0.00
$\geq$ 2+ Tag Counts	0.00 ± 0.00	0.01 ± 0.00	0.00 ± 0.00	0.00 ± 0.00	0.00 ± 0.00
CMUP					
ϵ_{pretag}(%)	0.08 ± 0.00	0.07 ± 0.00	0.02 ± 0.00	0.01 ± 0.00	0.00 ± 0.00
$\epsilon_{Pretag} * SF$	0.06 ± 0.00	0.06 ± 0.00	0.01 ± 0.00	0.00 ± 0.00	0.00 ± 0.00
ϵ_{pretag}(%)				0.02 ± 0.00	
$\epsilon_{pretag} * SF$(%)				0.02 ± 0.00	
Pretag Counts	0.29 ± 0.03	0.28 ± 0.03	0.06 ± 0.01	0.02 ± 0.00	0.00 ± 0.00
$\geq$ 1+ Tag Counts	0.01 ± 0.00	0.04 ± 0.01	0.01 ± 0.00	0.00 ± 0.00	0.00 ± 0.00
$\geq$ 2+ Tag Counts	0.00 ± 0.00	0.01 ± 0.00	0.00 ± 0.00	0.00 ± 0.00	0.00 ± 0.00
CMX					
ϵ_{pretag}(%)	0.03 ± 0.00	0.03 ± 0.00	0.01 ± 0.00	0.00 ± 0.00	0.00 ± 0.00
$\epsilon_{Pretag} * SF$	0.03 ± 0.00	0.03 ± 0.00	0.00 ± 0.00	0.00 ± 0.00	0.00 ± 0.00
ϵ_{pretag}(%)				0.01 ± 0.00	
$\epsilon_{pretag} * SF$(%)				0.00 ± 0.00	
Pretag Counts	0.13 ± 0.01	0.12 ± 0.01	0.02 ± 0.00	0.00 ± 0.00	0.00 ± 0.00
$\geq$ 1+ Tag Counts	0.01 ± 0.00	0.02 ± 0.00	0.00 ± 0.00	0.00 ± 0.00	0.00 ± 0.00
$\geq$ 2+ Tag Counts	0.00 ± 0.00	0.00 ± 0.00	0.00 ± 0.00	0.00 ± 0.00	0.00 ± 0.00
Total					
Pretag	0.73 ± 0.07	0.70 ± 0.07	0.17 ± 0.02	0.05 ± 0.01	0.00 ± 0.00
$\geq$ 1 Tag Counts	0.03 ± 0.01	0.10 ± 0.02	0.02 ± 0.01	0.01 ± 0.00	0.00 ± 0.00
$\geq$ 2 Tag Counts	0.00 ± 0.00	0.02 ± 0.01	0.00 ± 0.00	0.00 ± 0.00	0.00 ± 0.00

Table C.23: Summary table for ZZ. See Section C.3 for a description of the variables. These numbers are for the *optimized* analysis.

$Z \rightarrow \tau\tau$, $\sigma \int \mathcal{L}dt = 2835 \pm 369$					
	1 jet	2 jets	3 jets	4 jets	$\geq$ 5 jets
$\epsilon_{b-jet}(\%)$	47.62 ± 10.90	40.00 ± 10.95	0.00 ± 0.00	0.00 ± 0.00	0.00 ± 0.00
$\epsilon_{c-jet}(\%)$	6.98 ± 3.88	10.00 ± 5.48	14.29 ± 13.23	0.00 ± 0.00	0.00 ± 0.00
$\epsilon_{b-jet} * SF(\%)$	43.29 ± 10.31	36.36 ± 10.24	0.00 ± 0.00	0.00 ± 0.00	0.00 ± 0.00
$\epsilon_{c-jet} * SF(\%)$	6.34 ± 3.63	9.09 ± 5.12	12.99 ± 12.15	0.00 ± 0.00	0.00 ± 0.00
$\Phi_e^{\geq 1}(\%)$	90.90 ± 22.66	91.49 ± 20.78	92.15 ± 23.39	0.00 ± 0.00	0.00 ± 0.00
$\Phi_e^{\geq 2}(\%)$	0.00 ± 0.00	82.63 ± 32.97	82.63 ± 34.20	0.00 ± 0.00	0.00 ± 0.00
$\epsilon_{\geq 1}(\%)$	2.02 ± 0.33	3.86 ± 0.89	11.11 ± 6.05	0.00 ± 0.00	0.00 ± 0.00
$\epsilon_{\geq 2}$ (%)	0.00 ± 0.00	0.00 ± 0.00	0.00 ± 0.00	0.00 ± 0.00	0.00 ± 0.00
$\epsilon_{\geq 1} * \Phi_e$ (%)	1.84 ± 0.55	3.53 ± 1.14	10.24 ± 6.15	0.00 ± 0.00	0.00 ± 0.00
$\epsilon_{\geq 2} * \Phi_e(\%)$	0.00 ± 0.00	0.00 ± 0.00	0.00 ± 0.00	0.00 ± 0.00	0.00 ± 0.00
$\epsilon_{bjet}(\%)$				0.00 ± 0.00	
$\epsilon_{cjet}(\%)$				14.29 ± 13.23	
$\epsilon_{bjet} * SF(\%)$				0.00 ± 0.00	
$\epsilon_{cjet} * SF(\%)$				12.99 ± 12.15	
$\epsilon_{\geq 1}(\%)$				9.38 ± 5.15	
$\epsilon_{\geq 2}(\%)$				0.00 ± 0.00	
$\Phi_E^1(\%)$				92.15 ± 23.39	
$\Phi_E^2(\%)$				82.63 ± 34.20	
$\epsilon_{\geq 1}(\%) * \Phi_E^1$				8.64 ± 5.23	
$\epsilon_{\geq 2}(\%) * \Phi_E^2$				0.00 ± 0.00	
CEM					
$\epsilon_{pretag}(\%)$	0.09 ± 0.00	0.02 ± 0.00	0.00 ± 0.00	0.00 ± 0.00	0.00 ± 0.00
$\epsilon_{Pretag} * SF$	0.08 ± 0.01	0.02 ± 0.00	0.00 ± 0.00	0.00 ± 0.00	0.00 ± 0.00
$\epsilon_{pretag}(\%)$				0.00 ± 0.00	
$\epsilon_{pretag} * SF(\%)$				0.00 ± 0.00	
Pretag Counts	3.24 ± 0.49	0.75 ± 0.11	0.08 ± 0.02	0.00 ± 0.00	0.00 ± 0.00
$\geq$ 1+ Tag Counts	0.06 ± 0.02	0.03 ± 0.01	0.01 ± 0.01	0.00 ± 0.00	0.00 ± 0.00
$\geq$ 2+ Tag Counts	0.00 ± 0.00	0.00 ± 0.00	0.00 ± 0.00	0.00 ± 0.00	0.00 ± 0.00
CMUP					
$\epsilon_{pretag}(\%)$	0.05 ± 0.00	0.01 ± 0.00	0.00 ± 0.00	0.00 ± 0.00	0.00 ± 0.00
$\epsilon_{Pretag} * SF$	0.04 ± 0.00	0.01 ± 0.00	0.00 ± 0.00	0.00 ± 0.00	0.00 ± 0.00
$\epsilon_{pretag}(\%)$				0.00 ± 0.00	
$\epsilon_{pretag} * SF(\%)$				0.00 ± 0.00	
Pretag Counts	1.46 ± 0.22	0.41 ± 0.06	0.00 ± 0.00	0.00 ± 0.00	0.00 ± 0.00
$\geq$ 1+ Tag Counts	0.03 ± 0.01	0.01 ± 0.01	0.00 ± 0.00	0.00 ± 0.00	0.00 ± 0.00
$\geq$ 2+ Tag Counts	0.00 ± 0.00	0.00 ± 0.00	0.00 ± 0.00	0.00 ± 0.00	0.00 ± 0.00
CMX					
$\epsilon_{pretag}(\%)$	0.02 ± 0.00	0.01 ± 0.00	0.00 ± 0.00	0.00 ± 0.00	0.00 ± 0.00
$\epsilon_{Pretag} * SF$	0.02 ± 0.00	0.01 ± 0.00	0.00 ± 0.00	0.00 ± 0.00	0.00 ± 0.00
$\epsilon_{pretag}(\%)$				0.00 ± 0.00	
$\epsilon_{pretag} * SF(\%)$				0.00 ± 0.00	
Pretag Counts	0.84 ± 0.13	0.24 ± 0.04	0.00 ± 0.00	0.00 ± 0.00	0.00 ± 0.00
$\geq$ 1+ Tag Counts	0.02 ± 0.01	0.01 ± 0.00	0.00 ± 0.00	0.00 ± 0.00	0.00 ± 0.00
$\geq$ 2+ Tag Counts	0.00 ± 0.00	0.00 ± 0.00	0.00 ± 0.00	0.00 ± 0.00	0.00 ± 0.00
Total					
Pretag	5.55 ± 0.67	1.39 ± 0.17	0.08 ± 0.02	0.00 ± 0.00	0.00 ± 0.00
$\geq$ 1 Tag Counts	0.10 ± 0.03	0.05 ± 0.02	0.01 ± 0.01	0.00 ± 0.00	0.00 ± 0.00
$\geq$ 2 Tag Counts	0.00 ± 0.00	0.00 ± 0.00	0.00 ± 0.00	0.00 ± 0.00	0.00 ± 0.00

Table C.24: Summary table for $Z \rightarrow \tau\tau$. See Section C.3 for a description of the variables. These numbers are for the *optimized* analysis.

Single top, t-channel, $\sigma \int \mathcal{L}dt = 2835 \pm 369$					
	1 jet	2 jets	3 jets	4 jets	$\geq$ 5 jets
$\epsilon_{b-jet}(\%)$	46.29 ± 0.41	45.95 ± 0.37	45.54 ± 0.92	42.44 ± 1.81	44.44 ± 4.14
$\epsilon_{c-jet}(\%)$	7.77 ± 1.93	6.88 ± 0.86	13.46 ± 3.35	9.76 ± 4.63	0.00 ± 0.00
$\epsilon_{b-jet} * SF(\%)$	42.08 ± 2.80	41.77 ± 2.78	41.40 ± 2.86	38.58 ± 3.03	40.40 ± 4.61
$\epsilon_{c-jet} * SF(\%)$	7.06 ± 1.99	6.25 ± 1.14	12.24 ± 3.45	8.87 ± 4.37	0.00 ± 0.00
$\Phi_e^{\geq 1}(\%)$	90.90 ± 6.04	91.23 ± 5.87	92.49 ± 5.11	93.02 ± 4.83	93.29 ± 4.78
$\Phi_e^{\geq 2}(\%)$	0.00 ± 0.00	82.63 ± 11.57	82.70 ± 11.03	82.80 ± 11.00	83.07 ± 10.83
$\epsilon_{\geq 1}(\%)$	39.53 ± 0.37	47.11 ± 0.38	58.55 ± 1.12	61.08 ± 2.37	63.16 ± 5.53
$\epsilon_{\geq 2}$ (%)	0.00 ± 0.00	1.80 ± 0.10	11.86 ± 0.73	15.09 ± 1.74	21.05 ± 4.68
$\epsilon_{\geq 1} * \Phi_e$ (%)	35.93 ± 2.41	42.98 ± 2.79	54.15 ± 3.17	56.82 ± 3.68	58.92 ± 5.98
$\epsilon_{\geq 2} * \Phi_e(\%)$	0.00 ± 0.00	1.49 ± 0.22	9.81 ± 1.44	12.49 ± 2.20	17.49 ± 4.51
$\epsilon_{bjet}(\%)$				44.90 ± 0.80	
$\epsilon_{cjet}(\%)$				11.61 ± 2.57	
$\epsilon_{bjet} * SF(\%)$				40.81 ± 2.79	
$\epsilon_{cjet} * SF(\%)$				10.55 ± 2.72	
$\epsilon_{\geq 1}(\%)$				59.13 ± 0.99	
$\epsilon_{\geq 2}(\%)$				12.71 ± 0.67	
$\Phi_E^1(\%)$				92.65 ± 5.03	
$\Phi_E^2(\%)$				82.75 ± 11.01	
$\epsilon_{\geq 1}(\%) * \Phi_E^1$				54.78 ± 3.11	
$\epsilon_{>2}(\%) * \Phi_E^2$				10.52 ± 1.51	
CEM					
$\epsilon_{pretag}(\%)$	4.37 ± 0.05	4.47 ± 0.05	0.50 ± 0.01	0.10 ± 0.01	0.02 ± 0.00
$\epsilon_{Pretag} * SF$	3.99 ± 0.30	4.08 ± 0.31	0.45 ± 0.04	0.09 ± 0.01	0.02 ± 0.00
$\epsilon_{pretag}(\%)$				0.62 ± 0.01	
$\epsilon_{pretag} * SF(\%)$				0.57 ± 0.05	
Pretag Counts	8.38 ± 3.48	8.57 ± 3.56	0.96 ± 0.40	0.20 ± 0.08	0.04 ± 0.01
$\geq$ 1+ Tag Counts	3.01 ± 1.27	3.68 ± 1.55	0.52 ± 0.22	0.11 ± 0.05	0.02 ± 0.01
$\geq$ 2+ Tag Counts	0.00 ± 0.00	0.13 ± 0.06	0.09 ± 0.04	0.02 ± 0.01	0.01 ± 0.00
CMUP					
$\epsilon_{pretag}(\%)$	2.56 ± 0.04	2.67 ± 0.04	0.29 ± 0.01	0.07 ± 0.01	0.01 ± 0.00
$\epsilon_{Pretag} * SF$	1.93 ± 0.15	2.02 ± 0.15	0.22 ± 0.02	0.05 ± 0.01	0.01 ± 0.00
$\epsilon_{pretag}(\%)$				0.36 ± 0.01	
$\epsilon_{pretag} * SF(\%)$				0.27 ± 0.02	
Pretag Counts	4.06 ± 1.69	4.24 ± 1.76	0.46 ± 0.19	0.11 ± 0.05	0.01 ± 0.01
$\geq$ 1+ Tag Counts	1.46 ± 0.61	1.82 ± 0.77	0.25 ± 0.11	0.06 ± 0.03	0.01 ± 0.00
$\geq$ 2+ Tag Counts	0.00 ± 0.00	0.06 ± 0.03	0.05 ± 0.02	0.01 ± 0.01	0.00 ± 0.00
CMX					
$\epsilon_{pretag}(\%)$	0.94 ± 0.02	0.89 ± 0.02	0.10 ± 0.01	0.02 ± 0.00	0.00 ± 0.00
$\epsilon_{Pretag} * SF$	0.85 ± 0.07	0.81 ± 0.06	0.09 ± 0.01	0.02 ± 0.00	0.00 ± 0.00
$\epsilon_{pretag}(\%)$				0.13 ± 0.01	
$\epsilon_{pretag} * SF(\%)$				0.12 ± 0.01	
Pretag Counts	1.71 ± 0.71	1.63 ± 0.68	0.19 ± 0.08	0.04 ± 0.02	0.00 ± 0.00
$\geq$ 1+ Tag Counts	0.62 ± 0.26	0.70 ± 0.30	0.10 ± 0.04	0.02 ± 0.01	0.00 ± 0.00
$\geq$ 2+ Tag Counts	0.00 ± 0.00	0.02 ± 0.01	0.02 ± 0.01	0.01 ± 0.00	0.00 ± 0.00
Total					
Pretag	14.15 ± 4.05	14.44 ± 4.15	1.61 ± 0.46	0.36 ± 0.10	0.05 ± 0.02
$\geq$ 1 Tag Counts	5.08 ± 1.50	6.21 ± 1.83	0.87 ± 0.26	0.20 ± 0.06	0.03 ± 0.01
$\geq$ 2 Tag Counts	0.00 ± 0.00	0.21 ± 0.07	0.16 ± 0.05	0.04 ± 0.02	0.01 ± 0.00

Table C.25: Summary table for single top (t-channel). See Section C.3 for a description of the variables. These numbers are for the *optimized* analysis.

Single top, s-channel, $\sigma \int \mathcal{L}dt = 631 \pm 45$					
	1 jet	2 jets	3 jets	4 jets	$\geq$ 5 jets
$\epsilon_{b-jet}(\%)$	44.69 ± 0.47	44.34 ± 0.24	45.96 ± 0.66	42.96 ± 1.47	38.54 ± 3.40
$\epsilon_{c-jet}(\%)$	0.00 ± 0.00	4.91 ± 1.69	11.81 ± 2.86	0.00 ± 0.00	0.00 ± 0.00
$\epsilon_{b-jet} * SF(\%)$	40.62 ± 2.72	40.31 ± 2.67	41.78 ± 2.82	39.05 ± 2.90	35.03 ± 3.86
$\epsilon_{c-jet} * SF(\%)$	0.00 ± 0.00	4.46 ± 1.65	10.74 ± 2.96	0.00 ± 0.00	0.00 ± 0.00
$\Phi_e^{\geq 1}(\%)$	90.90 ± 6.02	93.07 ± 4.73	93.21 ± 4.70	93.23 ± 4.74	93.40 ± 4.86
$\Phi_e^{\geq 2}(\%)$	0.00 ± 0.00	82.63 ± 10.95	82.76 ± 10.92	82.91 ± 10.89	83.39 ± 10.70
$\epsilon_{\geq 1}(\%)$	42.62 ± 0.46	64.85 ± 0.32	68.30 ± 0.85	66.72 ± 1.96	61.39 ± 4.84
$\epsilon_{\geq 2}$ (%)	0.00 ± 0.00	18.11 ± 0.26	21.56 ± 0.75	17.59 ± 1.58	18.81 ± 3.89
$\epsilon_{\geq 1} * \Phi_e$ (%)	38.74 ± 2.60	60.36 ± 3.08	63.66 ± 3.31	62.20 ± 3.65	57.34 ± 5.42
$\epsilon_{\geq 2} * \Phi_e(\%)$	0.00 ± 0.00	14.96 ± 1.99	17.84 ± 2.43	14.58 ± 2.32	15.69 ± 3.82
$\epsilon_{bjet}(\%)$				45.27 ± 0.59	
$\epsilon_{cjet}(\%)$				7.85 ± 1.95	
$\epsilon_{bjet} * SF(\%)$				41.15 ± 2.77	
$\epsilon_{cjet} * SF(\%)$				7.14 ± 2.01	
$\epsilon_{\geq 1}(\%)$				67.86 ± 0.77	
$\epsilon_{\geq 2}(\%)$				20.85 ± 0.67	
$\Phi_E^1(\%)$				93.22 ± 4.72	
$\Phi_E^2(\%)$				82.82 ± 10.91	
$\epsilon_{\geq 1}(\%) * \Phi_E^1$				63.26 ± 3.28	
$\epsilon_{>2}(\%) * \Phi_E^2$				17.27 ± 2.34	
CEM					
$\epsilon_{pretag}(\%)$	3.02 ± 0.04	5.93 ± 0.06	0.80 ± 0.02	0.16 ± 0.01	0.03 ± 0.00
$\epsilon_{Pretag} * SF$	2.76 ± 0.21	5.41 ± 0.41	0.73 ± 0.06	0.14 ± 0.01	0.03 ± 0.00
$\epsilon_{pretag}(\%)$				0.99 ± 0.02	
$\epsilon_{pretag} * SF(\%)$				0.90 ± 0.07	
Pretag Counts	2.57 ± 0.29	5.05 ± 0.56	0.68 ± 0.08	0.13 ± 0.02	0.03 ± 0.00
$\geq$ 1+ Tag Counts	1.00 ± 0.13	3.05 ± 0.37	0.44 ± 0.06	0.08 ± 0.01	0.01 ± 0.00
$\geq$ 2+ Tag Counts	0.00 ± 0.00	0.76 ± 0.13	0.12 ± 0.02	0.02 ± 0.00	0.00 ± 0.00
CMUP					
$\epsilon_{pretag}(\%)$	1.71 ± 0.03	3.46 ± 0.04	0.47 ± 0.01	0.09 ± 0.01	0.01 ± 0.00
$\epsilon_{Pretag} * SF$	1.29 ± 0.10	2.61 ± 0.20	0.35 ± 0.03	0.07 ± 0.01	0.01 ± 0.00
$\epsilon_{pretag}(\%)$				0.58 ± 0.01	
$\epsilon_{pretag} * SF(\%)$				0.44 ± 0.04	
Pretag Counts	1.20 ± 0.14	2.44 ± 0.27	0.33 ± 0.04	0.06 ± 0.01	0.01 ± 0.00
$\geq$ 1+ Tag Counts	0.47 ± 0.06	1.47 ± 0.18	0.21 ± 0.03	0.04 ± 0.01	0.00 ± 0.00
$\geq$ 2+ Tag Counts	0.00 ± 0.00	0.37 ± 0.06	0.06 ± 0.01	0.01 ± 0.00	0.00 ± 0.00
CMX					
$\epsilon_{pretag}(\%)$	0.63 ± 0.02	1.18 ± 0.03	0.15 ± 0.01	0.03 ± 0.00	0.01 ± 0.00
$\epsilon_{Pretag} * SF$	0.57 ± 0.05	1.07 ± 0.08	0.13 ± 0.01	0.03 ± 0.00	0.01 ± 0.00
$\epsilon_{pretag}(\%)$				0.19 ± 0.01	
$\epsilon_{pretag} * SF(\%)$				0.17 ± 0.01	
Pretag Counts	0.51 ± 0.06	0.96 ± 0.11	0.12 ± 0.01	0.03 ± 0.00	0.01 ± 0.00
$\geq$ 1+ Tag Counts	0.20 ± 0.03	0.58 ± 0.07	0.08 ± 0.01	0.02 ± 0.00	0.00 ± 0.00
$\geq$ 2+ Tag Counts	0.00 ± 0.00	0.14 ± 0.03	0.02 ± 0.00	0.00 ± 0.00	0.00 ± 0.00
Total					
Pretag	4.29 ± 0.44	8.45 ± 0.86	1.13 ± 0.12	0.23 ± 0.03	0.04 ± 0.00
$\geq$ 1 Tag Counts	1.66 ± 0.20	5.10 ± 0.58	0.72 ± 0.08	0.14 ± 0.02	0.02 ± 0.00
$\geq$ 2 Tag Counts	0.00 ± 0.00	1.26 ± 0.21	0.20 ± 0.03	0.03 ± 0.01	0.01 ± 0.00

Table C.26: Summary table for single top (s-channel). See Section C.3 for a description of the variables. These numbers are for the *optimized* analysis.

W + LF Mistags					
	1 jet	2 jets	3 jets	4 jets	$\geq$ 5 jets
Raw Tag Matrix Predictions					
(+) Pred	440.36 ± 5.13	164.69 ± 1.02	26.06 ± 0.64	15.85 ± 0.10	4.51 ± 0.06
(-) Pred	94.43 ± 4.95	40.25 ± 0.94	7.80 ± 0.63	4.69 ± 0.07	1.32 ± 0.04
(+,-) Pred	0.00 ± 0.00	1.11 ± 0.15	1.07 ± 0.05	1.47 ± 0.08	0.52 ± 0.05
(-,-) Pred	0.00 ± 0.00	0.00 ± 0.00	0.00 ± 0.00	0.00 ± 0.00	0.00 ± 0.00
Tag Matrix Predictions, Including $\alpha_{LF} \times \beta$					
(-) Pred $\times\alpha_{LF}\beta$	107.95 ± 4.95	50.84 ± 0.94	10.84 ± 0.63	6.59 ± 0.07	1.87 ± 0.04
(+,-) Pred $\times\alpha_{LF}\beta$	0.00 ± 0.00	1.45 ± 0.15	1.50 ± 0.05	2.07 ± 0.08	0.74 ± 0.05
Number of W+LF Mistags (corrected for $\sigma_{t\bar{t}} = 8.7\,pb$)					
$\geq$ 1 Tag Counts	93.08 ± 19.09	38.23 ± 7.68	5.80 ± 1.21	1.86 ± 0.37	0.28 ± 0.06
$\geq$ 2 Tag Counts	0.00 ± 0.00	0.48 ± 0.11	0.10 ± 0.04	0.17 ± 0.04	0.05 ± 0.04

Table C.27: Raw mistag matrix prediction, prediction scaled to correct for light flavor asymmetry, and W+LF estimate removing other backgrounds (assuming $\sigma_{t\bar{t}} = 8.7$ pb). This is for the *optimized* analysis.

$W + c$					
	1 jet	2 jets	3 jets	4 jets	$\geq$ 5 jets
F_{1c} (%)	4.30 ± 0.90	6.00 ± 1.30	6.00 ± 1.30	5.90 ± 1.30	
WC, 1C, 1 Tag (%)	8.19 ± 1.10	8.86 ± 1.23	10.94 ± 2.10	14.37 ± 2.95	
$\Phi_e^{\geq 1}$(%)	90.90 ± 12.00	90.90 ± 12.00	90.90 ± 12.00	90.90 ± 12.00	
$\epsilon_{\geq 1} * \Phi_e * F_{HF}$ (%)	0.35 ± 0.09	0.51 ± 0.13	0.61 ± 0.15	0.78 ± 0.20	
Total					
Pretag	1207.59 ± 275.18	243.04 ± 60.01	12.57 ± 3.56	2.94 ± 1.25	0.37 ± 0.25
$\geq$ 1 Tag Counts	98.90 ± 26.31	20.78 ± 5.90	1.28 ± 0.41	0.39 ± 0.18	0.03 ± 0.02
$\geq$ 2 Tag Counts	0.00 ± 0.00	0.00 ± 0.00	0.00 ± 0.00	0.00 ± 0.00	0.00 ± 0.00

Table C.28: Summary table for the W+C background. F_{ic} is the heavy flavor fraction measured from [1], and the efficiencies given are the event tag rates in Monte Carlo. Φ_E is the ratio of event efficiencies with and without the b-tagging scale factor using the full binomial expression.

$W + c\bar{c}$					
	1 jet	2 jets	3 jets	4 jets	$\geq$ 5 jets
F_{1c} (%)	1.60 ± 0.40	2.40 ± 0.60	3.80 ± 1.00	3.50 ± 1.00	
F_{2c} (%)	0.00 ± 0.00	1.80 ± 0.50	2.90 ± 0.80	3.70 ± 1.00	
WCC, 1C, 1 Tag (%)	7.40 ± 1.03	8.91 ± 1.38	13.63 ± 2.79	15.22 ± 5.99	
WCC, 2C, 1 Tag (%)	0.00 ± 0.00	15.44 ± 2.39	18.71 ± 4.65	26.30 ± 6.33	
WCC, 2C, 2 Tag (%)	0.00 ± 0.00	0.33 ± 0.18	0.15 ± 0.15	0.00 ± 0.00	
$\Phi_e^{\geq 1}$(%)	90.90 ± 12.00	91.15 ± 11.71	91.20 ± 11.64	91.29 ± 11.54	
$\Phi_e^{\geq 2}$(%)	0.00 ± 0.00	82.63 ± 21.82	82.63 ± 21.82	0.00 ± 0.00	
$\epsilon_{\geq 1} * \Phi_e * F_{HF}$ (%)	0.12 ± 0.03	0.49 ± 0.15	1.06 ± 0.32	1.44 ± 0.44	
$\epsilon_{\geq 2} * \Phi_e * F_{HF}$(%)	0.00 ± 0.00	0.01 ± 0.00	0.00 ± 0.00	0.00 ± 0.00	
Total					
Pretag	449.33 ± 120.68	170.13 ± 49.70	14.04 ± 4.71	3.58 ± 1.73	0.45 ± 0.34
$\geq$ 1 Tag Counts	33.25 ± 10.02	19.92 ± 6.49	2.22 ± 0.81	0.72 ± 0.36	0.02 ± 0.02
$\geq$ 2 Tag Counts	0.00 ± 0.00	0.24 ± 0.10	0.01 ± 0.00	0.00 ± 0.00	0.00 ± 0.00

Table C.29: Summary table for the W+CC background. F_{ic} is the heavy flavor fraction measured from [1], and the efficiencies given are the event tag rates in Monte Carlo. Φ_E is the ratio of event efficiencies with and without the b-tagging scale factor using the full binomial expression.

$W + b\bar{b}$					
	1 jet	2 jets	3 jets	4 jets	$\geq$ 5 jets
F_{1b}(%)	1.00 ± 0.30	1.40 ± 0.40	2.40 ± 0.60	2.20 ± 0.60	
F_{2b}(%)	0.00 ± 0.00	1.40 ± 0.40	2.30 ± 0.60	2.60 ± 0.70	
WBB, 1B, 1 Tag (%)	34.94 ± 2.35	38.07 ± 2.34	45.77 ± 4.50	43.58 ± 3.65	
WBB, 2B, 1 Tag (%)	0.00 ± 0.00	57.90 ± 3.51	62.78 ± 4.82	62.23 ± 4.06	
WBB, 2B, 2 Tag (%)	0.00 ± 0.00	14.12 ± 1.93	18.17 ± 2.80	18.24 ± 3.02	
$\Phi_e^{\geq 1}$(%)	90.90 ± 6.00	92.17 ± 5.25	92.12 ± 5.27	92.33 ± 5.15	
$\Phi_e^{\geq 2}$(%)	0.00 ± 0.00	82.63 ± 10.91	82.79 ± 11.07	83.16 ± 11.43	
$\epsilon_{\geq 1} * \Phi_e * F_{HF}$ (%)	0.35 ± 0.11	1.34 ± 0.39	2.54 ± 0.67	2.57 ± 0.71	
$\epsilon_{\geq 2} * \Phi_e * F_{HF}$(%)	0.00 ± 0.00	0.20 ± 0.06	0.42 ± 0.12	0.47 ± 0.14	
Total					
Pretag	280.83 ± 89.47	113.42 ± 35.84	9.85 ± 3.17	2.39 ± 1.13	0.30 ± 0.22
$\geq$ 1 Tag Counts	98.13 ± 31.97	54.39 ± 17.49	5.32 ± 1.75	1.28 ± 0.61	0.15 ± 0.12
$\geq$ 2 Tag Counts	0.00 ± 0.00	8.01 ± 2.76	0.88 ± 0.32	0.24 ± 0.12	0.02 ± 0.02

Table C.30: Summary table for the W+BB background. F_{ib} is the heavy flavor fraction measured from [1], and the efficiencies given are the event tag rates in Monte Carlo. Φ_E is the ratio of event efficiencies with and without the b-tagging scale factor using the full binomial expression.

Non-W : Raw Counts					
	1 jet	2 jets	3 jets	4 jets	$\geq$ 5 jets
Electrons					
N_A^{pre}	51191	5955	887	95	16
N_B^{pre}	35939	3317	396	54	10
N_C^{pre}	2290	605	38	17	3
N_D^{pre}	17443	2779	198	94	18
N_A^{+}	1477	320	74	13	2
N_B^{+}	585	110	32	9	1
N_C^{+}	115	52	11	3	2
N_D^{+}	246	136	40	34	8
N_A^{++}	0	10	2	1	0
N_B^{++}	0	1	4	3	0
N_C^{++}	0	1	2	1	0
N_D^{++}	0	9	10	6	1
F_{Non-W} (%)	9.22 $\pm$ 2.31	12.13 $\pm$ 3.09	8.62 $\pm$ 2.53		
N_+^B/N_+^A (%)	39.61 $\pm$ 1.93	34.38 $\pm$ 3.80	47.19 $\pm$ 8.83		
$N_+^{tagmethod}$	45.55 $\pm$ 15.78	17.88 $\pm$ 6.70	5.19 $\pm$ 2.52	1.42 $\pm$ 0.98	0.94 $\pm$ 0.76
R_+^B (%)	1.63 $\pm$ 0.33	3.32 $\pm$ 0.74	8.08 $\pm$ 2.19	16.67 $\pm$ 6.86	10.00 $\pm$ 10.68
$N_+^{pretagmethod}$	26.18 $\pm$ 8.47	11.18 $\pm$ 3.78	1.37 $\pm$ 0.55	1.37 $\pm$ 0.69	0.16 $\pm$ 0.17
R_{++}^B (%)	0.00 $\pm$ 0.00	0.03 $\pm$ 0.03	1.01 $\pm$ 0.55	5.56 $\pm$ 3.48	0.00 $\pm$ 0.00
$N_{++}^{pretagmethod}$	0.00 $\pm$ 0.00	0.10 $\pm$ 0.11	0.17 $\pm$ 0.11	0.46 $\pm$ 0.31	0.00 $\pm$ 0.00
Muons					
N_A^{pre}	15286	1977	285	41	11
N_B^{pre}	6223	532	67	8	2
N_C^{pre}	1009	266	18	7	6
N_D^{pre}	12831	1870	124	46	15
N_A^{+}	859	194	30	8	3
N_B^{+}	109	25	8	4	1
N_C^{+}	50	28	2	1	1
N_D^{+}	180	95	22	24	10
N_A^{++}	0	5	1	0	0
N_B^{++}	0	0	2	0	1
N_C^{++}	0	3	0	0	0
N_D^{++}	0	5	5	9	2
F_{Non-W} (%)	3.20 $\pm$ 0.81	3.83 $\pm$ 1.01	3.83 $\pm$ 1.30		
N_+^B/N_+^A (%)	12.69 $\pm$ 1.29	12.89 $\pm$ 2.74	31.71 $\pm$ 10.09		
$N_+^{tagmethod}$	6.34 $\pm$ 2.37	3.61 $\pm$ 1.57	0.63 $\pm$ 0.53	0.32 $\pm$ 0.35	0.32 $\pm$ 0.35
R_+^B (%)	1.75 $\pm$ 0.39	4.70 $\pm$ 1.34	11.94 $\pm$ 5.06	50.00 $\pm$ 32.21	50.00 $\pm$ 62.05
$N_+^{pretagmethod}$	7.20 $\pm$ 2.42	3.41 $\pm$ 1.33	0.58 $\pm$ 0.32	0.90 $\pm$ 0.66	0.31 $\pm$ 0.39
R_{++}^B (%)	0.00 $\pm$ 0.00	0.00 $\pm$ 0.00	2.99 $\pm$ 2.22	0.00 $\pm$ 0.00	50.00 $\pm$ 62.05
$N_{++}^{pretagmethod}$	0.00 $\pm$ 0.00	0.00 $\pm$ 0.00	0.15 $\pm$ 0.12	0.00 $\pm$ 0.00	0.31 $\pm$ 0.39
Electrons					
Pretag Counts	1608.17 $\pm$ 403.78	337.11 $\pm$ 85.94	16.99 $\pm$ 4.99	8.19 $\pm$ 2.40	1.55 $\pm$ 0.46
$\geq$ 1+ Tag Counts	30.51 $\pm$ 7.42	12.80 $\pm$ 3.26	1.55 $\pm$ 0.53	1.38 $\pm$ 0.55	0.19 $\pm$ 0.17
$\geq$ 2+ Tag Counts	0.00 $\pm$ 0.00	0.10 $\pm$ 0.11	0.17 $\pm$ 0.11	0.46 $\pm$ 0.31	0.00 $\pm$ 0.00
Muons					
Pretag Counts	410.90 $\pm$ 103.78	72.57 $\pm$ 19.09	4.86 $\pm$ 1.66	1.80 $\pm$ 0.61	0.61 $\pm$ 0.21
$\geq$ 1+ Tag Counts	6.76 $\pm$ 1.67	3.49 $\pm$ 1.01	0.59 $\pm$ 0.27	0.45 $\pm$ 0.31	0.31 $\pm$ 0.26
$\geq$ 2+ Tag Counts	0.00 $\pm$ 0.00	0.00 $\pm$ 0.00	0.15 $\pm$ 0.12	0.00 $\pm$ 0.00	0.31 $\pm$ 0.39

Table C.31: Raw event counts for Non-W backgrounds. These numbers are for the *optimized* analysis.

$t\bar{t}$ (8.7 pb)					
	1 jet	2 jets	3 jets	4 jets	$\geq$ 5 jets
Electrons					
N_A^{pre}	0.03 ± 0.00	0.18 ± 0.02	0.51 ± 0.05	0.67 ± 0.06	0.62 ± 0.06
N_B^{pre}	0.27 ± 0.03	1.49 ± 0.14	3.51 ± 0.33	3.23 ± 0.31	1.12 ± 0.11
N_C^{pre}	0.85 ± 0.08	3.22 ± 0.31	3.64 ± 0.35	2.36 ± 0.22	1.17 ± 0.11
N_D^{pre}	5.19 ± 0.49	27.05 ± 2.58	45.60 ± 4.33	46.15 ± 4.39	14.65 ± 1.41
N_A^{+}	0.01 ± 0.00	0.08 ± 0.01	0.21 ± 0.02	0.27 ± 0.03	0.26 ± 0.03
N_B^{+}	0.09 ± 0.01	0.79 ± 0.09	2.00 ± 0.22	2.02 ± 0.22	0.70 ± 0.08
N_C^{+}	0.27 ± 0.03	1.40 ± 0.16	1.93 ± 0.21	1.32 ± 0.14	0.68 ± 0.07
N_D^{+}	1.74 ± 0.20	13.77 ± 1.53	26.60 ± 2.90	28.97 ± 3.12	9.26 ± 1.01
N_A^{++}	0.00 ± 0.00	0.01 ± 0.00	0.03 ± 0.01	0.03 ± 0.00	0.03 ± 0.01
N_B^{++}	0.00 ± 0.00	0.16 ± 0.03	0.49 ± 0.08	0.56 ± 0.09	0.21 ± 0.03
N_C^{++}	0.00 ± 0.00	0.12 ± 0.02	0.41 ± 0.07	0.32 ± 0.05	0.13 ± 0.02
N_D^{++}	0.00 ± 0.00	2.54 ± 0.43	6.33 ± 1.06	8.29 ± 1.37	2.79 ± 0.46
Muons					
N_A^{pre}	0.02 ± 0.00	0.17 ± 0.02	0.45 ± 0.04	0.63 ± 0.06	0.48 ± 0.05
N_B^{pre}	0.16 ± 0.02	1.19 ± 0.11	2.74 ± 0.26	2.73 ± 0.26	0.77 ± 0.07
N_C^{pre}	0.67 ± 0.06	2.61 ± 0.25	3.21 ± 0.30	2.31 ± 0.22	0.96 ± 0.09
N_D^{pre}	3.61 ± 0.34	20.08 ± 1.91	34.07 ± 3.24	33.33 ± 3.17	10.51 ± 1.02
N_A^{+}	0.01 ± 0.00	0.07 ± 0.01	0.21 ± 0.02	0.29 ± 0.03	0.22 ± 0.02
N_B^{+}	0.05 ± 0.01	0.59 ± 0.06	1.62 ± 0.18	1.67 ± 0.18	0.47 ± 0.05
N_C^{+}	0.22 ± 0.03	1.17 ± 0.13	1.78 ± 0.19	1.34 ± 0.14	0.58 ± 0.06
N_D^{+}	1.21 ± 0.14	10.22 ± 1.13	19.87 ± 2.17	20.92 ± 2.26	6.64 ± 0.73
N_A^{++}	0.00 ± 0.00	0.01 ± 0.00	0.04 ± 0.01	0.04 ± 0.01	0.02 ± 0.00
N_B^{++}	0.00 ± 0.00	0.11 ± 0.02	0.42 ± 0.07	0.50 ± 0.08	0.14 ± 0.02
N_C^{++}	0.00 ± 0.00	0.17 ± 0.03	0.40 ± 0.07	0.30 ± 0.05	0.15 ± 0.03
N_D^{++}	0.00 ± 0.00	1.88 ± 0.32	4.73 ± 0.79	5.99 ± 0.99	2.00 ± 0.33

Table C.32: Expectation of $t\bar{t}$ in Non-W sideband regions. These numbers are for the *optimized* analysis.

Non-W					
	1 jet	2 jets	3 jets	4 jets	$\geq$ 5 jets
Electrons					
N_A^{pre}	51190.97 ± 226.25	5954.82 ± 77.17	886.49 ± 29.78	94.33 ± 9.75	15.38 ± 4.00
N_B^{pre}	35938.73 ± 189.58	3315.51 ± 57.59	392.49 ± 19.90	50.77 ± 7.35	8.88 ± 3.16
N_C^{pre}	2289.15 ± 47.85	601.78 ± 24.60	34.36 ± 6.17	14.64 ± 4.13	1.83 ± 1.74
N_D^{pre}	17443.00 ± 132.07	2779.00 ± 52.72	198.00 ± 14.07	94.00 ± 9.70	18.00 ± 4.24
N_A^+	1476.99 ± 38.43	319.92 ± 17.89	73.79 ± 8.60	12.73 ± 3.61	1.74 ± 1.41
N_B^+	584.91 ± 24.19	109.21 ± 10.49	30.00 ± 5.66	6.98 ± 3.01	0.30 ± 1.00
N_C^+	114.73 ± 10.72	50.60 ± 7.21	9.07 ± 3.32	1.68 ± 1.74	1.32 ± 1.42
N_D^+	244.26 ± 15.69	122.23 ± 11.76	13.40 ± 6.96	5.03 ± 6.61	-1.26 ± 3.00
N_A^{++}	0.00 ± 0.00	10.29 ± 3.52	2.47 ± 1.75	1.54 ± 1.19	0.62 ± 0.62
N_B^{++}	0.00 ± 0.00	1.41 ± 1.18	4.07 ± 2.22	2.75 ± 1.99	0.53 ± 0.53
N_C^{++}	0.00 ± 0.00	1.45 ± 1.18	2.17 ± 1.67	1.26 ± 1.18	0.58 ± 0.58
N_D^{++}	0.00 ± 0.00	7.03 ± 3.23	4.25 ± 3.22	0.73 ± 0.73	0.27 ± 0.27
F_{Non-W} (%)	9.21 ± 2.31	12.06 ± 3.08	7.44 ± 2.34		
N_+^B/N_+^A (%)	39.60 ± 1.93	34.14 ± 3.79	42.24 ± 8.64		
$N_+^{tagmethod}$	45.43 ± 15.75	17.27 ± 6.56	3.83 ± 2.13	0.71 ± 0.80	0.56 ± 0.65
R_+^B (%)	1.63 ± 0.33	3.29 ± 0.74	7.64 ± 2.17	13.75 ± 6.96	3.39 ± 11.42
$N_+^{pretagmethod}$	26.16 ± 8.47	11.04 ± 3.75	1.12 ± 0.48	0.97 ± 0.59	0.05 ± 0.15
R_{++}^B (%)	0.00 ± 0.00	0.04 ± 0.04	1.04 ± 0.60	5.43 ± 4.14	5.99 ± 6.49
$N_{++}^{pretagmethod}$	0.00 ± 0.00	0.14 ± 0.13	0.15 ± 0.10	0.38 ± 0.32	0.08 ± 0.09
Muons					
N_A^{pre}	15285.98 ± 123.64	1976.83 ± 44.46	284.55 ± 16.88	40.37 ± 6.40	10.52 ± 3.32
N_B^{pre}	6222.84 ± 78.89	530.81 ± 23.07	64.26 ± 8.19	5.27 ± 2.84	1.23 ± 1.42
N_C^{pre}	1008.33 ± 31.76	263.39 ± 16.31	14.79 ± 4.25	4.69 ± 2.65	5.04 ± 2.45
N_D^{pre}	12831.00 ± 113.27	1870.00 ± 43.24	124.00 ± 11.14	46.00 ± 6.78	15.00 ± 3.87
N_A^+	858.99 ± 29.31	193.93 ± 13.93	29.79 ± 5.48	7.71 ± 2.83	2.78 ± 1.73
N_B^+	108.95 ± 10.44	24.41 ± 5.00	6.38 ± 2.83	2.33 ± 2.01	0.53 ± 1.00
N_C^+	49.78 ± 7.07	26.83 ± 5.29	0.22 ± 1.43	-0.34 ± 1.01	0.42 ± 1.00
N_D^+	178.79 ± 13.42	84.78 ± 9.81	2.13 ± 5.17	3.08 ± 5.39	3.36 ± 3.24
N_A^{++}	0.00 ± 0.00	6.12 ± 2.52	2.17 ± 1.34	1.26 ± 0.89	1.27 ± 0.90
N_B^{++}	0.00 ± 0.00	1.23 ± 0.87	2.83 ± 1.79	1.02 ± 0.73	2.12 ± 1.32
N_C^{++}	0.00 ± 0.00	3.91 ± 2.11	1.08 ± 0.77	1.13 ± 0.80	1.20 ± 0.85
N_D^{++}	0.00 ± 0.00	4.33 ± 2.54	2.42 ± 1.84	4.56 ± 2.90	1.80 ± 1.47
F_{Non-W} (%)	3.20 ± 0.81	3.78 ± 1.00	2.80 ± 1.10		
N_+^B/N_+^A (%)	12.68 ± 1.29	12.59 ± 2.73	22.93 ± 9.71		
$N_+^{tagmethod}$	6.31 ± 2.36	3.38 ± 1.51	0.05 ± 0.33	-0.08 ± 0.24	0.10 ± 0.24
R_+^B (%)	1.75 ± 0.39	4.60 ± 1.34	9.92 ± 5.09	44.27 ± 45.90	42.95 ± 95.94
$N_+^{pretagmethod}$	7.19 ± 2.42	3.30 ± 1.30	0.35 ± 0.23	0.58 ± 0.65	0.19 ± 0.44
R_{++}^B (%)	0.00 ± 0.00	0.23 ± 0.17	4.40 ± 2.98	19.45 ± 18.00	172.44 ± 230.49
$N_{++}^{pretagmethod}$	0.00 ± 0.00	0.17 ± 0.13	0.16 ± 0.12	0.26 ± 0.26	0.77 ± 1.08
Electrons					
Pretag Counts	1607.56 ± 403.69	335.18 ± 85.63	14.66 ± 4.61	7.07 ± 2.22	1.34 ± 0.42
$\geq$ 1+ Tag Counts	30.49 ± 7.41	12.58 ± 3.23	1.25 ± 0.47	0.88 ± 0.46	0.07 ± 0.15
$\geq$ 2+ Tag Counts	0.00 ± 0.00	0.14 ± 0.13	0.15 ± 0.10	0.38 ± 0.32	0.07 ± 0.09
Muons					
Pretag Counts	410.61 ± 103.74	71.71 ± 18.95	3.55 ± 1.40	1.31 ± 0.52	0.45 ± 0.18
$\geq$ 1+ Tag Counts	6.74 ± 1.66	3.33 ± 0.98	0.25 ± 0.17	0.00 ± 0.22	0.12 ± 0.21
$\geq$ 2+ Tag Counts	0.00 ± 0.00	0.17 ± 0.13	0.16 ± 0.12	0.00 ± 0.26	0.12 ± 1.08

Table C.33: Non-W expectation, removing $t\bar{t}$. These numbers are for the *optimized* analysis.

C.4 Electron Versus Muon Cross-Check

We have performed cross checks on the different trigger types. We perform the full analysis using only leptons from each trigger (CEM, CMUP, CMX). We then combine the CMUP and CMX results, and compare electrons versus muons.

The cross sections we obtain are

$$\sigma_{t\bar{t}}^{ele} = 8.8 \pm 1.2(stat) \pm 1.0(sys)\ pb \quad \text{(C.1)}$$

$$\sigma_{t\bar{t}}^{muo} = 8.7 \pm 1.4(stat) \pm 1.0(sys)\ pb \quad \text{(C.2)}$$

CEM Summary					
Jet Multiplicity	1 jet	2 jets	3 jets	4 jets	$\geq$ 5 jets
$\geq$ 1 Tags					
EW	2.50 ± 0.40	4.79 ± 0.73	0.65 ± 0.12	0.15 ± 0.03	0.06 ± 0.02
Single Top	4.01 ± 1.40	6.73 ± 1.92	0.95 ± 0.27	0.20 ± 0.06	0.04 ± 0.01
QCD	30.49 ± 7.41	12.58 ± 3.23	1.25 ± 0.47	0.88 ± 0.46	0.07 ± 0.15
W+LF Mistags	53.89 ± 11.35	22.77 ± 4.58	3.73 ± 0.82	1.43 ± 0.29	0.06 ± 0.01
$W + c$	55.42 ± 15.16	11.89 ± 3.51	0.78 ± 0.25	0.31 ± 0.13	0.01 ± 0.01
$W + c\bar{c}$	18.63 ± 5.75	11.40 ± 3.84	1.35 ± 0.50	0.57 ± 0.27	0.00 ± 0.01
$W + b\bar{b}$	54.99 ± 18.33	31.12 ± 10.36	3.23 ± 1.08	1.01 ± 0.45	0.04 ± 0.06
$t\bar{t}$ (8.7 pb)	1.74 ± 0.20	13.77 ± 1.53	26.60 ± 2.90	28.97 ± 3.12	9.26 ± 1.01
Bkg	219.92 ± 41.56	101.28 ± 18.76	11.94 ± 2.09	4.55 ± 1.00	0.28 ± 0.17
Bkg + $t\bar{t}$	221.66 ± 41.56	115.05 ± 18.82	38.54 ± 3.58	33.52 ± 3.28	9.53 ± 1.02
Data	246	137	40	34	8
$\geq$ 2 Tags					
EW	0	0.23 ± 0.05	0.04 ± 0.01	0.01 ± 0.00	0.01 ± 0.01
Single Top	0	0.88 ± 0.19	0.22 ± 0.06	0.04 ± 0.02	0.01 ± 0.00
QCD	0	0.14 ± 0.13	0.15 ± 0.10	0.38 ± 0.32	0.07 ± 0.09
W+LF Mistags	0	0.30 ± 0.07	0.14 ± 0.03	0.06 ± 0.01	-0.06 ± 0.01
W+HF	0	4.72 ± 1.69	0.54 ± 0.19	0.19 ± 0.09	0.01 ± 0.01
$t\bar{t}$ (8.7 pb)	0	2.54 ± 0.43	6.33 ± 1.06	8.29 ± 1.37	2.79 ± 0.46
Bkg	0	6.28 ± 1.71	1.08 ± 0.24	0.68 ± 0.33	0.03 ± 0.09
Bkg + $t\bar{t}$	0	8.82 ± 1.77	7.41 ± 1.08	8.97 ± 1.41	2.82 ± 0.47
Data	0	10	10	6	1

Table C.34: Summary table for CEM electrons only.

CMUP Summary					
Jet Multiplicity	1 jet	2 jets	3 jets	4 jets	$\geq$ 5 jets
$\geq$ 1 Tags					
EW	1.29 ± 0.21	2.39 ± 0.37	0.33 ± 0.06	0.09 ± 0.02	0.03 ± 0.01
Single Top	1.92 ± 0.67	3.30 ± 0.95	0.46 ± 0.13	0.10 ± 0.04	0.01 ± 0.00
QCD	6.74 ± 1.66	3.33 ± 0.98	0.25 ± 0.17	0.00 ± 0.22	0.12 ± 0.21
W+LF Mistags	25.38 ± 5.39	9.80 ± 2.00	1.28 ± 0.26	0.32 ± 0.06	0.09 ± 0.02
$W + c$	27.89 ± 7.28	5.56 ± 1.53	0.32 ± 0.11	0.06 ± 0.04	0.01 ± 0.01
$W + c\bar{c}$	9.38 ± 2.78	5.33 ± 1.69	0.56 ± 0.21	0.11 ± 0.07	0.01 ± 0.00
$W + b\bar{b}$	27.67 ± 8.88	14.55 ± 4.56	1.35 ± 0.45	0.19 ± 0.12	0.04 ± 0.03
ttbar (8.7 pb)	0.89 ± 0.11	7.36 ± 0.82	14.30 ± 1.57	15.08 ± 1.64	4.73 ± 0.53
Bkg	100.27 ± 19.78	44.25 ± 8.21	4.56 ± 0.85	0.87 ± 0.33	0.31 ± 0.21
Bkg + $t\bar{t}$	101.16 ± 19.78	51.61 ± 8.25	18.86 ± 1.78	15.95 ± 1.67	5.03 ± 0.57
Data	108	61	14	18	6
$\geq$ 2 Tags					
EW	0	0.12 ± 0.03	0.02 ± 0.01	0	0
Single Top	0	0.43 ± 0.09	0.10 ± 0.03	0.02 ± 0.01	0
QCD	0	0.17 ± 0.13	0.16 ± 0.12	0.00 ± 0.26	0.12 ± 1.08
W+LF Mistags	0	0.11 ± 0.03	-0.06 ± 0.01	0.11 ± 0.02	0.05 ± 0.01
$W + HF$	0	2.20 ± 0.75	0.22 ± 0.08	0.03 ± 0.02	0.01 ± 0.01
ttbar (8.7 pb)	0	1.36 ± 0.23	3.41 ± 0.57	4.32 ± 0.71	1.42 ± 0.24
Bkg	0	3.03 ± 0.77	0.44 ± 0.15	0.18 ± 0.26	0.18 ± 1.08
Bkg + $t\bar{t}$	0	4.39 ± 0.80	3.85 ± 0.59	4.50 ± 0.76	1.60 ± 1.11
Data	0	5	4	6	2

Table C.35: Summary table for CMUP muons only.

CMX Summary					
Jet Multiplicity	1 jet	2 jets	3 jets	4 jets	$\geq$ 5 jets
$\geq$ 1 Tags					
EW	0.59 ± 0.10	1.11 ± 0.17	0.15 ± 0.03	0.04 ± 0.01	0
Single Top	0.81 ± 0.29	1.28 ± 0.37	0.18 ± 0.05	0.04 ± 0.01	0
QCD	0	0	0	0	0
W+LF Mistags	13.81 ± 3.08	5.66 ± 1.15	0.78 ± 0.16	0.11 ± 0.02	0.13 ± 0.03
$W + c$	15.59 ± 3.87	3.33 ± 0.86	0.18 ± 0.05	0.02 ± 0.01	0.01 ± 0.00
$W + c\bar{c}$	5.24 ± 1.48	3.19 ± 0.96	0.31 ± 0.10	0.04 ± 0.03	0.01 ± 0.00
$W + b\bar{b}$	15.47 ± 4.76	8.71 ± 2.57	0.75 ± 0.22	0.08 ± 0.05	0.07 ± 0.03
$t\bar{t}$	0.32 ± 0.04	2.86 ± 0.32	5.57 ± 0.62	5.84 ± 0.65	1.91 ± 0.21
Bkg	51.52 ± 10.58	23.29 ± 4.57	2.35 ± 0.42	0.34 ± 0.09	0.23 ± 0.04
Bkg + $t\bar{t}$ (8.7 pb)	51.83 ± 10.58	26.15 ± 4.58	7.92 ± 0.75	6.17 ± 0.65	2.14 ± 0.21
Data	73	34	8	6	4
$\geq$ 2 Tags					
EW	0	0.06 ± 0.01	0.01 ± 0.00	0	0
Single Top	0	0.17 ± 0.04	0.04 ± 0.01	0.01 ± 0.00	0
QCD	0	0	0	0	0
W+LF Mistags	0	0.07 ± 0.02	0.02 ± 0.00	-0	0.07 ± 0.02
$W + HF$	0	1.32 ± 0.42	0.12 ± 0.04	0.01 ± 0.01	0.01 ± 0.00
$t\bar{t}$ (8.7 pb)	0	0.53 ± 0.09	1.33 ± 0.22	1.67 ± 0.28	0.58 ± 0.09
Bkg	0	1.61 ± 0.43	0.19 ± 0.04	0.02 ± 0.01	0.08 ± 0.02
Bkg + $t\bar{t}$	0	2.14 ± 0.44	1.52 ± 0.23	1.69 ± 0.28	0.65 ± 0.10
Data	0	0	1	3	0

Table C.36: Summary table for CMX muons only.

C.5 162 pb^{-1} Cross-Check

We have performed a cross-check of the analysis using only the initial 162 pb^{-1}. We find a cross section of

$$\sigma_{t\bar{t}}^{162\ pb^{-1}} = \sigma_{\geq 1} = 8.7 \pm 1.3(stat) \pm 1.0(sys) \tag{C.3}$$

Good Run List 4.0 Summary					
Jet Multiplicity	1 jet	2 jets	3 jets	4 jets	$\geq$ 5 jets
Pretags					
Data	14681	2286	153	70	13
$t\bar{t}$ (8.7 pb)	4.46 ± 0.42	23.86 ± 2.25	40.33 ± 3.80	40.24 ± 3.79	12.74 ± 1.21
$\geq$ 1 Tags					
EW	2.22 ± 0.35	4.19 ± 0.63	0.57 ± 0.10	0.14 ± 0.03	0.05 ± 0.01
Single Top	3.41 ± 0.86	5.73 ± 1.22	0.81 ± 0.17	0.17 ± 0.04	0.03 ± 0.01
Non-W	17.37 ± 4.30	6.66 ± 1.84	0.76 ± 0.33	0.61 ± 0.41	-0.12 ± 0.06
W + LF Mistags	44.27 ± 9.36	18.77 ± 3.78	2.86 ± 0.58	0.97 ± 0.20	-0.06 ± 0.01
$W + c$	48.07 ± 12.75	10.16 ± 2.88	0.59 ± 0.19	0.18 ± 0.09	-0.00 ± 0.01
$W + c\bar{c}$	16.16 ± 4.86	9.74 ± 3.17	1.02 ± 0.38	0.34 ± 0.18	-0.00 ± 0.01
$W + b\bar{b}$	47.70 ± 15.50	26.60 ± 8.55	2.44 ± 0.81	0.61 ± 0.31	-0.02 ± 0.04
$t\bar{t}$ (8.7 pb)	1.49 ± 0.17	12.14 ± 1.34	23.52 ± 2.55	25.25 ± 2.71	8.04 ± 0.87
Bkg	179.21 ± 34.70	81.85 ± 15.30	9.03 ± 1.56	3.04 ± 0.75	-0.13 ± 0.08
Bkg + $t\bar{t}$	180.70 ± 34.70	93.99 ± 15.36	32.55 ± 2.99	28.29 ± 2.81	7.92 ± 0.87
Data	201	98	27	34	8
$\geq$ 2 Tags					
EW	0	0.21 ± 0.04	0.03 ± 0.01	0.01 ± 0.00	0.01 ± 0.00
Single Top	0	0.75 ± 0.14	0.18 ± 0.04	0.04 ± 0.01	0.01 ± 0.00
Non-W	0	0.31 ± 0.19	0.11 ± 0.08	0.41 ± 0.49	-0.12 ± 0.64
W + LF Mistags	0	0.15 ± 0.03	-0.01 ± 0.03	0.25 ± 0.06	0.01 ± 0.01
$W + HF$	0	4.04 ± 1.40	0.40 ± 0.15	0.11 ± 0.06	-0.00 ± 0.01
$t\bar{t}$ (8.7 pb)	0	2.24 ± 0.37	5.60 ± 0.93	7.23 ± 1.19	2.42 ± 0.40
Bkg	0	5.45 ± 1.42	0.72 ± 0.18	0.81 ± 0.50	-0.10 ± 0.64
Bkg + $t\bar{t}$	0	7.69 ± 1.47	6.32 ± 0.95	8.04 ± 1.29	2.32 ± 0.76
Data	0	8	7	10	2

Table C.37: Summary for 162 pb^{-1} cross check.

C.6 Cross Check Using Muon χ^2 Probability Cut

We have performed a cross check cutting on the muon COT χ^2 probability $> 1 \times 10^{-8}$. This removes Non-W backgrounds that have been observed in the dilepton group. Because most of our sample is $t\bar{t}$ for the optimized case, the results are the

same as the default. We obtain

$$\sigma_{\geq 1} = 8.70 \pm 0.91(stat) \pm 1.00(sys) \quad \text{(C.4)}$$

$$\sigma_{\geq 2} = 8.82 \pm 1.67(stat) \pm 1.55(sys) \quad \text{(C.5)}$$

which is consistent with our results.

For the unoptimized analysis, we obtain

$$\sigma_{\geq 1} = 8.61 \pm 0.93(stat) \pm 1.08(sys) \quad \text{(C.6)}$$

$$\sigma_{\geq 2} = 8.34 \pm 1.63(stat) \pm 1.67(sys) \quad \text{(C.7)}$$

The single tag results are not consistent with the analysis we have performed for the unoptimized case. This is because the $t\bar{t}$ fraction is the smallest in this case, and the cross section is more sensitive to the background levels. However, because the unoptimized result is a cross check measurement, we do not feel obligated to use the muon χ^2 probability cut in our analysis at this time.

C.7 Backgrounds Assuming Theoretical Cross Section

The procedure adopted in this analysis was to attribute any excess over background in the W+jets channel to $t\bar{t}$ events, and iterate the $t\bar{t}$ contribution until the cross section was stable to 1%. However, it is possible that there is additional new physics in the top sample, masquerading as $t\bar{t}$ events. Therefore, we also include the backgrounds assuming the theoretical prediction of the $t\bar{t}$ cross section assuming $m_{top} = 178\ GeV/c^2$.

Summary					
Jet Multiplicity	1 jet	2 jets	3 jets	4 jets	$\geq$ 5 jets
		Pretags			
Data	29182	4483	304	136	32
$t\bar{t}$ (8.7 pb)	8.75 ± 0.82	46.87 ± 4.43	79.23 ± 7.48	79.05 ± 7.46	25.03 ± 2.38
		$\geq$ 1 Tags			
EW	4.36 ± 0.69	8.24 ± 1.24	1.12 ± 0.20	0.28 ± 0.06	0.09 ± 0.03
Single Top	6.71 ± 1.69	11.25 ± 2.40	1.58 ± 0.34	0.34 ± 0.08	0.05 ± 0.01
Non-W	35.88 ± 8.65	15.58 ± 3.94	1.39 ± 0.56	0.90 ± 0.54	0.20 ± 0.27
W + LF Mistags	90.08 ± 18.51	36.54 ± 7.34	5.31 ± 1.11	1.63 ± 0.33	0.19 ± 0.04
$W + c$	95.38 ± 25.35	19.84 ± 5.65	1.16 ± 0.38	0.35 ± 0.17	0.02 ± 0.02
$W + c\bar{c}$	32.06 ± 9.65	19.03 ± 6.21	2.02 ± 0.75	0.64 ± 0.34	0.01 ± 0.01
$W + b\bar{b}$	94.64 ± 30.80	51.94 ± 16.75	4.83 ± 1.62	1.14 ± 0.57	0.11 ± 0.10
$t\bar{t}$ (8.7 pb)	2.93 ± 0.34	23.85 ± 2.63	46.21 ± 5.02	49.61 ± 5.32	15.81 ± 1.71
Bkg	359.12 ± 68.95	162.41 ± 30.02	17.42 ± 3.06	5.27 ± 1.26	0.67 ± 0.31
Bkg + $t\bar{t}$ (8.7 pb)	362.04 ± 68.95	186.26 ± 30.13	63.63 ± 5.88	54.88 ± 5.47	16.48 ± 1.74
Data	411	222	62	56	17
		$\geq$ 2 Tags			
EW	0	0.41 ± 0.08	0.06 ± 0.02	0.01 ± 0.01	0.01 ± 0.01
Single Top	0	1.47 ± 0.28	0.36 ± 0.09	0.08 ± 0.02	0.02 ± 0.01
Non-W	0	0.30 ± 0.19	0.29 ± 0.17	0.39 ± 0.43	0.20 ± 1.05
W + LF Mistags	0	0.45 ± 0.10	0.11 ± 0.04	0.08 ± 0.02	0.00 ± 0.03
$W + c$	0	0	0	0	0
$W + c\bar{c}$	0	0.23 ± 0.10	0.01 ± 0.00	0	0
$W + b\bar{b}$	0	7.65 ± 2.64	0.79 ± 0.29	0.21 ± 0.11	0.02 ± 0.02
$t\bar{t}$ (8.8 pb)	0	4.45 ± 0.75	11.13 ± 1.86	14.36 ± 2.36	4.81 ± 0.79
Bkg	0	10.50 ± 2.77	1.62 ± 0.36	0.77 ± 0.45	0.24 ± 1.05
Bkg + $t\bar{t}$ (8.8 pb)	0	14.95 ± 2.87	12.75 ± 1.89	15.13 ± 2.40	5.06 ± 1.32
Data	0	15	15	15	3

Table C.38: Results of muon track χ^2 cut cross-check for the optimized analysis.

C.8 Backgrounds for Top Mass Analyses

The top mass analyses outlined in Ref [66] use a different event selection for the 3-jet bin. In order to more fully reconstruct the event in that bin while taking advantage of the increased statistics, that analysis allows one extra "half-jet" to be identified as a W decay product. It is not considered for tagging. The "half-jet" definition is $E_T > 8$ GeV and $|\eta_D| < 2.4$.

Tables C.42 and C.43 show the background contributions in the 3.5 jet bin for the theoretical cross section, and for the unoptimized measured cross section of 8.9 pb, respectively.

Summary					
Jet Multiplicity	1 jet	2 jets	3 jets	4 jets	$\geq$ 5 jets
Pretags					
Data	29511	4592	736	173	34
$t\bar{t}$ (8.6 pb)	8.84 ± 0.78	47.61 ± 4.24	92.88 ± 8.25	83.00 ± 7.38	25.60 ± 2.29
$\geq$ 1 Tags					
EW	4.44 ± 0.68	8.43 ± 1.24	2.09 ± 0.33	0.38 ± 0.08	0.10 ± 0.03
Single Top	6.83 ± 1.70	11.48 ± 2.41	2.48 ± 0.53	0.41 ± 0.09	0.06 ± 0.01
Non-W	41.16 ± 9.80	19.10 ± 4.71	6.62 ± 1.90	3.07 ± 1.05	0.64 ± 0.41
W + LF Mistags	90.97 ± 18.68	37.37 ± 7.51	10.48 ± 2.13	2.18 ± 0.44	0.18 ± 0.04
$W + c$	95.63 ± 25.63	20.10 ± 5.77	3.07 ± 0.93	0.49 ± 0.22	0.02 ± 0.02
$W + c\bar{c}$	32.31 ± 9.80	19.21 ± 6.31	4.64 ± 1.63	0.79 ± 0.39	0.02 ± 0.02
$W + b\bar{b}$	95.16 ± 31.19	52.63 ± 17.09	10.41 ± 3.28	1.64 ± 0.77	0.10 ± 0.11
$t\bar{t}$ (8.6 pb)	2.96 ± 0.33	24.21 ± 2.55	53.12 ± 5.52	51.68 ± 5.29	16.14 ± 1.67
Bkg	366.49 ± 69.92	168.34 ± 30.71	39.80 ± 6.56	8.96 ± 1.79	1.11 ± 0.43
Bkg + $t\bar{t}$ (8.6 pb)	369.46 ± 69.92	192.55 ± 30.81	92.92 ± 8.57	60.65 ± 5.59	17.25 ± 1.72
Data	416	232	92	61	18
$\geq$ 2 Tags					
EW	0	0.42 ± 0.09	0.14 ± 0.04	0.02 ± 0.01	0.01 ± 0.01
Single Top	0	1.51 ± 0.28	0.53 ± 0.13	0.09 ± 0.03	0.02 ± 0.01
Non-W	0	0.28 ± 0.16	0.88 ± 0.48	0.77 ± 0.49	0.36 ± 2.34
W + LF Mistags	0	0.52 ± 0.12	0.26 ± 0.06	0.11 ± 0.04	0.04 ± 0.04
$W + c$	0	0	0	0	0
$W + c\bar{c}$	0	0.25 ± 0.10	0.03 ± 0.01	0	0
$W + b\bar{b}$	0	7.75 ± 2.70	1.71 ± 0.58	0.31 ± 0.15	0.02 ± 0.02
$t\bar{t}$ (8.3 pb)	0	4.31 ± 0.71	11.76 ± 1.92	14.15 ± 2.28	4.66 ± 0.75
Bkg	0	10.74 ± 2.83	3.54 ± 0.78	1.29 ± 0.51	0.45 ± 2.34
Bkg + $t\bar{t}$ (8.3 pb)	0	15.05 ± 2.92	15.30 ± 2.08	15.45 ± 2.34	5.11 ± 2.46
Data	0	15	17	16	3

Table C.39: Results of muon track χ^2 cut cross-check for the unoptimized analysis.

Optimized Summary, Theoretical Cross Section					
Jet Multiplicity	1 jet	2 jets	3 jets	4 jets	$\geq$ 5 jets
Pretags					
Data	30283	4676	324	142	34
$t\bar{t}$ (6.1 pb)	6.17 $\pm$ 0.58	33.04 $\pm$ 3.12	55.86 $\pm$ 5.27	55.73 $\pm$ 5.26	17.64 $\pm$ 1.68
$\geq$ 1 Tags					
EW	4.38 $\pm$ 0.69	8.28 $\pm$ 1.25	1.13 $\pm$ 0.20	0.28 $\pm$ 0.06	0.09 $\pm$ 0.03
Single Top	6.75 $\pm$ 1.70	11.31 $\pm$ 2.41	1.59 $\pm$ 0.34	0.34 $\pm$ 0.08	0.05 $\pm$ 0.01
Non-W	37.24 $\pm$ 8.97	16.02 $\pm$ 4.03	1.68 $\pm$ 0.58	1.13 $\pm$ 0.56	0.28 $\pm$ 0.28
W + LF Mistags	93.09 $\pm$ 19.09	38.35 $\pm$ 7.70	6.42 $\pm$ 1.34	2.76 $\pm$ 0.55	0.62 $\pm$ 0.12
$W + c$	98.91 $\pm$ 26.31	20.85 $\pm$ 5.91	1.42 $\pm$ 0.43	0.57 $\pm$ 0.21	0.06 $\pm$ 0.02
$W + c\bar{c}$	33.25 $\pm$ 10.02	19.99 $\pm$ 6.50	2.46 $\pm$ 0.86	1.05 $\pm$ 0.43	0.04 $\pm$ 0.02
$W + b\bar{b}$	98.14 $\pm$ 31.97	54.57 $\pm$ 17.53	5.89 $\pm$ 1.85	1.87 $\pm$ 0.72	0.34 $\pm$ 0.15
$t\bar{t}$ (6.1 pb)	2.06 $\pm$ 0.24	16.82 $\pm$ 1.85	32.58 $\pm$ 3.54	34.97 $\pm$ 3.75	11.14 $\pm$ 1.20
Raw Bkg	371.75 $\pm$ 71.52	169.36 $\pm$ 31.39	20.60 $\pm$ 3.51	8.01 $\pm$ 1.58	1.48 $\pm$ 0.36
Bkg + $t\bar{t}$ (6.1 pb)	373.82 $\pm$ 71.52	186.18 $\pm$ 31.45	53.18 $\pm$ 4.98	42.99 $\pm$ 4.07	12.63 $\pm$ 1.26
Data	427	232	62	58	18
$\geq$ 2 Tags					
EW	0	0.41 $\pm$ 0.08	0.06 $\pm$ 0.02	0.01 $\pm$ 0.01	0.01 $\pm$ 0.01
Single Top	0	1.48 $\pm$ 0.28	0.36 $\pm$ 0.09	0.08 $\pm$ 0.02	0.02 $\pm$ 0.01
Non-W	0	0.32 $\pm$ 0.20	0.34 $\pm$ 0.19	0.52 $\pm$ 0.45	0.26 $\pm$ 0.91
W + LF Mistags	0	0.52 $\pm$ 0.12	0.40 $\pm$ 0.08	0.65 $\pm$ 0.13	0.23 $\pm$ 0.05
W+ HF	0	8.27 $\pm$ 2.87	0.98 $\pm$ 0.33	0.35 $\pm$ 0.14	0.05 $\pm$ 0.02
$t\bar{t}$ (6.1 pb)	0	3.10 $\pm$ 0.52	7.76 $\pm$ 1.29	10.01 $\pm$ 1.65	3.35 $\pm$ 0.55
Raw Bkg	0	11.00 $\pm$ 2.90	2.14 $\pm$ 0.41	1.61 $\pm$ 0.49	0.57 $\pm$ 0.92
Bkg + $t\bar{t}$ (6.1 pb)	0	14.10 $\pm$ 2.95	9.90 $\pm$ 1.36	11.62 $\pm$ 1.72	3.93 $\pm$ 1.07
Data	0	15	15	15	3

Table C.40: Summary table assuming theoretical $t\bar{t}$ production cross section for $m_{top} = 178\ GeV/c^2$ for optimized analysis.

Unoptimized Summary, Theoretical Cross Section					
Jet Multiplicity	1 jet	2 jets	3 jets	4 jets	$\geq$ 5 jets
Pretags					
Data	30628	4791	769	179	36
$t\bar{t}$ (6.1 pb)	6.30 $\pm$ 0.56	33.96 $\pm$ 3.02	66.25 $\pm$ 5.88	59.20 $\pm$ 5.25	18.26 $\pm$ 1.63
$\geq$ 1 Tags					
EW	4.47 $\pm$ 0.69	8.47 $\pm$ 1.25	2.10 $\pm$ 0.34	0.39 $\pm$ 0.08	0.10 $\pm$ 0.03
Single Top	6.86 $\pm$ 1.71	11.55 $\pm$ 2.42	2.50 $\pm$ 0.53	0.41 $\pm$ 0.09	0.06 $\pm$ 0.01
Non-W	42.27 $\pm$ 10.06	19.43 $\pm$ 4.79	7.05 $\pm$ 1.99	3.36 $\pm$ 1.10	0.72 $\pm$ 0.41
W + LF Mistags	94.06 $\pm$ 19.28	39.27 $\pm$ 7.89	11.62 $\pm$ 2.36	3.17 $\pm$ 0.64	0.60 $\pm$ 0.12
$W + c$	99.24 $\pm$ 26.61	21.13 $\pm$ 6.04	3.39 $\pm$ 1.00	0.71 $\pm$ 0.26	0.05 $\pm$ 0.02
$W + c\bar{c}$	33.53 $\pm$ 10.17	20.20 $\pm$ 6.61	5.13 $\pm$ 1.76	1.13 $\pm$ 0.47	0.06 $\pm$ 0.03
$W + b\bar{b}$	98.75 $\pm$ 32.37	55.33 $\pm$ 17.89	11.51 $\pm$ 3.53	2.37 $\pm$ 0.92	0.32 $\pm$ 0.15
$t\bar{t}$ (6.1 pb)	2.11 $\pm$ 0.24	17.27 $\pm$ 1.82	37.89 $\pm$ 3.94	36.86 $\pm$ 3.77	11.51 $\pm$ 1.19
Raw Bkg	379.17 $\pm$ 72.53	175.38 $\pm$ 32.12	43.29 $\pm$ 7.06	11.54 $\pm$ 2.09	1.90 $\pm$ 0.48
Bkg + $t\bar{t}$ (6.1 pb)	381.28 $\pm$ 72.53	192.65 $\pm$ 32.17	81.18 $\pm$ 8.08	48.40 $\pm$ 4.31	13.42 $\pm$ 1.28
Data	432	242	95	63	19
$\geq$ 2 Tags					
EW	0	0.42 $\pm$ 0.09	0.14 $\pm$ 0.04	0.02 $\pm$ 0.01	0.01 $\pm$ 0.01
Single Top	0	1.52 $\pm$ 0.29	0.53 $\pm$ 0.13	0.09 $\pm$ 0.03	0.02 $\pm$ 0.01
Non-W	0	0.29 $\pm$ 0.17	0.94 $\pm$ 0.51	0.81 $\pm$ 0.50	0.39 $\pm$ 2.17
W + LF Mistags	0	0.59 $\pm$ 0.13	0.54 $\pm$ 0.11	0.60 $\pm$ 0.12	0.24 $\pm$ 0.05
W + HF	0	8.41 $\pm$ 2.93	1.92 $\pm$ 0.64	0.43 $\pm$ 0.18	0.05 $\pm$ 0.03
$t\bar{t}$ (6.1 pb)	0	3.19 $\pm$ 0.52	8.69 $\pm$ 1.42	10.46 $\pm$ 1.69	3.44 $\pm$ 0.55
Raw Bkg	0	11.24 $\pm$ 2.97	4.06 $\pm$ 0.84	1.95 $\pm$ 0.55	0.70 $\pm$ 2.17
Bkg + $t\bar{t}$ (6.1 pb)	0	14.42 $\pm$ 3.01	12.75 $\pm$ 1.65	12.41 $\pm$ 1.77	4.14 $\pm$ 2.24
Data	0	15	17	16	3

Table C.41: Summary table assuming theoretical $t\bar{t}$ production cross section for $m_{top} = 178\ GeV/c^2$ for unoptimized analysis.

Summary	
Jet Multiplicity	3.5 jets
Pretags	
Data	280
$t\bar{t}$ (6.1 pb)	33.29 ± 2.98
$\geq$ 1 Tags	
EW	0.67 ± 0.11
Single Top	0.59 ± 0.13
Non-W	2.24 ± 0.78
Mistags	4.60 ± 0.91
$W + c$	1.22 ± 0.36
$W + c\bar{c}$	1.84 ± 0.63
$W + b\bar{b}$	4.12 ± 1.27
$t\bar{t}$ (6.1 pb)	18.97 ± 1.98
Bkg	15.28 ± 2.56
Bkg + $t\bar{t}$	34.25 ± 3.24
Data	39
$\geq$ 2 Tags	
EW	0.04 ± 0.01
Single Top	0.12 ± 0.03
Non-W	0.52 ± 0.32
Mistags	0.17 ± 0.03
$W + HF$	0.68 ± 0.23
$t\bar{t}$ (6.1 pb)	4.30 ± 0.70
Bkg	1.54 ± 0.40
Bkg + $t\bar{t}$	5.84 ± 0.81
Data	6

Table C.42: Method 2 background calculation summary for 318.5 pb^{-1} in the 3.5 jet bin. Here, the $t\bar{t}$ subtraction from the backgrounds is taken for $\sigma = 6.1$ pb.

Summary	
Jet Multiplicity	3.5 jets
Pretags	
Data	280
$t\bar{t}$ (8.9 pb)	48.57 ± 4.35
$\geq$ 1 Tags	
EW	0.67 ± 0.11
Single Top	0.59 ± 0.13
Non-W	1.99 ± 0.72
Mistags	4.30 ± 0.85
$W + c$	1.13 ± 0.35
$W + c\bar{c}$	1.72 ± 0.60
$W + b\bar{b}$	3.85 ± 1.22
$t\bar{t}$ (8.9 pb)	27.68 ± 2.89
Bkg	14.25 ± 2.45
Bkg + $t\bar{t}$	41.93 ± 3.79
Data	39
$\geq$ 2 Tags	
EW	0.04 ± 0.01
Single Top	0.12 ± 0.03
Non-W	0.39 ± 0.30
Mistags	0.02 ± 0.01
$W + HF$	0.64 ± 0.22
$t\bar{t}$ (8.9 pb)	6.28 ± 1.02
Bkg	1.22 ± 0.38
Bkg + $t\bar{t}$	7.50 ± 1.09
Data	6

Table C.43: Method 2 background calculation summary for 318.5 pb^{-1} in the 3.5 jet bin. Here, the $t\bar{t}$ subtraction from the backgrounds is taken for $\sigma = 8.9$ pb.

C.9 Cross Check: $W \rightarrow l\nu$ Cross Section

As a cross-check to the $t\bar{t} \rightarrow Wl\nu b\bar{b}qq$ analysis, we calculate the $W \rightarrow l\nu X$ cross section in the ≥ 0 jet bins. We do this in a rough and approximate way in order to be sure there are no major problems.

We perform the analysis in two ways. First, we examine the effect of using the same background fractions as the Gen4 analysis outlined in Ref [67]. This is not strictly correct because the electron analysis had higher E_T and $\not\!\!E_T$ cuts than we do (they use 25 GeV for both, we use 20 for both).

Then, we calculate the backgrounds for our analysis cuts. The method we have used is to calculate the electroweak backgrounds using Monte Carlo predictions and scale factors, along with the theoretical cross sections. The Non-W backgrounds are estimated in the same $\not\!\!E_T$ vs iso method as the $t\bar{t}$ analysis.

The Monte Carlo samples used are $W \rightarrow l\nu$ (for electrons, muons, and taus) and $Z \rightarrow l^+l^-$ (for electrons and muons), all generated with PYTHIA. We then require the events to pass the event selection for the $t\bar{t}$ analysis, except that we examine ≥ 0 jets.

Our results are summarized in Table C.44. We notice that the electron and muon results are not consistent with each other. This has been seen in the dilepton channel, and was attributed to a poor modelling of the track χ^2 probability of muons.

We have repeated the analysis using a cut on the COT χ^2 probability of $P < 1 \times 10^{-8}$. The results are outlined in Table C.45. In this table, the ratio of cross sections for the electron and muon channels are consistent within statistical errors (the dominant systematic is the luminosity, which is correlated between the two mea-

surements).

The effect on the $t\bar{t}$ cross section is lessened because of the optimization cuts. Most of the sample is $t\bar{t}$ anyway, so the effect of fake muons is smaller than the W cross section. Using this cut, the optimized cross sections change by 0.0 pb for the ≥ 1 tag, and +0.1 pb for ≥ 2 tags. The unoptimized cross sections change by -0.3 pb for the ≥ 1 tag, and +0.1 pb for ≥ 2 tags. The fit result changes by -0.2 pb.

We have not used this cut because the effect is small.

	CEM	CMUP	CMX
Pretag Efficiency	0.2328 ± 0.0000	0.1313 ± 0.0000	0.0586 ± 0.0000
Lepton ID SF	0.959 ± 0.015	0.794 ± 0.015	0.954 ± 0.016
Luminosity (pb^{-1})	318.5	318.5	305.2

	Electron	Muon
$\epsilon \int \mathcal{L}dt$	71.1 ± 4.4	51.4 ± 4.6
$N_{observed}$	198940	158498
Using Gen4 Background Fractions		
F_{BKG}, Gen4	0.045 ± 0.008	0.095 ± 0.005
Cross Section (pb)	2672 ± 6 (stat) ± 166 (sys)	2788 ± 7 (stat) ± 247 (sys)
Using Gen5 Background Fractions		
F_{Non-W}	0.029 ± 0.007	0.014 ± 0.003
$F_{Z\to l^+l^-}$	0.0030 ± 0.0002	0.038 ± 0.002
$F_{W\to\tau\nu}$	0.036 ± 0.002	0.029 ± 0.002
F_{BKG}, Gen5	0.068 ± 0.006	0.081 ± 0.011
Cross Section (pb)	2607 ± 6 (stat) ± 173 (sys)	2833 ± 7 (stat) ± 255 (sys)

Table C.44: Summary for W cross section calculation, *without* additional χ^2 probability cut on muons.

	CEM	CMUP	CMX
Pretag Efficiency	0.2328 ± 0.0000	0.1313 ± 0.0000	0.0586 ± 0.0000
Lepton ID SF	0.959 ± 0.015	0.794 ± 0.015	0.954 ± 0.016
Muon χ^2 Prob SF	-	0.987 ± 0.013	0.987 ± 0.013
Luminosity (pb^{-1})	318.5	318.5	305.2

	Electron	Muon
$\epsilon \int \mathcal{L}dt$	71.1 ± 4.4	51.4 ± 4.6
$N_{observed}$	198940	143980
Using Gen4 Background Fractions		
F_{BKG}, Gen4	0.045 ± 0.008	0.095 ± 0.005
Cross Section (pb)	2672 ± 6 (stat) ± 166 (sys)	2566 ± 6 (stat) ± 234 (sys)
Using Gen5 Background Fractions		
F_{Non-W}	0.029 ± 0.007	0.012 ± 0.003
$F_{Z\to l^+l^-}$	0.0030 ± 0.0002	0.038 ± 0.002
$F_{W\to\tau\nu}$	0.036 ± 0.002	0.029 ± 0.002
F_{BKG}, Gen5	0.068 ± 0.006	0.081 ± 0.011
Cross Section (pb)	2607 ± 6 (stat) ± 173 (sys)	2596 ± 6 (stat) ± 242 (sys)

Table C.45: Summary for W cross section calculation, *with* additional χ^2 probability cut on muons.

Bibliography

[1] H. Bachacou, C. Ferretti, J. Nielsen, and W. Yao, Heavy Flavor Contributions to the SECVTX-tagged W + Jets Sample, CDF Note 7007.

[2] C. Ferreti, Alpgen cross sections, http://cdfrh0.grid.umich.edu/ claudiof/physics/Wjets/xsec/alpgen_xsec.html.

[3] S. L. Glashow, Partial Symmetries OF Weak Interactions, *Nucl. Phys.* **22** 579 (1961).

[4] J. I. S. L. Glashow and L. Maiani, Weak Interactions With Lepton - Hadron Symmetry, *Phys. Rev.* **D 2** (1285) 1970.

[5] F. Halzen and A. Martin, Quarks and Leptons: An Introductory Course in Modern Particle Physics, 1984.

[6] S. E. et. al., Review of Particle Physics, 2004.

[7] D. Griffiths, Introduction to Elementary Particles, 1987.

[8] I. Aitchison and A. Hey, Gauge Theories in Particle Physics, 2nd Edition, 1989.

[9] V. Berger and R. Phillips, Collider Physics, 1984.

[10] J. Pumplin *et al.*, *J. High Energy Phys.* **0207** (012) 2002.

[11] D. Stump *et al.*, hep-ph/0303013.

[12] T. Sjostrand *et al.*, *Comput. Phys. Commun.* **135** (2001) 238.

[13] M. Mangano, ALPGEN, A Generator for Hard Multiparton Processes in Hadronic Collisions, JHEP 0307:001 (2003).

[14] G. Corcella *et al.*, HERWIG 6.5, *J. High Energy Phys.* **0101** (2001) 010.

[15] M. Cacciari, S. Frixione, M. L. Mangano, P. Nason, and G. Ridolfi, *J. High Energy Phys.* **0404** (068) 2004.

[16] N. Kidonakis and R. Vogt, *Phys. Rev.* **D 68** (114014) 2003.

[17] I. B. et. al., *Phys. Lett.* **B 181** (157) 1986.

[18] F. B. Division, Tevatron Rookie Books, http://www-bdnew.fnal.gov/operations/rookie_books/Concepts_PDF/Accelerator_Concepts.html.

[19] J. B. Flaugher, A Guide To JetClu: The CDF Jet Cluster Algorithm, CDF Note 1814.

[20] F. Canelli and A. Bhatti, Generic Jet Corrections for Run II, CDF Note 7358.

[21] D. A. et. al., The CDF Cherenkov Luminosity Monitor, *Nucl. Instrum. Meth.* **461** (540-544) 2001.

[22] D. A. et. al., The Performance of the CDF Run II Luminosity Monitor, *Nucl. Instrum. Meth.* **494** (57-62) 2002.

[23] C. H. O. behalf of the CDF Collaboration], Operational experience and performance of the CDFII silicon detector, *Nucl. Instrum. Meth.* **530** (1) 2004.

[24] A. S. et. al., The Performance of the CDF Run II Luminosity Monitor, *Nucl. Instrum. Meth.* **447** (1-8) 2000.

[25] D. A. et. al., The CDF Intermediate Silicon Layers Detector, *Nuovo Cim.* **112A** (1351) 1999.

[26] D. A. et. al., The CDF Intermediate Silicon Layers Detector at CDFII: Design and Progress, *Nucl. Instrum. Meth.* **435** (44) 1999.

[27] T. A. et. al., CDF Central Outer Tracker, *Nucl. Instrum. Meth.* **A526** (249) 2004.

[28] L. B. et. al., CDF Central Electromagnetic Calorimeter, *Nucl. Instrum. Meth.* **A267** (272) 1988.

[29] L. B. et. al., CDF Central Hadronic Calorimeter, *Nucl. Instrum. Meth.* **A267** (301) 1988.

[30] G. A. et. al., CDF Central Muon Detector, *Nucl. Instrum. Meth.* **A268** (33) 1988.

[31] A. A. et. al., CDF Central Muon Detector, *Prog. Part. Nucl. Phys.* **114** (25-39) 2002.

[32] Ayana Holloway and Daniel Sherman and Salvatore Rappoccio and Sebastian Grinstein and Joao Guimaraes da Costa, SecVtx Scale Factor Measurement for Gen5 Tagger, CDF Note 7333.

[33] S. *et al.*. Barioant, Measurement of Electron Trigger Efficiencies for Level1 and Level2 8 GeV Triggers, CDF Note 6257.

[34] E. Halkiadakis, C. Hays, M. Tecchio, and W. Yao, A Conversion Removal Algorithm for the 2003 Winter Coferences, CDF Note 6250.

[35] A. Foland, J. G. da Costa, and S. Rappoccio, Examination of Material Effects Using Jet Data In SecVtx For the Winter 2004 Conferences, CDF Note 6906.

[36] Thomas Wright, SecVtx B-Tag Efficiency using Muon Transverse Momentum, CDF Note 7448.

[37] H. Bachacou *et al.*, Combining the SecVtx B-Tagging Scale Factors for 5.3.3 Analyses, CDF Note 7480.

[38] A. Dominguez, J. G. da Costa, A. Holloway, and S. Rappoccio, The SecVtx Tag Rate Matrix for the 2003 Summer Conferences, CDF Note 6533.

[39] J. G. da Costa *et al.*, Measurement of the ttbar Production Cross Section using a Loose SecVtx Algorithm, CDF Note 6983.

[40] H. Bachacou, J. Nielsen, and W. Yao, Optimized Measurement of the t-tbar Production Cross Section with SECVTX, CDF Note 6902.

[41] J. ao Guimarães da Costa, S. Rappoccio, and D. Sherman, Measurement of the SecVtx Mistag Asymmetry in 5.3.3, CDF Note 7585.

[42] Joao Guimaraes da Costa and Salvatore Rappoccio, SecVtx Tag Matrices for 5.3.3_nt, CDF Note 7326.

[43] R. Cousins and G. Feldman, Unified approach to the classical statistical analysis of small signals, PRD V57 No.7, p3873-3889.

[44] G. Unal, $W + b\overline{b}$ and $W + c\overline{c}$ Backgrounds in the Top SVX Analysis, CDF Note 3389.

[45] R. Erbacher and Y. Ishizawa and B. Kilminster and K. Lannon and P. Lujan and T. Maki and B. Mohr and J. Nielsen and E. Palencia and S. Rappoccio and R. Rossin and M. Soderberg and V. Sorin and K. Yorita, Preliminary Event Selection and t-tbar Signal Acceptance for the Winter 2005 Top Lepton + Jets Sample, CDF Note 7372.

[46] Daniel Jeans, Offline track studies, CDF Note 7105.

[47] M. C. et al., THE T ANTI-T CROSS-SECTION AT 1.8-TEV AND 1.96-TEV: A STUDY OF THE SYSTEMATICS DUE TO PARTON DENSITIES AND SCALE DEPENDENCE., JHEP 0404:068 (2004).

[48] H. Bachacou, J. Nielsen, and W. Yao, Optimized Measurement of the t-tbar Production Cross Section with SECVTX, CDF Note 6902.

[49] C. Hill, J. Incandela, , and C. Mills, Electron Identification in Offline Release 5.3, CDF Note 7309.

[50] V. Martin, High-Pt Muon ID Cuts and Efficiencies for use with 5.3.1 Data and 5.3.3 MC, CDF Note 7367.

[51] K. Bloom, J. Conway, R. Erbacher, T. Maruyama, and M. Shochet, High Pt Lepton ID Efficiency Scale Factor Studies in 4.11.1, CDF Note 6858.

[52] H. Georgi, Lie Algebras in Particle Physics, 1999.

[53] R. Feynman, Mathematical Formulation OF THE Quantum Theory OF Electromagnetic Interaction, *Phys. Rev.* **80** (440-457) 1950.

[54] M. Veltman, *Nucl. Phys.* **B 7** (1968) 637.

[55] G. 't Hooft, *Nucl. Phys.* **B 35** (1971) 167.

[56] M. Veltman and G. 't Hooft, *Nucl. Phys.* **B 35** (1972) 189.

[57] N. Cabbibo, *Phys. Rev. Lett.* **10** 1950 (531).

[58] M. Kobayashi and K. Maskawa, *Prog. Theor. Phys.* **49** (1973) 652.

[59] J. Christenson, J. Cronin, V. Fitch, and R. Turlay, Evidence for the 2-PI Decay of the K(2)0 Meson, *Phys. Rev. Lett.* **13** 138-140 (1964).

[60] M. Gell-Mann, A Schematic Model of Baryons and Mesons, *Phys. Lett.* **8** (214-215) 1964.

[61] O. Greenberg and C. Nelson., Color models of hadrons, *Phys. Rept.* **32** (1977) 69-121.

[62] D. Gross and F. Wilczek, Ultraviolet Behaviour of Non-Abelian Gauge Theories, *Phys. Rev. Lett.* **30** 1343 (1973).

[63] H. Politzer, Reliable Perturbative Results for Strong Interactions, *Phys. Rev. Lett.* **30** 1346 (1973).

[64] D. Gross and F. Wilczek, Asymptotically Free Gauge Theories, *Phys. Rev.* **D 8** (3633) 1973.

[65] H. Politzer, Asymptotic Freedom: An Approach To Strong Interactions, *Phys. Rept.* **14** (129) 1974.

[66] J. Adelman *et al.*, Measurement of the Top Quark Mass using the Template Method in the Lepton plus Jets channel at CDF, CDF Note 7680.

[67] D. Amidei *et al.*, First Measurements of Inclusive W and Z Cross Sections from Run II of the Tevatron Collider, CDF Note 7014.

Glossary

Notation	Description
4.11.2	See Gen4., 86, 114, 178, 212
5.3.3_nt	See Gen5., 86, 114, 177, 178, 212, 235
bhel0d	High p_T central electron triggered dataset., 147
bhmu0d	High p_T central muon triggered dataset., 147
CDF	Collider Detector at Fermilab., 47
CEM	Central Electromagnetic Calorimeter for CDF detector., 73
CHA	Central Hadronic Calorimeter for CDF detector., 73
CLC	Cerenkov Luminosity Counters., 67
CMP	Central Muon Detector Upgrade for CDF detector., 75
CMU	Central Muon Detector for CDF detector., 75

Notation	Description
CMX	Central Muon Detector Extension for CDF detector., 75
COT	Central Outer Tracker. Drift chamber for CDF detector., 68, 147
DQM	Data Quality Monitoring group. This group creates a good run list based on availability of detector components., 147
E_T	Jet transverse energy., 147, 188
$\eta_{detector}$	Detector rapidity. This is the rapidity of the physical calorimeter tower., 147, 188
η	Pseudo-rapidity., 48
Gen4	CDF software version for previous PRD measurement [40]., 86, 212
Gen5	CDF software version for this measurement., 86, 212
ISL	Intermediate Silicon Layers. Used for linking tracks between SVX and COT. Also for silicon standalone tracks, 68

Notation	Description
`jetCorr04b`	Level of jet corrections., 147, 188
Jet energy scale	Energy discrepancy between data and simulation., 58
JetClu	Jet clustering algorithm for CDF detector., 57, 147, 188
L00	Layer 00. Innermost silicon detector at CDF. Used for better impact parameter measurement., 68
$\not\!\!E_T$	Missing transverse energy. This is calculated by negating the vector sum of the transverse energies of the event., 142
PEM	Plug Electromagnetic Calorimeter for CDF detector., 73
PHA	Plug Hadronic Calorimeter for CDF detector., 73
SecVtx	Secondary Vertex tagger for CDF, 83, 142
SVXII	Silicon Vertex Detector. Primary silicon detector for CDF., 68

Notation	Description
WHA	Wall Hadronic Calorimeter for CDF detector., 73
`ZVertexModule`	Simple vertex module for finding the z-vertex of the event., 147, 188